Modeling of Microstructure Evolution Induced by Surface Mechanical Attrition Treatment in TWIP/TRIP Steels

Zhenglin Chen

Thèse
de doctorat
de l'UTT

Zhenglin CHEN

Modeling of Microstructure Evolution Induced by Surface Mechanical Attrition Treatment in TWIP/TRIP Steels

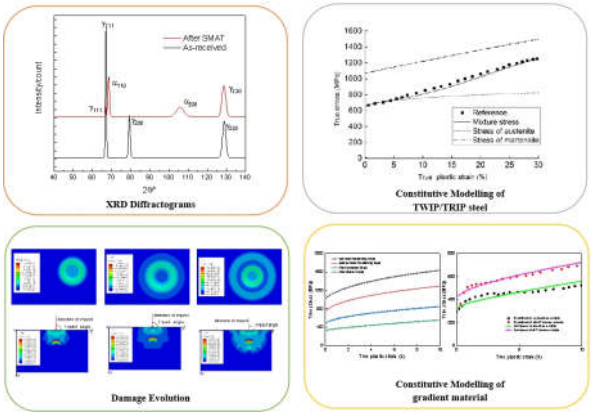

Champ disciplinaire :
Sciences pour l'Ingénieur

2020TROY0017 **Année 2020**

utt
UNIVERSITÉ DE TECHNOLOGIE
TROYES

THESE

pour l'obtention du grade de

DOCTEUR
de l'UNIVERSITE DE TECHNOLOGIE DE TROYES

EN SCIENCES POUR L'INGENIEUR

Spécialité : MATERIAUX, MECANIQUE, OPTIQUE, NANOTECHNOLOGIE

présentée et soutenue par

Zhenglin CHEN

le 21 octobre 2020

Modeling of Microstructure Evolution Induced by Surface Mechanical Attrition Treatment in TWIP/TRIP Steels

JURY

Mme Marion RISBET	PROFESSEURE DES UNIVERSITES	Présidente
M. Lahouari BENABOU	MAITRE DE CONFERENCES - HDR	Rapporteur
M. Laurent DELANNAY	PROFESSEUR	Rapporteur
M. Sylvain FREOUR	MAITRE DE CONFERENCES - HDR	Examinateur
M. Ludovic THILLY	PROFESSEUR DES UNIVERSITES	Examinateur
M. Benoit PANICAUD	PROFESSEUR DES UNIVERSITES	Directeur de thèse
M. Zhidan SUN	PROFESSEUR ASSOCIE UTT	Directeur de thèse

To my family, my teachers, and my friends.

Acknowledgments

I would like to express my heartfelt thanks to all those who have provided a lot of help and support in the process of writing my thesis.

First of all, my heartiest thanks flow to my supervisors Professor Benoit Panicaud and Doctor Sun Zhidan. It was their patient guidance, valuable advice, and constant encouragement that made me successfully complete my Ph.D. thesis.

Also, I would like to thank all the professors and colleagues in the LASMIS lab; most of my Ph.D. work was done in the LASMIS lab. During the experiment, I was much helped and supported by the professors and colleagues of the LASMIS lab. Your valuable suggestions on scientific research have benefited me a lot.

I also want to thank the scholars whose monographs and academic papers inspired me in the writing of my thesis.

Finally, I would like to extend my deep gratefulness to my family and friends, especially my wife Yang Jiaqi and my son Chen Qizhen, whose encouragement and accompany have made my accomplishments possible.

Abstract

This work focuses on modeling the microstructure evolution induced by surface mechanical attrition treatment (SMAT) in TWIP/TRIP steels. The features of the generated gradient microstructure of a 304L TWIP/TRIP steel are characterized by SEM, XRD, and nanoindentation. Nanoindentation is applied to a multilayer material for the investigation of the mechanical properties of the gradient microstructure. Based on the experimental results, a dislocation density model considering the influence of twinning and martensitic transformation of TWIP/TRIP steels is proposed to investigate the effect of SMAT controlling parameters. Then the dislocation density of austenite and martensite as well as the volume fraction of twin and martensite generated by impact loading is numerically evaluated using a full Finite Element (FE) model. Afterward, to study the evolution of damage during the SMAT process, the damage is introduced in the dislocation density model. Finally, a dislocation density based visco-elastoplastic model considering the effects of grain size, dislocation density, twin, and strain rate is proposed to further understand the effect of impact loadings on the mechanical properties of TWIP/TRIP steel with gradient microstructure based on the results of nanoindentation tests. To study the overall elastoplastic response of the SMATed material, the mixing rule is used by considering the SMATed gradient material as a gradient structure consisting of different layers with particular microstructures and mechanical properties.

Keywords: SMAT; Steel, Stainless; Dislocations in crystals; Martensitic transformations; Twinning (Crystallography)

Résumé

Ce travail est centré sur la modélisation de l'évolution de la microstructure induite par le procédé SMAT (surface mechanical attrition treatment) dans un acier TWIP/TRIP. Les caractéristiques de base d'un acier TWIP/TRIP sont mises en évidence par la microscopie électronique à balayage (MEB), la diffraction des rayons X (DRX) et la nanoindentation. La nanoindentation est appliquée sur différentes couches pour l'étude des propriétés mécaniques du matériau à gradient de microstructure. Un modèle basé sur la densité de dislocation tenant compte de l'influence du maclage et de la transformation de phase martensitique dans un acier TWIP/TRIP est proposé pour étudier l'influence des paramètres induits par SMAT. Ensuite, la densité de dislocations dans l'austénite et celle dans la martensite, ainsi que les fractions volumiques de macles et de martensite au cours d'un impact, sont évaluées numériquement avec un modèle d'éléments finis. Par ailleurs, afin d'étudier l'évolution de l'endommagement pendant le processus d'impact, l'endommagement a été introduit dans le modèle de la densité de dislocations. Enfin, un modèle visco-élastoplastique basé sur la densité de dislocations considérant l'effet de la taille de grain, le maclage et le taux de déformation a été proposé afin de mieux comprendre les effets du SMAT sur les propriétés mécaniques d'un acier TWIP/TRIP avec gradient de microstructure. Ainsi, pour étudier la réponse élastique globale du matériau SMATé, la loi de mélange est utilisée en considérant le gradient du matériau comme une structure composée de différentes couches avec des microstructures et des propriétés mécaniques différentes.

Mots clefs: SMAT ; Acier inoxydable ; Dislocations dans les cristaux ; Transformations martensitiques ; Maclage (cristallographie)

CONTENTS

LIST OF TABLES

LIST OF FIGURES

CHAPTER 1 INTRODUCTION

1.1 General background

Austenitic stainless steel (SS) is an alloy of iron with chromium (Cr) and nickel (Ni) elements and is known for its excellent corrosion resistance [1]. Therefore, stainless steel is widely used in modern industrial production fields, such as automotive, biomedical, chemical, food, aerospace, chemical processing, and nuclear industries [2]. However, stainless steel has some defects, such as low mechanical strength, low fatigue strength, and poor cutting performance. The mechanical properties of SS can reflect the changes of the microstructure caused by fatigue, while the fatigue depends on surface hardness, initial residual stress (IRS), etc. The progressive accumulation of plastic strain under cyclic loading caused by material fatigue may lead to the formation of microcracks [3]. When lacking compressive residual stress (CRS) of structural components, the fatigue performance of stainless steel is reduced, which can restrict the use of SS. Previous studies also showed that most of material failures start on top surfaces such as fatigue fracture, fretting fatigue, wear, corrosion, etc. These failures are very sensitive to the structure and characteristics of the material surface. The overall performance of the material can be significantly enhanced by effectively changing the surface structure and properties. Therefore, the CRS field can be introduced by surface engineering/modification technology to improve the fatigue performance of structural components [1], [2].

In the past few decades, due to the advantages over other methods (such as chemical deposition or composite materials), the technology of surface treatment by plastic deformation has attracted more and more attention. The performance improvements brought by the surface deformation process are mainly attributed to plastic deformation without changing its chemical composition. Various surface deformation processes have been proposed, and many experimental studies have also been conducted to obtain nanocrystalline structures under plastic deformation

[4]–[14]. These experimental results show that the main deformation modes and surface nanocrystallization mechanisms during high energy ball impacts depend on the crystal structure and the Stacking Fault Energy (SFE) of impacted solid. However, as many details of the grain refinement mechanism are unclear, there is still a lack of direct theoretical explanation or simulation of nanoscale grain formation.

1.2 Motivation and objectives

SMAT can transform coarse-grained material in the top surface into nanostructured material. Fig. I-1 shows a typical cross-sectional optical microstructure of a pure titanium sample after SMAT processing for 30 min [15]. An overall microstructure gradient with a grain size distribution from a few nanometers to several micrometers can be observed in the SMAT affected region. Three different areas can be roughly distinguished. They are respectively the nanostructured layer, the interior region non-affected by SMAT, and the transition region between them.

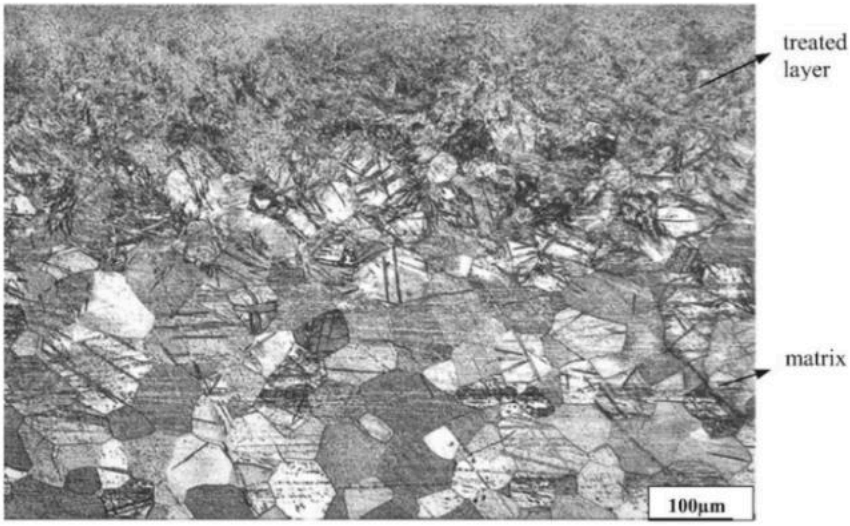

Fig. I-1. Optical micrograph of a SMATed pure titanium sample [15].

Due to some excellent mechanical properties of SMATed materials, it is necessary and useful to investigate the SMAT process both experimentally and numerically to obtain a better understanding and control of the process. Experimental studies performed previously in the literature [16]–[19] have shown that the mechanical properties of SMATed materials are highly influenced by the

microstructure such as grain size and by the mechanical state such as work hardening. From a modeling point of view, it would be highly beneficial to establish accurate numerical models of SMAT process to consider the influence of different parameters.

During SMAT, high compressive residual stresses are generally introduced in the mechanically affected layer due to the incompatibility of elastic deformation of the material [8]. The presence of the nanostructured layer and the high compressive residual stresses can significantly improve the mechanical properties of materials under various loading conditions. As the near-surface region is mechanically affected by SMAT, it can lead to a uniform grain size refinement due to severe plastic deformation, whereas the bulk of the part is not mechanically deformed so that its characteristics and mechanical properties remain unchanged [20]. A gradient microstructure is thus formed from the treated surface to the interior region of the material [21]. The particularity of the SMAT with respect to the conventional shot peening lies in the fact that it can transform the top surface layer of materials from coarse grains to nano-sized grains. This nanostructured layer, even if it is thin in general, may have a significant effect on the performance of materials since engineering components are mostly loaded on their surface, for example, in the case of friction, torsion, or contact loading [22]. To understand the mechanical behavior of SMATed materials, it is also important to characterize the mechanical properties of different regions, such as the nanostructured layer and the plastically deformed region.

TWIP/TRIP steels gain increasing attention, especially in automotive structural applications, due to their high energy absorption capacity and fatigue strength. Their mechanical behaviors in relation to microstructure evolution during deformation have been extensively studied [23]–[25], and the deformation mechanisms of this kind of steels, even if complex, have been well highlighted [26]. From the metallurgical point of view, TWIP/TRIP steels have a narrow range of SFE (from 15 to 22 mJ/m^{-2}, according to [27]), which is essential to ensure the presence of both twinning and martensitic transformation during deformation [28]. For these kinds of materials, during the material deformation process, twinning and martensitic transformation can be induced by plastic deformation [29]–[31]. The occurrence of twinning reduces the mean free path, through which a dislocation can slide [32]. The generated martensite makes the alloy harder and stronger due to its mechanical strength higher than that of the original austenite before transformation [33]. Therefore, it is interesting to study

the simultaneous influence of both twinning and martensitic transformation on the strength and the plasticity of such materials during and after SMAT treatment.

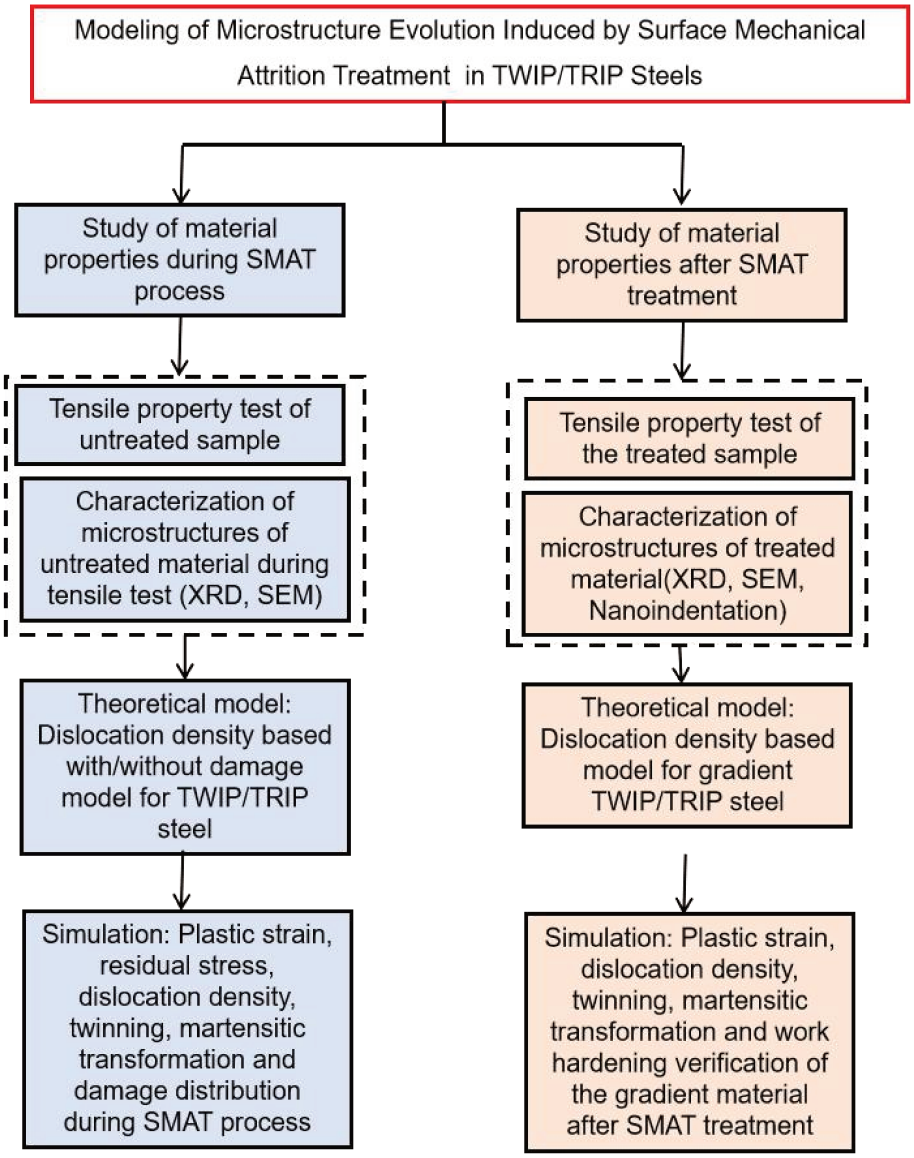

Fig. I-2. Flow chart of this work.

In summary, the goal of the whole project can be defined as "Modeling of microstructure evolution induced by Surface Mechanical Attrition Treatment in TWIP/TRIP steels." The main tasks of this work are described in Fig. I-2. First, a dislocation density-based model is used to study SMAT process and investigate the influence of various SMAT parameters, such as ball size, impact velocity, impact angle, impact duration, collision frequencies and so on. At the same time, twinning and phase transformation will be numerically evaluated. The studies provide more information for us to better understand the SMAT process. Then the hardening

properties of the gradient TWIP/TRIP steel with a nanostructured layer generated by SMAT are studied experimentally by nanoindentation in the cross-section at different distances from the top surface. Based on the dislocation density model, a dislocation density visco-elastoplastic model considering the effect of grain size, dislocation density, twinning, strain rate, and damage is proposed to better understand the influence of SMAT on the material.

1.3 Organization of this thesis

This thesis is mainly focused on the investigation of the SMAT process through modeling. The dissertation is organized as follows. A comprehensive literature review is presented in Chapter 2, which provides an overview of SMAT and the studied material. The SMAT set-up, the microstructural characteristics and the properties of materials after SMAT are introduced. The mechanism of grain refinement during SMAT is studied.

Chapter 3 introduces the investigation methodology and equipment used in this work, which includes scanning electron microscopy (SEM), X-ray diffraction (XRD), and nanoindentation.

In Chapter 4, a dislocation density model for TWIP/TRIP steel is developed and implemented to investigate the influence of SMAT controlling parameters. Then, a full FE model for a single impact simulation is established. The distribution and evolution of twin and martensite during SMAT are numerically evaluated.

Chapter 5 presents the constitutive model developed to take into account damage in the modeling. The user material subroutineVUMAT provided by the FEM software ABAQUS are used. The evolution function of damage during plastic deformation based on Gurson–Tvergaard–Needleman (GTN) model is introduced in the dislocation density constitutive model and programmed in the form of subroutine. The backward Euler algorithm is used to integrate the constitutive equation over the Gaussian points of each element. The distribution and evolution of twins, martensite and damage during impact loading are numerically evaluated.

In Chapter 6, the micromechanical behavior of a 316L TWIP steel with gradient microstructure is studied by nanoindentation tests at cross-sections at different distances from the top surface. Then a dislocation density-based model is adapted considering the effects of grain size, twinning and dislocation density, and strain rate

based on the experimental results, which is validated by comparing with tensile stress-strain curves available in the literature. The model is also implemented in a subroutine of ABAQUS Explicit to perform a 3D simulation of the nanoindentation test at different depths with different strain rates to study the properties of the gradient material after SMAT.

In Chapter 7, a summarization of the whole work is given, and an outlook on future researches is addressed.

CHAPTER 2 LITERATURE REVIEW

2.1 Introduction to SMAT

Mechanical surface treatment technologies are widely used to improve the mechanical properties of materials by changing the near-surface microstructures to enhance engineering components [34]. These mechanical surface treatment technologies, such as shot peening and its variants based on impact loadings, can give rise to severe plastic deformation in the near-surface area of materials. Therefore, the compressive residual stress field associated with the work hardening region will be generated after treatment, which is usually helpful for improving fatigue life of mechanical parts in use by delaying the initiation and propagation of fatigue cracks [12]. Based on grain refinement induced by severe plastic deformation in metals, Lu et al. [35] first proposed a new surface treatment technology known as Surface Mechanical Attrition Treatment (SMAT) in 1999. It is able to refine the grains in metals and alloys to improve their mechanical properties. This is presently one of the most widely studied mechanical surface treatment technologies. SMAT is based on the repeated and random multidirectional impacts between the material surface and spherical shot driven by ultrasonic generator. As shown in Fig. II-1a, SMAT machine has an ultrasonic generator that converts electrical energy into mechanical motion [36]. The balls are placed in the reflection chamber, and they are vibrated by this ultrasonic generator. The system's frequency is very high (20 kHz), producing very high sound pressure near the surface of the ultrasonic generator, which will project the balls with a desired speed. Generally speaking, the diameter of the steel balls is between 1 and 10 mm, and the speed of the balls is between 1 and 20 m/s [37]. Once the balls resonate, the surface of the engineering parts to be treated is impacted by these balls in a short time (in the order of $T = 1/f = 5*10^{-5}$ s) [38]. The shot directions of these balls in the vibration chamber are random, so the balls impact the surface of

the sample randomly. Each impact can cause a high strain rate plastic deformation on the surface of the specimen. Therefore, repeated multidirectional impacts can lead to severe plastic deformation along different crystal directions (Fig. II-1b). The diameter, the number, the kinetic energy of the balls, and the processing time are four of the main technological parameters of this process [39].

In the process of SMAT, due to the high strain rate and the considerable accumulated plastic strain, a large number of micro-defects, such as dislocation or deformation-induced twins, can be produced on the top treated surface, depending on the properties of materials, especially the Stacking Fault Energy (SFE) [38], [40]. For example, for Face-Centered Cubic (FCC) and Body-Centered Cubic (BCC) metals, dislocation walls and cells generally appear to accommodate strains. Moreover, twinning and slip are competitive deformation processes. In general, in high/medium-SFE materials, slip plays a major role at room temperature and low strain rate. However, in low SFE materials, twinning is likely to occur even during quasi-static deformation at room temperature [41].

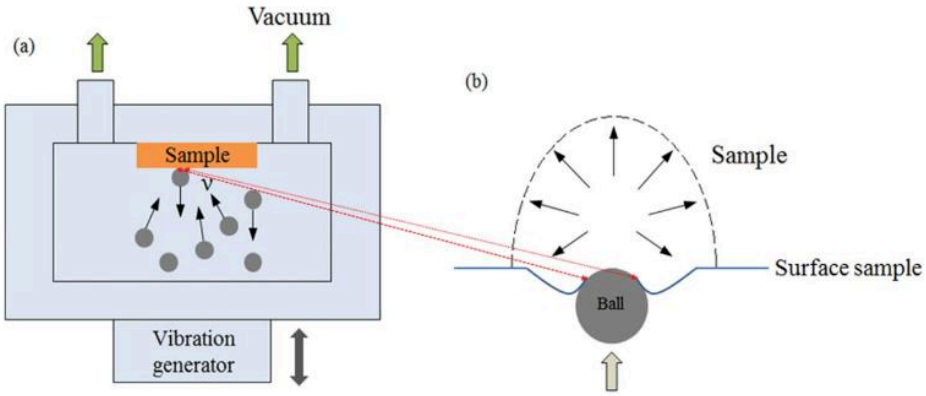

Fig. II-1. Schematic diagram of SMAT setup (a) and illustration shows the surface plastic deformation caused by the impact of a ball (b) [36].

In the SMAT process, due to the incompatibility of the elastic deformation of materials, high residual compressive stresses are generally introduced in the region affected by the treatment. The existence of nanostructured layer and high compressive residual stresses can significantly improve the mechanical properties of materials, such as hardness, yield strength, fatigue, and wear properties. In the past decades, due to the significant advantages of ultrafine-grained materials, nanocrystalline and

sub-microcrystalline materials have been synthesized and studied to optimize their microstructures to increase the strength of the materials [42].

2.2 Microstructural characteristics of AISI 316L and 304L stainless steels after SMAT

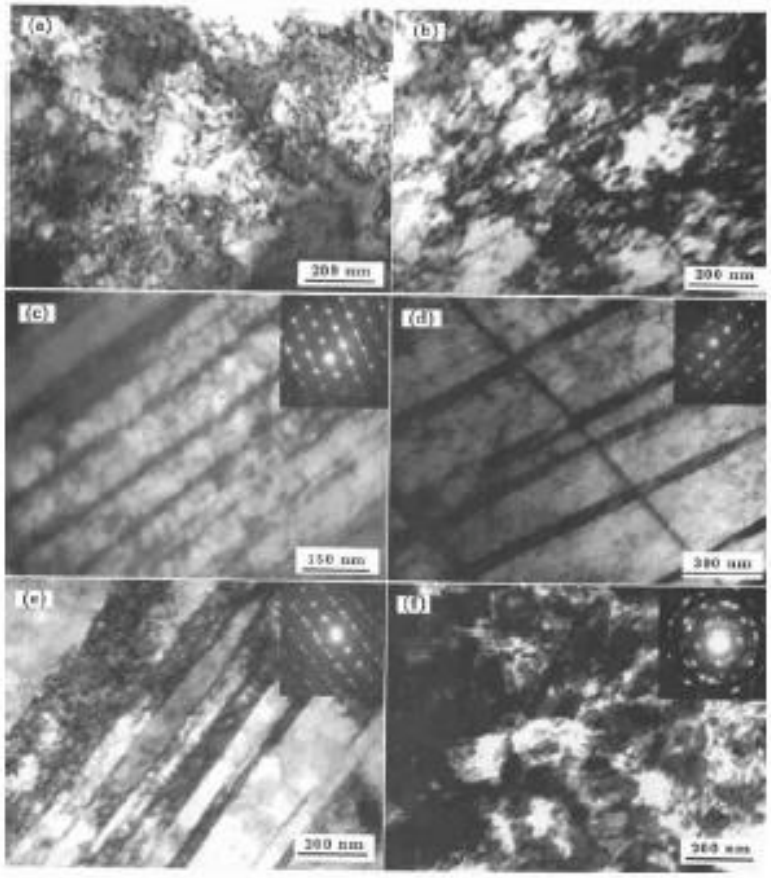

Fig. II-2. TEM images of SMAT samples at different depths and corresponding Selected Area Electron Diffraction (SAED) patterns (insets): the initially formed dislocations (a) and dislocation cells (b) at about 100-150 μm depth, the twins (c) and twin intersection (d) in austenite grains at about 50-100 μm depth, and the lamellar twins (e) and ultra-fine equiaxed austenite grains (f) at about 20-50 μm depth in AISI 316L stainless steel [43].

The two materials used in this project are AISI 316L stainless steel and AISI 304L stainless steel. AISI 316L and AISI 304L are low carbon austenitic stainless steels. AISI 316L stainless steel has medium SFE (40.0 mJ/m^2), while AISI 304L has very low SFE (16.8 mJ/m^2), much lower than other FCC metals such as aluminum (166 mJ/m^2), nickel (128 mJ/m^2) or copper (78 mJ/m^2). They are widely used as

structural materials and components of offshore oil and gas platforms, and also as components and structural materials in many nuclear applications. In recent decades, more and more attention has been paid to strengthen stainless steels. Many methods have been developed, such as changing the chemical composition of stainless steels to induce solid solution [44] and grain refinement [45].

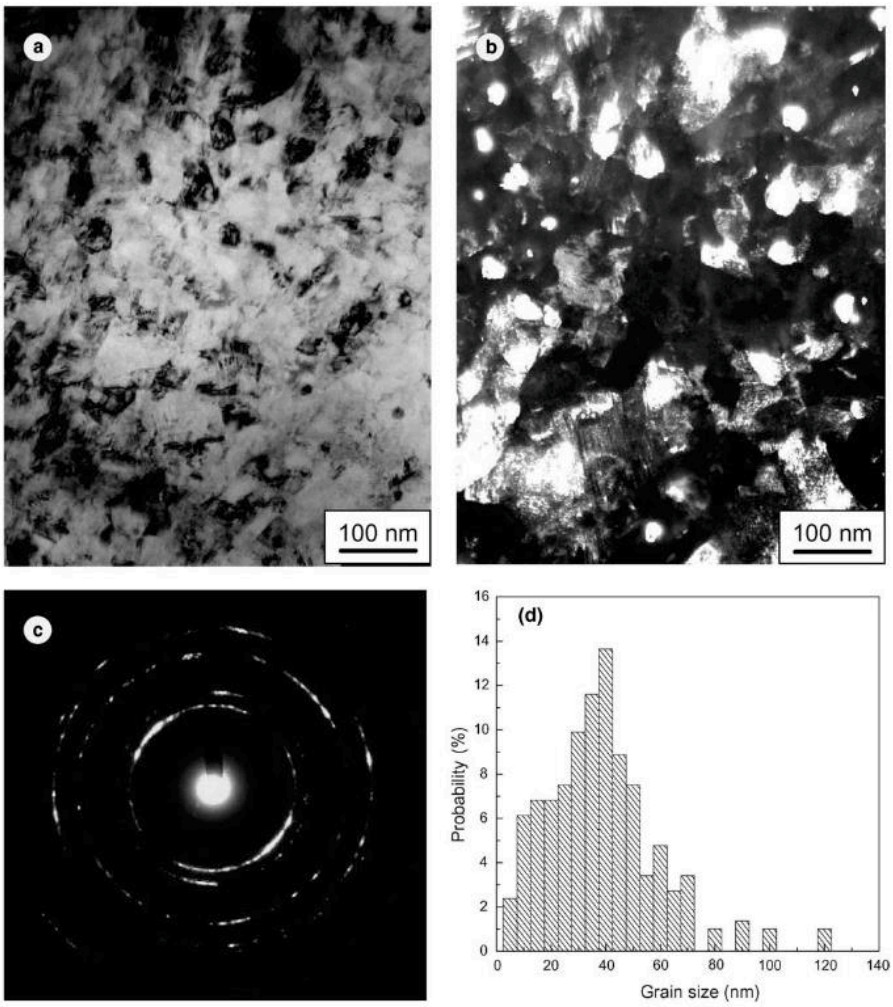

Fig. II-3. Plane diagrams of bright-field TEM (a), dark-field TEM (b), and corresponding SAED diagrams (c) showing the microstructures of 316L samples at 11 μm below the surface after SMAT treatment, and grain size distribution (d) determined by TEM [46].

In the work of Lu et al. [43], the surface nanocrystallization of 316L stainless steel was successfully achieved through SMAT. During SMAT, the vibration frequency was 50 kHz, the diameter of the balls was 8 mm, and the processing time was 60 min. The evolution of the structure, as well as the grain refinement behavior,

was observed by XRD and TEM. The experimental results show (see Fig. II-2) that high-density dislocations are formed at a depth of about 100 μm below the surface of the sample. Then as the strain and the strain rate increase, the mechanical twins are induced to a depth of about 50 μm. The lamellar twins cross each other to refine the grains. Finally, after the SMAT process, a nanostructured surface layer with a thickness of about 20 μm is formed, whose microstructure is composed of a mixture of austenite and martensite with a grain size of about 10-30 nm. The realization of surface nanocrystallization seems to be attributed to the grain refinement due to dislocation-twin and twin-twin interactions, and its hardness is greatly improved after SMAT treatment.

Lu et al. [46] also studied the microstructural characteristics of 316L steel on the top layer (about 6-8 μm from the polished top surface). Samples of the same type as [43] were used with a thickness of 1.8 mm. The diameter of the balls was 3 mm, the vibration frequency was changed to 20 kHz, and the treatment duration was 30 min. Fig. II-3a and II-3b are respectively the bright and the dark field TEM images of 316L samples. As shown in Fig. II-3c, SMAT induces ultrafine twining grains with random orientation on the top surface. The histogram of grain size distribution obtained from bright and dark field images shows a positive logarithmic distribution of narrow grain size. As shown in Fig. II-3d, the grain size of the top layer is about 40 nm.

Lu et al. [47] also experimentally studied AISI 304L samples as a plate (100 *100 mm^2) using SMAT treatment. Before SMAT, the samples were annealed in vacuum at 1080 °C for one hour to obtain a single austenitic phase (FCC) with uniform grain structure. Typical microstructures of the annealed samples are shown in Fig. II-4a. The grain size is in the range of 100-200 μm, and annealing twins can be seen in some grains. SMAT was performed on AISI 304 stainless steel in vacuum for 15 min at room temperature, and the vibration frequency was 50 kHz. A surface layer of nanostructure was generated by SMAT, and its microstructure evolution was studied by SEM and TEM (Fig. II-4). Microstructure examination shows that the grain refinement process of this material includes: (1) formation of plane dislocation arrays and twins; (2) grain refinement and martensitic transformation; (3) formation of random orientation crystals [47].

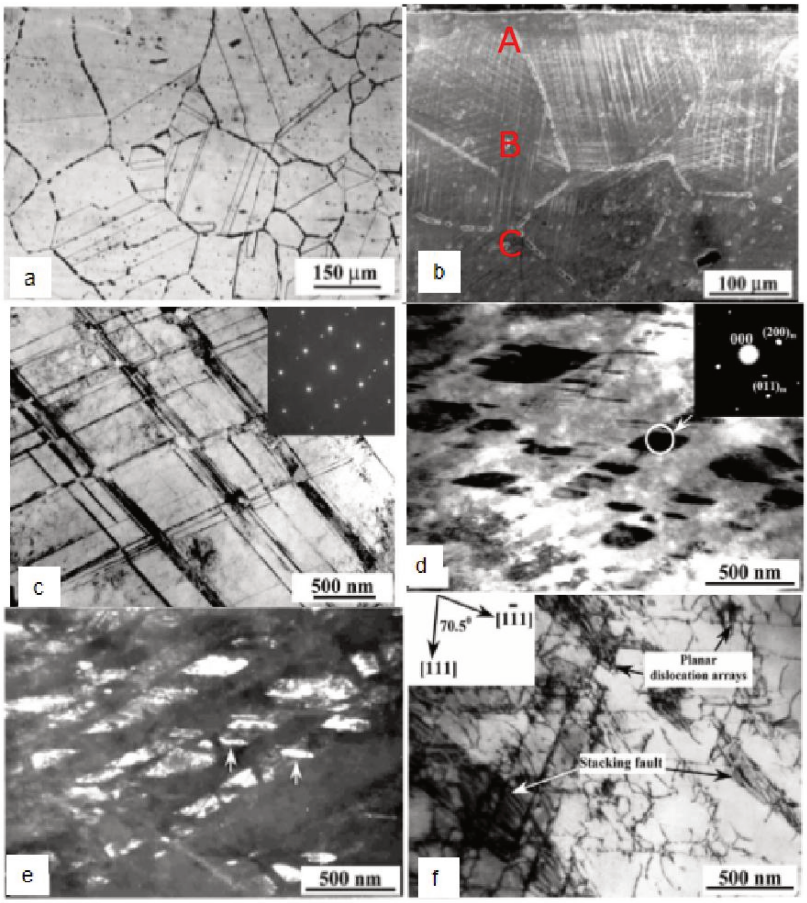

Fig. II-4. The microstructures of AISI 304 stainless steel after welding annealed (1 h under 1080 °C in a vacuum) observed by SEM (a). The cross-sectional SEM observation (b) of the typical microstructure for the SMATed AISI 304 stainless steel, and the letters A, B, and C denote three, two, and one directions of mechanical twin. The cross-sectional TEM observations (c) at a depth of about 150 μm from the treated surface. A bright-field (d) and a dark field cross-sectional TEM images (e) at about 100 μm deep from the top treated surface. The cross-sectional TEM observation (f) of the microstructure at a depth of about 300 μm from the treated surface in the SMATed samples [47].

Tao et al. [48] also studied the grain refinement process during SMAT of AISI 304 stainless steel with low SFE by TEM and High-Resolution Electron Microscopy (HREM). The material was treated by SMAT for 15 min. The vibration frequency was 50 kHz, and the diameter of the steel balls was 8 mm. Fig. II-5a and b show the bright and dark images of SMATed nanocrystals (NC) 304L samples under TEM, which indicates that the formation of rhombic blocks is caused by the intersection of mechanical twins. The corresponding Selected Area Electron Diffraction (SAED) diagram shows that some of these blocks are BCC martensitic phase. The martensitic phase is formed at the intersection of two sets of mechanical twins, which is similar to that for AISI 304 stainless steel shock loaded in cylindrical geometry [49] and

balanced biaxial straining during balanced biaxial tension test [50]. Typical planar TEM micrographs and top statistical grain size distribution are shown in Fig. II-5c, and d. The microstructures have uniformly distributed nano-sized grains. The grain size distribution obtained from the dark field image has the characteristics of positive logarithmic distribution, and its grain size distribution is narrow, ranging from 8 to 50 nm. The average grain size is about 10 nm.

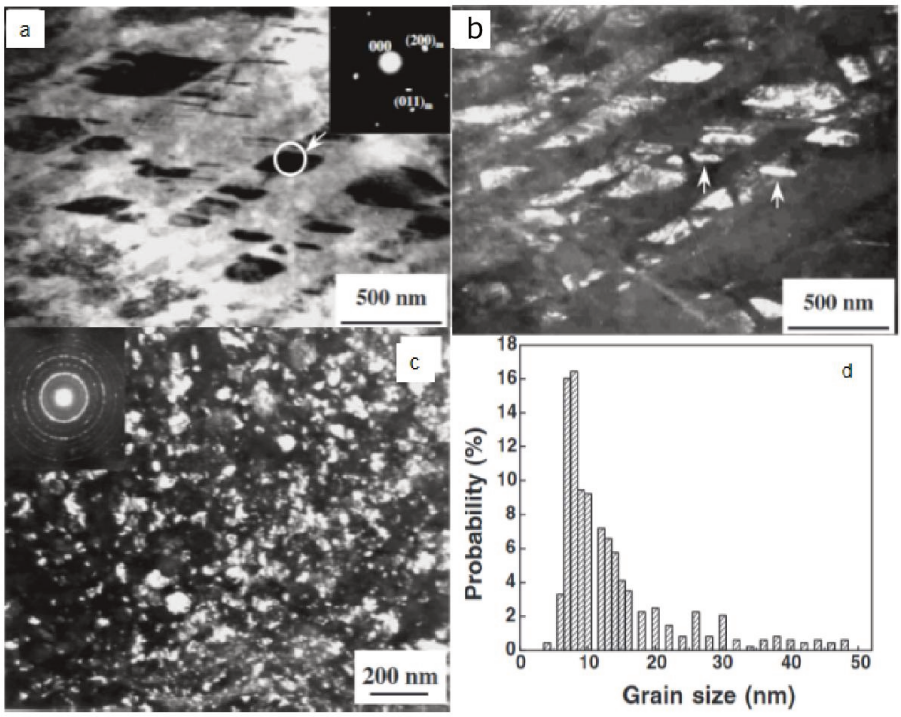

Fig. II-5. Plane-view bright-field TEM image (a), dark-field TEM image (b) at a depth of about 100 μm, and typical plane TEM observation results (c), and statistical grain size distribution (d) from the top surface of AISI304 sample observed by TEM [48].

2.3 Mechanical properties of SMATed materials

The compressive residual stresses and the nanostructured layer induced by SMAT can significantly improve the mechanical properties of workpieces and the strength of materials. The validity of SMAT treatment for improving yield strength at room temperature was verified by tensile tests. Fig. II-6 shows the true stress-strain curves [51] of a stainless steel treated by SMAT with different numbers of balls and different time durations for SMAT. The results show that the nanostructured samples have higher strength than the coarse-grained samples. After 20 min of treatment, the

yield strength (0.2% offset) of the material treated with 200 balls reaches 980 MPa, about three times higher than that of coarse-grained samples (350 MPa), and the ultimate tensile strength is about 1250 MPa.

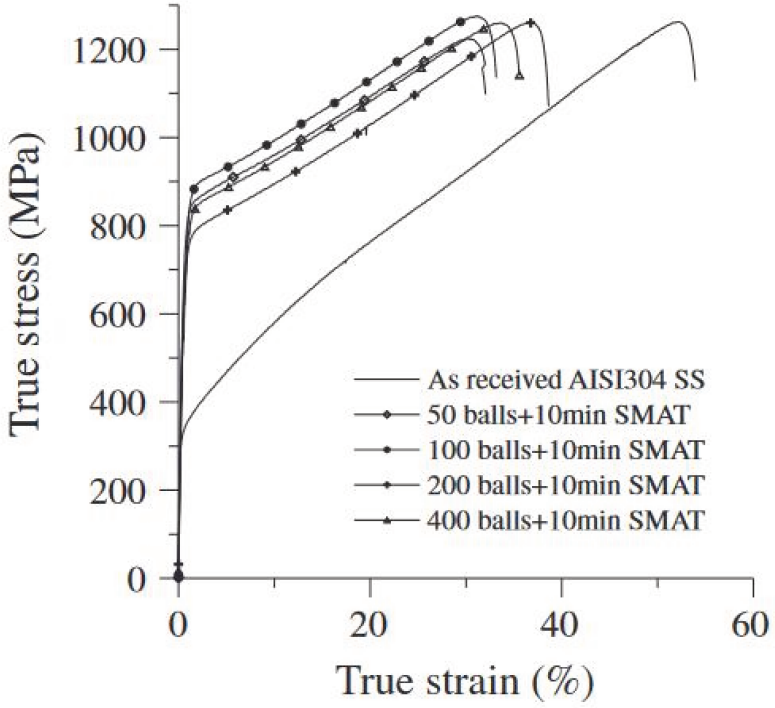

Fig. II-6. True stress-strain curves of the as-received 304 stainless steel and treated by SMAT [51].

Fig. II-7a [52] shows the cross-sectional morphology of SMAT specimens, which were treated for 180 min. The microhardness measurement was performed in the near-surface area. Fig. II-7b shows the hardness variation of SMAT processed specimens with different treatment durations. From Fig. II-7a, we can see from the microstructural characteristics that the surface layer is severely deformed, and the thickness of the deformed layer is about 200 μm. In the heavily deformed area, the mechanical twins are highly present, while, near the surface, the multidirectional twinning phenomenon in the grain occurs with two or three groups of systems of twining named as “operating systems” by the authors. It can be seen by removing a thin layer about 10 μm from the surface treated with SMAT after slight grinding and polishing. As the distance from the surface increases, the number of mechanical twins operating systems gradually decreases to two, followed by one. This deformation behavior is related to the refinement and nanocrystallization of the surface area. In addition to severe plastic deformation and surface nanocrystallization, another

well-known phenomenon, strain-induced martensite formation, can be observed in severely deformed austenitic stainless steels [52]. It has been proved that martensite is formed at the intersection of multidirectional mechanical twins. Therefore, strain hardening, nanostructure, and martensite formation are helpful for improving the hardness of the deformed layer. It can be seen from Fig. II-7b that the hardness and the thickness of the deformed layer increase by increasing SMAT treatment time, but after prolonged treatment, it seems to have been saturated.

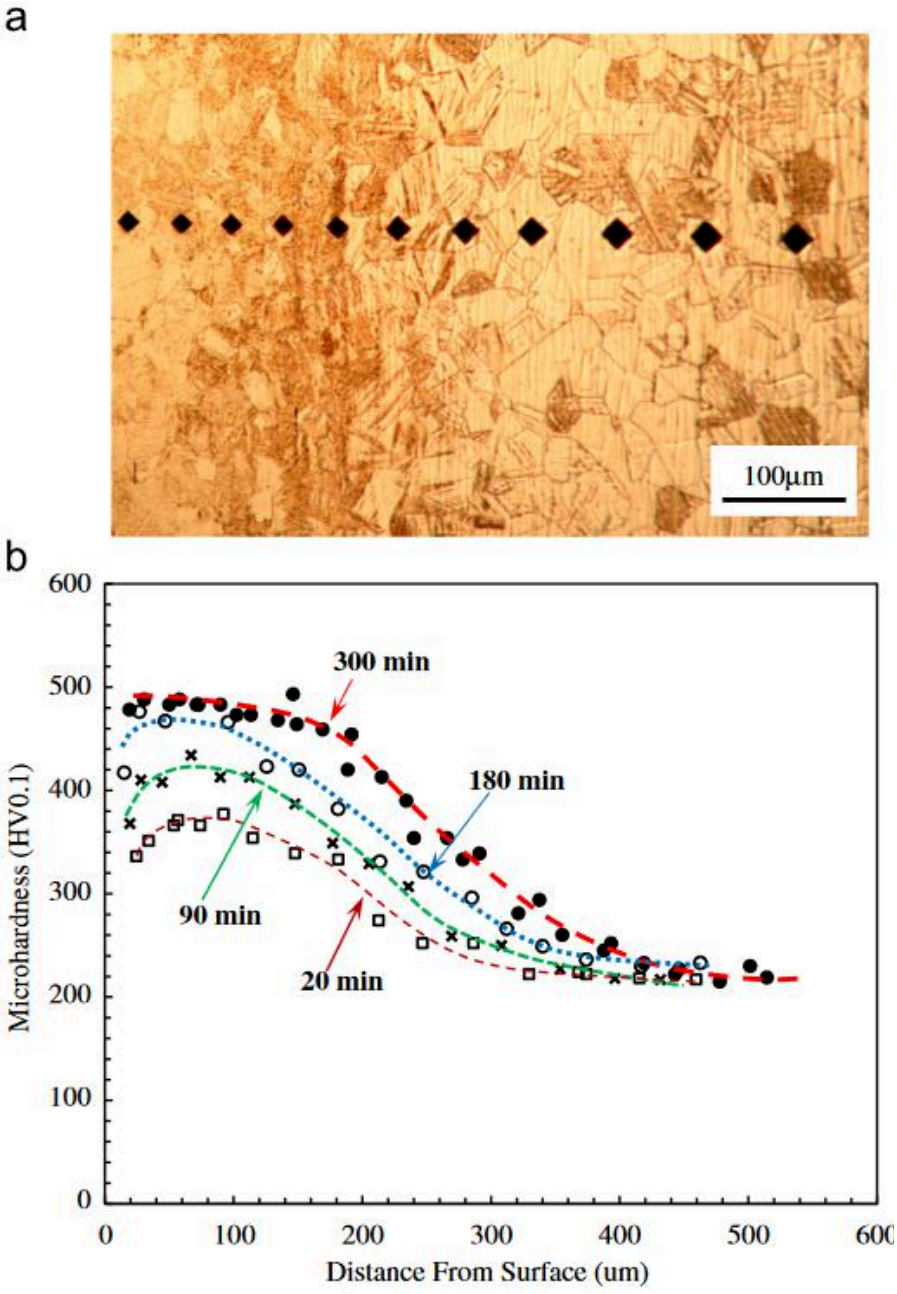

Fig. II-7. The cross-sectional morphology (a) of SMAT samples processed for 180 min and the microhardness variation (b) measured on SMAT layers processed at different durations [52].

Zhou et al. [53] studied the fatigue behavior of a surface nanostructured AISI 316L stainless steel generated by SMAT. Compared with the untreated material, the fatigue strength of the nanostructured AISI 316L steel is improved. There were two investigated SMAT conditions: SMAT low amplitude (SLH) and SMAT very high amplitude (SVH). For SLH, 30% of the generator power is used for 30 min, As for SVH, 30% of the generator power is used for 15 min, followed by a generator power of 50% for 5 min. The cyclic stress amplitude evolution during fatigue loading is a good indicator of the properties of the material in terms of softening or hardening.

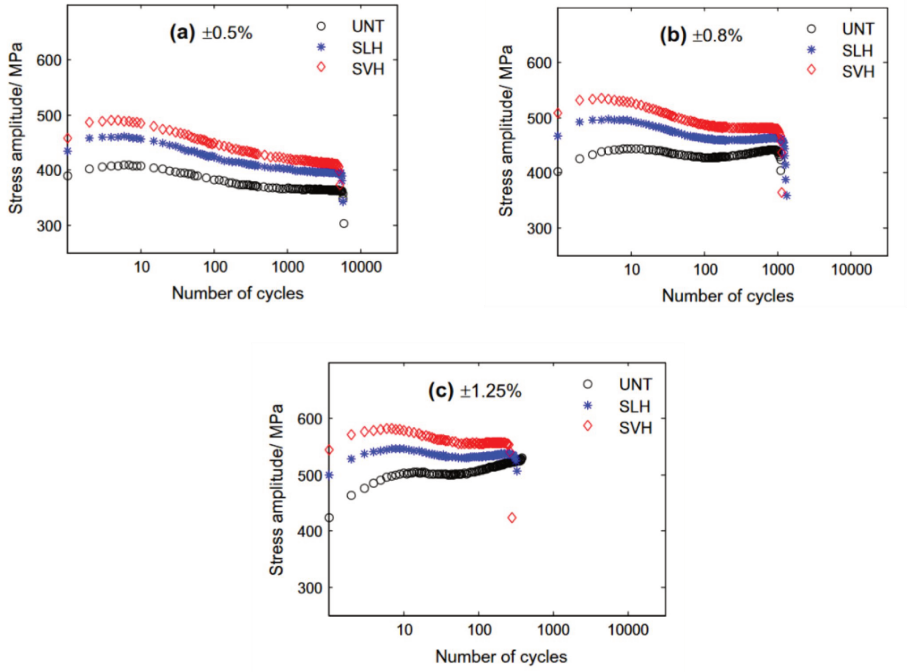

Fig. II-8. Cyclic stress amplitude curves for different material states under strain amplitudes of ±0.5% (a), ±0.8% (b), and ±1.25% (c) [53].

As shown in Fig. II-8, the cyclic stress amplitude evolves with the number of cycles for different material states under strain amplitudes of 0.5%, 0.8%, and 1.25%. It can be seen that the mechanical strength has been significantly improved, and SMAT has changed the cyclic hardening/softening behavior of samples. Fig. II-8 shows that the greater the strain is, the greater the cyclic stress is. For a given strain range, the cyclic stress amptitude of SMATed specimens is much higher than that of untreated specimens. In addition, higher SMAT intensity leads to higher stress amplitude.

Compared with untreated samples, the increase in stress amplitude of SVH and SLH samples is due to the SMAT affected area. Because of dislocation entanglement, strain hardening can increase mechanical strength, which will hinder further permanent deformation of materials. At the same time, according to the Hall-Petch relationship [54], nanocrystalline materials have high yield strength. However, the contribution of the nanostructured layer to the overall mechanical properties of the sample is very small because its thickness is very thin (5 μm) compared to the thickness of the work-hardened region (about 500 μm).

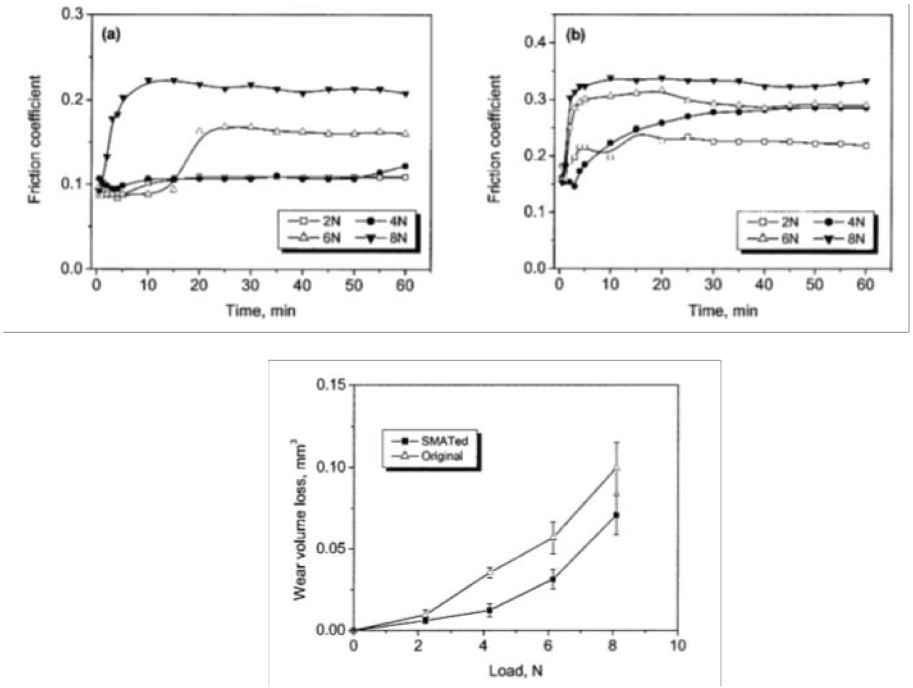

Fig. II-9. Variations of the friction coefficient with wear time under different loads for SMATed (a) and the original (b) samples and the variations of the wear volume loss (c) with the load for SMATed and the original samples [55].

Fig. II-9 shows the wear and friction characteristics of low carbon steel sheets after SMAT [55]. In most cases, the friction coefficient increases first and then tends to be stable. However, for samples under 6 N load, the friction coefficient remains unchanged during the first 15 min of sliding (about 0.09). When the sliding time exceeds 20 min, the friction coefficient increases from 0.07 to 0.16. The variation of the friction coefficient shows that the wear mechanism changes during sliding in Fig. II-9c, the wear volume loss of the SMATed specimens under different loads was compared with that of the original specimens. The wear volume loss of both

specimens increases with the increase of load, but the volume loss of the treated specimens is lower than that of the original specimens under each test load, especially under 4-8 N. This means that SMAT can improve the wear resistance of high and low carbon steels. After SMAT, the friction coefficient significantly decreases, and the wear volume loss decreases consequently. As a matter of fact, the harder the nanostructured surface layer is, the better the friction and wear properties are. The improvement in friction and wear properties may be attributed to the harder nanostructured surface layer which reduces the degree of plowing and micro-cutting under the lower load and the degree of plastic removal and surface fatigue fracture under the higher load, respectively.

2.4 Mechanisms of grain refinement

Grain refinement caused by plastic strain in metals is a well-known phenomenon. SMAT has been used to synthesize ultra-fine grain materials to significantly improve their mechanical strength. From a theoretical point of view and the development of advanced engineering applications for plastic deformation technology, it is important to well understand the basic mechanisms of strain-induced grain refinement during SMAT [34].

Grain refinement mechanisms based on plastic strain have been extensively studied for many materials [16], [17], [56]. For copper, iron, aluminum and other high and medium-level SFE materials, coarse grains can be refined through various dislocations activated gliding. Microstructure studies showed that ultrafine grain structure from nanometer to micrometer is formed on the surface of iron samples due to the process of SMAT. In the deformed surface layer, according to the microstructural characteristics of different strain sections, it can be found that the grain refinement process involves the following elements, as shown in Fig. II-10:

1. The development of Dense Dislocation Walls (DDWs) and Dislocation Tangles (DTs) in raw grain and refined cells (further straining);

2. The transformation of DDW and DTs into sub-boundaries with small misorientations separating individual units or sub-grain;

3. The evolution of subs-boundaries to high misorientation grain boundaries;

4. The nanostructure formed at the top layer (with a thickness of about 60 μm).

According to the microstructural characteristics from the top surface to the unstrained bulk material, the formation mechanism of nanocrystals in AISI 304 samples with low SFE (about 17 mJ/m^2) was proposed [48]. The grain refinement mechanisms during SMAT can be seen in Fig. II-11.

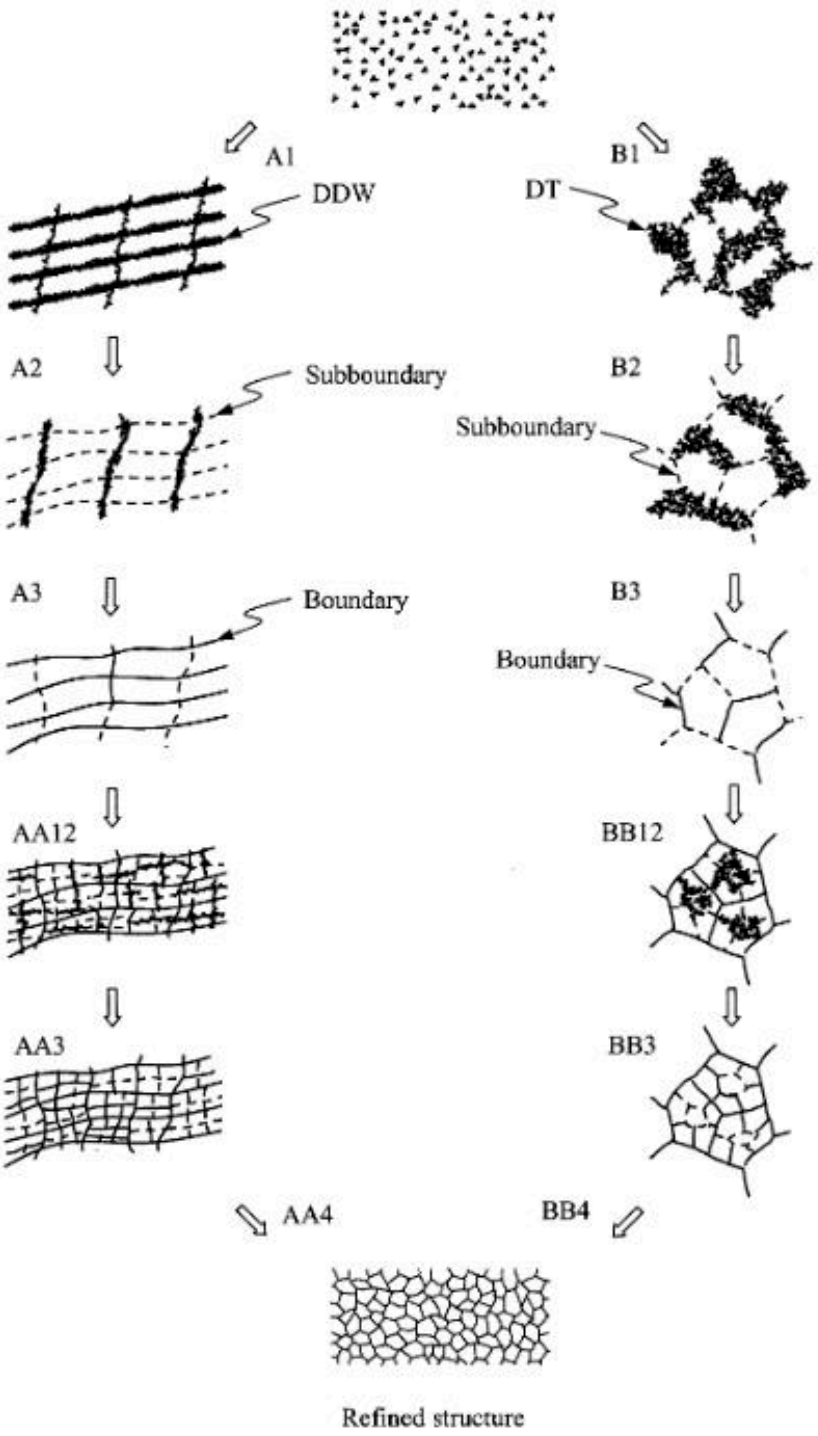

Fig. II-10. Schematic illustration of grain refinement induced by plastic deformation in Fe [34].

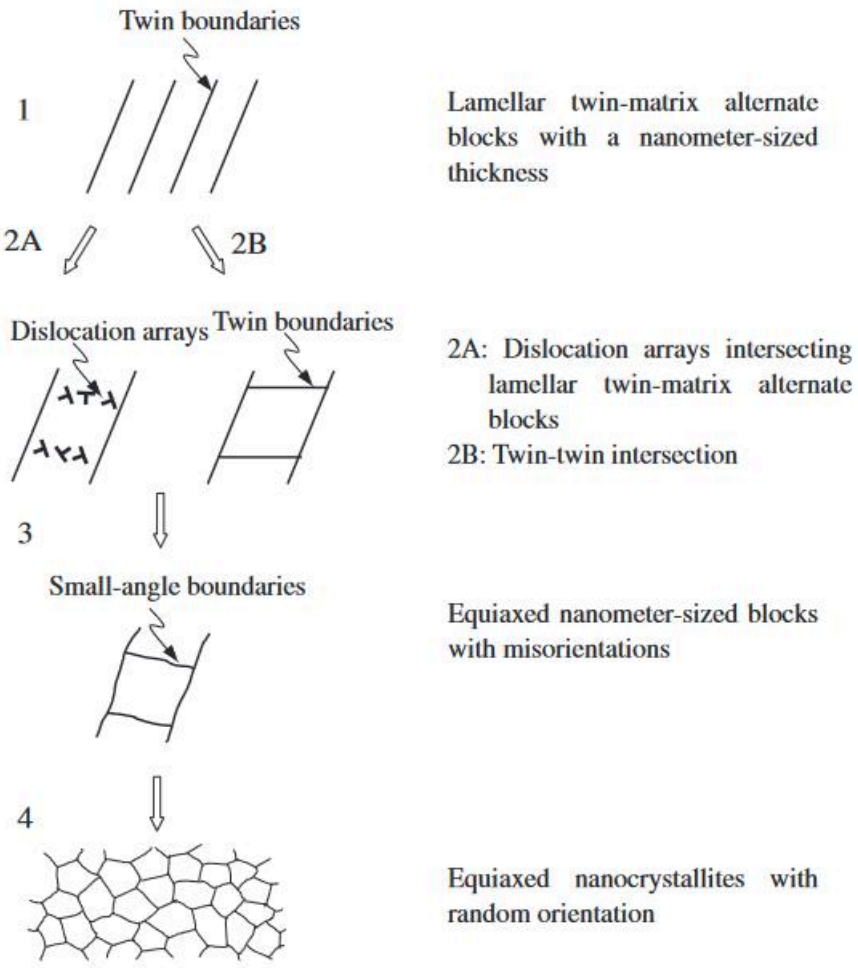

Fig. II-11. Schematic illustration of grain refinement during SMAT for the AISI 304 stainless steel with low SFE [48].

2.4.1 Formation of planar dislocation arrays and mechanical twins

Planar dislocation arrays and mechanical twins are formed under specific low strain and strain rate conditions. Strain-induced dislocations in AISI 304 stainless steel are mainly on {111} plane, forming planar dislocation arrays and grids instead of irregular dislocation elements (as shown in FCC such as aluminum alloys) or dense dislocation walls (such as BCC Fe). Planar dislocation arrays and grids are typical dislocation structures observed in low SFE alloys deformed at low strain and low strain rates. This structure can be attributed to the low SFE, which makes it difficult for some dislocations to slip laterally and causes them to be arranged more easily in a

planar array on their main slip planes. In general, sliding dominates the deformation processes in all kinds of plastic deformation materials for medium to high SFE values. However, the critical shear stress of twin decreases with the decrease of SFE value, i.e., low SFE materials are prone to the formation of mechanical twins, especially at high strain rate and low temperature. For AISI 304, SMAT process can provide priority for the development of mechanical micro-twins due to the low deformation temperature (close to ambient temperature) and high strain rate leading to the inhibition of thermal activation of dislocation processes [39].

It thus generates sufficiently high stress to nucleate and grow mechanical micro-twins by forming stacking faults. The formation of high-density ultra-thin (nano-scale) mechanical twins means that the surface layer undergoes plastic deformation at a very high strain rate (estimated to be 10^3-10^4/s) without significant temperature rising during the SMAT process. For AISI 304 samples, the development of nano-thick twins plays an important role in the formation of surface layer nanocrystals [39].

2.4.2 Grain subdivision

A twin boundary is a very simple periodic boundary condition or a highly coincident "special" large-angle boundary. A high-density parallel twin with unidirectional orientation was formed in AISI 304 samples, and a large number of twin boundaries was introduced to subdivide the original coarse grains into lamellar twin-matrix alternate blocks (LTMAB) (step 1 in Fig. II-11).

For materials with smaller SFE, the driving force of mechanical twin growth may be large enough to overcome the obstacles encountered at the boundary of micro-twins, leading to twins crossover. In an AISI 304 sample with SFE as small as 16.8 mJ/m^2, twins and twins intersect to form rhombic blocks. Therefore, twin intersection points in AISI 304 can subdivide the initial coarse grains into rhombic blocks with different directions and take the large-angle boundary as the boundary (steps 2B and 3 in Fig. II-11. These boundaries are formed at large angular boundaries that are different from the dislocation boundary generated by other plastic deformation materials with medium to high SFE, which increases the boundary misorientations with accumulating and eliminating more dislocations at the grain boundaries.

For AISI 304, the intersection of twins can not only effectively subdivide the original grains by introducing different boundaries, but also induce martensitic transformation (introducing phase boundary) to form smaller grains [35].

2.4.3 Formation of randomly oriented nanocrystals

The formation of randomly oriented nanocrystals requires significant changes in the relative orientation of these nano-sized blocks (step 4 in Fig. II-11). The mechanism that may lead to the formation of random orientation may involve grain boundary sliding and grain boundary rotation. When the grain size is reduced to the nanometer range, the grain rotation and grain boundary sliding are much easier compared to coarse grains. Grain rotation is another way to accommodate plastic deformation of nanocrystals. It can effectively increase the misorientation and lead to the formation of disordered nanocrystals [57].

2.5 Martensitic transformation

In AISI 304 stainless steel, martensitic transformation is a common phenomenon related to plastic deformation, which is considered as a strain-induced process rather than a pressure-assisted process. In this case, the plastic deformation of the parent phase produces an appropriate defect structure, which can be used to initiate the transformation. Specifically, in austenitic stainless steel, martensite embryos are found at some intersections of the micro-shear zone, including dislocations, twins, and initial existing martensite. In AISI 304 stainless steel, the formation of martensite is strongly influenced by the chemical composition of austenite and deformation conditions (strain, strain rate, strain path, and rolling temperature) [58].

The results of Gauzzi et al. [59] show that in AISI 304 stainless steel, when the temperature rises above 400 °C, a reverse transformation from martensite to austenite occurs. The dynamic recovery of the high strain zone and the recrystallized austenite structure is very spatially uneven, which is related to the non-uniform dislocation substructure. The martensitic transformation is sensitive to stress and plastic strain, and its size depends to some extent on the disorder of the atomic arrangement within the grain boundary region. Grain boundary atoms can be disordered because macroscopic loading promotes grain deformation and grain boundary rotation. As the temperature increases, the grain boundary energy increases, and the grain boundary distortion becomes more and more important. The defect region (dislocation-dense

region) in the austenite grains becomes a nucleation site and the nucleation sites of the new phase increase. However, not all grain boundaries can nucleate, and only some special grain boundaries with higher energy are available to nucleate. When the grain diameter becomes smaller, the additional compressive stress caused by the surface tension of the grain sharply increases, and martensite nucleation is suppressed [60]. At the same time, grain refinement increases the grain boundary area and the yield strength of the parent phase, thereby inhibiting the nucleation of martensite. This is the main reason why fine austenite grains hinder martensitic transformation and lower Ms (start of martensitic transformation) temperature. Moreover, although martensite nucleation is considered to be heterogeneous and martensite nucleates before austenite grain boundaries, the high-density dislocations accommodated in ultrafine grain boundaries impose restrictions on the growth of martensite. Therefore, a large number of nonequilibrium curved grain boundaries formed during severe plastic deformation hinder the continuous growth of martensite.

2.6 Mechanisms of damage formation

According to the residual stress distribution, strain hardening, and corresponding surface roughness, SMAT can be considered similar to controlled shot peening (CSP) (note that CSP is a cold working treatment of surface under controlled kinetic conditions). SMAT mainly affects the fatigue damage stage corresponding to the initiation and propagation of short cracks. There is evidence that these stages account for more than 70% of the fatigue life of components [61]. Crack initiation is a controversial topic and has provided the basis for several different theories over the years, especially in the case of single crystals [62], [63]. In most commercial polycrystalline alloys, it is assumed that cracks occur almost immediately under stresses above the fatigue limit. Therefore, the crack initiation stage can be regarded as the early propagation of micro-defect cracks in materials [64].

According to the experimental results, it is obvious that the stable propagation of short cracks will determine the life expectancy of components. Similar to crack initiation, the propagation of short fatigue cracks is another controversial research topic, which has been studied in various ways in the past two decades [65], [66]. Therefore, in order to better understand the effect of surface modification of CSP on

fatigue damage, it is necessary to divide it into (a) arrest/delay of fatigue crack initiation, and (b) crack propagation.

It is well known that when the material is tested under stress below the fatigue limit, the material will not fail due to fatigue. Early on, people mistakenly believed that when the stress level was lower than the fatigue limit, fatigue cracks would not nucleate. Over the past two decades, people's understanding of fatigue limits has changed. Today, the fatigue limit is considered to be the maximum stress level, below which existing cracks or crack-like defects will not extend to failure within the expected life (10-100 million cycles). With the recognition that grain boundaries and other microstructural characteristics become obstacles to crack growth [67]–[69], threshold stress has been redefined as stress that cannot overcome the microstructural barrier crack of a given length [67]. According to the research of Navarro et al. [67], [70], the cracks will stop when two conditions are met: (a) the plastic zone at the crack tip is constrained by the barriers, and (b) the local stress at the barriers ahead of the crack cannot extend the crack tip plasticity beyond these barriers.

On the shot peening treated surface, cracks may be formed at the micro-notches. Early studies by Smith, Miller, and Tanaka [71], [72] show that crack growth depends on the bluntness of the notch. From these early works, our understanding of the notch effect has been improved. In order to study the relationship between the geometry of the notch and the microstructure of the material, Vallellano et al. [73] gave a micromechanical description of the fatigue crack growth process at the notch and inherently considered the crack interaction with the plastic slip barrier of the material (such as the grain boundary) and the influence of the notch stress gradient in the model, then both the initiation limit and the propagation limit of notch fatigue cracks up to failure can be identified and calculated. Based on the work of Vallellano et al. [73], Curtis et al. [74] studied the parameters of surface roughness and residual stress distribution which are considered to determine the performance of CSP in terms of fatigue resistance based on following assumptions: (a) the residual stress will not relax; (b) for cyclic hardening materials, strain hardening is not obvious; (c) the stress gradient will not promote subsurface cracks. The results shows that the compressive residual stresses are beneficial to fatigue resistance, and surface roughening can decrease the fatigue life of engineering components by allowing earlier initiation and faster propagation of short fatigue cracks.

2.7 Dislocation density model

Alternatively, the microstructure can be indirectly modeled to account for the effects of microscopic processes on an averaging basis at a macroscopic level. Unlike the discrete dislocation dynamics method, the dislocation-based model is established at the macroscopic level, that is, all quantities (dislocation density, flow stress, etc.) can be calculated as a uniform representative elementary volume of material. In a series of studies conducted by Swedish researchers in the 1970s, several basic dislocation density based models were proposed by Bergström et al. [75], Kocks et al. [76] independently using similar viewpoints, which were later developed by Estrin & Mecking et al. [77]. Many other researchers also include dislocation density implicitly [78] or explicitly [79] into material models. Through the indirect method mentioned above, the dislocation density model provides a bridge between micro-phenomena and continuous macro-level for quantities such as stress and strain.

Within the scope of this study, the objective of material models is to apply manufacturing or material processes, such as SMAT, to mechanical parts. These material models should describe the thermomechanical deformation based on macroscopic stress and strain. In classical continuum mechanics, several phenomenological types of constitutive models are well known: elasticity, plasticity, viscosity, etc. This study deals with visco-elastoplasticity because these phenomena are most relevant to the deformation of metals.

2.7.1 Yield surface and flow rule

Yield criterion and yield stress define the region in stress space where the elastic surface and the non-elastic region outside the surface are separated by [80]:

$$\mathrm{f}(\boldsymbol{\sigma}, \sigma_Y) = 0 \tag{II-1}$$

where f is the yield function, $\boldsymbol{\sigma}$ is the applied stress, σ_Y is the yield stress.

The flow model establishes the relationship between stress and plastic strain increment (or velocity). The yield surface function is used as the plastic dissipation potential for correlated plasticity. This method has the advantage of being widely applicable to different metals and can be effectively implemented in the calculation. Associated flow rule is [80]:

$$d\varepsilon_p = d\lambda \frac{\delta f}{\delta \sigma} \tag{II-2}$$

which defines the increment of plastic strain $d\varepsilon_p$ perpendicular to the yield surface. In Eq. II-2, $d\lambda$ is the plastic multiplier, which can be determined by ensuring that the stress-state lies on the yield surface during plastic flow. In other words, for rate-independent plasticity theory, the plastic multiplier is evaluated by the consistency condition [80]:

$$\dot{f} = 0 \tag{II-3}$$

Combined with the yield criterion, the above conditions show that the stress remains on the yield surface (the yield function is zero for plastic behavior), and the increment of the yield function is zero in the process of continuous plastic deformation.

2.7.2 Internal variables and hardening

Kinematic hardening changes the position of yield surface and isotropic hardening changes the yield surface size, while developing anisotropy changes the shape of the surface. The plastic multiplier can be regarded as a controlling variable related to internal plastic deformation. In the case of von Mises yield criterion and for simple models without damage, it is simply equivalent to the equivalent plastic strain rate, leading to the cumulated plastic deformation.

2.7.3 Viscoplastic constitutive framework

In the small deformation theory, the total strain rate can be decomposed into the sum of the elastic and viscoplastic parts:

$$\dot{\varepsilon} = \dot{\varepsilon}^{e} + \dot{\varepsilon}^{vp} \tag{II-4}$$

The elastic strain rate is related to the stress rate by Hooke's model $\dot{\sigma} = D\dot{\varepsilon}$, with the fourth-rank stiffness tensor D given by the standard formulation based on Lamé's coefficients, i.e., λ and μ:

$$D_{ijkl} = \mu\left(\delta_{ik}\delta_{jl} + \delta_{il}\delta_{jk}\right) + \lambda\delta_{ij}\delta_{kl} \tag{II-5}$$

where δ is the Krönecker's symbol

The viscoplastic strain rate follows a normality hypothesis and can be calculated from a viscoplastic potential:

$$\dot{\varepsilon}^{vp} = \frac{\partial \phi}{\partial \sigma} \tag{II-6}$$

We introduce the equivalent stress, calculated as:

$$\bar{\sigma} = f(\sigma) = \sqrt{\frac{3}{2} S : S} \tag{II-7}$$

where f is a homogeneous function and S is the deviatoric part of the stress tensor. The viscoplastic potential is expressed as [81]:

$$\phi = \dot{\varepsilon}_0 \frac{\sigma_{ref}}{m+1} \left(\frac{\bar{\sigma}}{\sigma_{ref}} \right)^{m+1} \tag{II-8}$$

From the balance of viscoplastic work rate, the following relations can be written:

$$W^{vp} = \bar{\sigma} \dot{\bar{\varepsilon}}^{vp} = \sigma \dot{\varepsilon}^{vp} \tag{II-9}$$

From Eqs. II-6, II-8, and II-9, the model for viscoplastic behavior can be expressed:

$$\dot{\bar{\varepsilon}}^{vp} = \dot{\varepsilon}_0 \left(\frac{\bar{\sigma}}{\sigma_{ref}} \right)^{m^{vp}} \tag{II-10}$$

With σ_{ref} the reference flow strength linked to the current dislocation microstructure measured at an instant of deformation. It depends on the accumulated viscoplastic strain $\bar{\varepsilon}^{vp} = \int \dot{\bar{\varepsilon}}^{vp} dt$; m^{vp} is a material parameter, and $\dot{\varepsilon}_0$ a constant of strain rate unit.

2.8 Damage model

During the SMAT process, collisions between the material surface and the shots may lead to microstructural damage of the material. Ductile damage is caused by micro-void under local stress-strain field and it is almost impossible to observe it experimentally because the time between the growth of the void and the last material failure is too short. While the GTN model can effectively simulate the nucleation, growth, and coalescence of micro void [82]. The ductile failure process in metallic materials usually consists of three stages, namely micro-void nucleation, growth, and coalescence of these voids. To simulate the plastic flow and the fracture of ductile metals, Gurson et al. [82] proposed an approximate mesoscopic yield function of porous materials considering the influence of hydrostatic pressure [83]. It is assumed that the metal matrix is isotropic, completely plastic and incompressible, obeying the von Mises yield function. Tvergaard et al. [84] modified the original model by

introducing three additional fitting parameters. The GTN model is now one of the well-known meso-mechanical models of ductile fracture. It has been used in different materials and processes [85], [86].

Gurson's expansive plasticity theory can consider the influence of the existence of voids in isotropic materials on the bearing capacity. The main difference between the Gurson model and classical plastic model is that the yield surface of the former is hydrostatic stress-dependent, while the classical plastic model assumes that the yield is independent of hydrostatic stress.

GTN damage model can be described as follows:

$$\Phi = \left(\frac{\sigma_e}{\sigma_y}\right)^2 + 2q_1 f^* Cosh(-\frac{3}{2}\frac{q_2\sigma_m}{\sigma_y}) - (1 + q_3 f^{*2}) = 0 \qquad \text{(II-11)}$$

where the involved variables are defined as follows: f^* refers to the volume fraction of void in the material and σ_y is the yield stress of the matrix material. σ_e is the macroscopic von Mises equivalent stress. σ_m is the macroscopic average normal stress, and q_1 , q_2 , q_3 are the parameters to predict the strain more accurately when the fracture occurs. Gurson et al. [82] found that it was effective to predict fractures when $q_1 = 1.5$, $q_2 = 1$, and $q_3 = 2.25$.

Gurson model describes the fracture of materials as the increase of the void volume fraction f. f is modified by Tvergaard and Needleman to an effective void volume fraction f^* , as shown in the following equation:

$$f^* = \begin{cases} f & \text{if} \quad f \le f_c \\ f_c + \dfrac{f_F - f_c}{f_f - f_c}(f - f_c) & \text{if} \quad f_c \le f \le f_f \\ f_F & \text{if} \quad f_f \le f \end{cases} \qquad \text{(II-12)}$$

In the above equation, f_c is the critical value of void volume fraction, and f_f is the value of void volume fraction in materials that completely lose the stress-bearing capacity. It is noteworthy that the ultimate value of macro stress-bearing capacity is given by $f_F = 1/q_1$. As shown in Eq. II-6, when the void volume fraction is smaller than the critical value, the effective void volume fraction is applied according to the void volume fraction. However, if it is greater than the critical value, it will increase rapidly due to the influence of hydrostatic pressure. In

this case, plastic instability begins. It is assumed that the evolution of void volume fraction during plastic deformation is the result of void growth and nucleation of new voids:

$$\dot{f} = \dot{f}_{nucleation} + \dot{f}_{growth} \tag{II-13}$$

Nucleation is considered to depend entirely on the effective strain of material and can be estimated by the following equation:

$$\dot{f}_{nucleation} = A\dot{\varepsilon}^{p}_{eq} \tag{II-14}$$

where A is a parameter defined as a function of the equivalent plastic strain:

$$A = \frac{f_n}{S_n\sqrt{2\pi}}\exp(-\frac{1}{2}(\frac{\varepsilon^p - \varepsilon_n}{S_n})^2) \tag{II-15}$$

where f_n is the void volume fraction of void nucleating particles ε_n is the mean void nucleating strain, S_n is the corresponding standard deviation of the nucleating strain distribution and ε^p is the effective plastic strain.

In addition, the void growth is a function of the plastic strain rate, which can be expressed by the following relation:

$$\dot{f}_{growth} = (1-f)\dot{\varepsilon}^{p}_{kk} \tag{II-16}$$

where $\dot{\varepsilon}^{p}_{kk}$ is the trace of the plastic strain rate tensor.

In order to study the evolution of damage caused by impact during SMAT, we have extended the GTN model by combining dislocation density-based models and GTN damage, and a dislocation density damage model is thus proposed [87]. The constitutive model and the damage model are implemented by the user-defined subroutine of the finite element code of ABAQUS. It will be detailed in Chapter 5 of the present manuscript. By considering different factors such as incident angle and velocity, a single impact is numerically simulated to study deformation and damage evolution, and different parameters such as residual stress, equivalent plastic strain, dislocation density, volume fraction of twin and damage evolution are also studied. The results allow us to better understand the evolution of damage and other mechanical properties.

2.9 Numerical simulation tools

The Finite Element Method (FEM) (which is commonly referred to as the Finite Elemental Analysis (FEA) in practice) is a numerical technique for finding approximate solutions to partial differential equations (PDE) and integral equations [88]. Finite element analysis is widely used to analyze behavioral loads that are subject to a variety of complex parts and structures. Behavior can be static or dynamic, and the structural response can be linear or non-linear. The basic idea of FEM is to subdivide the structure to be analyzed into a grid of finite-size elements with simple shapes. For each element, the change in displacement is determined by a simple polynomial shape and the node displacement [89].

There are various FEA packages available on the market, such as ABAQUS, ANSYS, COSMOS, etc. [89], [90]. These packages with good pre/post-processing capabilities can analyse various problems: for example, the distribution of stress and strain, the deformation of materials in static and dynamic processes in elastic or plastic regions, fatigue phenomena, diffusion processes, heat transfer, electromagnetic field distribution, and fluid dynamics.

In this study, ABAQUS is used for pre-treatment and post-treatment. The secondary development platform UMAT/VUMAT (user material subroutine) is used to implement new constitutive equations. Unlike the elastic problem, the solution to the nonlinear plastic problem cannot be directly obtained. Instead, an iterative process must be involved. Each iteration consists of two steps. First, the global step involves calculating the displacement at the structural node and the total strain and stress ε, σ at the Gaussian point, assuming an increment of the plastic strain $\Delta\varepsilon^p$ between the instants t and t+ Δt at all points. Second, the local step involves considering the total strain ε (or rather its increment $\Delta\varepsilon$) obtained from the global step given by each point and then using the equation to calculate the elastic and plastic strains $\Delta\varepsilon^e$, $\Delta\varepsilon^p$ and stress σ [91].

Usually, the VUMAT subroutine is used to define the mechanical constitutive behavior of materials, and update or use the State-Dependent Variables (SDV) to track the material response as needed. An important feature of VUMAT is that it uses a two-stage architecture consisting of "old" and "new". The initial value at the beginning of each increment must be specified in the "old" array. At the end of each increment, a "new" array must be allocated for the "updated" results. ABAQUS

automatically performs "old" and "new" transformations, setting the value of the "new" array to the next incremental "old" array. Developing and writing user material subroutines involve four steps [92]:

1. The proper definition of the constitutive equation including an explicit definition of stress (Cauchy stress for finite deformation applications) and definition of the stress rate only (in corotational framework);

2. Definition of dependence on time, temperature, or field variable and definition of internal state variables, either explicitly or in rate form;

3. Transformation of the constitutive rate equation into an incremental equation using a suitable integration procedure: Forward Euler (explicit integration), Backward Euler (implicit integration) or Midpoint method;

4. Coding the UMAT or VUMAT and verifying it with a small (one element) input file.

2.10 Conclusions

In this chapter, Surface mechanical attrition treatment (SMAT) is first introduced. The nanostructured layer induced by SMAT can significantly improve some of the mechanical properties of materials, such as hardness, yield strength, fatigue and wear properties. Subsequently, the surface nanocrystallization mechanism of SMATed 316L and 304L steels with different stacking fault energy (SFE) are described. Then, the mechanisms of grain refinement (formation of planar dislocation arrays and mechanical twins, grain subdivision, and formation of randomly oriented crystals) are introduced in detail. Afterward, a brief presentation is given about the current understanding of the mechanism of martensitic transformation and damage. At last, we focused on the dislocation density model and GTN damage model. At the end of this chapter, the UMAT/VUMAT (user-defined material subroutine) of ABAQUS finite element package is briefly introduced. This chapter is dedicated to the literature review and will be applied in the following chapters for the explanation of the experimental results and the construction of the constitutive models.

CHAPTER 3 EXPERIMENTAL STUDY

This chapter lists the main characterization techniques that have been used to characterize the properties of the SMATed samples, such as Scanning Electron Microscopy (SEM), X-ray Diffraction (XRD), and Nanoindentation. The microstructure of 304L steel was investigated by SEM and XRD. The mechanical properties of the SMATed samples were mainly studied by Nanoindentation. The details of the experimental techniques are described as follows.

3.1 SMAT equipment

Different strategies have been proposed to accomplish surface alteration, especially through the usage of nanocrystallization treatment. To obtain grain refinement, the technology called Surface Mechanical Attrition Treatment (SMAT) has been used. SMAT was first proposed by Lu et al. [35], and it is based on the vibration of the balls boosted by a high-power ultrasonic generator [93].

Fig. III-1 shows the illustration and the schematic representation of the SMAT equipment. The SMAT machine used in this work consists of an ultrasonic generator. The electrical energy is converted into mechanical vibrations by the ultrasonic converter. The vibration is amplified by the booster and then is applied to the horn, which causes the balls in the confined chamber to actuate and hit the sample.

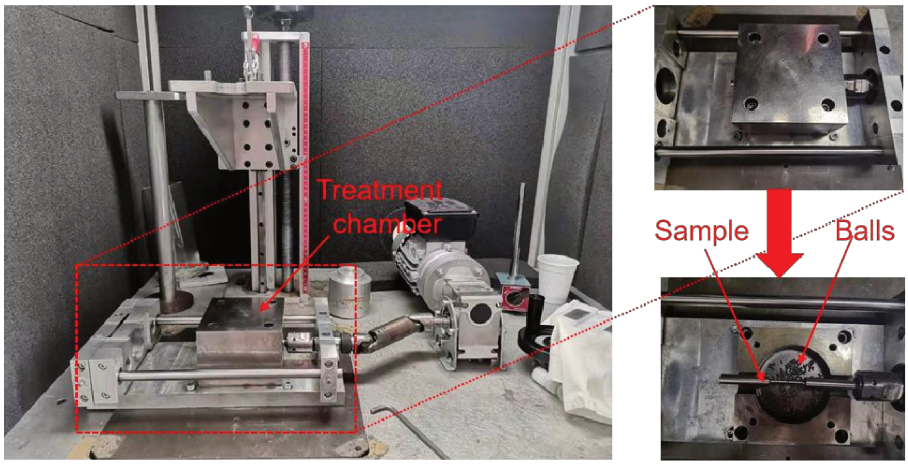

(a)

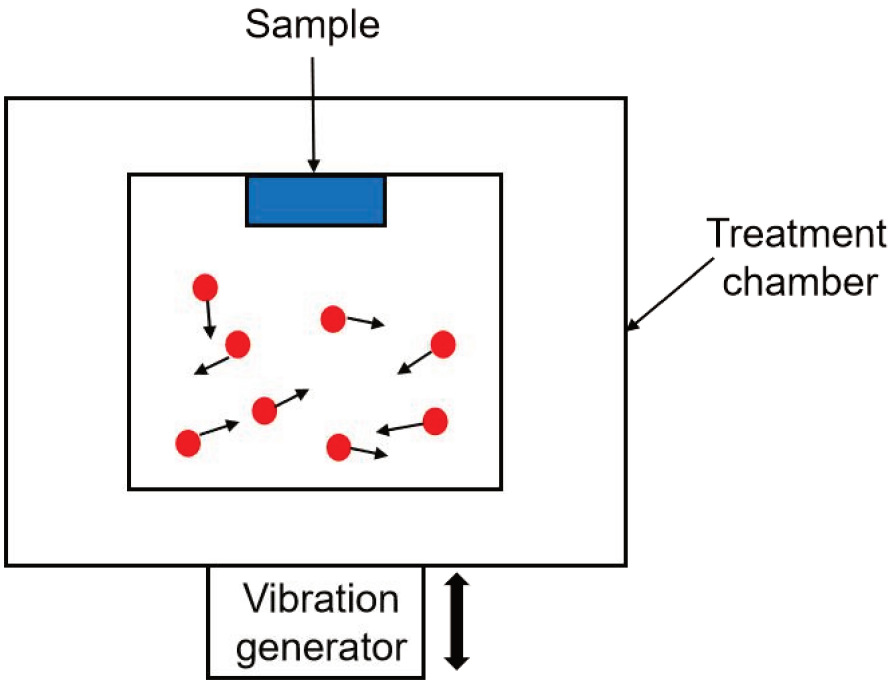

(b)

Fig. III-1. Pictures (a) and schematic description (b) of the SMAT machine.

3.2 Material

The material studied in this chapter is a 304L stainless steel provided by Goodfellow. Tab. III-1 shows the chemical composition of this alloy. Fig. III-2 gives the dimensions of the tensile test sample. The sample was processed into a dumbbell

shape with a gauge length of 20 mm and a diameter of 3 mm in the gauge section. The gauge length is the useful length of the sample to test.

Tab. III-1. Chemical composition (wt.%) of the studied 304L steel.

Fe	C	Cr	Ni	Mn	Mo	Si	S	P	Cu	Co	V
Balance	0.003	18.22	6.0	1.6	0.45	0.5	0.005	0.01	0.8	0.1	0.1

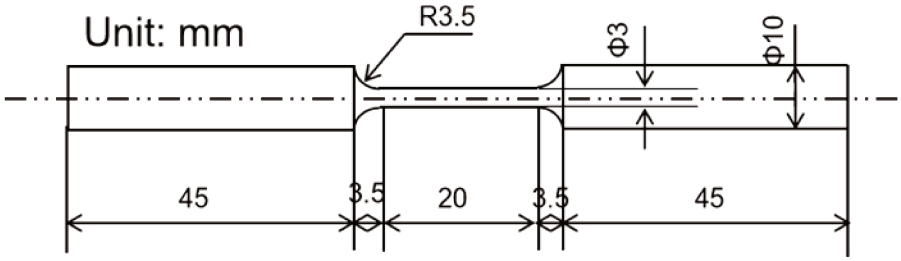

Fig. III-2. The dimensions of the tensile test sample for 304L steel.

3.3 SMAT conditions

The sample was processed by SMAT to generate a gradient microstructure in the near-surface region. As the strength of the 304L steel is not very high, smaller diameter balls are chosen in this work, and the diameter of the balls is 2 mm. SMAT is based on the vibration of the spherical shots boosted by high frequency (20 kHz) ultrasonic generator. Also SMAT is performed to cover the entire gauge of the sample. Regarding the SMAT conditions, the samples are treated by SMAT for 15 min at 30% generator power, followed by a treatment of 5 min at 50% generator power, which corresponds to a relatively high processing intensity [53].

3.4 Materials characterization techniques

Some characteristics, including microstructure and basic mechanical properties of the 304L steel, were investigated by X-ray Diffraction (XRD) and Nanoindentation. Details of these characterization techniques are described in the following sections.

3.4.1 X-ray diffraction (XRD)

3.4.1.1 Introduction to XRD

XRD is a widely used method in materials science. It is an analytical technique used to reveal crystal structure and material composition, as well as to investigate

mechanical stress or texture. XRD can be applied to study various materials. In this work, XRD 3000 X-ray diffractometer (developed by Seifert company) was used, as shown in Fig. III-3.

XRD is based on the fact that electrons in an oscillating electromagnetic field oscillate at the same frequency as the electric field. When X-ray beam hits an atom, the electrons in the atom start to oscillate at the same frequency as the incident beam. Due to the regular/periodic pattern of atomic arrangements in the crystalline material, specific directions allow constructive interferences, i.e., the ones that fulfill the Bragg's relations. Bragg's law can be expressed as [94]:

$$n\lambda = 2d \sin \theta \tag{III-1}$$

where n is the order of reflection, generally speaking, the probability of the process drops down with increasing momentum transfer (reflection order n), so n = 1 gives the major reflection peak; λ is the wavelength of the incident X-ray beam; d is the interplanar distance; θ is the Bragg angle.

As the grain size decreases, the peak of the diffraction pattern becomes wider. Indeed, the crystallite size can be calculated according to Scherrer's formula:

$$D = \frac{K\lambda}{w\cos\theta} \tag{III-2}$$

where D is the average grain size; K is a constant that depends on how the width is determined, the shape of the crystal, and the size distribution, for example, 0.94 for Full-Width-At-Half-Maximum (FWHM) of spherical crystals with cubic symmetry and 0.89 for the integral breadth of spherical crystals cubic symmetry. With other methods, K varies from 0.62 to 2.08 [95]. λ is the wavelength of the incident X-ray beam; w is the peak width and θ is the Bragg angle of the peak center [96].

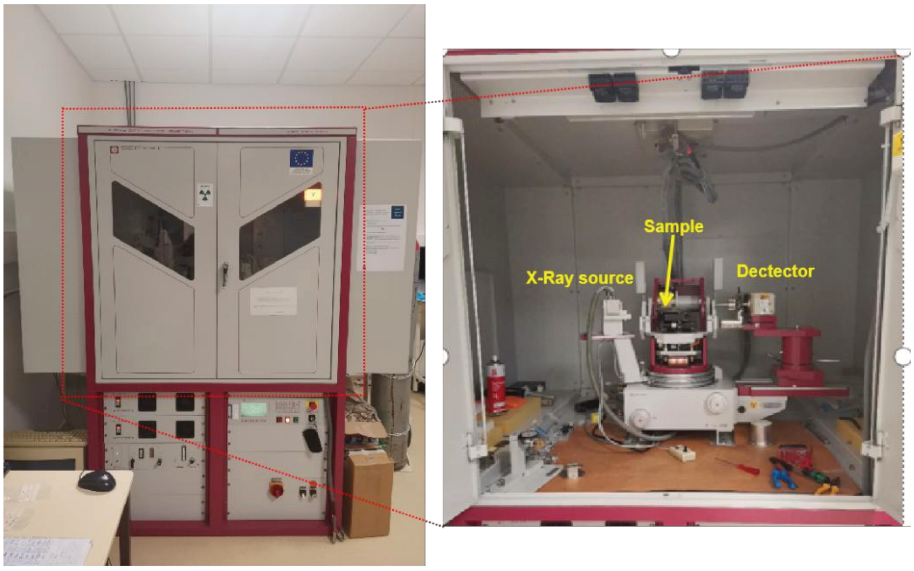

Fig. III-3. XRD equipment used in this work.

3.4.1.2 Analysis of the volume fraction of austenite and martensite through XRD

XRD measurements were performed by using a Cr anode (wavelength λ= 0.2291 nm). The penetration depth of X-rays (Cr radiation) of the steel is a few micrometers [97]. The quantitative estimation of austenite and martensite content is based on the principle that the volume fraction of each phase is proportional to the integrated intensity of all diffraction peaks for that phase [98]. It is well established that, in the case of the random orientation of the grains in each phase, the integrated intensity I_i of any diffraction peak from phase i is given by:

$$I_i = \frac{1}{32\pi r} I_0 \left(\frac{e^2}{mc^2} \right)^2 N^2 \lambda^3 V_i P |F|^2 \frac{1+\cos^2 2\theta}{\sin^2 \theta \cos\theta} e^{-2M} \frac{1}{\mu} \quad \text{(III-3)}$$

where r is the radius of diffractometer circle [99], I_0 is the intensity of the incidental beam, e and m are respectively the charge and the mass of the electron, c is the speed of light, N is the number of unit cells in the crystal ($N = 1/\mu$), λ is the wavelength of the incident X-ray beam, V_i is the volume fraction of the phase i detected by X-ray beam, P is the multiplicity factor, F is the structure factor for reflecting plane (hkl), θ is the Bragg angle, e^{-2M} is the temperature factor (Debye-Wähler), and μ is the linear absorption coefficient.

The scattering factors of individual phases were calculated by the minimization of factor R, as shown in Eq. III-4:

$$R = \frac{1}{\mu^2} P\left|F\right|^2 \frac{1+\cos^2 2\theta}{\sin^2\theta\cos\theta} e^{-2M} \tag{III-4}$$

First, the lattice parameters of different crystal planes can be solved using the Bragg equation and the reflection angle, and then the lattice parameters and the value $1/\mu^2$ are used to determine the unit cell volume.

Then the volume fraction of martensite can be calculated by measuring the integral intensity of each reflection plane of each phase with a single XRD scan according to the following equation:

$$V_m = \frac{1/n^p \sum_{j=1}^{n^p} I_i^j / R_i^j}{1/n^p \sum_{j=1}^{n^p} I_\gamma^j / R_\gamma^j + 1/n^p \sum_{j=1}^{n^p} I_\alpha^j / R_\alpha^j} \tag{III-5}$$

where n^p is the number of peaks examined, and the subscripts γ and α represent the austenite and martensite in 304L steel, respectively. Austenite peaks (111) and (220) and martensite peaks (110) and (200) are selected to calculate the volume fraction of the phases. It is assumed that the phase content uncertainty given by this method is less than 3% [100].

Fig. III-4 shows the XRD patterns of the 304L sample deformed before and after SMAT. The top diffractogram corresponds to the sample after SMAT, and the one below corresponds to the sample before SMAT, i.e., as-received state. From the XRD measurements shown in Fig. III-4, it can be identified that there is only austenite in the sample before SMAT; while for the sample after SMAT, there is a phase transformation from austenite to martensite in the sample and the volume fraction of martensite increases up to 78%. Similar results have also been noticed in the literature [101].

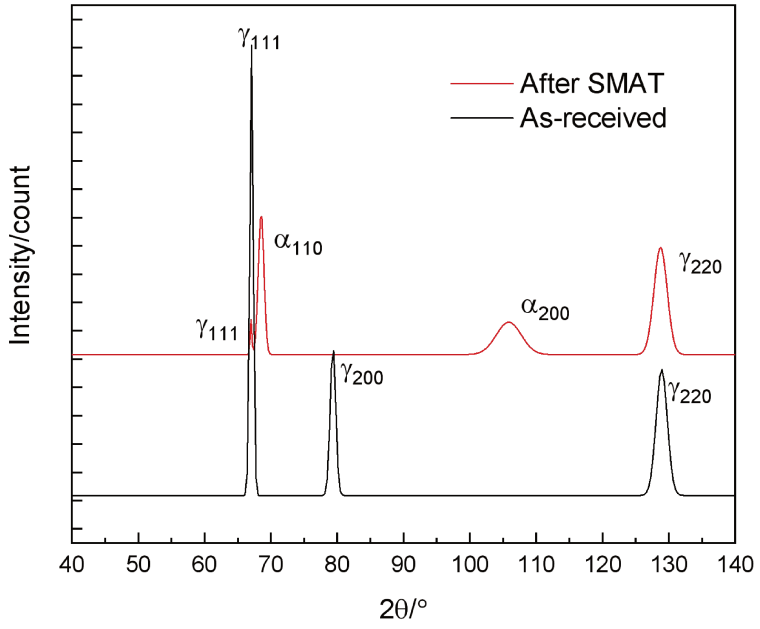

Fig. III-4. X-ray Diffraction diffractograms of the 304L steel before and after SMAT.

3.4.1.3 Analysis of residual stress through XRD experiment

We first consider the law of $\sin^2\psi$ in the general case, which is derived in different situations. We have:

$$\varepsilon_{\varphi\psi}^{elas} = \left(\overline{\overline{\varepsilon}}^{elas} \cdot n_{\varphi\psi}\right) \cdot n_{\varphi\psi}$$

$$= \left(\varepsilon_{11}\cos^2\varphi + \varepsilon_{22}\sin^2\varphi + \varepsilon_{12}\sin 2\varphi - \varepsilon_{33}\right)\sin^2\psi + \left(\varepsilon_{13}\cos\varphi + \varepsilon_{23}\sin\varphi\right)\sin 2\psi + \varepsilon_{33}$$

$$= \ln\left(\frac{d}{d_0}\right) = \ln\left(\frac{\sin\theta_0}{\sin\theta}\right)$$

$$= \frac{S_2}{2}\left(\sigma_{11}\cos^2\varphi + \sigma_{22}\sin^2\varphi + \sigma_{12}\sin 2\varphi - \sigma_{33}\right)\sin^2\psi + \frac{S_2}{2}\left(\sigma_{13}\cos\varphi + \sigma_{23}\sin\varphi\right)\sin 2\psi \quad \text{(III-6)}$$

$$+ S_1\left(\sigma_{11} + \sigma_{22}\right) + \left(S_1 + \frac{S_2}{2}\right)\sigma_{33}$$

where $\varepsilon_{\varphi\psi}^{elas}$ is the elastic strain measured in the direction defined by the angles φ (azimuth, or rotation angle in the plane of the sample surface) and ψ (the tilt angle of the sample relative to the normal of the sample surface), $\overline{\overline{\varepsilon}}^{elas}$ is the elastic strain tensor, $n_{\varphi\psi}$ is the normal vector of the plane defined by the angles φ and ψ, d_0 and θ_0 are respectively the interplanar distance and Bragg angle in the unstressed state

(i.e., free of stress), d and θ are the interplanar distance and Bragg angle in the stressed state, S_1 and S_2 are the radiocrystallographic elastic coefficients.

The Hooke elastic model (linear, homogeneous, and isotropic), hence assuming no macrotexture, is used to link the elastic strain to the stress. The effects of plastic deformation incompatibility and strain or stress gradients will also be ignored. The macroscopic modulus of elasticity has to be replaced by radiocrystallographic elastic coefficients S_1 and ½ S_2 (that may depend on hkl). We consider symmetrical Bragg-Brentano diffraction using a punctual detector. Experimentally, the stress tensor can be determined by using the approximation $\sigma_{33} = 0$, which is usually related to the fact that sample surface measurements and/or thin layers are considered.

$$\varepsilon_{\varphi\psi}^{elas} = \ln\left(\frac{\sin\theta_0}{\sin\theta}\right)$$

$$= \frac{S_2}{2}\left(\sigma_{11}\cos^2\varphi + \sigma_{22}\sin^2\varphi + \sigma_{12}\sin 2\varphi\right)\sin^2\psi + \frac{S_2}{2}\left(\sigma_{13}\cos\varphi + \sigma_{23}\sin\varphi\right)\sin 2\psi + S_1\left(\sigma_{11} + \sigma_{22}\right) \quad \text{(III-7)}$$

There are two ways to solve this equation and determine the stress components: the ellipsoid given by Eq. III.7 (related to variables ψ and φ) degenerates into an ellipse in the plane defined when plotting stress vs. ψ for a given φ. The first method then consists of regressing the data by an ellipse and identifying the different stress components with the obtained coefficients.

Data treatment with Dölle method

The second method proposed by Dölle in the context of stress measurement consists in transforming the elliptical equation into two straight-line equations [102].

In both cases, the operation must be repeated a minimum number of 3 times to obtain all components of the stress tensor. It is sufficient to use three angles φ such as 0 °, 45 °, and 90°. We will introduce the Dölle method for the three angles in detail. The Dölle method is obtained by summation, and then the difference between ψ> 0 and ψ <0. Therefore, due to the equality of terms, we obtain:

$$A^+ = \frac{1}{2}\left(\varepsilon_{\varphi\psi>0}^{elas} + \varepsilon_{\varphi\psi<0}^{elas}\right)$$

$$= \frac{S_2}{2}\left(\sigma_{11}\cos^2\varphi + \sigma_{22}\sin^2\varphi + \sigma_{12}\sin 2\varphi\right)\sin^2\psi + S_1\left(\sigma_{11} + \sigma_{22}\right) \quad \text{(III-8)}$$

$$\Rightarrow A_{\varphi=0}^{+} = \frac{S_2}{2}\sigma_{11}\sin^2\psi + S_1\left(\sigma_{11} + \sigma_{22}\right) \quad \text{(III-9)}$$

$$\Rightarrow A^{+}_{\varphi=45^\circ} == \frac{S_2}{2}\left(\sigma_{11}+\sigma_{22}+2\sigma_{12}\right)\sin^2\psi + S_1\left(\sigma_{11}+\sigma_{22}\right) \quad \text{(III-10)}$$

$$\Rightarrow A^{+}_{\varphi=90^\circ} == \frac{S_2}{2}\sigma_{22}\sin^2\psi + S_1\left(\sigma_{11}+\sigma_{22}\right) \quad \text{(III-11)}$$

Using the slope of these 3 lines, we get 3 equations with 3 unknowns. We can even check the sum of the three coordinates of the origin ($\sigma_{11} + \sigma_{22}$) and compare them. Then, due to the parity of the terms, we have:

$$A^{-} = \frac{1}{2}(\varepsilon^{elas}_{\varphi\psi>0} - \varepsilon^{elas}_{\varphi\psi<0})$$

$$= \frac{S_2}{2}\left(\sigma_{13}\cos\varphi + \sigma_{23}\sin\varphi\right)\sin 2\psi \quad \text{(III-12)}$$

$$\Rightarrow A^{-}_{\varphi=0} = \frac{S_2}{2}\sigma_{13}\sin 2\psi \quad \text{(III-13)}$$

$$\Rightarrow A^{-}_{\varphi=45^\circ} == \frac{S_2}{2}\frac{\sqrt{2}}{2}\left(\sigma_{13}+\sigma_{23}\right)\sin 2\psi \quad \text{(III-14)}$$

$$\Rightarrow A^{-}_{\varphi=90^\circ} == \frac{S_2}{2}\sigma_{23}\sin 2\psi \quad \text{(III-15)}$$

Using the slope of these three lines, we obtain three equations, in which there are two unknowns. We can then check the consistency of the results using the third equation. In this data treatment method, it is worth noting that the interarticular distance for free stress (d_0) is an important parameter which needs to be a priori known.

XRD analysis can distinguish the microstructure constituents according to their crystallographic structure. Diffraction peaks of austenite appear at different 2θ positions than the peaks of martensite, enabling to determine selectively the stress in each structure. XRD stress determination has been performed in the austenite on the {220} peak using a Cr radiation. The stress in the martensite has also been determined on the {200} peak using the same Cr radiation. Three ϕ angles 0°, 45°, and 90° have been used and thirteen ψ angles 0°, $\pm 23^\circ$, $\pm 33^\circ$, $\pm 42^\circ$, $\pm 50^\circ$, $\pm 59^\circ$, and $\pm 70^\circ$ have been used as required by the standard of measurement [103].

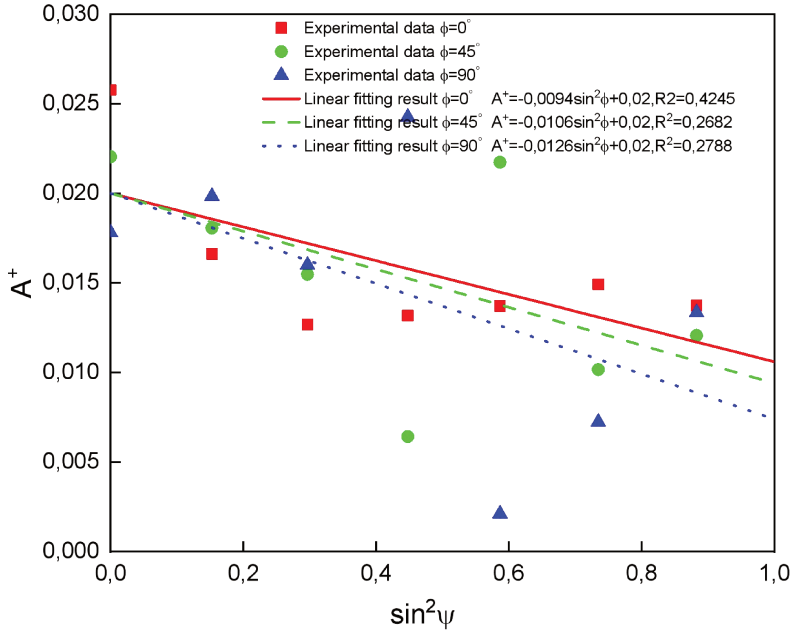
Experimental data ϕ=0°
Experimental data ϕ=45°
Experimental data ϕ=90°
Linear fitting result ϕ=0° A+=-0,0094sin2ϕ+0,02,R2=0,4245
Linear fitting result ϕ=45° A+=-0,0106sin2ϕ+0,02,R2=0,2682
Linear fitting result ϕ=90° A+=-0,0126sin2ϕ+0,02,R2=0,2788
A+
sin2ψ
0,030
0,025
0,020
0,015
0,010
0,005
0,000
0,0
0,2
0,4
0,6
0,8
1,0

(a)

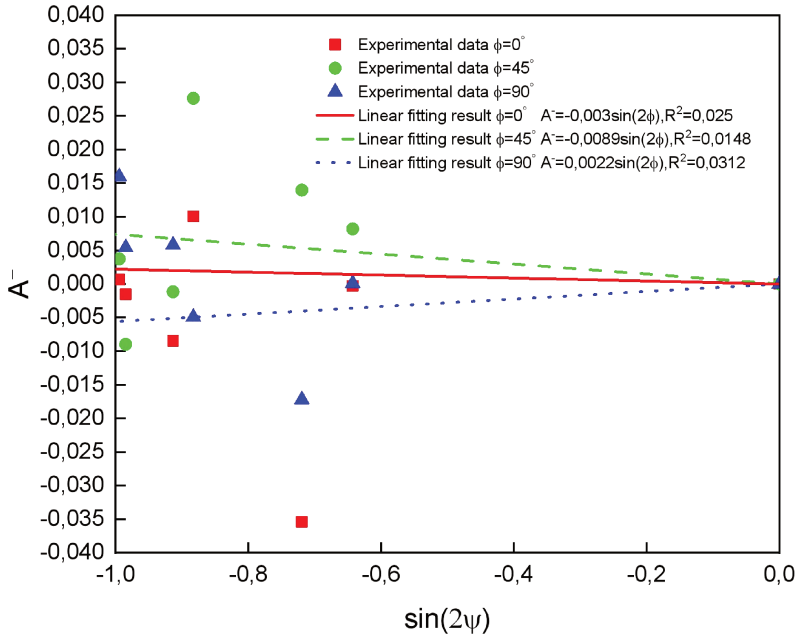
Experimental data ϕ=0°
Experimental data ϕ=45°
Experimental data ϕ=90°
Linear fitting result ϕ=0° A-=-0,003sin(2ϕ),R2=0,025
Linear fitting result ϕ=45° A-=-0,0089sin(2ϕ),R2=0,0148
Linear fitting result ϕ=90° A-=0,0022sin(2ϕ),R2=0,0312
A-
sin(2ψ)
0,040
0,035
0,030
0,025
0,020
0,015
0,010
0,005
0,000
-0,005
-0,010
-0,015
-0,020
-0,025
-0,030
-0,035
-0,040
-1,0
-0,8
-0,6
-0,4
-0,2
0,0

(b)

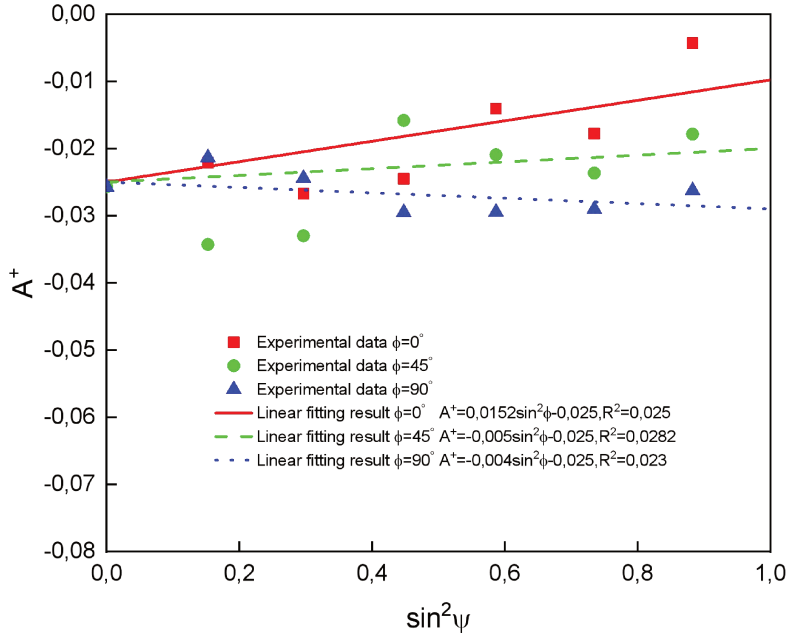

(c)

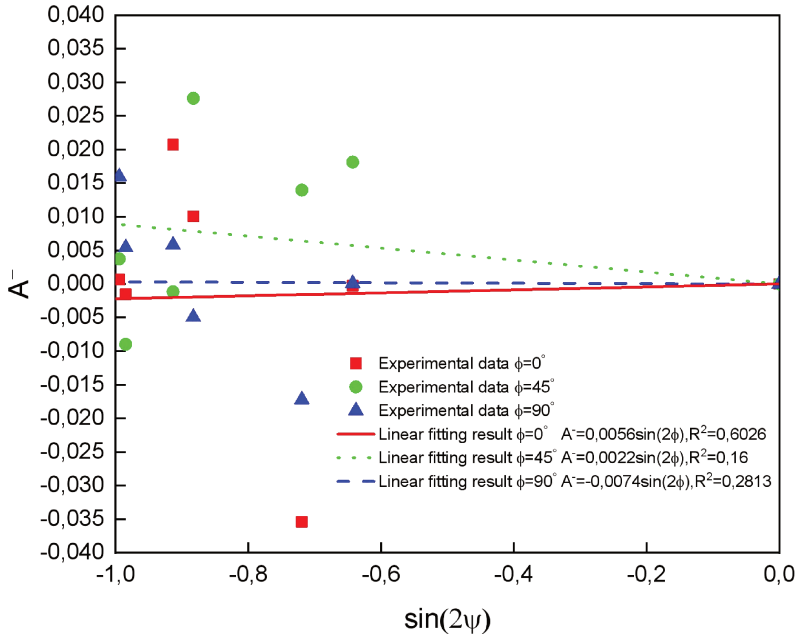

(d)

Fig. III-5. Results for $A^{+}-\sin^{2}\phi$ (a), $A^{-}-\sin 2\phi$ (b) of austenite for {220} peak, and $A^{+}-\sin^{2}\phi$ (c), $A^{-}-\sin 2\phi$ (d) of martensite for {200} peak.

Fig. III-5 gives the relationship for $A^{+}-\sin^2\phi$ and $A^{-}-\sin 2\phi$ for austenite on {220} and martensite on {200}. The slopes between A^{+} and $\sin^2\phi$ and that between A^{-} and $\sin 2\phi$ have been obtained by using a linear fitting tool in Origin software. A negative slope of the linear fitting implies a compressive stress state inside the sample. However, some experimental points are scattered, as shown in Fig. III-5. This can be interpreted as inhomogeneous stress distribution or stress gradients in the volume, which have been neglected for the previous data treatment.

Calculation of XECs for stress determination

Tab. III-2. Stiffness values of the austenite and martensite in 304L steel [104].

Stiffness	Austenite	Martensite
c11 (GPa)	198	268
c12 (GPa)	125	110
c44 (GPa)	122	79

To calculate X-ray/radiocrystallographic elastic coefficients (XECs) S_1 and S_2, models are required. The most simple model is the isotropic model using the elastic constants Young's modulus E and Poisson's ratio *v* [97] :

$$S_1 = -\frac{v}{E}, \frac{1}{2}S_2 = \frac{1+v}{E} \tag{III-16}$$

The XECs S_1 and S_2 shown in Eq. III-16 can be used to analyze the residual stress but are independent of the {hkl} reflection. More advanced models exist describing grain interactions and are based on single-crystal elastic stiffness. The Voigt model assumes that all grains have the same strain state, and the calculated XECs are independent of {hkl}. In the Voigt model, the strain in each crystal is assumed to be uniform and equal to the macro-strain. The diffraction compliances, S_1 and S_2, are given from the single-crystal elastic constants, c_{ij} as follows:

$$S_1 = -\frac{v}{E} = \frac{-2c_{11}-13c_{12}+4c_{44}}{3(c_{11}+2c_{12})*(3c_{11}-3c_{12}+4c_{44})} \tag{III-17}$$

$$\frac{1}{2}S_2 = \frac{1+v}{E} = \frac{5}{3c_{11}-3c_{12}+4c_{44}} \tag{III-18}$$

The Reuss model assumes that all grains have the same stress state, and the calculated XECs are related to {hkl}. Reuss model assumes that the stress in each

crystal is uniform and equal to the macro-stress. The values of S_1 and S_2 are expressed in terms of single-crystal compliances, s_{ij}, as follows [105]:

$$S_1 = -\frac{v}{E} = s_{12} + \frac{1}{2}(2s_{11} - 2s_{12} - s_{44})\cos^2\phi - \frac{1}{2}(2s_{11} - 2s_{12} - s_{44})\cos^4\phi \quad \text{(III-19)}$$

$$\frac{1}{2}S_2 = \frac{1+v}{E} = s_{11} - s_{12} - \frac{3}{2}(2s_{11} - 2s_{12} - s_{44})\cos^2\phi - \frac{3}{2}(2s_{11} - 2s_{12} - s_{44})\cos^4\phi \quad \text{(III-20)}$$

where ϕ is the angle between the normal of the diffraction plane (hkl) and the c-axis. The mechanical elastic constants can be obtained by taking the average. The average over ϕ in the range 0 to π of $\cos^2\phi$ is 1/3, and the average of $\cos^4\phi$ is 1/5. The corresponding elastic compliances matrix s_{ij} can be obtained by the inverse matrix of the stiffness constants c_{ij} as follows [106]:

$$s_{11} = \frac{c_{11}^2 - c_{12}^2}{c_{11}(c_{11}^2 - c_{12}^2) + 2c_{12}^2(c_{12} - c_{11})} \quad \text{(III-21)}$$

$$s_{12} = \frac{c_{12}^2 - c_{12}c_{11}}{c_{11}(c_{11}^2 - c_{12}^2) + 2c_{12}^2(c_{12} - c_{11})} \quad \text{(III-22)}$$

$$s_{44} = \frac{1}{c_{44}} \quad \text{(III-23)}$$

Here, we use the Neerfeld-Hill model to calculate the XECs, which is based on the Voigt and Reuss models to make arithmetic mean of these two models [97]. In the 304L steel processed by SMAT, austenite and martensite can be assumed as isotropic polycrystalline materials. Therefore, Young's modulus E and the Poisson's ratio *v* of austenite and martensite in the Neerfeld-Hill model can be calculated by the stiffness values proposed in Tab. III-2 [104]. Once Young's modulus E and the Poisson's ratio *v* are obtained, the radiocrystallographic elastic constants can be calculated for the austenite$\{220\}$ and martensite$\{200\}$ by Eqs. III-19 and III-20 [107], and the corresponding values for XECs are as follows:

$$S_1^{\gamma} = -1.288\times10^{-6}\,MPa^{-1}, \frac{1}{2}S_2^{\gamma} = 6.097\times10^{-5}\,MPa^{-1}$$

$$S_1^{\alpha} = -1.439\times10^{-6}\,MPa^{-1}, \frac{1}{2}S_2^{\alpha} = 6.357\times10^{-5}\,MPa^{-1}$$

Stress results and discussion on experiments

With the slope of the lines fitted from experimental results, the residual stress in each direction in austenite and martensite can be calculated by Eqs. III-8 to III-15 as follows (values are in MPa):

$$\sigma_{ij}^{\gamma}=\begin{pmatrix}\sigma_{11} & \sigma_{12} & \sigma_{13}\\ \sigma_{21} & \sigma_{22} & \sigma_{23}\\ \sigma_{31} & \sigma_{32} & \sigma_{33}\end{pmatrix}=\begin{pmatrix}-154.2 & 93.5 & -49.2\\ 93.5 & -206.7 & 36.1\\ -49.2 & 36.1 & 0\end{pmatrix} \quad \text{(III-24)}$$

$$\sigma_{ij}^{\alpha}=\begin{pmatrix}\sigma_{11} & \sigma_{12} & \sigma_{13}\\ \sigma_{21} & \sigma_{22} & \sigma_{23}\\ \sigma_{31} & \sigma_{32} & \sigma_{33}\end{pmatrix}=\begin{pmatrix}239.1 & -88.1 & 88.1\\ -88.1 & -70.8 & 34.6\\ 88.1 & 34.6 & 0\end{pmatrix} \quad \text{(III-25)}$$

SMATed metal alloys are almost ideal samples for XRD residual stress measurement. However, problems do arise, some related to the method itself, and some related to the nature and form of the sample.

(1) Errors due to hardware and software treatment

The XRD method requires expensive precision instruments (usually controlled by computer) and a large amount of data processing to reliably determine the position of the broad diffraction peaks to achieve the required accuracy (0.01 degree at least). Errors in XRD residual stress measurements can come from a variety of reasons and are often difficult to detect, as previously mentioned.

(2) Stress gradients

The near-surface residual stress gradient is the rapid change of residual stress with surface depth and the main source of systematic error, which directly affects the use of XRD methods for non-destructive surface measurement. Presently, the measure is averaged in all the penetration depth. Many surface treatments produce a residual stress distribution that changes rapidly near the surface of the material. The attenuation rate of the X-ray beam can be determined by calculating the linear absorption coefficient from the density and the composition of the alloy. If XRD measurements are performed at small increments of depth by electropolishing, the true residual stress distribution could be calculated from the apparent distribution.

(3) Effects of prior processing

When using residual stress measurement to study SMAT, it is important to realize that the residual stress distribution after SMAT depends not only on the SMAT parameters used but also on the previous processing of the material. e.g., carburizing

before SMAT. Liu et al. [108] studied the effect of surface nanocrystallization on low-temperature gas carburization (LTGC) for AISI 316L austenitic stainless steel treated with shot peening. The stress distribution can be observed under the surface of the region with the decarburized surface layer on the same sample as the original sample, and then the sample is electropolished to remove the decarburized layer. The results show that even two regions are treated by the same shot peening conditions, the residual surface stress in the decarburization area is greatly reduced.

(4) The ambiguity of results measured from the top surface

Non-destructive surface XRD residual stress measurements are often insufficient to characterize the residual stresses produced by SMAT. All cold-grinding processes, such as grinding, wire brushing, polishing, sandblasting, and shot peening, can induce additional compressive surface stresses, usually of comparable magnitude. If several micrometers are removed by etching, residual stress induced by SMAT can be eliminated, and the surface stress would be nearly identical to the original one before SMAT [20].

Stress uncertainties

It is worth noting that calibration of the XRD machine is initially performed by use of a standard sample, especially to ensure that no stress arises from measurement on a powder sample. Secondly, before each measurement, the height of the sample surface is controlled and positioned with accuracy to avoid systematic errors. However, as for other experiments, the residual stress measurement technologies are not perfect, and imperfections cause measurement uncertainties in the measurement results. In this case, uncertainty statements are required. The three main factors that have the greatest impact on measurement uncertainty are the measurement repeatability, the calculation of the stress constant K, and the slope fitting for stress factor M determination.

One important for these uncertainties for XRD is the measurement of the unstressed d-spacing. There are several ways to determine the unstressed lattice spacing d_0. Since the difference between the lattice spacing value measured at $\psi = 0$ and the unstressed lattice spacing does not exceed 0.1%, the intercept can be substituted by d_0. Residual stresses can then be calculated without reference to unstressed standards. Another method uses data obtained during stress measurements. If the stress state is biaxial, the method can be used to determine d_0 from the d vs. $\sin^2\psi$ curve. The method of determining unstressed d-space influences the accuracy of

measurements. Increasing d_0 will reduce the magnitude of the measured residual stress [109].

In addition to the above factors, many parameters may also cause measurement uncertainties, such as the number of ψ angles of the $\sin^2\psi$ technique, the peak position method, the plane curvature, the aperture dimension, and the fluctuation of the beam. However, X-ray diffraction is one of the most advanced methods that can be used to determine residual stress. There are many improvements in the hardware and software of XRD equipment and the calculation of correction factors to improve XRD measurement accuracy. The residual stress measurement accuracy of the XRD method is presently around ± 20 MPa as it will be further proved. The penetration depth of X-ray for 304L steel is around 20 μm for the considered wavelength and geometrical measurement conditions [110], [111].

We will now propose a systematic treatment of the three above listed kind of uncertainties:

(1) Uncertainty of the measurement repeatability

Three measurements were performed on the 304L steel, and the results are shown in Tab. III-3.

Tab. III-3. Measurement results of residual stress for 304L steel.

Stress component	Average stress in austenite σ_γ (MPa)	The standard deviation of the stress in austenite s(x) (MPa)	Average stress in martensite σ_m (MPa)	Standard deviation of the stress in martensite s(x) (MPa)
σ_{11}	-154.2	6.8	239.1	5.8
σ_{22}	93.5	6.3	-88.1	2.1
σ_{12}	-206.7	9.7	-70.8	1.9
σ_{13}	-49.2	5.2	88.1	2.9
σ_{23}	36.1	2.3	34.6	1.1

The average value of the test results is calculated, and the standard deviation is obtained. The uncertainty component introduced by the repeatability of the measurement results $U(\sigma)$ is [112], [113]:

$$U(\sigma)=\frac{s(x)}{\sqrt{n_t}} \tag{III-26}$$

where $s(x)$ is the standard deviation, n_t is the number of measurements (here $n_t = 3$). The results are given in Tab. III-4.

Tab. III-4. Uncertain component of repeatability.

Stress component	Uncertain component of repeatability in austenite $U(\sigma)$ (MPa)	Uncertain component of repeatability in martensite $U(\sigma)$ (MPa)
σ_{11}	3.9	3.3
σ_{22}	3.6	1.2
σ_{12}	5.6	1.1
σ_{13}	3.0	1.7
σ_{23}	1.3	0.6

(2) Uncertainty of the stress constant K

The operator will estimate or select a stress constant based on the material information provided. The error δ between the estimated value and the real value is usually within ± 3%. The uncertainty of stress constant $U(K)$ can be obtained by [112], [113]:

$$U(K) = \frac{\delta \sigma_m}{\sqrt{k_t}} \tag{III-27}$$

where σ_m is the average residual stress, k_t is the confidence factor, usually $k_t = 3$. The results are given in Tab. III-5.

Tab. III-5. Uncertainty of stress constants.

Stress component	Uncertainty of stress constant in austenite $U(K)$ (MPa)	Uncertainty of stress constant in martensite $U(K)$ (MPa)
σ_{11}	2.7	4.1
σ_{22}	1.6	1.5
σ_{12}	3.6	1.2
σ_{13}	0.9	1.5
σ_{23}	0.6	0.6

(3) Uncertainty of the stress factor M

The uncertainty of stress factor M obeys the uniform distribution. The uncertainty of stress constant $U(M)$ is affected by many factors, and it is quite

difficult to determine. We assume that the value of $U(M)$ is 1 MPa as proposed in [112], [113]. The synthetic uncertainty is calculated as follows:

$$U_c(\sigma)=\sqrt{U^2(\sigma)+U^2(K)+U^2(M)} \quad \text{(III-28)}$$

Tab. III-6 gives the synthetic uncertainty $U_c(\sigma)$ for the different stress components.

Tab. III-6. The synthetic uncertainty.

Stress component	The synthetic uncertainty in austenite $U_c(\sigma)$ (MPa)	The synthetic uncertainty in martensite $U_c(\sigma)$ (MPa)
σ_{11}	4.9	5.4
σ_{22}	4.1	2.2
σ_{12}	6.7	1.9
σ_{13}	3.3	2.5
σ_{23}	1.8	1.3

According to international standards [112], [113], with a confidence probability of 95% and a factor $k_i = 2$, the expanded uncertainty U is:

$$U=k_iU_c(\sigma) \quad \text{(III-29)}$$

Hence we can obtain the residual stress and corresponding uncertainties in different directions for austenite and martensite as follows:

$$\sigma_{ij}^{\gamma}=\begin{pmatrix}\sigma_{11} & \sigma_{12} & \sigma_{13}\\ \sigma_{21} & \sigma_{22} & \sigma_{23}\\ \sigma_{31} & \sigma_{32} & \sigma_{33}\end{pmatrix}=\begin{pmatrix}-154.2\pm9.7 & 93.5\pm8.2 & -49.2\pm6.6\\ 93.5\pm8.2 & -206.7\pm13.4 & 36.1\pm3.6\\ -49.2\pm6.6 & 36.1\pm3.6 & 0\end{pmatrix} \quad \text{(III-30)}$$

$$\sigma_{ij}^{\alpha}=\begin{pmatrix}\sigma_{11} & \sigma_{12} & \sigma_{13}\\ \sigma_{21} & \sigma_{22} & \sigma_{23}\\ \sigma_{31} & \sigma_{32} & \sigma_{33}\end{pmatrix}=\begin{pmatrix}239.1\pm10.8 & -88.1\pm4.4 & 88.1\pm5\\ -88.1\pm4.4 & -70.8\pm3.9 & 34.6\pm2.7\\ 88.1\pm5 & 34.6\pm2.7 & 0\end{pmatrix} \quad \text{(III-31)}$$

From Eqs. III-30 and III-31, the von Mises residual stress in austenite and martensite can be calculated, which are $318.4\pm25.2MPa$ and $367.2\pm18.2MPa$, respectively. The hydrostatic stress in austenite and martensite can also be calculated, and are $-120.3\pm8MPa$ and $56.1\pm4.9MPa$, respectively. A negative hydrostatic stress means that the residual stress in martensite is compressive. Thus, after SMAT, due to the mutual mechanical constraints between the phases, austenite will be in a compressed state, and martensite will be in a stretched state. This result is in good agreement with previous studies [7].

The residual stress of austenite on the top surface is $318.4 \pm 25.2 MPa$, and the residual stress of martensite on the top surface is $367.2 \pm 18.2 MPa$. According to the reference [114], the maximum residual stress of austenite is on the top surface while for martensite, the maximum residual stress located below the surface (with an average distance at 20 μm). This is because, for austenite with lower hardness, plastic stretching in the area on the surface dominates, and the maximum elongation occurs on the surface and decreases with the increase in the depth towards the center. However, on the surface for martensite with a higher hardness, due to the Hertz pressure distribution below the surface, a significant maximum residual stress will appear compared to our case. This is because the Hertzian pressure distribution under the shot of an impact predicts the maximum stress at a point below the surface.

Fatigue cracks are not easily generated or propagated on the specimen surface under compression, SMAT can push the crack initiation point beneath the compressive residual stress zone, therefore, the slight surface roughness caused by SMAT does not lead to a reduction of fatigue strength, when the roughness is severe, the craters and folds produced by SMAT treatment may be the origin of the cracks, SMAT treatment can actually reduce the fatigue strength, which is called overtreatment, and overtreatment reduces the fatigue strength [115]. Previous studies have shown that SMAT will affect fatigue strength, so it is important to quantify the contribution of residual stress to fatigue strength [115], [116]. However, in reality, the residual stress is usually subjected to mechanical and/or thermal loads, so the residual stress may be redistributed and relaxed. The relaxation of residual stress reduces the achievable benefits of shot peening and makes life prediction more difficult. Therefore, studying the effect of effective shear stress after SMAT treatment on residual stress may help predict the life of materials [117]. Since hydrostatic stress does not cause yielding alone, we can find a plane of material called an octahedron plane, in which the stress state can be decomposed into dilatation strain energy and distortion strain energy. On the octahedron plane, the octahedral normal stress only contributes to the expansion of strain energy. The remaining stain energy under stress is determined by the octahedral shear stress and is given by:

$$\tau_8 = \frac{1}{3}\sqrt{(\sigma_{11}-\sigma_{22})^2+(\sigma_{22}-\sigma_{33})^2+(\sigma_{33}-\sigma_{11})^2+6(\sigma_{12}^2+\sigma_{23}^2+\sigma_{31}^2)} \qquad \text{(III-32)}$$

From Eq. III-32, the octahedral shear stress of austenite and martensite can be calculated, which are $150.1 \pm 11.9 MPa$ and $173.1 \pm 8.5 MPa$, respectively. It can be

seen that the octahedral shear stress of austenite is at least two times higher than that of martensite. According to the reference [118], after shot peening, the introduction of residual stress leads to an increase in the octahedron shear stress of the surface, and this increase in the subsurface area is more obvious than in the surface area because the residual stress amplitude in the subsurface areas is larger.

3.4.2 Nanoindentation

To understand the mechanical behavior of SMATed materials, it is important to characterize the mechanical properties of the different mechanically deformed regions at different depths, especially in the nanostructured layer. Characterization of the local mechanical behavior of the nanostructured layer is quite difficult, because of its very small thickness (from several microns to tens of microns, depending on SMAT intensity). To measure the mechanical properties of small-sized materials, nanoindentation can be used to measure the indentation hardness. This is interesting because the indenter size and the load of the nanoindentation are relatively small, and the smallest area that can be measured can reach a few square microns or even nanometers [119].

For nanoindentation, the indenter has a known high-precision geometry. The depth and the area of the indentation can be determined through the geometry of the indenter. During the experiment, the indenter is subjected to an increasing load. The tip of the head is pressed into the sample until a specific value is reached. In this process, the load and the displacement of the indenter are recorded to draw the load-displacement curve, and the mechanical properties of the material can be analyzed through the load-displacement curve [120]. The nanoindenter XP (nanoindentation, Knoxville, TN) is used in the present work. Nanoindenter XP microprobe hardware consists of an indenter, a positioning microscope, and a controlling hardware. A variety of tip geometries are available, including Berkovitch, cube corner, and cone. Tab. III-7 gives the range and resolution of nanoindenter XP with different load modes. For the indentation head assembly, the displacement resolution is less than 0.01 nm, the total usable indenter travel is 1.5 mm, and the max indentation depth is larger than 500 μm. For the load application by coil/magnet assembly, the load resolution is 50 nN, and the load frame stiffness is $1*10^7$ N/m. The motorized x-y sample manipulation table is under computer mouse control. Positioning accuracy is 1.5 μm, due to a high-performance vibration isolation system:

Air isolation table and passive environmental enclosure. The optical imaging system with 4X and 40X lenses is fully automated with computerized data acquisition and control system.

Tab. III-7. The range and resolution of nanoindenter XP with different load modes.

	Range	**Resolution**
Displacement	1.5 mm	<0.01 nm
DCM Mode: Loads	10 mN	1 nN
XP Mode: Loads	500 mN	50 nN
High Load: Loads	10 N	50 nN

Nanoindentation can measure the mechanical properties of many materials, such as Young's modulus, which describes the stiffness of the material and defines the relationship between strain and stress in the elastic domain. Other measurements, including fatigue, elastoplasticity, and viscoelastic deformation, can also be achieved by nanoindentation [121]. Nanoindentation is also an important tool for measuring the mechanical properties of small-sized materials, and the indentation depth can range from tens of nanometers to more than one micron [122]. This technique has been widely used by researchers all over the world to study elastic modulus, hardness, size effect, sinking-in, and piling up.

3.4.2.1 Factors affecting nanoindentation on SMATed material

In conventional indentation testing, the projected area between the indenter and the sample at maximum load, the depth of contact, and the stiffness at unloading are usually used to calculate hardness and Young's modulus. Various errors may occur in the process of obtaining these parameters, resulting in deviations from reliable and accurate measurement results. Some of these factors are caused by environmental changes, such as thermal drift during testing (because nano-indent displacement sensors are sensitive to sub-nanometer displacements). Any thermal expansion of the indenter, the indenter shaft, and the specimens during the test may be caused by temperature changes and can be incorporated into the test results. The indentation shape of the nanoindentation is also related to whether the indentation dimensions are ideal, because the projected area is calculated based on the geometry of the indentation. Other factors are material-related issues that may affect the validity of the results, such as indentation size effects and piling up/sinking. The sensitivity of

nanoindentation tests to these factors is the subject of ongoing researches. The most common factors and methods are given as follows.

(1) Geometrical drifts

Two types of drift behavior may occur during nanoindentation testing, which will affect the recording of depth data [123]. The first is the creep within the sample material due to plastic flow when the force load is held constant. The problem can be solved by increasing the peak holding time (duration held at peak loading). The second type of drift is caused by dimensional changes caused by thermal expansion or contraction of the device, which is called thermal drift, and it can cause errors in actual depth data. To solve this problem, the rate of change of depth over time needs to be measured for a constant load value during the indentation test.

(2) Piling up and sinking in phenomena

Young's modulus can be calculated by nanoindentation using the Oliver-Pharr method of indentation, where the key parameters are the contact depth stiffness and the projected area between the indenter and the material [124]. During the nanoindentation test, piling up and sinking in phenomena may occur. Tabor in his classic work (The hardness of metals) describes both phenomena as a noticeable deformation of the metal around the indentation [125]. On one hand, the displaced metal will squeeze upwards, forming a raised crater, which is called piling up. On the other hand, metal tends to be depressed around the indentation, which is called sinking in. The piling up and sinking in phenomena will affect the measurement accordingly.

(3) Initial contact point

At the beginning of indentation test, the indenter needs to be in contact with the surface. Ideally, the penetration depth is measured based on the level of the sample surface, which is a function of the controlled load. However, in practice, the indenter must be in contact with the sample surface before the depth measurement is performed [123], [126], [127]. Therefore, it is necessary to make actual contact with the sample surface to record the depth. To this end, an initial contact point is given at the beginning of the test to bring the indenter into contact with the sample. This value is usually set as small as possible to minimize the corresponding error. However, no matter how small the initial indentation depth, there is always a corresponding error in the indentation depth data. The initial indentation depth can be corrected by the Hertz

equation, which gives the relationship between the load and the penetration of the elastic response [123].

(4) Indentation size effect

Indentation size effects are usually observed during the nanoindentation of certain materials, which is exhibited through the change of hardness and modulus with indentation depth. According to references [123], [126], [127], continuously measured hardness is a function of the depth of the indentation. For small depth, the measured hardness is higher, but for homogeneous, isotropic materials, it is desirable to measure a hardness/modulus value regardless of the indentation depth. There are many reasons for this phenomenon, such as thinner layers than bulk materials, residual stress, strain hardening during sample preparation and polishing, and friction between the indenter and the sample. But all of the above factors can be minimized. Although the effect can be minimized, the effect of indentation size is still observed as a result of dislocation nucleation in the plastic region, especially for soft materials.

(5) Residual stress

Residual stresses are usually produced by inhomogeneous heat treatment, or local plastic deformation involving bulk solids, films, or coatings used in various industrial components [19]. The residual stress fields in these components affect their properties (such as fatigue strength, wear, and fracture) and have a significant impact. In the process of nanoindentation measurement, residual stress can affect the measurement of hardness and Young's modulus, load-displacement curve, piling up, and true contact area. For compressive residual stress, a higher indentation load is required to reach a given indentation depth, and the nanoindentation unloading curve moves to the left with low residual stress, while for tensile residual stress, the opposite effect can be observed.

As already mentioned, SMAT can introduce severe plastic deformation along the cross-section of the sample, where a gradient microstructure is formed. During SMAT, grain size effect, residual stress effect, and phase transformation are induced as a function of the depth, and they can influence the properties.

Grain refinement can be achieved by SMAT, and mechanical properties are determined by the corresponding microstructure of the material [123]. As a result, materials with nanocrystalline structures often exhibit excellent physical and chemical properties. In the case of nanoindentation, grain refinement has a significant effect on

the mechanical properties of the material such as hardness and indentation size effects.

3.4.2.2 Analysis of the load-displacement curves.

In this section, we focus on the gradient microstructures generated by SMAT, especially the nanostructured layer at the top surface of the treated surface.

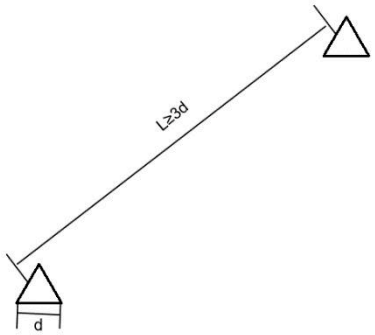

Fig. III-6. Distance between two neighboring indentations.

Nanoindenter XP with a Berkovich indenter has been used to measure hardness and Young's modulus on cross-section samples as a function of depth below the treated surface. The maximum displacement of the indentation is 800 nm, the strain rate is 0.05/s, and the distance between two neighbor indentations is 20 μm. The distance is chosen to avoid possible effects of the stress field caused by neighbor indentations. The distance between two neighbor indentations should be at least greater than 3 times the area size of the indentation [128]. Fig. III-6 shows the distance between the two neighboring indentations.

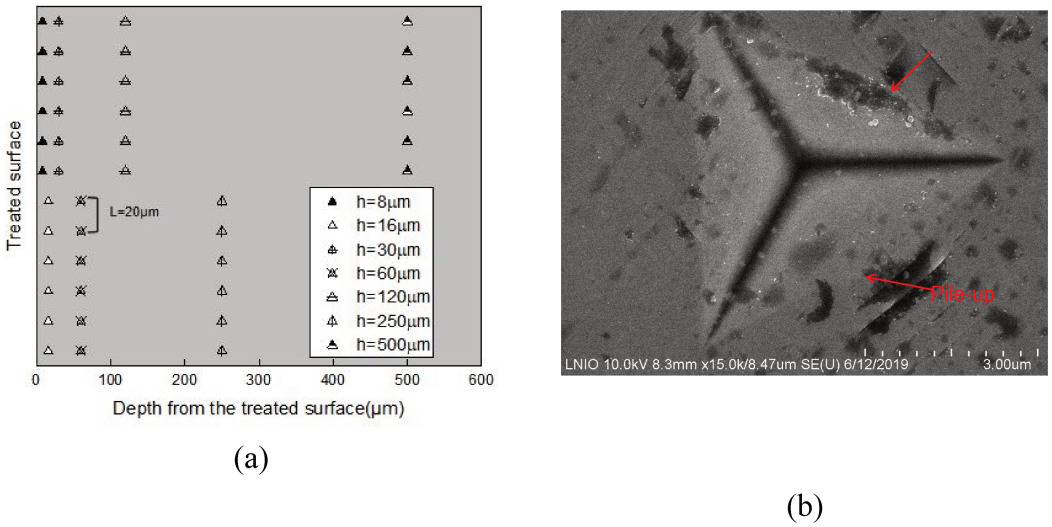

(a) (b)

Fig. III-7. Illustration of nanoindentation (a) carried out on the SMATed sample with strain rate 0.05/s, Indentation area (b) at 8 μm beneath the treated surface with strain rate 0.05/s, where red arrows indicate piling up, which occurred during nanoindentation.

As shown in Fig. III-7a, multiple indentations were selected below the treated surface as 8, 16, 30, 60, 120, 250, and 500 μm, respectively. Each nanoindentation test was run at a constant ratio $\dot{h}/h$, equal to 0.005, 0.05, and 0.5/s, where h is the maximum displacement into the sample, which is 800 nm. Five indentations were conducted for each depth with a distance L = 20 μm. To distinguish each indentation easily, we give each indentation a number, and the number consists of two parts. The first part is the depth of the indentation, and the second part is the position of the indentation from top to bottom for each depth. For example, position 8-1 in Fig. III-7a represents the top indentation operated at the depth of h = 8 μm from the treated surface, as shown in Fig. III-7a. Fig. III-7b shows the result of SEM observation of the area of residual indentation. For each depth, 6 indentations were performed. As shown in Fig. III-7b, the size of the indentation is around 5.5 μm.

The observed residual indentations show that piling up can be observable when the contact depths exceed 50 nm [129]. The piling up behavior of various materials has been a research hotspot, and it can be related to the material's strain hardening exponent, residual stress, and E/Y ratio (Young's modulus/yield stress). For 304L steel with high strain hardening exponent and high E/Y ratio, sinking in is expected. Fig. III-7b shows an example of the indentation area at 8 μm below the treated surface

with strain rate being 0.05/s and the presence of piling up. The reason for the piling up observed in the SMAT-affected area is the change of local microstructure and mechanical properties. These properties are mainly grain refinement, residual stress, and strain hardening.

During the nanoindentation tests, displacement is usually monitored by capacitance or inductance, while force actuation is provided by electrostatic force generation, expansion of electromagnetic coils, or piezoelectric elements [130]. Fig. III-8 shows typical load-displacement curves of 304L steel at different depths with loading rate $\dot{h}/h$ =0.05/s, which exhibits significant grain size, phase transformation dependence at different depths. The various color curves in Fig. III-8 correspond to different nanoindentation experimental data obtained with varying positions at the same depth where the grain size is the same. It can be seen from Fig. III-8 that for all load-displacement curves, when the indenter begins to contact the upper surface of the sample, the initial nonlinearity of several curves occurs, up to about 30 mN. Then, the force increases linearly with displacement, which corresponds to the elastic deformation range of steel (plastic deformation exists beneath the surface but is constrained by the surrounding elastic material). Finally, the plastic region extends and continues to grow in size so that the indentation contact area increases at a rate that gives too few or no increase in the mean contact pressure for further increase of the indentation load.

As shown in Fig. III-8, the load-displacement (L-D) curves of 304L steel exhibit apparent grain size and phase transformation characteristics, i.e., the load will be lower when the distance from the top surface is deeper (the grain size is larger) in nanocrystalline layer and transition layer. For example, when the depth h increases from 8 μm to 500 μm, the maximum peak force varies from approximately 80 to 70 mN, and the minimum peak force varies from about 70 to 50 mN. Meanwhile, at the same depth (same grain size), the L-D curves at different positions show significant differences, i.e., for depth h = 500 μm, the maximum peak force is approximately 70 mN, and the minimum peak force is about 50 mN. This is because the martensitic transformation decreases gradually along the depth, and the mechanical properties of martensite and austenite are different, as the martensite strength and stiffness are stronger than austenite ones. Hence, a higher peak force means a higher martensitic transformation content under the indenter. However, this difference becomes smaller when the depth decreases, because when the depth decreases, the grain size becomes

smaller compared to the size of the indenter so that the effect of uneven martensite distribution under the indenter on the force-displacement curve gets bigger.

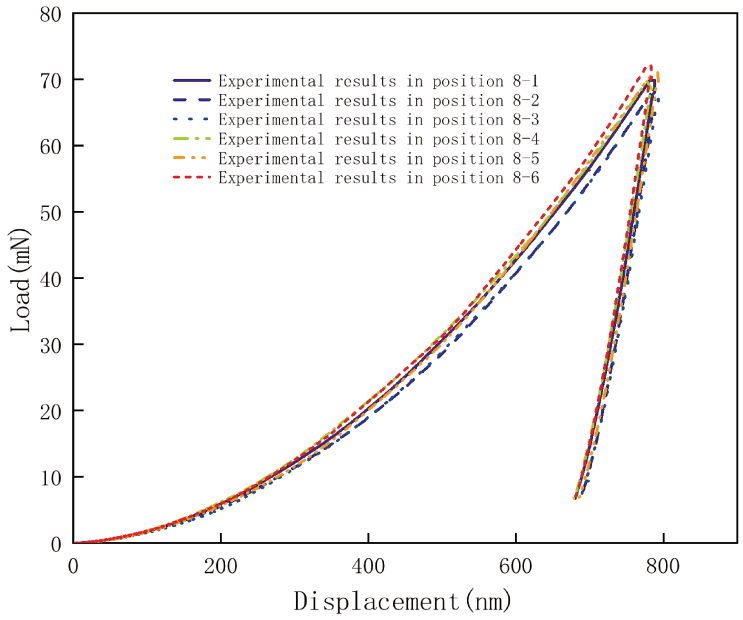

(a)

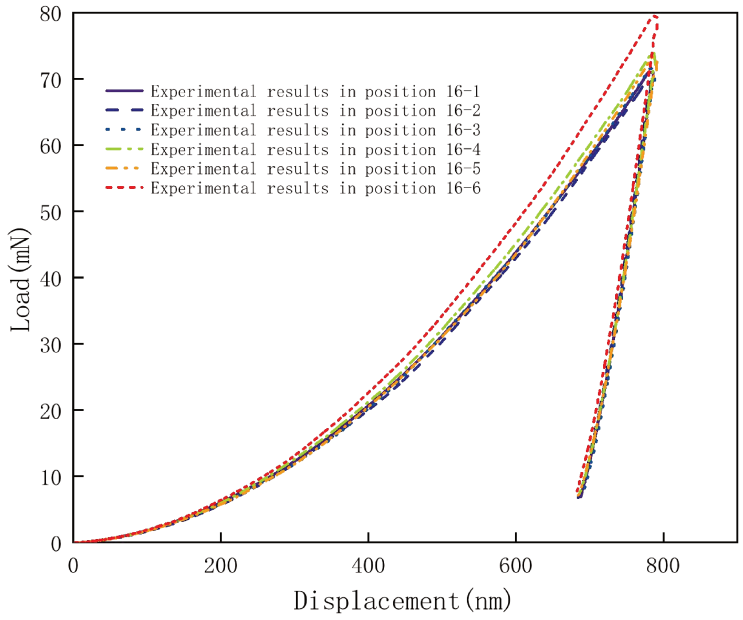

(b)

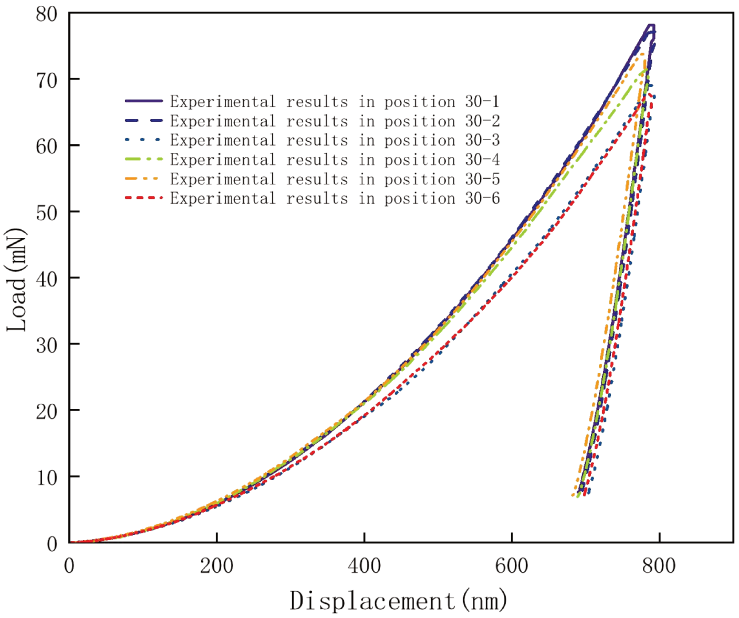
Experimental results in position 30-1
Experimental results in position 30-2
Experimental results in position 30-3
Experimental results in position 30-4
Experimental results in position 30-5
Experimental results in position 30-6
Load (mN)
Displacement (nm)
0
10
20
30
40
50
60
70
80
0
200
400
600
800

(c)

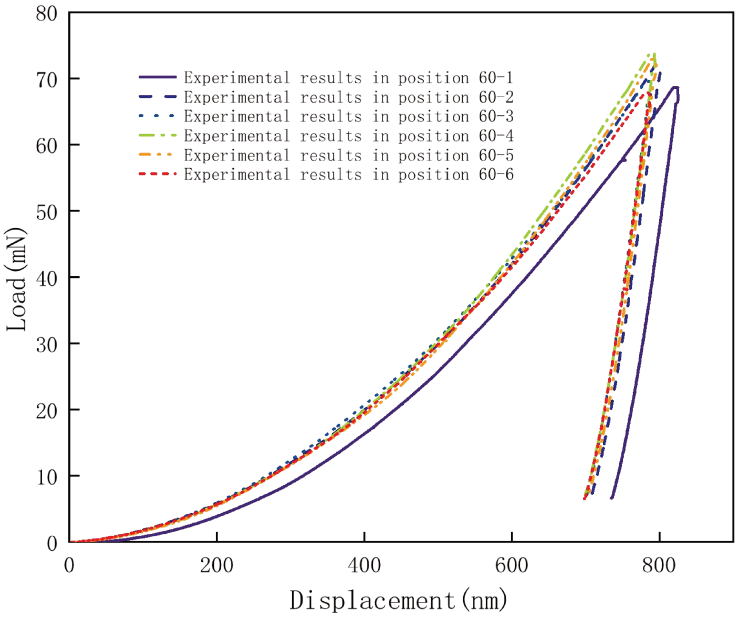
Experimental results in position 60-1
Experimental results in position 60-2
Experimental results in position 60-3
Experimental results in position 60-4
Experimental results in position 60-5
Experimental results in position 60-6
Load (mN)
Displacement (nm)
0
10
20
30
40
50
60
70
80
0
200
400
600
800

(d)

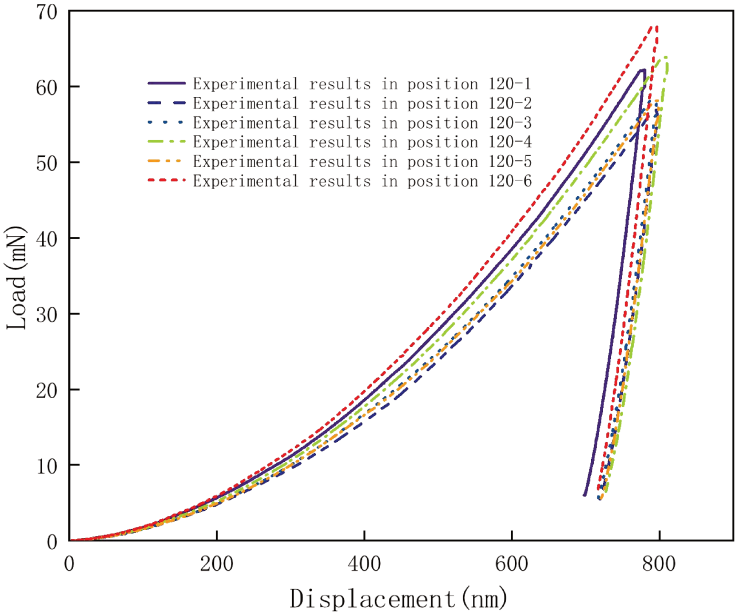
Experimental results in position 120-1
Experimental results in position 120-2
Experimental results in position 120-3
Experimental results in position 120-4
Experimental results in position 120-5
Experimental results in position 120-6
Load (mN)
Displacement (nm)
0
10
20
30
40
50
60
70
0
200
400
600
800

(e)

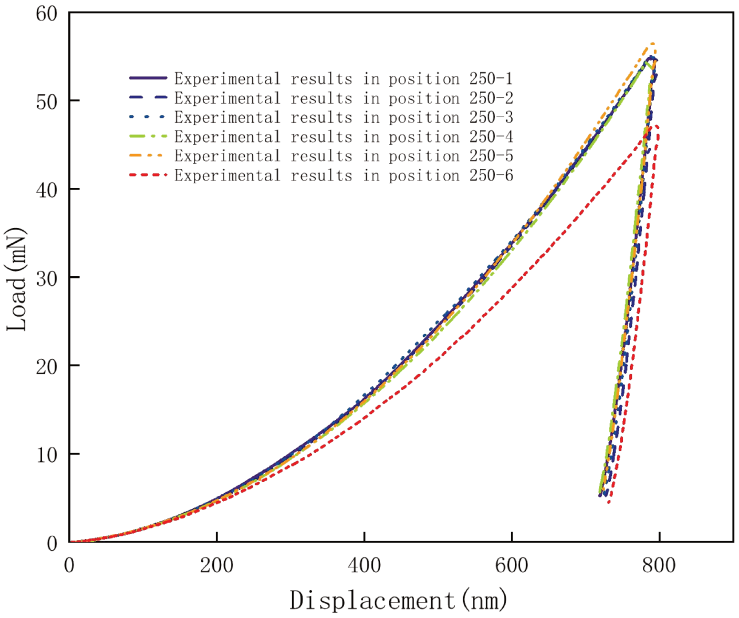
Experimental results in position 250-1
Experimental results in position 250-2
Experimental results in position 250-3
Experimental results in position 250-4
Experimental results in position 250-5
Experimental results in position 250-6
Load (mN)
Displacement (nm)
0
10
20
30
40
50
60
0
200
400
600
800

(f)

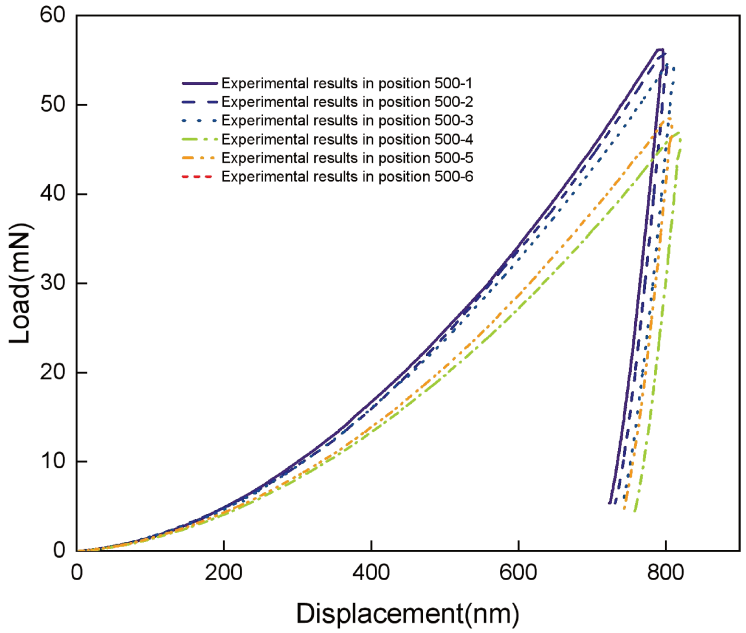

(g)

Fig. III-8. Typical load-displacement curves in different depth h=8 μm (a), 16 μm (b), 30 μm (c), 60 μm (d), 120 μm (e), 250 μm (f) and 500 μm (g) with strain rate $\dot{h}/h$ =0.05/s as shown in Fig. III-7a.

Fig. III-9 shows the peak force of the L-D curves of the nanoindentation at different depths with different strain rates. It can be seen that when nanoindentation operated at small depths where the grain size is also small compared to the size of the indenter, the difference of values obtained between the maximum peak force and minimum peak force is very small. Indeed in Fig. III-9b, the difference between the maximum peak force and the minimum peak force is about 4.17 MPa at a depth of 16 μm, which is about 5% of the peak force. For SMATed 304L steel, austenite and martensite are not evenly distributed in the sample and are staggered with each other. However, in the nanostructured layer, the grain size of austenite and martensite is very small in comparison to the size of the indenter, about tens of nanometers, which means that at this depth, the microstructure can be considered as homogeneous and consists of ultra-fine austenite and martensite.

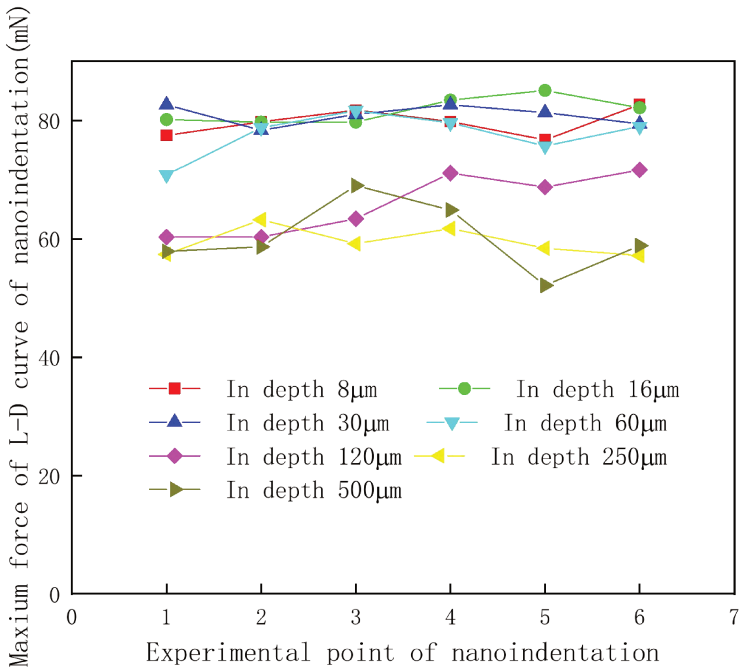
Maxium force of L-D curve of nanoindentation(mN)
Experimental point of nanoindentation
In depth 8μm
In depth 16μm
In depth 30μm
In depth 60μm
In depth 120μm
In depth 250μm
In depth 500μm

(a)

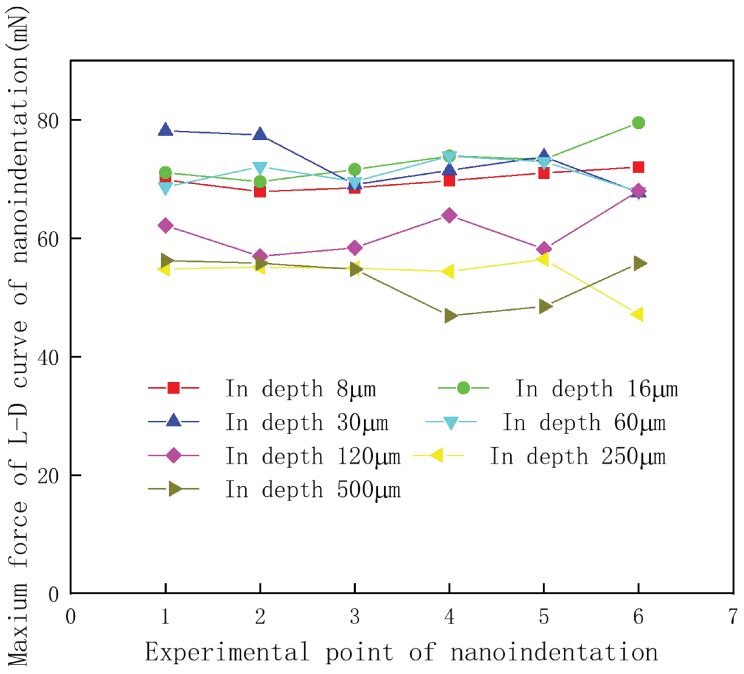
Maxium force of L-D curve of nanoindentation(mN)
Experimental point of nanoindentation
In depth 8μm
In depth 16μm
In depth 30μm
In depth 60μm
In depth 120μm
In depth 250μm
In depth 500μm

(b)

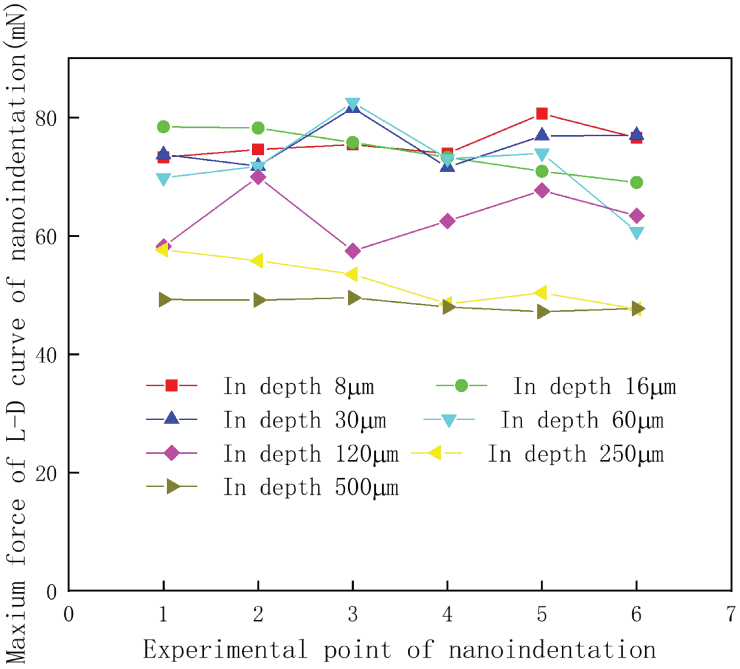

(c)

Fig. III-9. Peak force of the L-D curves of the nanoindentation at different depths with different strain rates $\dot{h}/h$ =0.005/s (a), $\dot{h}/h$ =0.05/s (b), $\dot{h}/h$ =0.5/s (c).

However, when the depth increases and the grain size is about 30-50 microns which is large enough compared to the size of the indenter, the size effect cannot be ignored. It is no longer useful to consider that martensite and austenite are evenly distributed; in Fig. III-9b, at a depth of 120 μm, the difference between maximum peak force and minimum peak force is about 10.06 MPa, which is about 16% of the peak force. The distribution of the maximum value is very scattered, and the dispersion is relatively large. The reason is that in this depth, the grain size is relatively large compared to the size of the indenter, so when the nanoindentation is operated on austenite, or martensite, or austenite-martensite separately, the nanoindentation curve shows apparent differences due to the different mechanical properties between austenite and martensite. When the indenter is mainly pressed on the austenite, because the hardness and the strength of the austenite are relatively low, the slope and peak force of the load-displacement curve is relatively low. When only austenite exists under the indenter, the slope and peak force of the LD curve are the lowest. On the contrary, when the indenter is mainly pressed on martensite, as the hardness and the strength of martensite are high, so the slope and peak force is

relatively high. When the only martensite exists under the indenter, the slope and peak force of the LD curve are the highest. When both austenite and martensite exist under the indenter, the slope and peak force of the LD curve will be between the two values. The peak force is thus related to the different ratios/amount of austenite and martensite under the indenter. When the percentage of martensite is relatively large, the slope and peak force will also be larger. Therefore, because of the martensitic transformation in 304L steel, nanoindentation analysis performed to study the mechanical properties after SMAT processing will be complicated while analyzing the mechanical properties of materials at different depths with different grain sizes because of the evolution of the martensite content.

To study the influence of the grain size and strain rate on the peak force of the nanoindentation, the distribution of the average peak force of the L-D curves of the nanoindentation at different depths with different strain rates is shown in Fig. III-10. It can be seen that the maximum load increased by about 20% from the core region to the nanocrystalline area with a strain rate of 0.5/s. The maximum indentation load is stabilized at a depth of about 300 μm from the top surface, which indicates that the depth of the SMAT affected region is at least 300 μm. Meanwhile, with the same strain rate, the peak force first increases with the depth; then, when the depth is about 20 μm, the peak force reaches its maximum value; then the peak force decreases with the depth increasing in the affected region. This is because when the indentation depth of the indenter is constant, the peak force is mainly affected by the hardness. According to the study of [131], the hardness is directly proportional to the compressive residual stress. The XRD analysis in Section 3.1 shows that for SMATed 304L steel, the residual stress of austenite is compressive residual stress. The residual stress in martensite is tensile residual stress. This residual stress increases with depth within a small depth range of the surface when the depth is smaller than 20 μm according to the reference [132], where the residual stress reaches a maximum value. Then the residual stress decreases with the depth increasing in the affected region.

Except for the compressive residual stress and martensitic transformation, grain refinement and strain hardening can also lead to a high indentation load. When SMAT intensity is high, the significant changes induced by SMAT are mainly compressive residual stress, grain refinement, and martensitic transformation compared to the core non-affected region. If SMAT intensity is low, there will be no grain refinement and martensitic transformation [53]. Therefore, a higher indentation load in the strongly

affected nanocrystalline region may lead to information on the grain refinement, compressive residual stress, and martensitic transformation. Many works have been done to study the effect of residual stress on the nanoindentation load [133]–[135]. The nanoindentation performed by Zhu [133] on single crystal copper with different residual stress levels from -137.4 MPa to 68.4 MPa shows that the influence of residual stress on indentation is negligible, which is only a few μN compared to the maximum load which usually is several mN. The finite element method was conducted by Mady [135] to investigate the influence of residual stress during the indentation loading on 8009 aluminum alloy. The residual stress simulated ranges from -300 MPa to 500 Mpa. The results indicated that the maximum indentation load increased by about 1 mN with an increase of compressive residual stress by 300 MPa. Mady [135] also found similar results by using the finite element method to simulate the ceramic films. The maximum load increased by 2 mN when the compressive residual stress increased by 5 GPa.

In our work, 304L steel is studied, which has a higher Young's modulus, and hardness compared to aluminum and copper. From Fig. III-10, it can be seen that the strain rate has a significant influence on the peak force of nanoindentation. When the strain rate is higher, the average peak force is also larger, i.e., when the strain rate increased from 0.005/s to 0.5/s, the average peak force increased by 10% of the average peak force.

For a sharp indenter, the L-D curve generally follows the relation $P = Ch^2$, where P is the load and h is the displacement into the sample. C is the loading curvature, which is a measure of the "resistance" of the material to indentation. The shape of the L-D curve, and especially the loading curvature, C, gives important information about the indented material. According to the references, the mechanical properties of the indented material and residual stress influence the loading curvature. Khan [136] studied the nanoindentation response of an aerospace-grade aluminum alloy to investigate the effect of residual stresses. He found out that tensile and compressive residual stresses lead to changes in the nanoindentation L-D curves and the curvature of the loading curve was found to have a linear relationship with residual stress in both compressive or tensile regions.

Another important mechanical property that influences the loading curvature is the strain hardening exponent, n, according to the study of Lee [137]. They aim to reduce

the data and experimental errors in the reverse analysis of nanoindentation to extract the elastic-plastic properties of materials from P-h curves. The work was accomplished by using various representative strains and choosing only C and the ratio of total work to plastic work as the independent parameters representing the P-h curve in establishing a series of dimensionless functions for Al6061-T6, AISI 1010, 1045 and copper. According to the work of Lee, a decrease of about 25% of loading curvature was found when the strain hardening exponent varied from 0.5 to 0.01. For 304L TWIP/TRIP steel, another factor that influences the loading curvature is martensitic transformation. Ye [138] performed nanoindentation to study the effects of Ultrasonic Nano-crystal Surface Modification (UNSM) on the microstructure changes and the mechanical properties of austenitic stainless steel 304. The experimental results show that loading curvature increased by about 25% when operated on the top surface compared to the core region as after shot peening. The material is assumed to be a multi-layer microstructure with two strong nanocrystalline surface layers and a ductile interior with gradually changing martensite volume fraction. The nanocrystalline surface layer with high martensite content provides strong resistance to plastic flow that increases the loading curvature.

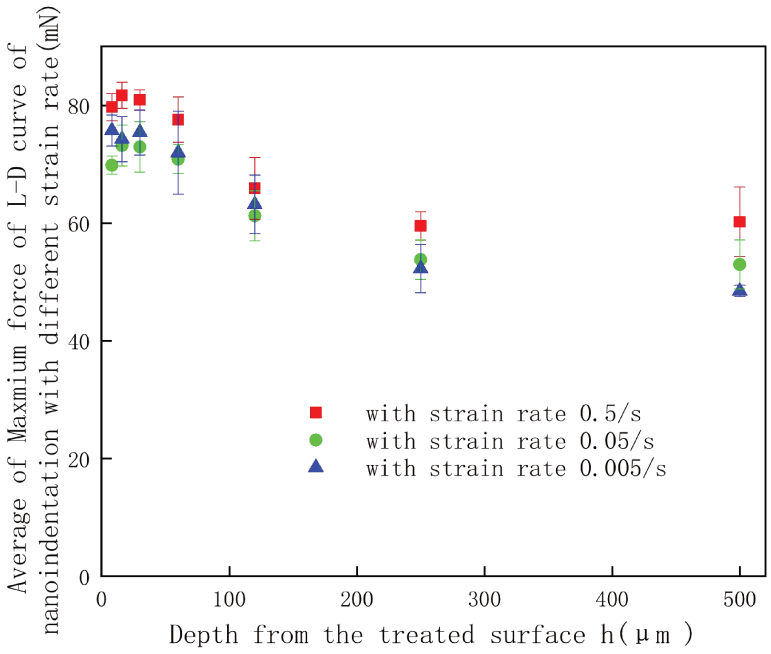

Fig. III-10. Average of the peak force of the L-D curves of the nanoindentation at different depth with different strain rates.

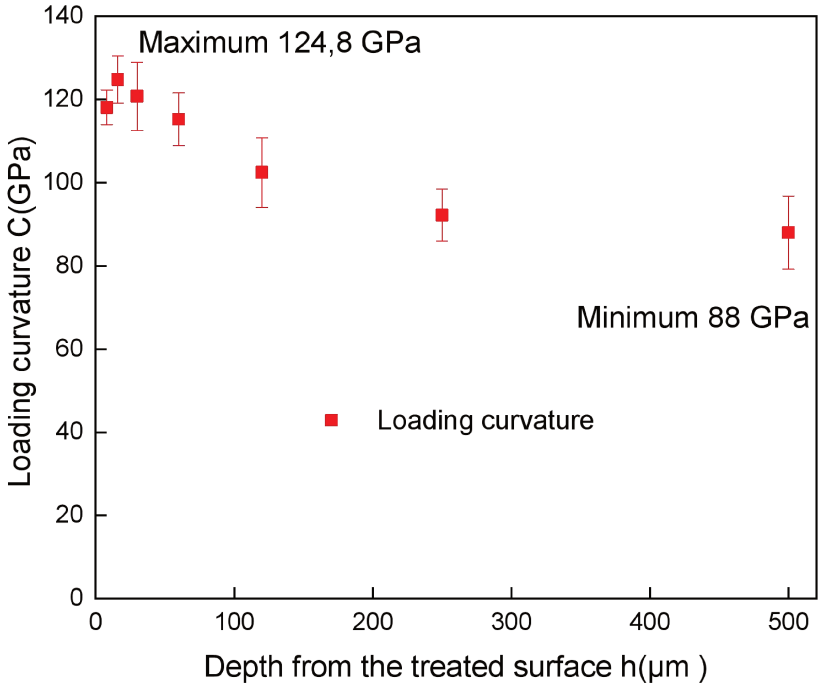

Fig. III-11. Variation of loading curvatures for indentation curves along the cross-section of the SMATed 304L steel with $\dot{h}/h$ =0.05/s.

The loading curvatures of the L-D curves of the 304L steel are plotted in Fig. III-11. It can be seen that the loading curvature is highest in the nanocrystalline region with a maximum value of about 124.8 GPa and stabilizes at a depth of about 250 μm below the treated surface. A variation of about 40% of the loading curvature value can be detected between the nanocrystalline region and the bulk interior of the non-affected region. This is due to the fact that in our case, not only the strain hardening exponent varies, but also the effect of grain refinement reduces the grain size, while the martensitic transformation occurs due to the TRIP effect. Smaller grain size can increase the yield stress according to the Hall-Petch law, and the martensitic transformation also results in higher yield stress as the yield stress of martensite is higher than austenite, which can explain the higher loading curvature in our study.

3.5 Conclusions

In this chapter, 304L steel was briefly introduced and chosen as the target material for SMAT treatment to obtain experimental results. The SMAT conditions for the 304L steel and the sample preparation procedure for XRD and Nanoindentation were listed as well.

XRD analysis results show that about 78% volume fraction of martensite was found due to strain-induced transformation. And, after SMAT, austenite will be in compression and martensite in tension as a result of the mutual constraints between them.

For the nanoindentation test, the factors affecting nanoindentation on SMATed material were briefly introduced. The obtained results (load-displacement, peak force, and average peak force) are interpreted subsequently in terms of SMAT that induced changes along the cross-section of the SMATed samples. The results show that the grain size, martensitic phase transformation, and strain rate have a significant influence on the mechanical properties derived from nanoindentation.

CHAPTER 4 DISLOCATION DENSITY, TWINING AND MARTENSITIC PHASE TRANSFORMATION DISTRIBUTION DURING SMAT WITHOUT DAMAGE

4.1 Introduction

As mentioned in Chapter 3, nanocrystalline (NC) materials exhibit superior strength to their coarse counterparts, so they have attracted the interest of many scientists in the past 20 years. SMAT is one of the recently developed methods for forming a nanocrystalline surface layer and refining the grains on the top surface at the nanometer scale by shooting the surface of the sample with spherical balls. This technology of surface treatment has been used by material scientists for many materials such as pure iron, pure titanium, pure copper, pure cobalt, aluminum alloys, and stainless steel for the production of NC materials.

The mechanical behavior of TWIP/TRIP steels related to the evolution of their microstructure during deformation has also been extensively studied [23]–[25]. Moreover, the deformation mechanisms of this steel, even complex, have been quite well documented [139]. From a metallurgical point of view, the SFE range of TWIP/TRIP steel is very narrow (according to [27], from 15 to 22 mJ/m^{-2}), but is essential to ensure the presence of twinning and martensitic transformations during deformation [28]. For these materials, plastic deformation can induce twinning and martensitic transformation during material deformation [29]–[31]. The presence of twins would effectively reduce the mean free path. Due to its higher strength compared to the original austenite before transformation, the resulting martensite makes the alloy harder and stronger [33]. Therefore, it is meaningful to study the simultaneous effects of twinning and martensitic transformation on material strength and plasticity from a modeling point of view.

In this chapter, a dislocation density-based model, which can describe the main deformation mechanisms of TWIP/TRIP steels is developed. The overall tensile stress-strain curve and the kinetics of twinning and martensitic transformation predicted by the model are validated with experimental data available in the literature. The model is implemented in a subroutine of ABAQUS Explicit. Furthermore, because it is not easy to numerically model SMAT process as SMAT is a process involving lots of random balls against the surface of the material, in this work, numerical simulations are performed to study a single shot impact process during SMAT, based on the obtained fields of residual stress, equivalent plastic strain, volume fractions of twin and martensite, etc. It is, therefore, necessary to first understand the development of deformation mechanisms during a single impact, in order to optimize SMAT conditions. The basic idea of this work is to develop a predictive approach based on dislocation density, which allows finally optimizing the treatment conditions through a series of numerical simulations, including multi-impact simulation. Anyway, all the parameters involved in the model should be obtained by experiments. However, this chapter is mainly focused on modeling and demonstrates the capability of the model through single impact simulations.

4.2 Dislocation density-based model

One goal of this work is to model the mechanical behavior of TWIP/TRIP steels during material processing such as SMAT, which could simultaneously create deformation-induced twinning and martensitic transformation. It is important to notice that the deformation process during SMAT inevitably causes an increase in temperature of the deformed material, as highlighted through particle impact simulations using a dislocation-based material model [140]. However, according to [39], the temperature at the surface of materials is about 50-100°C, which varies with the intensity of impacts and the treated materials. As the rising of the temperature is not very high for the steels compared to their melting temperature, the effect of the temperature is thus not considered in this work. It is important to note that strain rate may influence the mechanical behavior, for example, by changing the kinetics of martensitic transformation. During SMAT, maximum strain rate can reach $10^{5/}$s evaluated through both numerical simulations [141] and experiments [48]. It would be thus interesting to take into account the strain rate in the model to describe more

precisely the impacting process. However, according to the results presented in the literature, the effect of strain rate is significant only when the accumulated plastic strain is very high [50].

In this dislocation density constitutive model, assumptions are proposed to calculate the flow stress for TWIP/TRIP steels. These assumptions are as follows:

1. The material is assumed to be isotropic with elastic-plastic behavior which obeys a dislocation density hardening rule with finite deformation, and the viscosity is not considered;

2. As this work aims to study the effect of one single impact, and the reached plastic strain is not high (less than 0.1), the strain rate is not taken into account in the constitutive model of this chapter. In this work, only the plasticity part is further modified, and for the elasticity, the stress and strain obey Hooke's model;

3. As the maximum strain of the material during SMAT is much smaller than the fracture strain of the material, so we mainly consider the elastoplasticity properties of the material, and the damage is not considered in our model;

4. Flow stress only depends on the plastic strain, not on other relevant process parameters such as strain rate or temperature;

5. Regarding the contribution of twinning and martensitic transformation to the overall deformation, it is assumed that the contribution of slip, twinning and martensitic transformation to the overall deformation obeying a mixing rule;

6. Flow stress is assumed to be determined by the flow stress of both austenite and martensite, which can be calculated using a mixing rule, taking into account the weighted sum of the contributions in austenite and martensite. And the twining is assumed only to occur in austenite and only contributes to the flow stress of austenite.

Consequently, to take into account of the contribution of both twinning and martensitic transformation, the variation of the total plastic shear strain can be described using a mixing rule expressed as follows [142]:

$$d\gamma = (1 - f_m)[(1 - f_t)d\gamma_a + \gamma_t df_t] + f_m d\gamma_m \quad \text{(IV-1)}$$

The total effective plastic shear strain γ is combined with austenite, martensite and twins: γ_a is the shear strain caused by dislocation slip in austenite, γ_t is the twin shear strain, γ_m is the shear strain due to dislocation slip in martensite, and f_t, f_m are the volume fraction of twin and martensite respectively. Throughout this

chapter, the following subscripts a and m refer to austenite and martensite, respectively.

Since the strain energy of the Shockley local dislocation is related to the energy of perfect dislocations, the following linear relationship between the shear strain due to dislocation slip in martensite γ_m and dislocation slip in austenite γ_a is considered, as proposed by [27]:

$$d\gamma_m = kd\gamma_a \tag{IV-2}$$

where k is a material parameter.

According to Olson and Cohen [57], [143], the kinetics of mechanical twinning can be considered similar to the kinetics of martensitic transformation. Therefore, the volume fraction of twin and martensite can be expressed as a function of the effective plastic strain ε which is a scalar (calculated by $\varepsilon = \sqrt{\frac{2}{3}\varepsilon_{ij}^p \varepsilon_{ij}^p}$), for example:

$$f_t = f_{t.\max} * \left(1 - \exp\left(-\beta\varepsilon\right)\right) \tag{IV-3}$$

$$f_m = f_{m.max} * (1 - \exp\,(-\mathrm{m}(1 - \exp * (-\mathrm{u}\varepsilon))^n)) \tag{IV-4}$$

where β , m , μ and n are material parameters, $f_{t.\max}$ and $f_{m.\max}$ correspond to the maximum volume fraction of twin and martensite, respectively.

The effective plastic shear strain γ and the effective plastic strain ε are related by the Taylor factor M, which is a scalar, through the following relationship [29]:

$$\gamma = M\varepsilon \tag{IV-5}$$

From Eqs. IV-1 to IV-5, the derivative of the effective plastic shear strain due to dislocation slip in austenite γ_a and martensite γ_m with respect to the effective plastic strain ε, can be respectively deduced as follow:

$$\frac{d\gamma_a}{d\varepsilon} = \frac{M - \beta\gamma_t\left(1 - f_m\right)\left(f_{t.\max} - f_t\right)}{\left(1 - f_m\right)\left(1 - f_t\right) + kf_m} \tag{IV-6}$$

$$\frac{d\gamma_m}{d\varepsilon} = k\frac{M - \beta\gamma_t\left(1 - f_m\right)\left(f_{t.\max} - f_t\right)}{\left(1 - f_m\right)\left(1 - f_t\right) + kf_m} \tag{IV-7}$$

The flow stress σ , which is a scalar, represents the instantaneous value of the stress required to continue the plastic deformation of the material. It can be calculated using a mixing rule, taking into account the weighted sum of the contributions in austenite and martensite [144], [145]:

$$\sigma = \left(1 - f_m\right)\sigma_a + f_m\sigma_m \tag{IV-8}$$

The relation between the flow stress σ and the dislocation density ρ for both the austenite and the martensite is assumed to obey the classical form [146]:

$$\sigma_i = \sigma_{0i} + \alpha_i M G b_i \sqrt{\rho_i} \qquad i = a,m \tag{IV-9}$$

where σ_0 is the initial flow stress of the material, α is a material parameter, M is the Taylor factor previously introduced. G and b are the shear modulus and the Burgers vector, respectively.

It is important to note that the strain rate can affect the mechanical properties and can change the kinetics of twinning and martensitic transformation.

Therefore, the evolution of dislocation density is described by the following differential equations, based on the Mecking-Kocks theory [147]:

$$\frac{d\rho_i}{d\gamma_i} = \frac{1}{\Lambda_i b_i} - K_{\alpha.i}\rho_i \quad i = a,m \tag{IV-10}$$

where K_α is the parameter related to the athermal dislocation dynamic recovery, and Λ is the dislocation mean free path, which can be calculated using:

$$\frac{1}{\Lambda_i} = \frac{1}{d_i} + K_{p.i}\sqrt{\rho_i} \quad i = a,m \tag{IV-11}$$

where d is the grain size, K_p is the parameter related to the athermal dislocation storage. Note that K_p describes the pile-up of dislocations on the forest dislocation obstacles.

In austenite, the mechanical twin boundaries act as strong obstacles for the movement of dislocations. Therefore, the dislocation means free path in austenite Λ_a can be modified to take into account the influence of twinning:

$$\frac{1}{\Lambda_a} = \frac{1}{d_a} + \frac{1}{\lambda_t} + K_{pa}\sqrt{\rho_a} \tag{IV-12}$$

where λ_t is the average twin spacing. The volume fraction of twin f_t and the average twin thickness c_t both contribute to the average twin spacing λ_t with the following equation [148]:

$$\lambda_t = 2c_t \frac{1 - f_t}{f_t} \tag{IV-13}$$

From Eqs. IV-9 to IV-13, the relationship between the dislocation density ρ and the shear strain due to dislocation slip γ can be expressed as:

$$\frac{d\rho_a}{d\gamma_a}=\frac{1}{b_a}\left(\frac{1}{d_a}+\frac{f_t}{2c_t(1-f_t)}+K_{p.a}\sqrt{\rho_a}\right)-K_{\alpha.a}\rho_a \quad \text{(IV-14)}$$

$$\frac{d\rho_m}{d\gamma_m}=\frac{1}{b_m}\left(\frac{1}{d_m}+K_{p.m}\sqrt{\rho_m}\right)-K_{\alpha.m}\rho_m \quad \text{(IV-15)}$$

Finally, from Eqs. IV-7 to IV-8 and IV-14 to IV-15, the dislocation density evolution with respect to the effective plastic strain ε can be expressed as follows for the austenite and the martensite, respectively:

$$\frac{d\rho_a}{d\varepsilon}=\left(\frac{M-\beta\gamma_t(1-f_m)(f_{t.\max}-f_t)}{(1-f_m)(1-f_t)+kf_m}\right)\left[\frac{1}{b_a}\left(\frac{1}{d_a}+\frac{f_t}{2c_t(1-f_t)}+K_{p.a}\sqrt{\rho_a}\right)-K_{\alpha.a}\rho_a\right] \quad \text{(IV-16)}$$

$$\frac{d\rho_m}{d\varepsilon}=\left(K.\frac{M-\beta\gamma_t(1-f_m)(f_{t.\max}-f_t)}{(1-f_m)(1-f_t)+kf_m}\right)\left[\frac{1}{b_m}\left(\frac{1}{d_m}+K_{p.m}\sqrt{\rho_m}\right)-K_{\alpha.m}\rho_m\right] \quad \text{(IV-17)}$$

4.3 Model parameters

The primary purpose of this chapter is to introduce the developed model by considering twinning and martensitic transformation in TWIP/TRIP steel. Therefore, in this chapter, parameter values are taken directly from the literature or fitted according to the experimental results obtained in some articles [149], [150]. Tab. IV-1 summarizes the values of all the parameters mentioned in Section 4.2. The physical meaning of each parameter is also given to facilitate the comprehension of the model.

In summary, $f_{t.\max}$ and β are fitted from the curve of twin volume fraction. $f_{m.\max}$, m, μ and n are fitted from the curve of the volume fraction of martensite. Moreover, other parameters such as k, σ_{a0}, σ_{m0}, ρ_{a0}, ρ_{m0}, $K_{\alpha.a}$, $K_{\alpha.m}$, $K_{p.a}$, and $K_{p.m}$ are fitted iteratively until a good agreement with experimental stress-strain curves is reached. In the case where the values are taken from the literature, their sources are indicated in the last column of Tab. IV-1.

4.4 Model validation

As shown in Section 4.2, the model developed in this work is based on the evolution of dislocation density, which enables the description of twinning and phase transformation during material deformation. To verify the implementation of the model, the uniaxial tensile results of a TWIP/TRIP steel studied experimentally by

Latypov et al. [149] were used to examine the evolution of the different variables involved in the model. The stress-plastic strain curve is first plotted, as shown in Fig. IV-1. It can be seen that there is a reasonable agreement between the stress-strain curve predicted by the model (solid line) and the experimental curve (solid square point) given in [149]. The good agreement between the two curves also means that the model should be able to describe the strain hardening behavior of TWIP/TRIP steel. In addition to the overall stress-strain curve, the stress evolution curve is plotted as a function of strain both in austenite and martensite. It can be seen that the flow stresses of the austenite and the martensite increase continuously with deformation (Fig. IV-1). Fig. IV-1 also shows that the flow stress level in the martensite is higher than the flow stress level in the austenite, which is consistent with the higher mechanical strength of martensite.

Tab. IV-1. Physical parameters identified for TWIP/TRIP steel.

Parameters	Physical meaning	Numerical values and units
γ_t	Twinning shear strain	0.707 [149]
k	Parameter for the strain of martensite	0.3
σ_{a0}, σ_{m0}	Initial flow strain of austenite and martensite	650 MPa, 1000 MPa
α_α, α_m	Taylor parameter of austenite and martensite	0.25, 0.25
M	Taylor factor	3.06 [149]
G_a, G_m	Shear modulus of austenite and martensite	75GPa, 80 GPa [149]
b_a, b_m	Burgers vector of austenite and martensite	0.25, 0.25 nm [149]
d_a, d_m	Grain size of austenite and martensite	58 μm [149]
ρ_{a0}, ρ_{m0}	Initial dislocation density of austenite and martensite	1×10^{10} m^{-2}, 1×10^{14} m^{-2}
$K_{\alpha.a}$, $K_{\alpha.m}$	Dynamic recovery parameter of austenite and martensite	0.01, 0.1
$K_{p.a}$, $K_{p.m}$	Forest hardening parameter of austenite and martensite	45, 6
c_t	Average twin thickness	30 nm [150]
$f_{t.max}$, $f_{m.max}$	Saturation volume fraction of twin and martensite	0.2, 0.8
β	Parameters for the volume fraction of austenite	2.6
m, μ, n	Parameters for the volume fraction of martensite	2, 1.6, 2.6

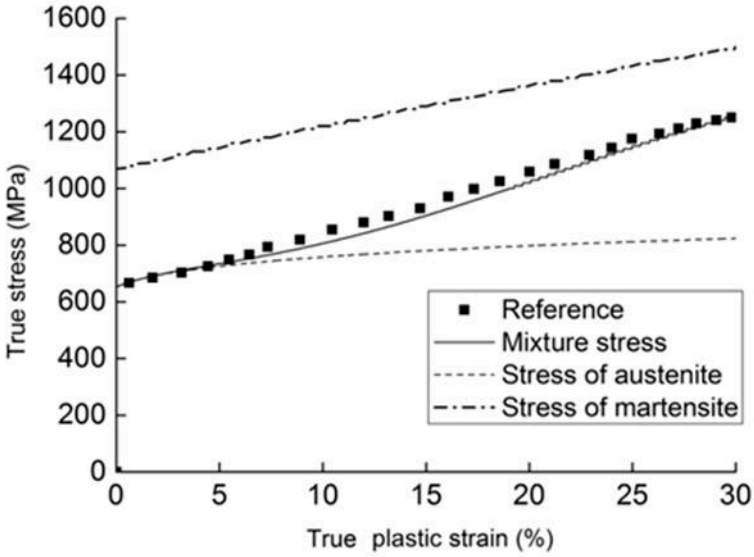

Fig. IV-1. Overall stress-plastic strain curves for austenite and martensite, compared to the experimental data provided in the reference [149].

More detailed examinations of other involved physical variables, for example, twinning, phase transformation, and dislocation activities can be performed. Fig. IV-2 shows the predicted evolution of the twin and martensite volume fractions. It can be observed that the evolution of the martensite volume fraction is consistent with the experimentally curves presented in [149]. At the beginning of the deformation process, the increase in the volume fraction of the martensite is quite slight, since the curve is almost horizontal and the slope is very small. Then, as the applied deformation increases, the volume fraction of the martensite increases sharply, and this increase remains important until the high strain level (Fig. IV-2a). For the evolution of twinning, the increase of the volume fraction of twin at the beginning of the deformation loading is fast, and when the total strain is higher than 0.15, this increase is reduced (Fig. IV-2b). Figs. IV-3a and IV-3b show the evolution of dislocation density inside the austenite and martensite, respectively, calculated using Eqs. IV-16 and IV-17.

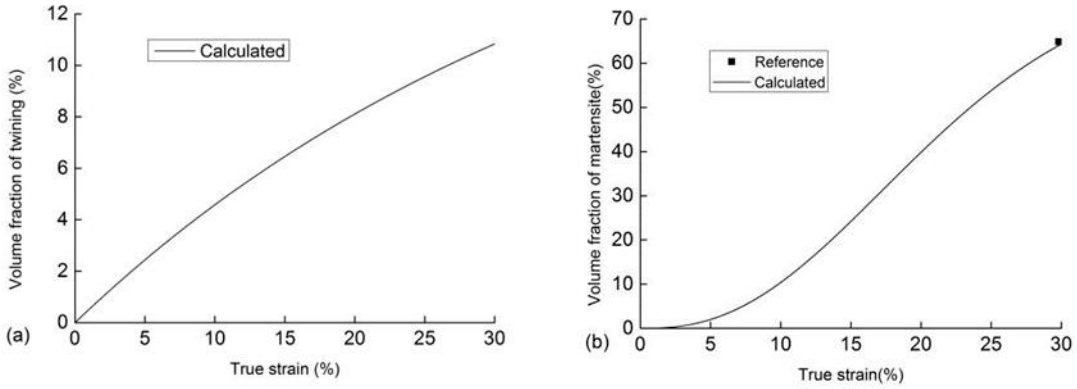

Fig. IV-2. Evolution of volume fraction of twin (a), and volume fraction of martensite (b), versus true strain.

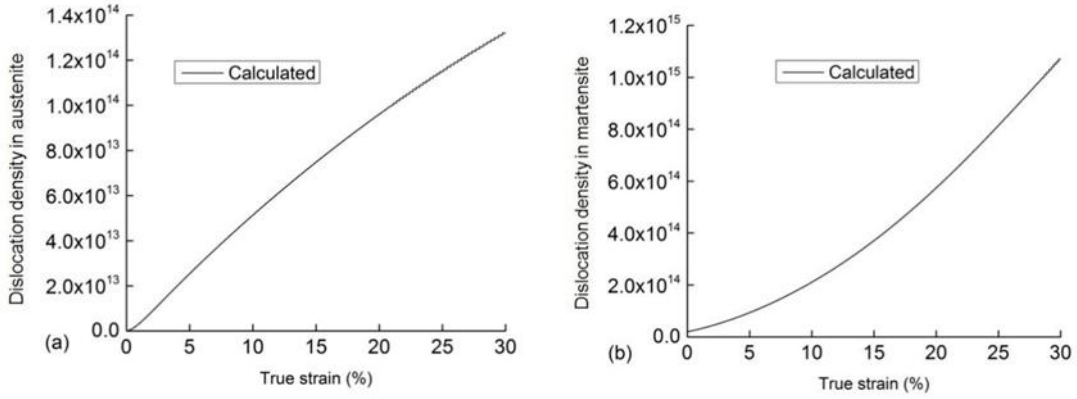

Fig. IV-3. Dislocation density evolution in the austenite (a) and martensite (b).

4.5 Finite element model

As mentioned above, SMAT is based on repeated impact loadings between the material and spherical balls. Therefore, the final metallurgical parameters, obtained by SMAT, such as grain refinement and work hardening, strongly depend on the basic response of the material under a single impact loading. It is interesting to study such a basic case by use of the previous modeling. To numerically simulate such a single impact process during SMAT, the model given above is implemented in the subroutine VUMAT of the code ABAQUS. A three-dimensional finite element (FE)

part has been built with a cylindrical shape (Fig. IV-4). The part has a diameter of 8 mm and is large enough compared to the ball size (2 mm). The height of the cylinder is 1 mm, which is much higher than the mechanical depth achieved by a single impact load (around 200 µm). These chosen dimensions allow avoiding the effects of boundary conditions on numerical simulation results.

The cylindrical model is meshed with the eight-node incompatible mode brick element (C3D8I). The C3D8I element is an improved version of the C3D8-element. In particular, shear locking is removed, and volumetric locking is much reduced. This is obtained by supplementing the standard shape functions with specific functions, which have a zero value at all nodes and non-zero values only in between.

The ball and the target material are assumed to be isotropic and homogeneous, and the general contact is defined between them, which can define contact between many or all regions of a model with a single interaction. To reduce computation time and ensure satisfactory accuracy, the mesh in the area affected by the ball is much finer than the mesh in other places. For the target material, in addition to the parameters presented in Tab. IV-1, other material constants such as Young's modulus, mass density, and Poisson's ratio are respectively taken as 210 GPa, 7800 kg/m^3, and 0.3. The ball is considered as a rigid body, and a reference point is defined in its center. An initial velocity (ranging from 3 m/s to 5 m/s, in this work) is imposed on the ball to create an impact loading when the ball is put in contact with the material. For the boundary conditions, only the bottom of the model is fixed to avoid rigid body displacements and rotations.

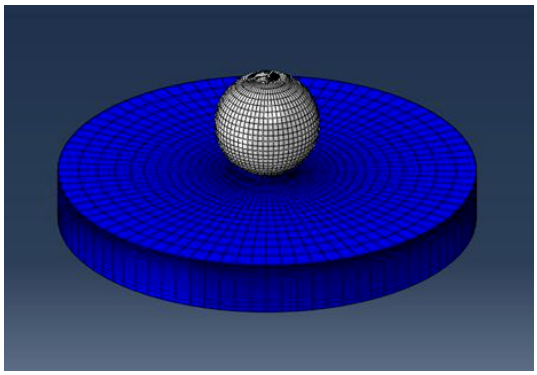

Fig. IV-4. Overall view of the FE model, including the ball (sphere) and the target material (cylinder).

4.6 Results and discussion

In this section, the results are presented in the form of fields and 2D curves, in order to better understand the evolution of key parameters during an impact loading, such as twinning and martensitic transformation, as well as the consequences of the impact including the residual stress and the residual plastic strain.

4.6.1 Evolution of the equivalent plastic strain

Fig. IV-5 shows the evolution of the equivalent plastic strain observed on a central cross-section of the model. For this purpose, three ball positions corresponding to different loading levels are chosen to illustrate the results. It can be seen that the maximum depth reached by the effect of ball impact, represented by the equivalent plastic strain, is about 200 µm (Fig. IV-5c), which is consistent with the experimental observations presented in Chapter 3 and obtained in the literature [32], [151]. In addition, the maximum value of the equivalent plastic strain is not located in the center of the contact region, but in a region near the center. Comparing the three figures, it can be observed that the position of the maximum equivalent plastic strain moves slightly in the direction far from the impact surface. This phenomenon can be interpreted using the Hertz contact theory. According to this theory, the depth of the maximum shear stress is proportional to the size of the contact region [152].

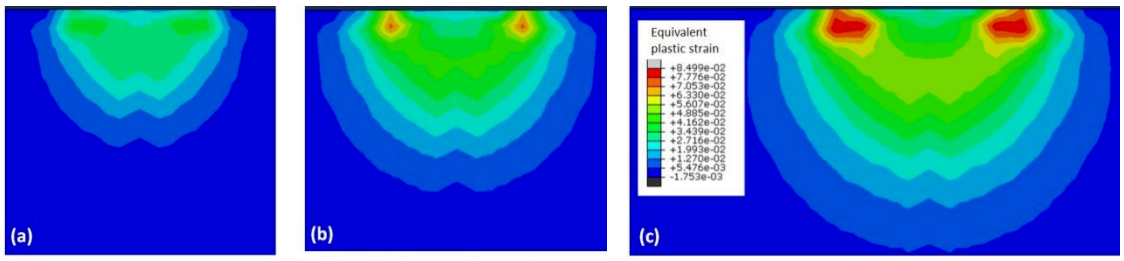

Fig. IV-5. Examples of equivalent plastic strain fields on a central cross-section of the FE model. Three loading levels are chosen to illustrate the evolution of the equivalent plastic strain during an impact loading.

4.6.2 Residual equivalent plastic strain and equivalent residual von Mises stress

Fig. IV-6 shows the distribution of the equivalent plastic strain, the equivalent residual von Mises stress, the dislocation density in the austenite and martensite, and the volume fraction of twin and martensite on the treated target surface. The impact velocity has been chosen as 5 m/s for all the same single impact simulations. It can be seen that all of these parameters have a very similar overall distribution on the top surface. Since the evolution of dislocations and twins are consistent with plastic deformation, the maximum values of the dislocation density of the austenite and martensite and the volume fraction of twin and martensite are almost at the same position where the equivalent plastic strain is the largest. Fig. IV-6a shows that the maximum equivalent residual von Mises stress after a single impact is about 700 MPa, which is largely dependent on the equivalent plastic strain stored in the material after one impact (see Fig. IV-6b). It is worth noting that the equivalent plastic strain is related to the evolution of the microstructure, as shown in Figs. IV-1, and IV-2.

4.6.3 Dislocation density in the austenite and martensite

Also, as shown in Fig. IV-6c and IV-6d, the dislocation density in the austenite increases by about three orders of magnitude after a single impact (e.g., from 1 x 10^{10} m^{-2} to 4.4 x 10^{13} m^{-2}), while in the martensite, the dislocation density remain roughly constant in the range from 1 x 10^{14} m^{-2} to 3 x 10^{14} m^{-2}. Therefore, the increase in dislocation density in the martensite is much lower than the dislocation density in the austenite.

4.6.4 Volume fraction of twin and martensite

The volume fraction of twin and martensite also changed due to a single shot effect. Figs. IV-6e and IV-6f show that the volume fraction of twin and martensite increases by 4.0% and 7.2%, respectively, with respect to the initial state before impact.

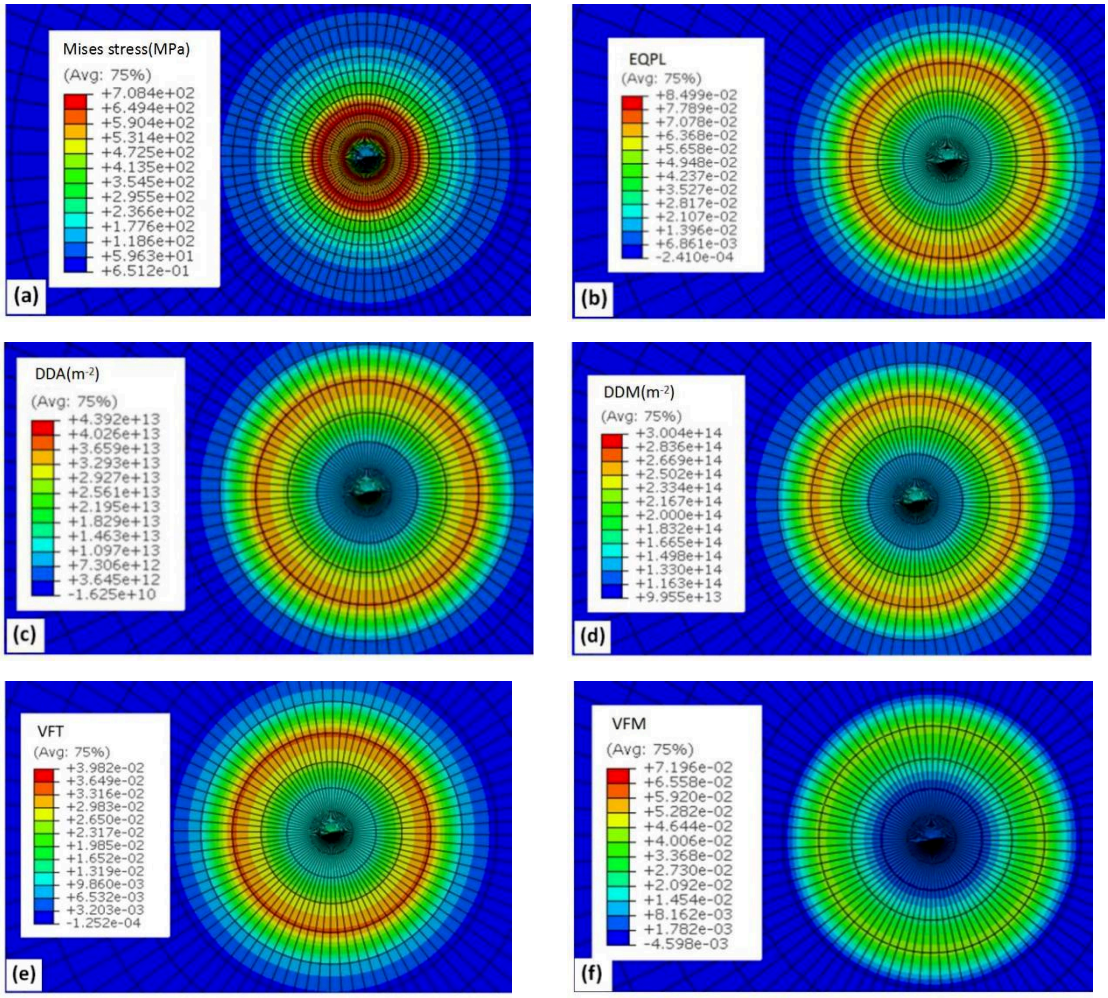

Fig. IV-6. Residual von Mises stress (a), equivalent plastic strain (EQPL) (b), dislocation density (DDA) in austenite (c), dislocation density in martensite (DDM) (d), distribution of volume fraction of twin (VFT) (e) and volume fraction of martensite (VFM) (f) observed at a target velocity of 5m/s after a single impact.

4.6.5 Influence of ball velocity on twinning and martensitic transformation

Figs. IV-7a and 7b show changes in the volume fraction of twin and martensite, respectively, plotted on the path passing through the center of the impact region on the contact surface, for different ball velocities. At an overall scale, the higher is the impact velocity applied, the higher is the volume fraction of twin and martensite. It can be seen that when the velocity is 3 m/s, the volume fraction of twin and martensite is 2.0% and 1.2%, respectively, and when the velocity is increased to 5 m/s, the volume fraction is increased to 3.0% and 4.0%, respectively. These results imply

that the impact velocity has a significant effect on the generation of deformation-induced twins and the transformation from austenite to martensite.

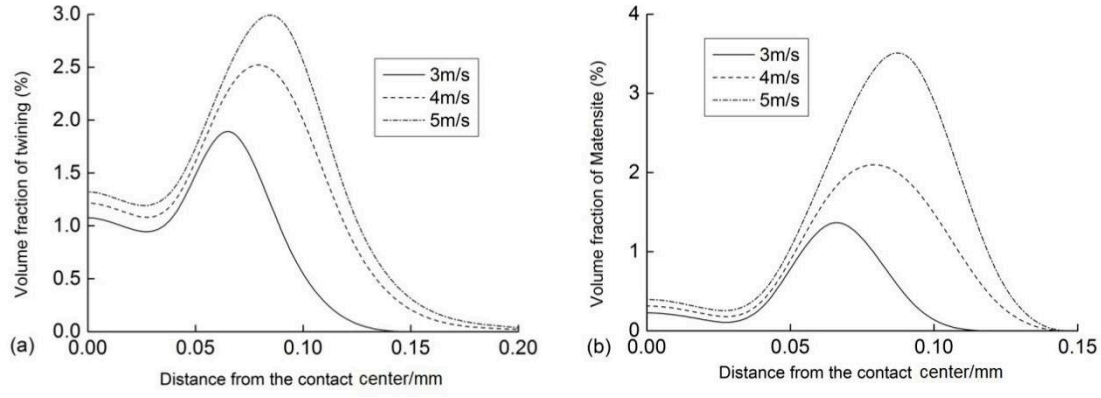

(a) (b)

Fig. IV-7. The change in the volume fraction of twin (a), and the volume fraction of martensite (b) obtained with different impact velocities, plotted along the path through the center of the impact region on the target surface.

4.6.6 Influence of the ball velocity on the displacement

The impact of the ball velocity is also studied in this work on the displacement of the surface. For this purpose, the impact velocity varies from 3 m/s to 5 m/s. Fig. IV-8 shows the variation in residual vertical displacement as a function of distance from the center of the contact area for different ball speeds of 3 m/s, 4 m/s, and 5 m/s, respectively. For these three impact simulations, balls of the same diameter (2 mm) and the same incidence angle ($\theta = 90°$) have been used. As it can be seen from Fig. IV-8, the maximum vertical displacement increases as the ball speed increases. When the impact speed is increased from 3 m/s to 5 m/s, the displacement is increased from 4.2 mm to 7 mm. The residual vertical displacement is the result of permanent plastic deformation due to impact loadings. During the impacts, a certain amount of kinetic energy of the ball is converted into potential energy stored in the material in the form of plastic deformation, twinning, and phase transformation.

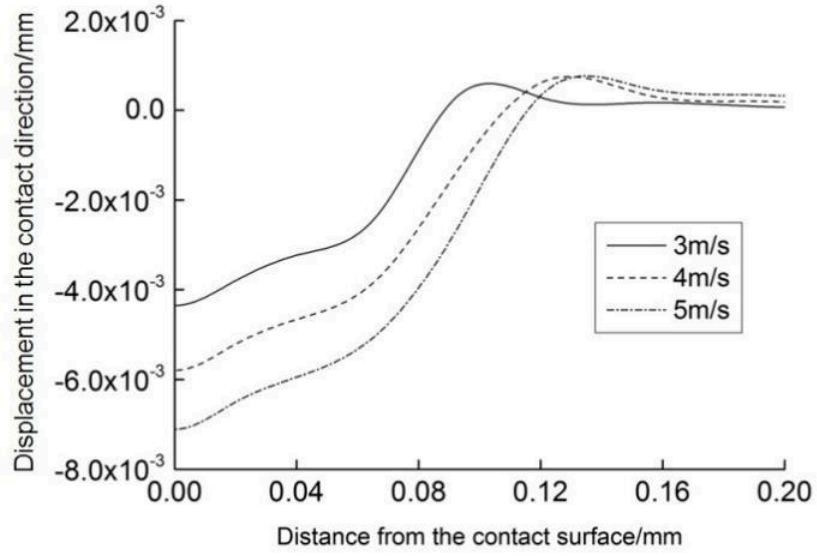

Fig. IV-8. The displacement of the points on the contact surface obtained at different impact velocities varies with distance from the center.

4.7 Conclusions

This chapter presents a dislocation density-based model to study the strain hardening behavior of TWIP/TRIP steel. In this model, the dislocation density and the volume fraction of twin and martensite are related to the equivalent plastic strain. Numerical simulation of a single impact has been performed using the dislocation density-based model to study the SMAT process. The residual equivalent stress, the equivalent plastic strain, the dislocation density in the austenite and martensite, and the volume fraction of twin and martensite after a single impact are analyzed.

The comparison between the modeling results and the experimental data shows that the proposed model can predict the evolution of the volume fraction of twin and martensite, as well as the macroscopic mechanical behavior. The results of the evolution of the equivalent plastic strain observed in the central cross-section of the model indicate that the maximum depth reached by the ball impact effect represented by the equivalent plastic strain is about 200 μm. The maximum value of the equivalent plastic strain is not located at the center of the contact area but is located in the vicinity of the center. It can also be observed that the position of the maximum

equivalent plastic strain moves slightly in the direction away from the impact surface, which can be well explained using the Hertz contact theory.

The distribution of the equivalent plastic strain, the equivalent residual von Mises stress, the dislocation density in the austenite and martensite, and the volume fraction of twin and martensite on the treated target surface have also been studied. The results reveal that all of these parameters have a very similar distribution on the top surface, as dislocation generation and twinning are both related to the plastic deformation. The maximum values of the dislocation density of austenite and martensite and the volume fraction of twin and martensite are almost at the same position where the equivalent plastic strain is the largest.

The study of the changes in the volume fraction of twin and martensite shows that the higher is the impact velocity applied, the higher is the volume fraction of twin and martensite. It implies that the impact velocity has a significant effect on the generation of deformation-induced twins and the phase transformation from austenite to martensite. The study of the effect of the ball velocity shows that the maximum vertical displacement increases, as the ball speed increases and the residual vertical displacement are the result of permanent plastic deformation due to impact loading, during which a certain amount of kinetic energy of the ball is converted into potential energy stored in the material. These results demonstrate the ability of the model to analyze the SMAT process of TWIP/TRIP steel.

CHAPTER 5 DEVELOPMENT OF DISLOCATION DENSITY BASED CONSTITUTIVE MODEL INCLUDING DAMAGE

5.1 Introduction

SMAT is a cold working treatment, in which media impact the surface under the kinetic/impact conditions. The surface modifications produced by the treatment are: (a) roughening of the surface; (b) an increase, at the near-surface, of dislocation density (i.e., strain hardening); and (c) the development of a characteristic profile of residual stresses. In terms of fatigue damage, surface roughening generally accelerates the nucleation and early propagation of cracks, and strain hardening delays the crack propagation by increasing the resistance of plastic deformation [153]. A compressive residual stress distribution provides a corresponding crack closure stress, thereby reducing the force that drives the crack propagation. Due to the applied stress level, neither the crack tip nor the operating temperature will cause relaxation of the residual stress profile, and surface fatigue cracks rather than subsurface fatigue cracks are the cause of fatigue damage. Therefore, it can be assumed that the performance of SMAT will depend on the balance between its beneficial and harmful effects [5], [8]. Therefore, to obtain helpful fatigue performance, it is necessary to analyze and understand the damage effects. To achieve such a goal, it is essential to understand its interaction with other parameters, such as the properties of the target material and the loading conditions. The ductile damage process in metallic materials usually consists in three stages, i.e., micro-voids nucleation, growth, and coalescence. To model the plastic flow and the fracture of ductile metals, Gurson et al. [82] proposed an approximate mesoscopic yield function for porous materials considering the effects of

hydrostatic stress. The metal matrix was firstly assumed isotropic, elastic-perfectly plastic, and incompressible obeying the von Mises yield function. Tvergaard and Needleman [66] modified the original model by introducing three additional fitting parameters, which leads to the Gurson–Tvergaard–Needleman (GTN) model. Nowadays, the GTN model is one of the well-known meso-mechanical models used to describe and predict ductile fracture. It has been widely used to model damage evolution for different materials and processes and is presently considered. So in this chapter, the GTN yield criterion is combined with the dislocation density-based constitutive model to propose a TWIP steel damage model to predict the damage evolution in ductile steel. Due to the high strain rate and large cumulative plastic strain in the SMAT process, ball impact can cause damage of the surface [154]. Then a user-defined subroutine has been developed to implement the model. A three-dimensional numerical simulation of a single impact has also been performed to study the impact process and the evolution of damage caused by high strain rate impact loadings.

In this chapter, to predict the deformation and the subsequent damage in SMAT process simultaneously, a dislocation density-based viscoplastic model, which can describe the main deformation process of TWIP/TRIP steels based on the dislocation-based model proposed in chapter 4, is developed and coupled with the GTN damage model. It describes the material response during impact loading to first understand the damage development during a single impact and optimize SMAT conditions in order to limit such an overtreatment. The basic idea of this work is to develop a predictive approach based on damage mechanics, which would eventually allow optimizing the treatment conditions through a series of numerical simulations, including multi-impact loading. However, this chapter is mainly focused on the development of the damage coupled constitutive model and demonstrates the capability of this model for a single impact simulation.

In the framework of constitutive modeling, a combination of plasticity and damage theories is physically possible since many materials exhibit an interaction between inelastic mechanisms related to micro-cracks or micro-voids growth and plastic flow. As a result, the plasticity and damage couplings can be analyzed either in a small deformation formalism [155] or in a finite deformation formalism [156], [157]. Despite these achievements, there are few studies about damage evolution during severe plastic deformation processes. Therefore, suitable advanced materials models

are required for better describing the plastic behavior and damage development of 316L TWIP steels during SMAT process.

In this chapter, to determine the state of deformation and damage during the SMAT process, the isotropic GTN constitutive model is thus adopted. This damage model is modified to be combined with the dislocation density-based viscoplastic model. Numerical simulations of a single impact are then performed to investigate the deformation and the damage evolution by taking into account different factors, including velocity. Various parameters such as residual stresses, equivalent plastic strain, dislocation density, twinning and damage evolution are eventually investigated through numerical simulations.

5.2 Dislocation density constitutive model involving damage evolution

In this dislocation density constitutive model which couples damage, a few fundamental assumptions are proposed to calculate the flow stress for the TWIP steel:

1. The material is assumed to be isotropic with visco-elastoplastic behavior, which obeys a dislocation density hardening rule with finite deformation;

2. The strain rate is taken into account in the constitutive model of this chapter. In this work, only the viscoplasticity part is further modified, and for the elasticity, the stress and strain obey Hooke's model;

3. The ductile fracture is considered in our model, and the damage is considered by GTN model. The GTN coefficients are assumed to be constant, which will not change with the void volume fraction;

4. In the model, the TRIP effect is not considered, and it is only suitable for describing TWIP materials but not TRIP materials;

5. For TWIP steel, the reference flow stress is assumed to be contributed only by the flow stress of austenite, and the twining will occur in austenite and contributes to the flow stress of austenite;

6. For the dislocation density hardening rule, considering the contribution of twinning to the overall deformation, we assume that the contribution of slip and twinning to the overall deformation obeys a mixing rule.

5.2.1 Dislocation density viscoplastic model

Chen et al. [132] have proposed a dislocation density-based model based on the work of Chapter 4 to describe the properties of TWIP/TRIP steel. The model can well predict the evolution of the volume fraction of twin and martensite, as well as the macroscopic mechanical behavior. So in this chapter, a dislocation density-based viscoplastic model is proposed based on the dislocation density model considering the influence of strain rate.

In this model, according to the work of Estrin et al. [77], the flow stress σ_y is related to the governing parameter in a kinetic equation defined by a power law:

$$\frac{\sigma_y}{\sigma_{ref}} = \left(\frac{\dot{\bar{\varepsilon}}^{vp}}{\dot{\varepsilon}_0} \right)^{1/m} \tag{V-1}$$

To take into account the contribution of twinning, the variation in the total plastic shear strain can be described using a mixture model expressed as follows [142]:

$$d\gamma^{vp} = (1 - f_t) d\gamma_g^{vp} + \gamma_t df_t \tag{V-2}$$

where γ^{vp} is the effective shear strain, γ_g^{vp} is the shear strain due to dislocation gliding, γ_t is the shear strain related to twinning, and f_t is the volume fraction of twin.

According to different authors [17], [143], the volume fraction of twin can be expressed as a function of the effective plastic strain ε^{vp} :

$$f_t = f_{t.\max}(1 - \exp(-\beta \varepsilon^{vp})) \tag{V-3}$$

where β is a constant, and $f_{t.\max}$ is the maximum volume fraction of twin.

The effective plastic shear strain γ^{vp} and the effective plastic strain ε^{vp} are linked by the Taylor factor M through the following relation [158]:

$$\gamma^{vp} = M\varepsilon^{vp} \tag{V-4}$$

From Eqs. V-2 to V-4, the derivative of the shear strain due to dislocation gliding in austenite γ_g^{vp} with respect to the effective plastic strain ε^{vp} is deduced as follow:

$$\frac{d\gamma_g^{vp}}{d\varepsilon^{vp}} = \frac{M - \beta\gamma_t (f_{t.\max} - f_t)}{1 - f_t} \tag{V-5}$$

The mechanical flow strength, σ_{ref} , of TWIP steels is assumed to be determined by the information on microstructure, which is composed of two parts [146]:

$$\sigma_{ref} = \sigma_0 + \sigma_f \tag{V-6}$$

where σ_0 is the friction stress due to solid solution, and σ_f is related to the isotropic hardening induced by the forest of dislocations. σ_f can be expressed by the Taylor relation as:

$$\sigma_f = \alpha M G b \sqrt{\rho} \tag{V-7}$$

where α is a material constant. G , b and ρ are shear modulus, Burger's vector and dislocation density, respectively.

The dislocation density ρ evolves with deformation as described by the following equation [147]:

$$\frac{d\rho}{d\gamma_{\mathrm{g}}^{vp}} = \frac{1}{bL} + \mathrm{K}_1\sqrt{\rho} - \mathrm{K}_2\rho \tag{V-8}$$

where L is a length scale parameter. The strain rate sensitivity of the dynamic recovery process is defined via:

$$K_2 = K_{20}\left(\frac{\dot{\bar{\varepsilon}}^{vp}}{\dot{\varepsilon}_0}\right)^{-1/n} \tag{V-9}$$

where K_{20} is a material parameter, and n is the strain rate sensitivity.

During the deformation of TWIP steels, besides grain boundaries, mechanical twins act as additional obstacles for the motion of dislocations, which leads to additional sources of dislocations storage in the materials. This effect is introduced in the equations by means of the length scale parameter L , which is defined as:

$$\frac{1}{L} = \frac{1}{d} + \frac{1}{t} \tag{V-10}$$

where d is the average grain size of the material, t represents the average twin spacing between slip bands, which is related to the twin volume fraction f_t and the average twin thickness e according to the following relation [148]:

$$t = 2e\frac{1-f_t}{f_t} \tag{V-11}$$

From Eqs. V-5 and V-8 to V-11, the relationship between the dislocation density ρ and the shear strain by dislocation γ can be written as:

$$\frac{d\rho}{d\varepsilon^{\mathrm{vp}}} = \left(\frac{M - \beta\gamma_t\left(f_{t.\max} - f_t\right)}{1-f_t}\right)\left(\frac{1}{b}\left(\frac{1}{d} + \frac{f_t}{2e(1-f_t)}\right) + k_1\sqrt{\rho} - k_2\rho\right) \tag{V-12}$$

5.2.2 Damage model

Dilatational plasticity theory developed by Gurson et al. [82] can take into account the degradation of the load-carrying capacity by the presence of porosity within isotropic materials. The main difference between the Gurson model and classical plasticity is that the yield surface in the former exhibits hydrostatic stress dependence. In contrast, the classical plasticity assumes that yielding is independent of the hydrostatic stress. GTN damage model can be described by the following relation [159]:

$$\Phi = \left(\frac{\sigma_e}{\sigma_y}\right)^2 + 2q_1 f^* Cosh\left(-\frac{3}{2}\frac{q_2\sigma_m}{\sigma_y}\right) - (1 + q_3 f^{*2}) = 0 \qquad \text{(V-13)}$$

The variables involved in this equation are defined as follows. f^* is the volume fraction of void in the material, σ_y refers to the yield stress of the material, which is calculated by Eq. V-1. σ_e is the macroscopic von Mises equivalent stress, σ_m is the macroscopic mean normal stress, and q_1 , q_2 , q_3 are constitutive parameters introduced by Tvergaard [159] to amplify the hydrostatic stress effect for all strain levels to predict the strain up to the fracture more precisely. Tvergaard [159] found that the set $q_1 = 1.5$, $q_2 = 1$, and $q_3 = 2.25$ is valid to predict fractures, especially for 316L steel. The Gurson model describes material damaging up to the fracture as an increase in the void volume fraction up to a critical threshold. Tvergaard and Needleman modified the effective void volume fraction f , as shown in the following equation:

$$f^* = \begin{cases} f & \text{if} \quad f \le f_c \\ f_c + \dfrac{f_F - f_c}{f_f - f_c}(f - f_c) & \text{if} \quad f_c \le f \le f_f \\ f_F & \text{if} \quad f_f \le f \end{cases} \qquad \text{(V-14)}$$

In the above equations, f_c is a critical value of the void volume fraction and f_f is the value of void volume fraction at which there is a complete loss of stress carrying capacity in the material, i.e., the material is supposed fractured. It is noted that the ultimate value, $f^* = f_F$, at which the macroscopic stress of carrying capacity vanishes, is given by $f_F = \dfrac{1}{q_1}$.

As shown in Eq. V-14, when the void volume fraction is below a critical value, the effective void volume fraction is applied only through the void volume fraction *f*, as it should be. However, if it is larger than the critical value, due to the effect of hydrostatic pressure, the value rapidly increases. In this case, plastic instability is initiated. The evolution of the void volume fraction *f* during plastic deformation is assumed to be the result of both void growth and new voids nucleation, which is given by the additive decomposition:

$$\dot{f} = \dot{f}_{nucleation} + \dot{f}_{growth} \tag{V-15}$$

Nucleation is considered to be entirely dependent on the effective strain of the material and can be estimated by the following equation:

$$\dot{f}_{nucleation} = A\dot{\varepsilon}^{p}_{eq} \tag{V-16}$$

where A is a parameter defined as a function of the equivalent plastic strain:

$$A = \frac{f_n}{S_n\sqrt{2\pi}}\exp\left(-\frac{1}{2}\left(\frac{\varepsilon^{p}-\varepsilon_n}{S_n}\right)^2\right) \tag{V-17}$$

where f_n is the volume fraction of void nucleating particles, ε_n is the mean void nucleation strain, S_n is the corresponding standard deviation and ε^{p} is the effective plastic strain.

Also, the void growth is a function of the plastic strain rate, which can be expressed by the following relation:

$$\dot{f}_{growth} = (1-f)\dot{\varepsilon}^{p}_{kk} \tag{V-18}$$

where $\dot{\varepsilon}^{p}_{kk}$ is the plastic part of the trace of the strain rate tensor.

5.2.3 Numerical implementation methodology

In a pressure-dependent constitutive model, the equivalent stress and the mean stress are two independent variables. Nichols [160] proposed a general backward Euler procedure for pressure-dependent plasticity. A detailed derivation of models similar to Gurson can be found in Simonsen and Li [161]. The forward Euler scheme was proposed by Worswick and Pelletier [162]. The backward Euler stress integration process is used by Xue [163]. Here, the backward Euler stress integration process is used in our calculations. The implementation details of the improved GTN damage model in the finite element software ABAQUS are given hereafter.

There are two types of methods for stress integration: explicit methods and implicit methods. In an explicit method, the yield function and plasticity parameters are evaluated under known stress conditions, and it is not necessary to use an iterative process. In the implicit method, the current stress is unknown, and the nonlinear equation is usually solved by an iterative method. Implicit algorithms can provide better precision in finite element solvers than explicit algorithms [164]. However, it must be consistent with the tangent module and cannot be easily exported and programmed. Compared with implicit algorithms, explicit algorithms present an advantageous stiffness matrix that avoids large stiffness and accurate contact processing, so that numerical analysis can be economically and easily implemented using explicit solvers, especially for sheet metal forming simulations [165]. In this work, the user's material subroutine VUMAT is used to implement the isotropic GTN damage model of the material into the explicit solver ABAQUS/Explicit. The backward Euler algorithm is used to integrate the constitutive equation over the Gaussian points of each element.

The procedure eventually consists of two steps: an elastic predictor and a plastic corrector. For small deformation, the total strain which is a tensor is divided into elastic and plastic parts: $\varepsilon = \varepsilon^e + \varepsilon^p$. The elastic trial stress is calculated by assuming that strain increment is purely elastic in the current time step. After calculating the yield function, the current elastic and plastic state can be assessed. If $\Phi^e_{t+\Delta t} \le 0$, the elastic trial state is the final state. Otherwise, if $\Phi^e_{t+\Delta t} \ge 0$, the stress state is plastic and a correction has to be applied. The Newton-Raphson scheme is used locally to solve a set of nonlinear equations obtained by integrating the elastoplastic equation, thus correcting the trial state back to the yield surface. Successive iterations will continue until both convergence criteria are met, as described below. Void volume fraction f and equivalent plastic strain $\bar{\varepsilon}^{pl}_m$ are treated as two scalar internal variables, H^1 , H^2 . The value f at time t and $t+\Delta t$ are denoted with f_t and $f_{t+\Delta t}$, respectively. The details of the implementation procedures of the stress update algorithm are presented as follows:

Step 1. Get initial values at t = 0, t_i for the quantities:

$$\sigma_t, \varepsilon_t, H^\alpha_t, \Delta\varepsilon_{t+\Delta t}$$

where H^{α} are the state variables, for example, the void volume fraction *f* and the equivalent plastic strain.

Step 2. Trial elastic state is obtained by assuming that the strain increment is purely elastic:

$$\sigma^{e}_{t+\Delta t} = \sigma_{t} + C : \Delta\varepsilon_{t+\Delta t} \tag{V-19}$$

where C is the fourth-rank elastic stiffness tensor.

$$p^{e}_{t+\Delta t} = -\frac{1}{3}\sigma^{e}_{t+\Delta t} : I \tag{V-20}$$

calculates the hydrostatic stress of the total trial stress.

Then calculation of the deviatoric stress q:

$$q^{e}_{t+\Delta t} = (\frac{3}{2} S^{e}_{t+\Delta t} : S^{e}_{t+\Delta t})^{1/2} \tag{V-21}$$

Step 3. Calculate the yield potential and check the current state. If $\Phi^{e}_{t+\Delta t} \le 0$, the current time step is elastic, $\sigma_{t+\Delta t} = \sigma^{e}_{t+\Delta t}$, go to Step 5; else if $\Phi^{e}_{t+\Delta t} \ge 0$, the step is plastic, go to Step 4 for calculation of the plastic correction.

Step 4. Plastic calculation. During this step, the subscript $t+\Delta t$ is omitted in order to simplify the notation.

a. Calculate the flow direction:

$$n = \frac{3}{2q^{e}} S^{e} \tag{V-22}$$

b. A Newton-Raphson iterative method is used to solve the nonlinear equations, Eqs. V-23 and V-24. The flow rule and the yield condition must be satisfied simultaneously, and the consistency condition Eq. V-25 should also be met at the same time.

$$f_1 = {}^{k+1}\Delta\varepsilon_{p} \frac{\partial\Phi}{\partial q} + {}^{k+1}\Delta\varepsilon_{q} \frac{\partial\Phi}{\partial p} = 0 \tag{V-23}$$

$$f_2 = \Phi({}^{k+1}p, {}^{k+1}q, {}^{k+1}H^{\alpha}) = 0 \tag{V-24}$$

$${}^{k+1}\sigma_{m} = \frac{d\sigma^{k+1}_{m}}{d\bar{\varepsilon}^{pl}_{m}} \bar{\varepsilon}^{pl}_{m} \tag{V-25}$$

where ${}^{k+1}\Delta\varepsilon_{p}$ and ${}^{k+1}\Delta\varepsilon_{q}$ are the increment of volumetric strain tensor and spherical tensor of strain for K+1 step, $\bar{\varepsilon}^{pl}_{m}$ is a matrix that denotes the current strain hardening of the material. Iteration continues until both $|f_1|$ and $|f_2|$ < Tolerance

(10^{-8}), which means the convergence of the Newton method is achieved, then go to Step 5, otherwise end the calculation if the convergence of the Newton method can not be achieved.

Step 5. Update hydrostatic stress *p*, equivalent stress *q*, and state variables H^{α}

$$p = p^{e} + K^{m}\Delta\varepsilon_{p} \tag{V-26}$$

$$q = q^{e} - 3G\Delta\varepsilon_{q} \tag{V-27}$$

$$\begin{cases} \Delta H^{1} = \Delta\bar{\varepsilon}_{m}^{pl} = \dfrac{-p\Delta\varepsilon_{p} + q\Delta\varepsilon_{q}}{(1-f)\sigma_{m}} \\ \Delta H^{2} = \Delta f = (1-f)\Delta\varepsilon_{p} + A\Delta\bar{\varepsilon}_{m}^{pl} \end{cases} \tag{V-28}$$

$$\begin{cases} H^{1} = \bar{\varepsilon}_{m}^{pl} = \bar{\varepsilon}_{m(t)}^{pl} + \Delta\bar{\varepsilon}_{m}^{pl} \\ H^{2} = f = f_{t} + \Delta f \end{cases} \tag{V-29}$$

where $G = \dfrac{E}{2(1+\nu)}$ is the shear modulus, and $K^{m} = \dfrac{E}{3(1-2\nu)}$ is the bulk modulus. E and ν are Young's modulus and Poisson's ratio, respectively.

According to Eq. V-14, If $f_c \le f \le f_f$, $f^{*} = \dfrac{f_F - f_c}{f_f - f_c}(f - f_c)$; If $f_f \le f$, $f^{*} = f_F$.

5.3 Model validation

The material used for comparison in this chapter is an AISI 316L steel which has been studied by many other researchers [166], [167]. 316L steel is a kind of TWIP steel which is different from the 304L TWIP/TRIP steel that we studied in Chapter 3, as 316L steel can deform by the only glide of individual dislocations and mechanical twinning without martensitic transformation. Tab. V-1 presents the material constants related to the constitutive model described in the previous section for this TWIP steel.

5.3.1 Constitutive model parameters

In summary, $f_{t.\max}$ and β are fitted from the curve of twin volume fraction. As for other parameters such as m, ρ_0, K_1 and K_{20}, they are fitted iteratively until a good consistency with experimental stress-strain curves is reached. For the values taken from the literature, their sources are indicated in Tab. V-1.

As indicated in Section 5.2, the model developed in this work is based on the evolution of dislocation density. It also enables the description of twinning during the deformation process of the material. To validate the implementation of the model, uniaxial tensile loadings with different strain rates have been considered on a material point in order to examine the evolution of the different variables involved in the constitutive model and the damage model. The stress-strain curves can first be plotted and are shown in Fig. V-1. It can be observed that there is reasonable consistency between the stress-strain curves predicted by the model and the ones obtained with experiments from the literature. Therefore, this constitutive model is able to well describe the strain hardening behavior of 316L TWIP steels.

Tab. V-1. Physical constants and identified parameters for 316L TWIP steel.

Parameters	Physical meaning	Numerical values and units
E	Young's modulus	210 GPa [148]
ρ_{m}	Volume density	7800 kg/m^3
ν	Poisson's ratio	0.3 [148]
γ_t	Twinning shear strain	0.707 [148]
σ_0	Initial flow stress	330 MPa [167]
α	Taylor parameter	0.25 [148]
M	Taylor factor	3 [148]
G	Shear modulus	75 GPa [148]
b	Burgers vector	0.25 nm [148]
d	Grain size	20 μm [167]
ρ_0	Initial dislocation density	1×10^{11}
K_1	Forest hardening parameter	0.04
K_{20}	Dynamic recovery parameter	4
$\dot{\varepsilon}_0$	Reference stain rate	10
m	Strain rate sensitivity linked to true stress	50
n	Strain rate sensitivity related to dynamic recovery of dislocation density	5 [168]
c_t	Average twin thickness	30 nm [148]
$f_{a.\max}$	Saturation volume fraction of twin	0.26
β	Parameter for the volume fraction of twin	1.67

More detailed examinations can be given for other physical variables concerning, for example, twinning and dislocation activities. Fig.V-2 shows the predicted evolution of the volume fraction of twin. It can be observed that the evolution of the volume fraction of twin is well consistent with the experimentally obtained curve. For the evolution of twinning, at the beginning of the deformation loading, the increase of the volume fraction of twin is rapid, and this increase is reduced with the strain (Fig. V-2). Fig. V-3 shows the evolution of dislocation density calculated using Eq. V-2. This evolution corresponds to the multiplication mechanism of dislocations induced under the tensile loading.

5.3.2 Damage parameters

For the GTN damage model, there are nine parameters in the model, and they are as follows: the constitutive parameters q_1, q_2 and q_3, the initial void volume fraction f_0, the void nucleation parameter f_n, ε_n and S_n, the critical void volume fraction f_c and the final failure parameter f_F. To simplify the complex calibration process, q_1, q_2 and q_3 are fixed to be $q_1 = 1.5$, $q_2 = 1$ and $q_3 = 2.25$ according to [84]. The values $\varepsilon_n = 0.3$ and $S_n = 0.1$ have been used in most investigations presented in the literature [66], [169]. The parameters f_0, f_n, f_c and f_F are usually obtained by fitting the numerical calculations with experimental results. Samal et al. [170] has obtained these parameters for 316L steel. The input parameters used in the damage simulation are listed in Tab. V-2.

Tab. V-2. GTN damage parameters used for 316L steel.

Material	f_0	f_c	f_F	f_n	q_1	q_2	q_3	ε_n	S_n
316L	0.000001	0.05	0.4	0.0055	1.5	1	2.25	0.3	0.1

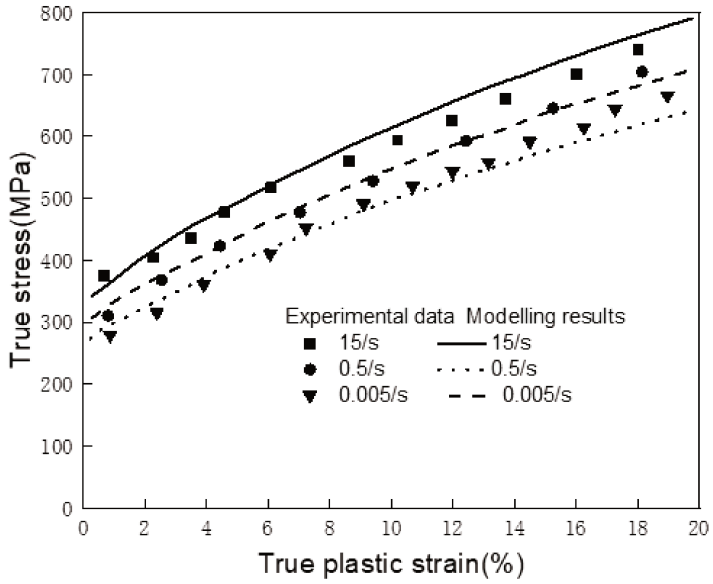

Fig. V-1. Stress-strain curves calculated using the model developed in this work at different strain rates, compared to the experimental data from the references [167].

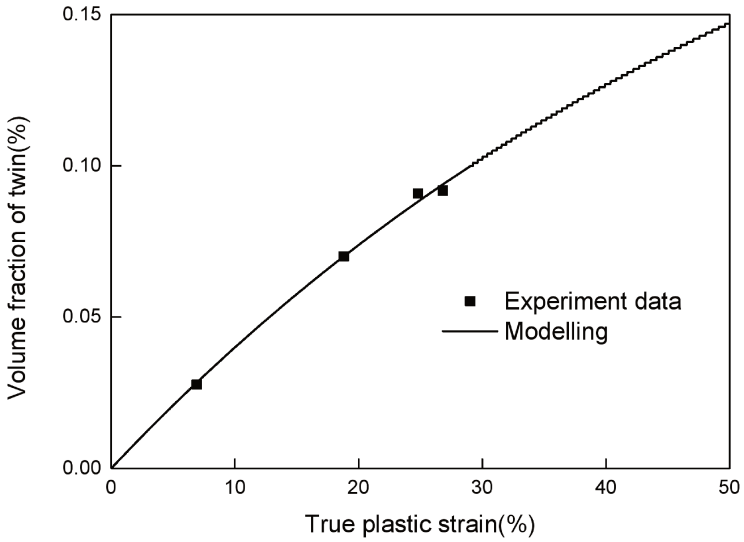

Fig. V-2. Evolution of volume fraction of twin versus true plastic strain, compared to the experimental data presented in the reference [167].

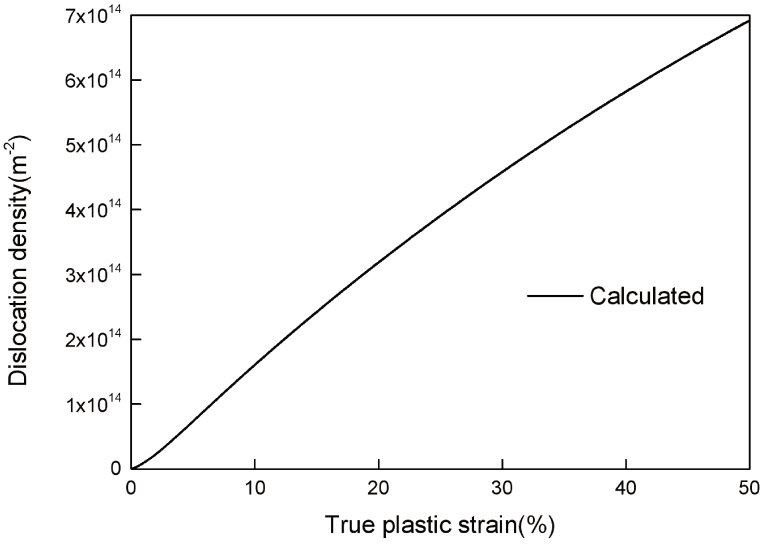

Fig. V-3. Evolution of dislocation density versus true plastic strain.

5.4 Finite element model

A three-dimensional FE model has been built using the commercial finite element code ABAQUS Explicit 6.13 to investigate the impact process and the damage evolution under the effect of a single impact. The model presented above is implemented in a subroutine VUMAT of the code ABAQUS through Euler backward algorithm. Some details of this finite element model are depicted in Fig.V-4. A steel shot with a diameter of 1.0 mm has been considered to impact the surface with an impact angle of 90°, i.e., the loading direction is perpendicular to the impacted surface. As shown in Fig. V-4, the target is a cylinder with a diameter of d = 2 mm and a height of 0.5 mm. This value of height is large enough to avoid the effects of boundary conditions on the results of simulations.

The target has been meshed using elements of C3D8I. The C3D8I element is a first-order fully integrated C3D8 element enhanced by incompatible modes to improve its bending behavior. The formulation of the first-order fully integrated elements leads to extra shear strain in bending called parasitic shear. The incompatible elements can, not only improve the bending analysis but also reduce the computational time compared to second-order elements [171]. An early study has shown that modeling the shot as rigid or deformable balls does not remarkably

influence the results [169]. Therefore, a rigid shot has been used in this work to simplify the modeling. A reference point is defined in the center of the cylinder to impose the initial velocity.

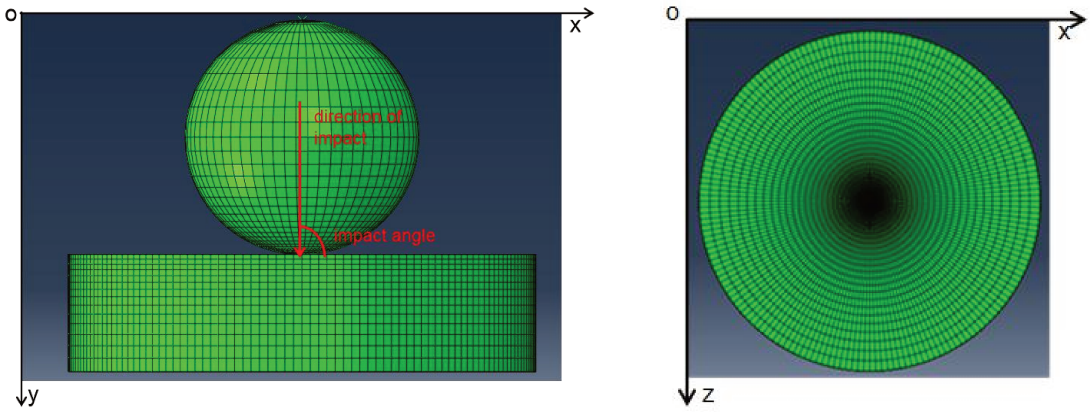

(a) (b)

Fig. V-4. Finite element model: side view (a) of the model showing the cylindrical target and the rigid spherical ball, and top view (b) showing thinner elements in the impact region of the target.

Convergence tests have been performed using different mesh sizes. The results indicate that the mesh depicted in Fig. V-4 is able to describe SMAT process in a cost-effective manner, as measured by the marginal/residual difference in the equivalent plastic strain results obtained with different mesh sizes. Accordingly, this mesh has been chosen in this study.

For the target material, all the parameters are presented above in Tab. V-1. As for the boundary conditions, only the bottom of the finite element model is constrained to avoid the rigid body displacements and rotations. It is worth mentioning that all the simulations were performed in the framework of small strain because the total strain reached by a single impact is rather small.

5.5 Results and discussion

In this section, the results are presented in the form of fields or curves, in order to better understand the evolution of key parameters during the impact loading, such as twinning and damage, as well as the residual effects of the impact including the residual stress and the residual plastic strain. During impact loading, strain rate can reach a very high value [14], as indicated above. In addition, the twinning and damage

processes are strongly strain-rate dependent [172]–[174]. It has been thus interesting to take into account the strain rate in the model, as described in Section 5.3.

Fig. V-5 shows the distribution of different parameters after a single impact with a velocity of 4 m/s. The residual stress, the equivalent plastic strain, the dislocation density, the volume fraction of twin, and the damage induced by a single impact are presented on the impacted target surface. Due to the occurrence of damage, the strength of the material with damage will be lower than the strength of the material without damage, especially when the plastic strain of the material during deformation is relatively large. Due to the reduction of the strength, it is easier for the material to develop plastic strain with damage during SMAT process. As the parameters such as dislocation density, volume fraction of twin, etc. are functions of plastic strain, compared with the material without damage, their values will also change accordingly, but with basically similar distribution rules. It can be seen that all of these parameters have globally a very similar distribution on the top surface, like the distribution of the parameters without damage observed in Chapter 4.

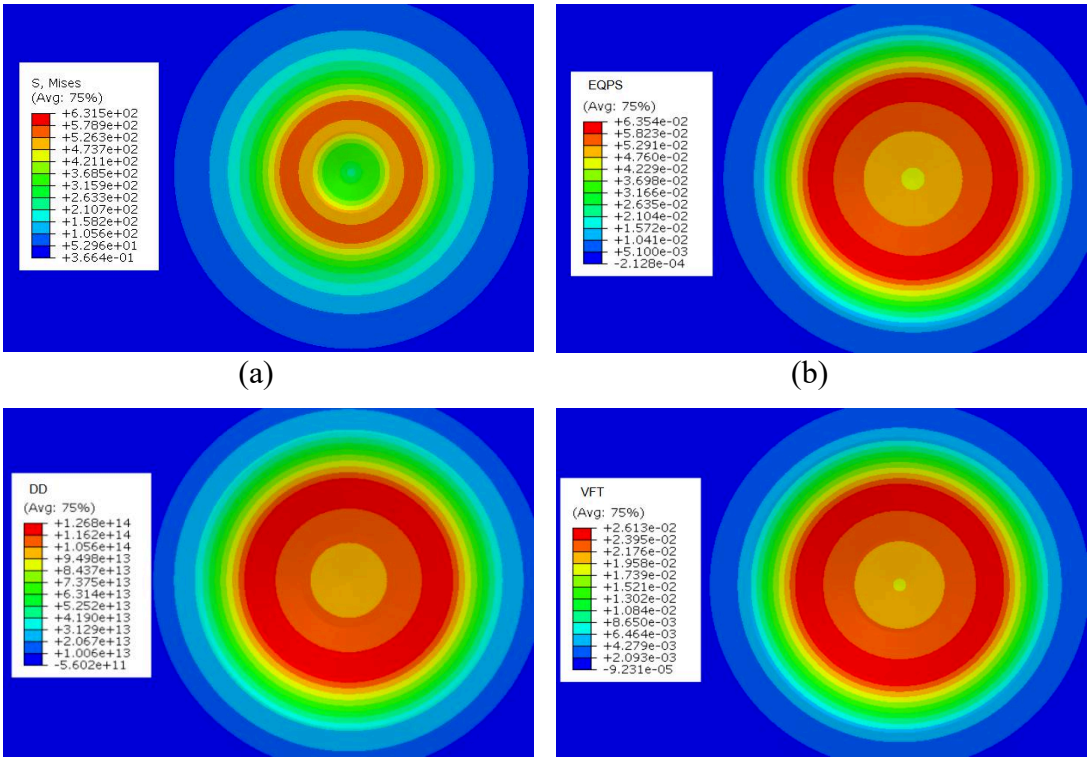

(a) (b)

(c) (d)

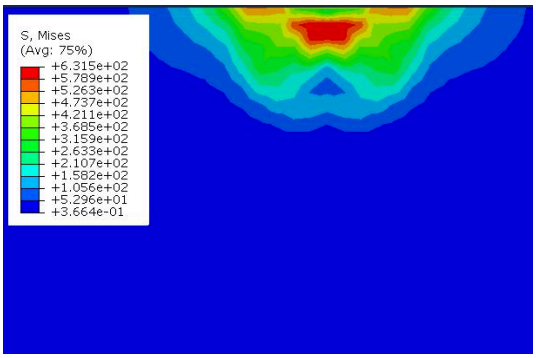

(e)

Fig. V-5. Distribution of equivalent residual stress (EQRS) (a), equivalent plastic strain (EQPS) (b), dislocation density (DD) (c), and volume fraction of twin (VFT) (d) on the treated target surface and equivalent residual stress (EQRS) (e) in depth obtained after single impact with an impact velocity of 4 m/s.

For the distribution of dislocation density, the volume fraction of twin and martensite of the dislocation density-based model in Chapter 4 and the distribution of dislocation density, the volume fraction of twin, the volume fraction of void and the volume fraction of the dislocation density-based damage model in this chapter is almost at the same position where the equivalent plastic strain is the largest. In both the models, the distribution of the maximum equivalent residual von Mises stress is strongly dependent on the equivalent plastic strain stored in the material after one impact (see Fig. IV-6b and Fig. V-5a). The equivalent plastic strain is directly related to the evolution of the microstructure. It can be seen that globally all these parameters have a very similar distribution on the impacted surface. According to Fig. V-5a, the maximum equivalent residual stress reaches 635 MPa after a single impact. The stored equivalent plastic strain is also observed after a single impact, as shown in Fig. V-5b. As the development of dislocations and the increase of volume fraction of twin are both linked to the plastic strain and strain rate, the maximum volume fraction of twin is located almost at the same place where the plastic strain is maximum. As observed in Fig. V-5c, the dislocation density of the austenite is increased by about three orders of magnitude after a single impact from $1*10^{11}$ to $1.26*10^{14}\ m^{-2}$. Fig. V-5d reveals that the volume fraction of twin is increased by up to 2.6% due to the effect of a single impact, with respect to the initial state before impact. Fig. V-5e shows the residual stress obtained by numerical simulation, which distributes

symmetrically with respect to the centreline of the model. The maximum compressive residual stress is 635 MPa and located at a depth of about 0.15 mm from the treated surface.

The effect of impact velocity has also been studied in this work. For this purpose, the impact velocity has been varied from 2 m/s to 4 m/s. Fig. V-6. shows the void volume fraction with a ball velocity respectively of 2 m/s (Fig. V-6a), 3 m/s (Fig. V-6b), and 4 m/s (Fig. V-6c), on the target surface after a single impact. According to the GTN equations, the nucleation is considered to be based exclusively on the effective plastic strain, and the void nucleation follows a normal distribution. The increase of the impact velocity enhances the equivalent viscoplastic strain and the equivalent viscoplastic strain rate in SMAT process. Thus the damage value VVF increases with the increase of impact velocity [154]. Moreover, the damage is caused by local tension loading due to SMAT.

The form of the damage distribution field is annular, which is consistent with the symmetry of the problem. The maximum damage value is located deeper in the impacted zone. The center of the impacted area is not affected by SMAT from the point of view of void growth, as highlighted by Fig. V-6. Moreover, Fig. V-7 shows the evolution of the distribution of the void volume fraction observed in the impacted area with a ball velocity of 4 m/s. For this purpose, three ball positions corresponding to different loading levels are chosen to illustrate the results. The depth affected by the single impact can reach up to 0.15 mm, while the maximum value of the void volume fraction locates at the distance of 0.1 mm from the impacted surface (Fig. V-7c). In addition, the maximum value of the void volume fraction is not located in the center of the contact region, but in a region in a small depth near the center. When comparing the three figures, it can be observed that the position of the maximum void volume fraction moves slightly in the direction far from the impact surface. This phenomenon can be interpreted using the Hertz contact theory. According to this theory, the depth of the maximum shear stress is dependent on the size of the contact region [6]. The progress of ball impact increases the size of the contact region, and consequently, the depth of the maximum shear stress. Therefore, in practice, it is reasonable to remove about 0.1 mm thickness of material from the treated surface to avoid contamination, surface roughness, and plastic damage in the surface of the treated materials.

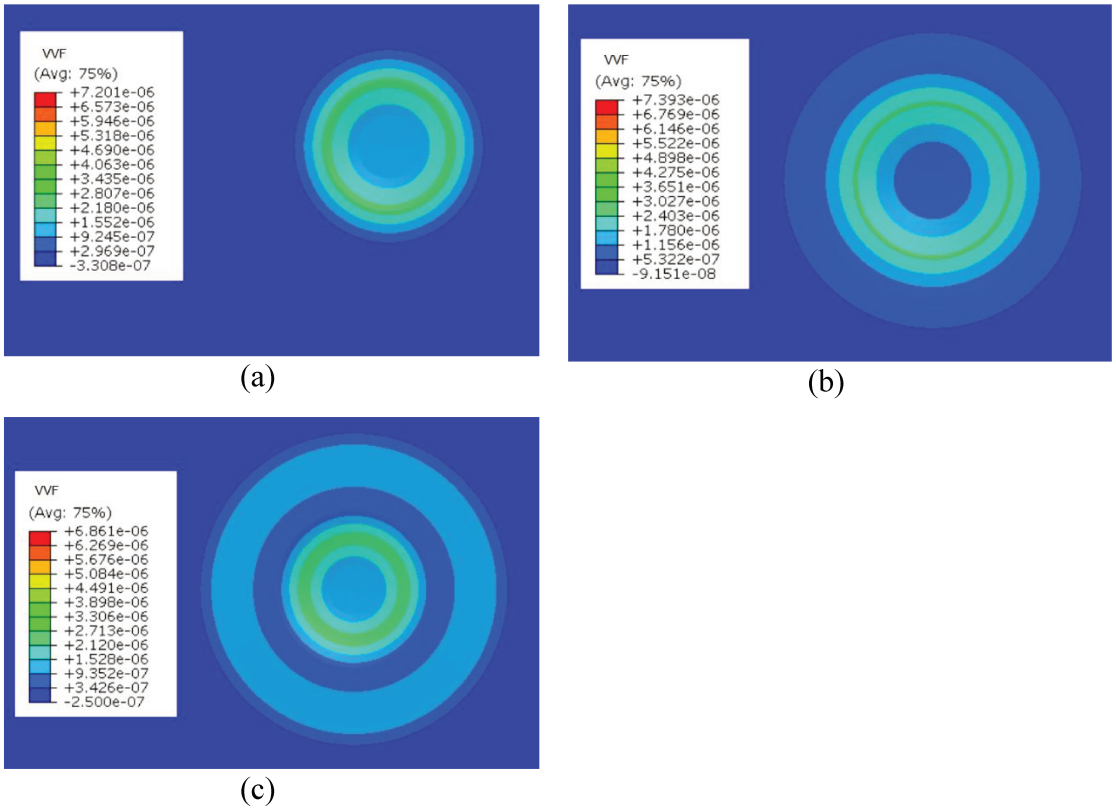

Fig. V-6. Distribution of void volume fraction (VVF) obtained with different ball velocities: 2 m/s (a), 3 m/s (b), and 4 m/s (c) on the treated target surface after a single impact.

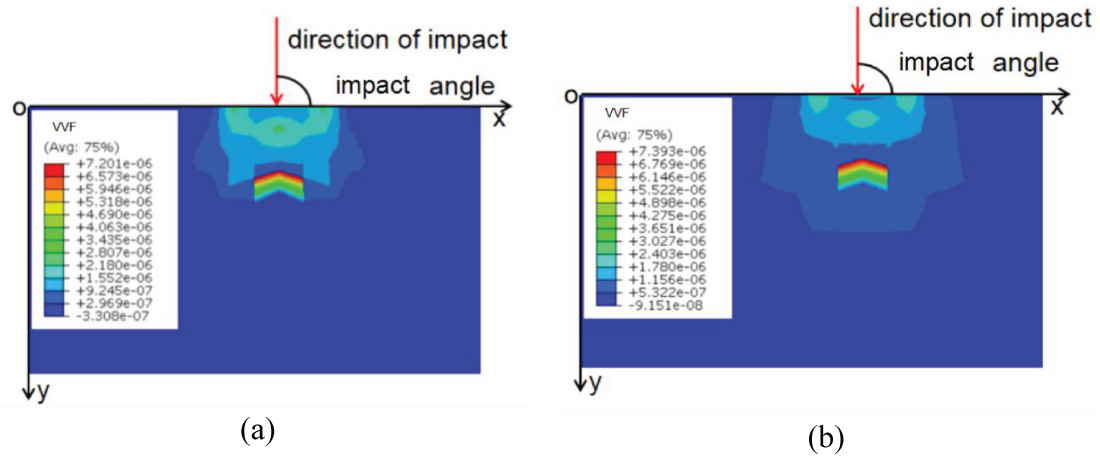

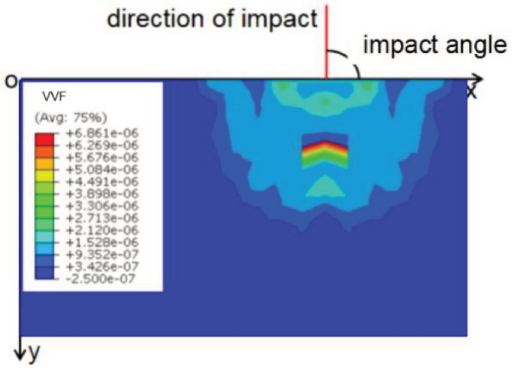

(c)

Fig. V-7. Evolution of the in-depth distribution of void volume fraction (VVF) obtained with a ball velocity of 4 m/s.

Fig. V-8 presents the variation of the volume fraction of twin and the dislocation density plotted following a path through the center of the impacted area on the target surface. Globally, higher is the imposed impact velocity, higher are the volume fraction of twin and the dislocation density. It can be observed that the highest volume fraction of twin is 1.9%, and the highest dislocation density is $9.8*10^{13}m^{-2}$ for the velocity of 2 m/s. In contrast, the volume fraction of twin is increased up to 2.4%, and the dislocation density is increased up to $1.2*10^{14}m^{-2}$ when the velocity is increased up to 4 m/s. These results imply that the impact velocity has a significant influence on the generation of deformation-induced twins and the development of dislocations in TWIP steels.

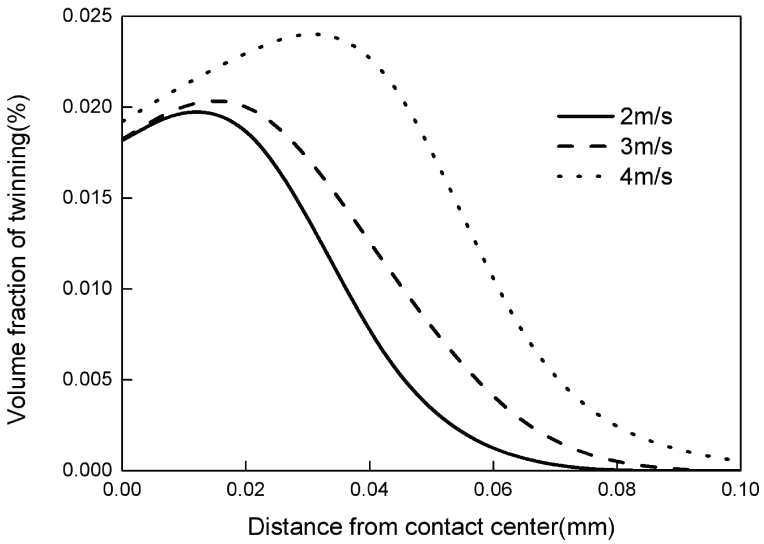

(a)

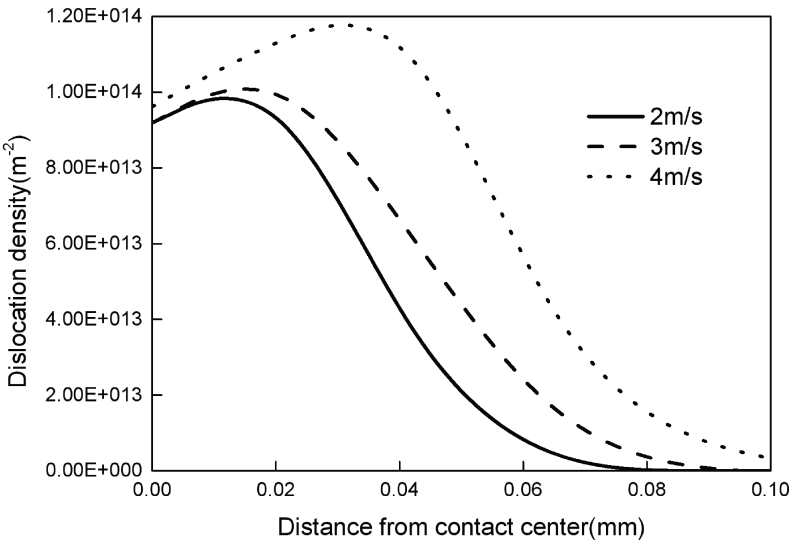

(b)

Fig. V-8. Variation of the volume fraction of twin (a), and the dislocation density (b) obtained with different impact velocities, plotted following a path passing through the center of the impact area on the target surface.

Fig. V-9 shows the variation of the residual vertical displacement as a function of the distance from the center of the contact region, after one ball impact with different ball velocities of 2 m/s, 3 m/s, and 4 m/s, respectively. For these three simulations, the same diameter of ball (2 mm) and the same incident angle ($\theta = 90°$) have been used. From Fig. V-9, it can be seen that the maximum vertical displacement is increased with the increase of the ball velocity. The displacement is increased from 16 μm to 32 μm for the impact velocity increased from 2 m/s to 4 m/s. As a matter of fact, the residual vertical displacement is the consequence of permanent plastic deformation generated due to the impact loading. During such an impact, a certain quantity of kinetic energy of ball has been transformed into potential energy stored in the material in the form of plastic deformation, twinning, etc. In the case of impact velocity of 4 m/s, the kinetic energy of the ball is much higher than that of 2 m/s, and accordingly more kinetic energy has been transformed to potential energy stored in the material. Considering the basic concepts of various peening methods, the obtained surface roughness is due to the random nature of impact of metallic balls. Compared with such peening methods, like shot peening, the roughness obtained after SMAT, which

is related to the vertical displacement, is large. This is because the impact of metallic balls can lead to deeper and wider indent for SMAT. As can be seen in Fig. V-9, after the recovery of elastic deformation of a material after SMAT, the remained indents obtained with different velocities almost have the same width, whereas their depths are much more different. Hence, it can be concluded that increasing impact velocity can increase the deformation concentration and consequently the residual stress level for SMATed materials [154]. This is the reason for which a material shot-peened with a high impact velocity generally has a better performance than a material shot-peened with a low-velocity impact.

However, particular attention should be paid to the occurrence of damage induced by the over-treatment when the treatment intensity is too high. Based on the energy consideration of the fracture of bulk metallic glasses, the elastic deformation will be ended when the developed energy is equal to the shear fracture energy or the critical dilatation energy [175]. For ductile materials, the input energy can also be related to the shear work and dilatation work. The shear work can induce a dislocation slip to cause the plastic deformation, while the dilatation work is induced by the hydrostatic stress, which cannot cause plastic deformation. Once the dilatation work reaches the critical value, fracture occurs [176], which constitutes the main motivation of this work to investigate the damage process due to a single impact. The ultimate goal would be to model the damage development during a multi-impact loading representative of a real shot peening process as used in the SMAT process, which will be addressed in a further work.

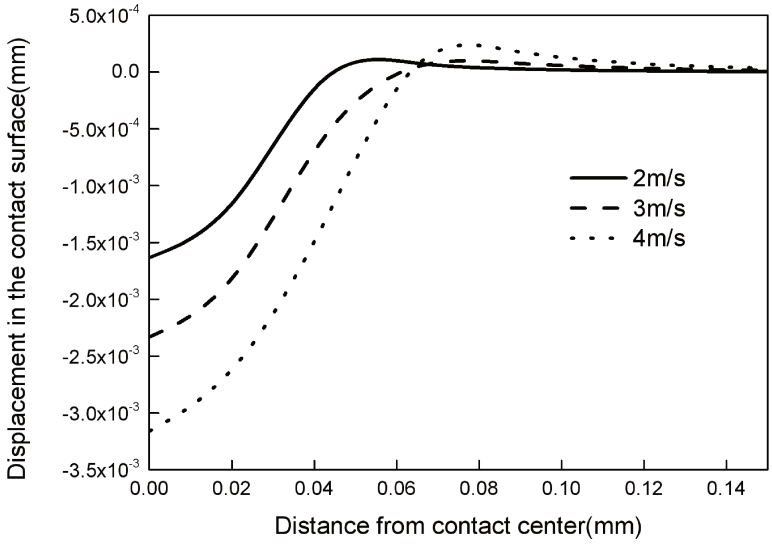

Fig. V-9. Variation of residual displacement after a single impact for the points on the contact surface with nodal value as a function of the distance to the center, obtained with different impact velocities in the plane $(o, \vec{x}, \vec{y})$.

5.6 Conclusions

In this chapter, a viscoplastic damage model based on dislocation density is proposed to study the single impact loading process of TWIP/TRIP steel. In this model, the dislocation density and the volume fraction of twin are related to the equivalent plastic strain, and the effect of strain rate is now considered (compared to Chapter 4). The viscoplastic constitutive model based on dislocation density is combined with the GTN yield criterion to study the failure process during a single impact. Then, a numerical simulation of a single impact has been performed using this constitutive model based on coupled dislocation density and a GTN damage model to study the SMAT process. The residual equivalent stress, the equivalent plastic strain, the dislocation density, the volume fraction of twin and martensite and the damage represented by the void volume fraction after a single impact have been analyzed. Compared to the dislocation density model without damage in Chapter 4, due to the occurrence of damage, the values of the parameters such as the dislocation density, volume fraction of twin, etc., change accordingly. Still, their distribution rules are similar, and they are almost at the same position where the equivalent plastic strain is the largest. It is found that as the impact velocity increases, the damage value and the impact area increase as the values of these parameters are dependent on the equivalent plastic strain stored in the material after one impact, and the equivalent plastic strain is related to the evolution of the microstructure.

Also, the results show that during the impact load, the maximum of the affected depth and void volume fraction increases. The depth affected by a single impact can reach 0.15 mm, while the maximum value of the void volume fraction is located at a distance of 0.1 mm from the impact surface. So it should be reasonable to remove approximately 0.1 mm thick material from the treated surface to avoid surface roughness and plastic damage to the material in order to improve the benefit of SMAT process.

The results concerning the variation of the volume fraction of twin and the dislocation density with different impact velocities also indicate that the impact

velocity has a significant effect on the generation of deformation-induced twins and the development of dislocations. In addition, the results of variation of the residual displacement with different impact velocities show that the maximum vertical displacement increases as the ball speed increases. The residual vertical displacement is the result of permanent plastic deformation due to the impact load. It indicates that special attention should be paid to the occurrence of damage caused by excessive treatment, which constitutes the main motivation for studying destructive processes due to a single impact. These results demonstrate the ability of the model to analyze the mechanical properties and damage processes of a material during a single impact.

This work of modeling a single impact will be further completed by more investigations of 316L TWIP steels under multi-impact loadings representative of SMAT process. In this case, the model should be enriched to describe different phenomena, such as finite deformation or anisotropic aspects.

CHAPTER 6 A NANOINDENTATION STUDY OF THE VISCO- ELASTO PLASTIC BEHAVIOR OF GRADIENT NANOSTRUCTURED AISI 316L TWIP STEEL INDUCED BY SMAT

6.1 Introduction

During SMAT, high compressive residual stresses are typically introduced in the mechanically affected layer due to the incompatibility of the plastic and elastic deformation of material. The presence of nanostructured layer and high compressive residual stress can significantly improve the mechanical properties of materials under various loading conditions, such as fatigue [177], wear [11]. The near-surface area is mechanically affected by SMAT. Due to severe plastic deformation, it can lead to gradual grain size refinement. At the same time, the bulk of the part does not mechanically deform under SMAT, so its properties remain unchanged. Thus, a gradient microstructure is formed from the treated surface to the inner region in the material. The particularity of SMAT over conventional shot peening is that it converts the top surface layer of the material from coarse grains to nano-sized grains. The nanostructured layer, even though typically thin (about 5-10 μm), can have a significant impact on the properties of the material, as the engineered component is primarily loaded on its surfaces, such as in the case of friction, torsion, or contact guidance. To understand accurately the mechanical properties of SMATed materials, it is necessary to characterize the mechanical properties of different regions, such as nanostructure layers and mechanically deformed areas.

Nanoindentation is an important tool for measuring the mechanical properties of materials at a small scale, and the indentation depth can range from tens of nanometers to more than one micron [122]. This technique has been widely used by

researchers all over the world to study elastic modulus, hardness, size effect, sinking-in, and piling up. For instance, Wang et al. [178] determined a visco-plastic constitutive model for Li based on an iterative finite element (FE) modeling approach, by which the elastic modulus was determined. The results show that the elastic modulus has a negligible influence on the nanoindentation response of Li at ambient temperature. Chen et al. [179] used an inverse finite element method (IFEM) to investigate the indentation size effect (ISE), and the results show that the yield stress is highly dependent on indentation depth. Xiao et al. [180] proposed a strain-gradient crystal plasticity theory that incorporated the contributions of geometrically necessary dislocations and non-uniformly distributed defects to characterize the indentation size effect and irradiation hardening of materials.

Recently, there has been an increasing interest in understanding the deformation behavior of TWIP steel, and numerous techniques allowing the estimation of mechanical properties by nanoindentation have been developed. For example, Pierce et al. [181] developed a method to extract single-crystal elastic stiffnesses from orientation-specific indentation moduli and used this method to calculate the elastic stiffnesses of TWIP alloy. Li et al. [182] elucidated the strain rate dependence on the deformation behavior and accompanying deformation mechanisms in Fe-30Mn-0.3C TWIP steel using nanoindentation and post-mortem microscopy of the deformed region. Moreover, Zhang et al. [183] studied the geometry of dislocation patterns in the surrounding of nanoindenters in a TWIP steel using electron channeling contrast imaging and discrete dislocation dynamics simulations. However, the size of the grains, the density of dislocations, and the effects of twinning and loading rates of the TWIP material induced by mechanical surface treatment techniques such as SMAT are not adequately considered [184]–[186].

The purpose of this work is to study the characteristics of the material processed by SMAT such as the distribution of grain size, dislocation density, twin and so on to develop a coupled numerical nanoindentation technique to better understand and predict the mechanical properties of 316L TWIP steel treated with SMAT. Based on previous studies, we propose an analytical model taking into account the effect of grain size, dislocation density, twin and strain rate to study the nanoindentation of TWIP steel [132], [187]. The global tensile stress-strain curves predicted by the model are validated with experimental data available in the literature. Furthermore, the model is implemented in a subroutine of ABAQUS Explicit so that numerical

simulations can also be performed to study the nanoindentation process. To consider the elastoplastic behavior of SMATed materials, the mixing rule will be used to take into account for the strength contributed by different layers. Finally, the Load-Displacement curves predicted by the model will be compared with the curves obtained by nanoindentation experiments.

6.2 Dislocation density based visco-plasticity model

In this chapter, assumptions are also proposed to calculate the flow stress of the gradient TWIP steel:

1. The material is assumed to be isotropic with visco-elastoplastic behaviour, and it obeys a dislocation density hardening rule with finite deformation;

2. The strain rate is taken into account in the constitutive model of this chapter. In this work, only the viscoplasticity part is further modified, and for the elasticity, the stress and strain obey Hooke's model ;

3. As the maximum strain of the gradient material treated with SMAT during the tensile test is much smaller than the fracture strain of the material, we mainly consider the elastoplasticity properties of the material, and the damage is not considered in our model;

4. In the model, the TRIP effect is not considered, and it is only suitable for describing TWIP materials;

5. Considering the contribution of twinning to the overall deformation, we assume that the contribution of slip and twinning to the overall deformation obeys a mixing rule;

6. For TWIP steel, the flow stress is assumed to be contributed by isotropic hardening induced by forest dislocations and the back stress related to kinematic hardening, and the TRIP effect is not considered;

7. The SMATed 316L TWIP steel is assumed as a gradient structure consisting of four layers with particular microstructures and mechanical properties.

8. The overall visco-elastoplastic deformation behavior of gradient nanostructured materials is assumed to be obtained from the linear superposition of the four layers.

According to the work of Estrin [77] and our previous work [132], the flow stress σ_y is related to the governing parameter in a kinetic equation defined by a power law:

$$\frac{\sigma_y}{\sigma_{ref}} = \left(\frac{\dot{\bar{\varepsilon}}^{vp}}{\dot{\varepsilon}_0} \right)^{1/m} \tag{VI-1}$$

where σ_{ref} is the reference flow stress, $\dot{\varepsilon}_0$ is the reference strain rate, and m is the strain rate sensitivity.

To take into account the twinning contribution, the variation in the total plastic shear strain γ^p can be described using a mixing rule expressed as follows [142]:

$$d\gamma^p = (1 - f_t) d\gamma_g^p + \gamma_t df_t \tag{VI-2}$$

where γ_g^p is plastic shear strain by dislocation gliding, γ_t is the plastic shear strain of twin, f_t is the volume fraction of twin.

According to Olson and Cohen [188], the volume fraction of twin can be expressed as a function of effective plastic strain ε^p:

$$\frac{df_t}{d\varepsilon^p} = \beta (f_{t.\max} - f_t) \tag{VI-3}$$

where β is constant, $f_{t.\max}$ is the maximum volume fraction of twin.

The Taylor factor *M* links effective plastic shear γ^p strain to effective plastic strain ε^p as follows [189]:

$$\gamma^p = M\varepsilon^p \tag{VI-4}$$

From Eqs. VI-2 to VI-4, the relationship between the shear plastic strain γ^p and the dislocation gliding of austenite γ_g^p can be expressed:

$$\frac{d\gamma_g^p}{d\varepsilon^p} = \frac{M - \beta\gamma_t (f_{t.\max} - f_t)}{1 - f_t} \tag{VI-5}$$

The measure of the mechanical flow strength, σ_{ref}, of TWIP steel is assumed to contain the information on microstructure, which is composed of three parts [190]:

$$\sigma_{ref} = \sigma_0 + \sigma_f + \sigma_{GB} \tag{VI-6}$$

where σ_0 is the friction stress due to a solid solution, σ_f is related to the isotropic hardening induced by forest dislocations, and σ_{GB} is the back stress related to kinematic hardening. σ_f can be expressed by Taylor relation as [191]:

$$\sigma_f = \alpha M G b \sqrt{\rho} \tag{VI-7}$$

where α is a material constant, M is the Taylor factor. G, b and ρ are shear modulus, Burgers vector and dislocation density, respectively. σ_{GB} is defined as [18]:

$$\sigma_{GB} = \frac{K_{HP}}{\sqrt{d}} \tag{VI-8}$$

where K_{HP} is the Hall-Petch constant and d denotes grain size.

The dislocation density ρ evolves with deformation as [76]:

$$\frac{d\rho}{d\gamma_g^p} = \frac{1}{bL} + k_1\sqrt{\rho} - k_2\rho \tag{VI-9}$$

where L is a length scale parameter. The strain rate sensitivity k_2 of the dynamic recovery process is defined via [192]:

$$k_2 = k_{20}\left(\frac{\dot{\varepsilon}^{vp}}{\dot{\varepsilon}_0}\right)^{1/n} \tag{VI-10}$$

where k_{20} is a material parameter, and n the strain rate sensitivity.

During the deformation of TWIP steels, in addition to grain boundaries, mechanical twins also act as additional obstacles for the movement of dislocations, leading to additional sources of dislocations storage in the materials. This effect is introduced in the equations using the dislocation mean free path L, which is defined as [193]:

$$\frac{1}{L} = \frac{1}{d} + \frac{1}{t} \tag{VI-11}$$

where d is the average grain size of the material, t represents the average twin spacing which is related to the twin volume fraction f_t and the average twin thickness e as follows [194]:

$$t = 2e\frac{1 - f_t}{f_t} \tag{VI-12}$$

From Eqs. VI-4 and VI-8 to VI-11, the relationship between the dislocation density ρ and the plastic shear strain by dislocation γ_g^p can be expressed as follow:

$$\frac{d\rho}{d\gamma_g^p}=\left(\frac{M-\beta\gamma_t\left(f_{t.\max}-f_t\right)}{1-f_t}\right)\left(\frac{1}{b}\left(\frac{1}{d}+\frac{f_t}{2e(1-f_t)}\right)+k_1\sqrt{\rho}-k_{20}\left(\frac{\dot{\varepsilon}^{vp}}{\dot{\varepsilon}_0}\right)^{1/n}\rho\right) \qquad \text{(VI-13)}$$

6.3 Material parameters

The material studied in this chapter is an AISI 316L TWIP steel. Tab. VI-1 presents the mechanical properties and material constants related to the material model for this TWIP steel. In this work, all the parameter values are directly taken from the literature or fitted from the experimental results [54], [132].

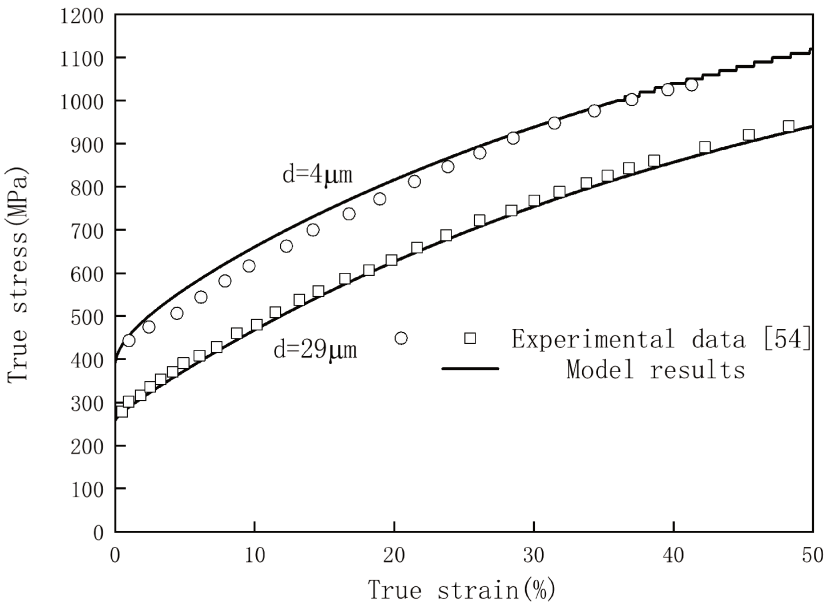

Fig. VI-1. The stress-strain curves calculated using the developed model, compared to the experimental data [54] with grain sizes of 4 and 29 μm.

The specific numerical values of the material parameters are given in Tab. VI-1. Material parameters for elastoplastic characteristics are fitted to the alloy 316L at 25°C. Typical values are assigned to the Taylor model parameters, α, b, and M. The parameters describing the dislocation evolution (k_1 and k_{20}), and the strain rate sensitivity exponents (m and n) are reasonably chosen within the suggested range from the literature [132]. The value of the initial density of statistically stored

dislocations ρ_0 corresponds to annealed materials. They are fitted iteratively until a good consistency with experimental stress-strain curves is reached. The stress-strain curve is plotted, as shown in Fig. VI-1, compared to the experimental data with grain sizes 4 and 29 μm [54]. It can be seen that there is a reasonable agreement between the stress-strain curve predicted by the model and the stress-strain curve obtained experimentally. The excellent agreement between the two curves also means that the model can well describe the strain hardening behavior of TWIP steel.

Tab. VI-1. Physical constants and identified parameters for TWIP steel.

Parameters	Physical meaning	Numerical values and units
γ_t	Twinning plastic shear strain	0.707 [87]
σ_0	Initial flow stress	250 (MPa)
α	Taylor parameter	0.25 [87]
M	Taylor factor	3 [87]
G	Shear modulus	75 (GPa) [87]
b	Burgers vector	0.25 (nm) [87]
d	Grain sizes	4 (μm), 29 (μm) [54]
ρ_0	Initial dislocation density	1×10^{11} (m^{-2})
K_1	Forest hardening parameter	0.0001
K_{20}	Dynamic recovery parameter	2
m	Strain rate sensitivity	3
n	Strain rate sensitivity	5
c_t	Average twin thickness	30 (nm) [87]
$f_{t.\max}$	The saturation volume fraction of twin	0.15
β	Parameters for the volume fraction of twin	1.67
K_{hp}	Hall-Petch slope	520 ($MPa.mm^{0.5}$)

6.4 Finite element implementation

In this work, four indentations at a specific distance beneath the SMATed surface: 3, 70, 300, and 600 μm, were performed using the continuous stiffness measurement

with the elastic modulus calculated using Oliver and Pharr's method [195]. The parameters for the four depth in the material can be obtained from Tab. VI-2 except for grain size and the initial volume fraction of twin, which are obtained from the experimental method introduced in Chapter 3. A three dimensional model for nanoindentation has been built, as shown in Fig. VI-2 The Berkovich indenter was set as a rigid solid. In contrast, the specimen was established as a deformable part that consists of eight-node incompatible mode brick elements (C3D8I), where the mesh size is finer around the contact area and gradually rougher away from the nanoindentation. The diameter of the specimen is 10 mm, with a depth of 5 mm. The coefficient of friction between the indenter and the 316L TWIP steel is set to 0.2, which is typical for nanoindentation analysis [196]. For the nanoindentation with a constant value of $\dot{h}/h$, as shown in Fig. VI-2a, the finite element model is performed using the displacement control mode. The independent parameter in finite element modeling is the loading rate, set to the same value as the indentation measurement. For the FEM input, a Young's modulus of 200 GPa and a Poisson's ratio of 0.3 are used. As for the boundary conditions, only the bottom of the model is fixed to block all displacements and rotations.

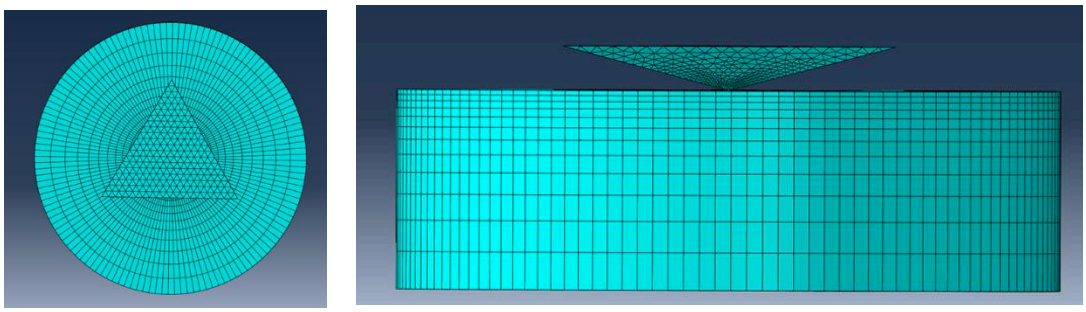

(a) (b)

Fig. VI-2. Finite element model: top view (a) of the model showing the target and the rigid indenter, and side view (b) showing the mesh in the impact region of the target.

As shown in Fig. VI-3, the experimental load-displacement curves obtained by [197] are compared with the FE modeling results, with different depths h_d of 3, 70, 300, and 600 μm, with strain rate $\dot{h}/h$ = 0.05/s where h is the displacement of the indenter. For material parameters, it should be noted that the only differences at different depths are the grain size, the initial volume fraction of twin, and the initial

dislocation density of austenite; while for the other material parameters, they are the same and obtained from the experiments or references as shown in Tab. VI-2.

Tab. VI-2. Parameters of grain size, the initial volume fraction of twin, and initial dislocation density of austenite for 316L TWIP steel.

Parameters/Depth(μm)	3	70	300	600
Grain size d (nm)	500	950	2800	10000
Initial volume fraction of twin $f_{t0}(\%)$	5	4.4	1.6	0
Initial dislocation density of austenite $\rho_{\alpha 0}(m^{-2})$	$1.2*10^{14}$	$2.6*10^{13}$	$3.6*10^{12}$	$1.1*10^{11}$

As SMAT generates nanostructure [198], the peak force of the force-displacement curve of the nanoindentation will be higher if it is closer to the treated surface (indeed the smaller the depth from the treated surface, the smaller the grain size). The peak force at the top surface is twice as large as in the area not affected by SMAT. It can be observed that the experimental results and the FE prediction results have good consistency in the initial and the final loading stage at different depths during the loading process. However, the predicted values in the intermediate stage of loading are lower than the experimental values, but the difference is not very significant. So it can be considered that the model can relatively well predict the loading process. During the unloading process, the predicted peak indentation depth is significantly less than the experimentally measured recovery, which indicates that the elastic recovery process during the unloading process is more pronounced than the elastic recovery predicted by the finite element model. This is because there are many factors that affect the loading and unloading characteristics of nanoindentation, including residual stress, piling-up and sinking-in phenomenon. For example, in our model, the effect of residual stress, piling-up and sinking-in phenomenon on nanoindentation are not considered. However, after severe plastic deformation, the elastoplastic and elastic response during indentation can be affected by residual stress. At a given penetration depth, the load-depth curve of the sample with biaxial compression residual stress is steeper than that of the stress-free sample and shallower for the tensile residual stress. The unloading curve behaves similarly; compressive residual stress shifts the unloading curve to shallower penetration depth,

and conversely, tensile residual stress shifts to higher penetration depth. There is a linear relationship between the residual stress and the change in the actual contact area. At the same time, compressive residual stress increases the contact area due to more piling-up, while tensile residual stress reduces the contact area due to the sinking-in area or less piling-up.

Twinning has an effect on the nanoindentation results when the plastic zone underneath the indenter interacts with the twins. When the twin boundaries occur, the space for dislocation nucleation and dislocation pile-ups becomes smaller. The twin boundaries will serve as obstacles to the dislocation motion which will lead to the increase of the strength and ductility of crystal. In order to study the role of twinning in the process of nanoindentation, two kinds of models were established by taking into account twinning or not.

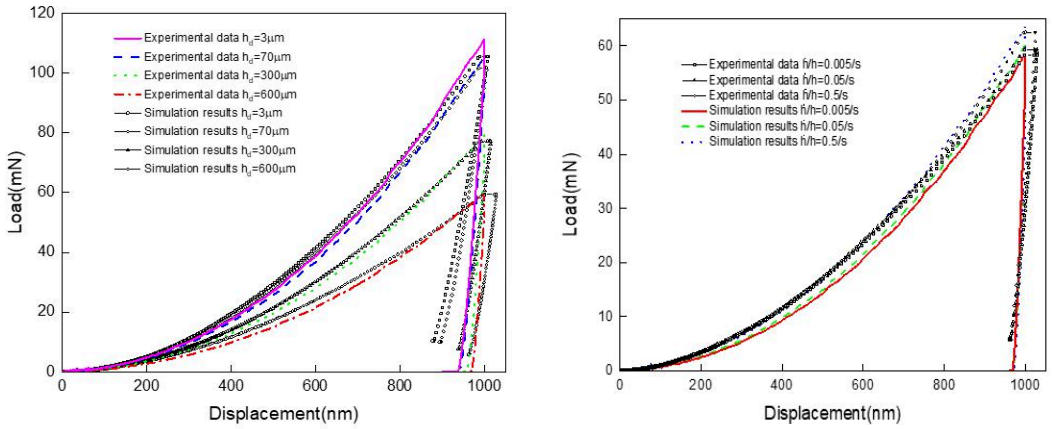

Fig. VI-3. Comparisons of averaged experimental loading curves [197] with FE modeling results at different depths 3, 70, 300, and 600 μm with strain rate ḣ/h =0.05/s (a), and with different strain rates ḣ/h =0.005, 0.05 and 0.5/s at the depth 600 μm (b).

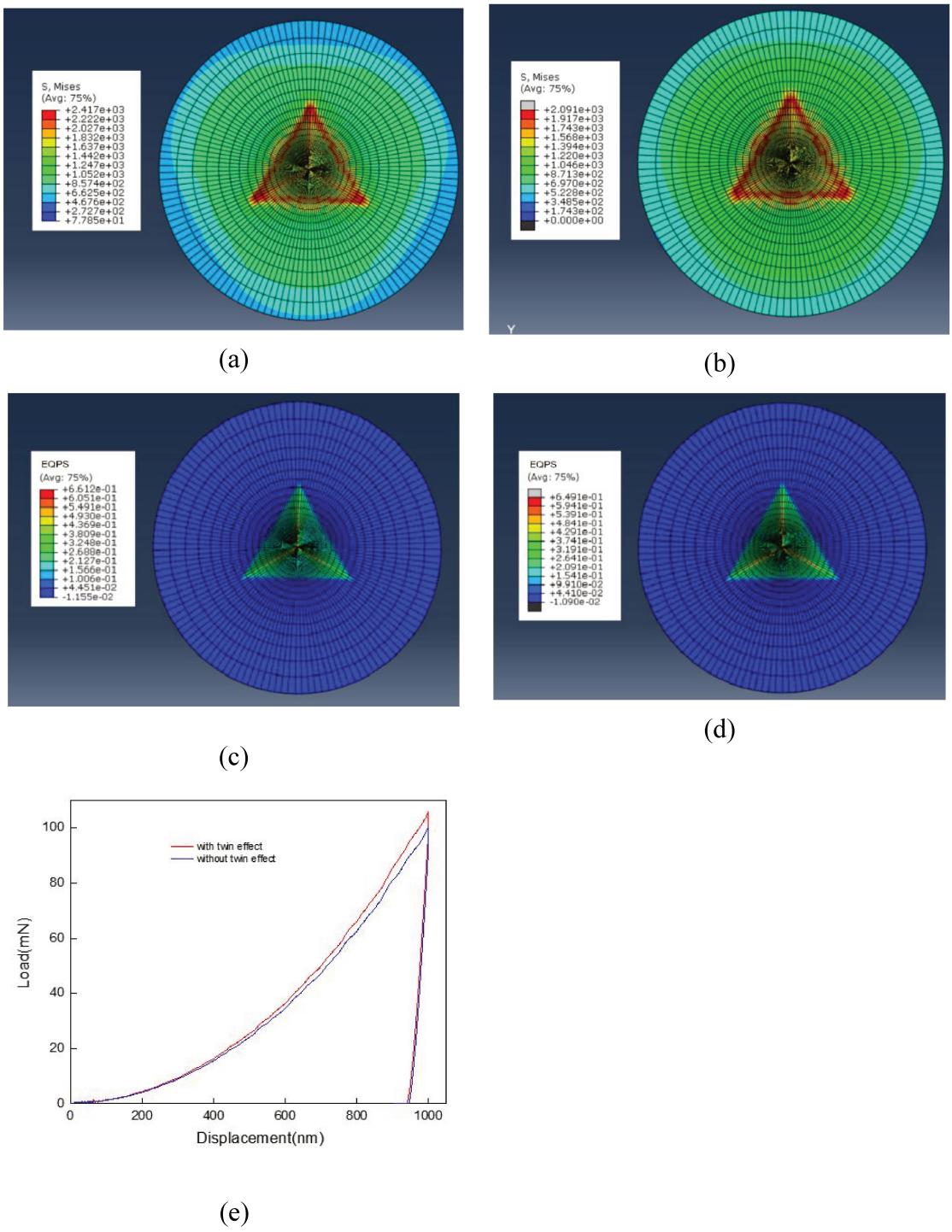

Fig. VI-4. Comparison of FE model-predicted stress field with the effect of twinning (a), without the effect of twinning (b), equivalent plastic strain (EQPS) field with the effect of twinning (c), without the effect of twinning (d) in the contact surface when the displacement of the indenter reaches 1000 nm, and the Load-Displacement curve with/without the effect of twinning (e) at the depth 3 μm from the top surface with a strain rate $\dot{h}/h$ =0.005/s.

Fig. VI-4 shows a comparison of FE model-predicted stress and equivalent plastic strain field with/without the effect of twinning in the contact surface when the displacement of the indenter reaches 1000 nm, and the Load-Displacement curve with/without the effect of twinning at the depth 3μm with a strain rate $\dot{h}/h$ =0.005. There are some differences in stress and equivalent plastic strain in the contact surface with and without the effect of twinning. The Load-Displacement curve in Fig. VI-4e shows that as the displacement of the indenter becomes larger, the difference between the simulated curve considering twinning effect and that not considering twinning effect becomes larger, especially when displacemnt is greater than 300 μm , which means that when the displacement is greater than 300 μm, the effect of twinning can not be ignored. However, the two curves coincide with each other during unloading stage, which means that the twinning has almost no effect on the unloading curves.

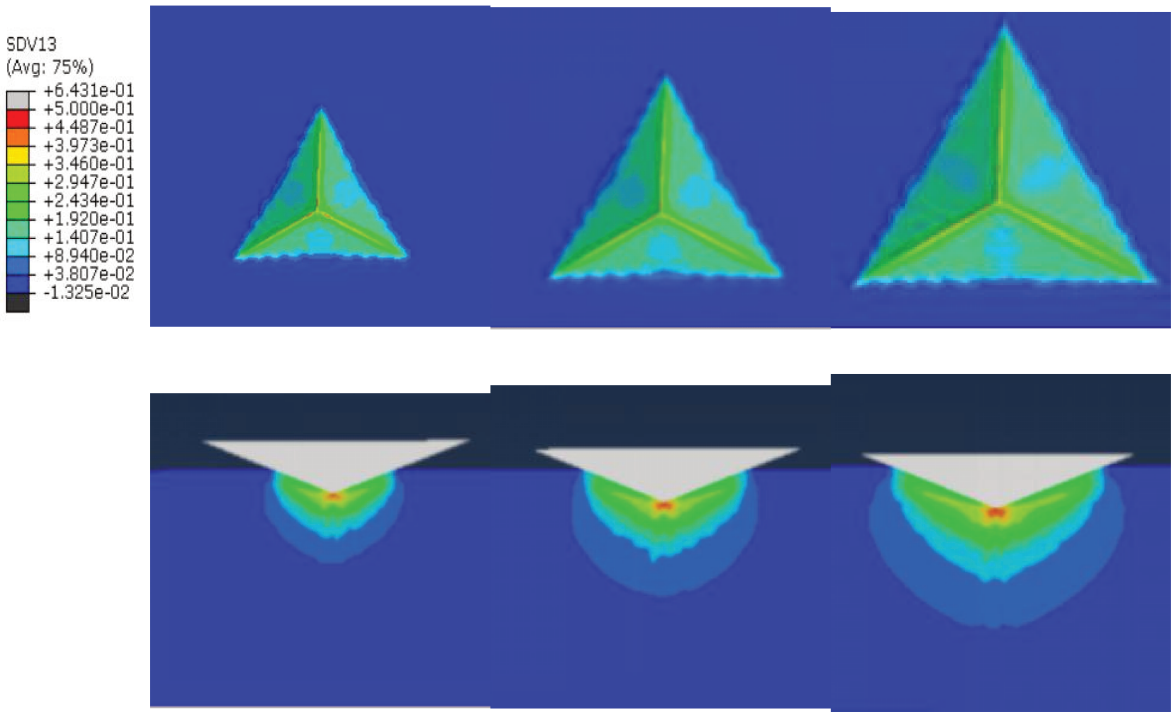

Fig. VI-5. Contours of plastic strain at the indenter in 600, 800, and 1000 nm depth computed by the model at the depth 3μm from the top surface with a strain rate $\dot{h}/h$ =0.005/s with top view and vertical cutaway view.

Fig. VI-5 shows the top view and vertical cut-away view of the contours of plastic strain at the indenter in 600, 800, and 1000 nm depth computed by the model

at the depth 3 μm from the top surface with a strain rate $\dot{h}/h$ =0.005/s. Usually, the nanoindentation contains three distinguishable regimes [199]:

(i) The initial elastic regime, in which the indentation stress varies linearly with the deformation of the indentation zone.

(ii) It shows an obvious elastoplastic transition state of strain, which is due to the deformation of the indentation zone from being mainly elastic to being mainly elastoplastic,

(iii) The production regime that exhibits the expected full plastic response. So the plastic area under the indenter is initially surrounded by the elastically deformable material. Therefore, this initial plasticity is significantly limited until the plastic zone has grown to reach the surface of the sample. At this point, plasticity is relatively easy to develop, which marks the beginning of the third state of complete plastic response. In particular, this transition can be seen by the contour plot of the equivalent plastic strain (PEEQ) field in Fig. VI-5.

6.5 Mechanical behavior of SMAT processed material

Fig. VI-6 shows the results of the EBSD observation performed on the cross-section of a SMATed sample. Globally, a microstructure gradient can be observed in the SMAT affected region. So the SMATed 316L steel can be considered as a gradient structure consisting of different layers with particular microstructures and mechanical properties. Four different regions can be roughly distinguished. They are respectively the surface hardening layer, subsurface hardening layer, the interior region non-affected by SMAT, and the transition region between them. The surface hardening layer corresponds to a refined layer with a grain size ranging from 50 nm to 300 nm (Fig VI-6b). This grain refinement is due to the multi-directional severe plastic deformation induced by the impingement of shots. According to Fig. VI-6b), the thickness of the surface hardening layer (first layer) is presently about 5 μm. Underneath this nanostructured layer is the subsurface hardening layer (second layer) where the initial grain boundaries have not been much modified by SMAT, and they can still be identified (Fig. VI-6b). However, within each grain, many plastic slip traces can be noticed, and the color (which gives information about grain orientation) in each grain is no longer uniform due to the effect of impact loading (Fig. VI-6b). The grains in this subsurface hardening layer region (fourth layer) are split by plastic

slips activated by the multi-directional impacts during SMAT [34]. This layer was less than 250 µm. The transition layer (third layer) is located between the subsurface hardening layer and the bulk/core metal. Its microstructure is similar to the bulk/core, but occasionally there are some twins. According to the reference [200], the depth of the transition layer is less than 500 µm.

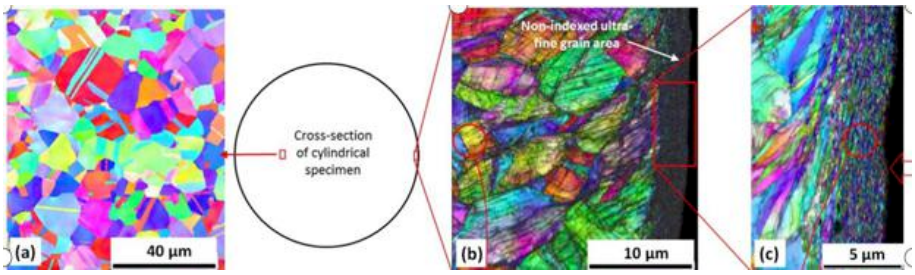

Fig. VI-6. Microstructure observation on the cross-section of a SMATed specimen obtained from the reference [197]: interior region (non-affected by SMAT) (a), mechanically deformed region (transition region) (b), and nanostructured layer (hollow red arrow indicates the treated surface) (c).

Following the mixing rule, the overall visco-elastoplastic deformation behavior of gradient nanostructured materials can be expressed:

$$\sigma_y^t = \sum_{i=1}^{N} f_i \sigma_y^i \tag{VI-21}$$

where σ_y^t is the average flow stress of the gradient material, N is the number of the layers, σ_y^i is the flow stress of the ith layer. f_i is the volume fraction of the ith layer which can be calculated by dividing the area of the ith layer by the entire cross-sectional area of the gradient material, as shown in Tab. VI-3.

Tab. VI-3. The volume fraction of the ith layer.

The layer	The surface hardening layer	Subsurface hardening layer	The transition region	The interior region non-affected by SMAT
f_i(%)	0.33	15.64	14.58	69.44

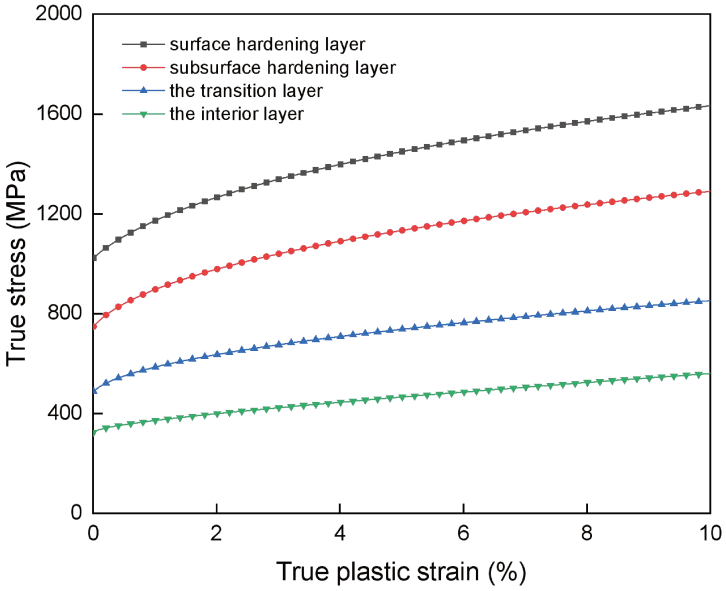

Fig. VI-7. Stress-strain curves for the different layers.

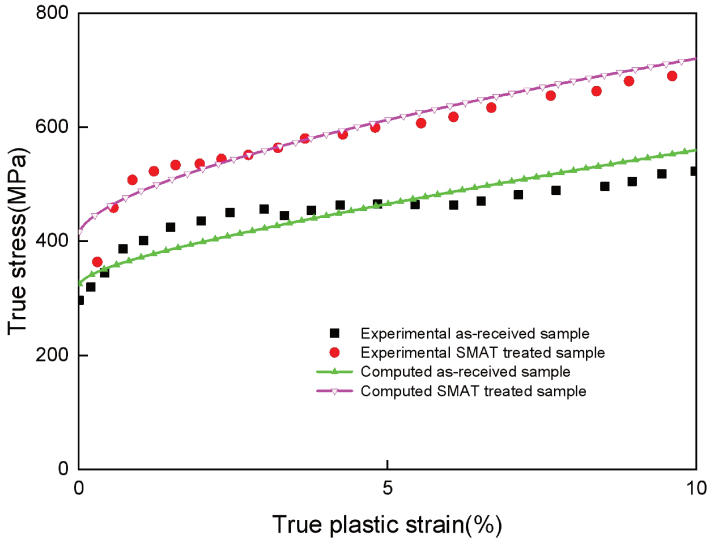

Fig. VI-8. Computed and experimental stress-strain curves [201].

Four stress-strain curves calculated by the dislocation density model presented in section 6.3 using the parameters in Tabs. VI-1 and VI-2 are shown in Fig.VI-7, which correspond to the four distinctive layers. As shown in Fig.VI-8, using the four calculated stress-strain relationships, the stress-strain relationship of the SMATed

316L steel were calculated by Eq. VI-21. Fig. VI-8 also shows the experimental stress-strain relationship of the treated material. It can be seen that the strength of the SMATed material is enhanced, although the thickness of the strengthening layer is much smaller than the core substrate.

To study the strength contributed by strengthening layer to the SMATed material, the load sharing mechanism of composite materials is given as follows:

$$F_i = \frac{\sigma_y^i f_i}{\sigma_y^t} \tag{VI-21}$$

where F_i is the fraction of the load sharing of the i[th] layer.

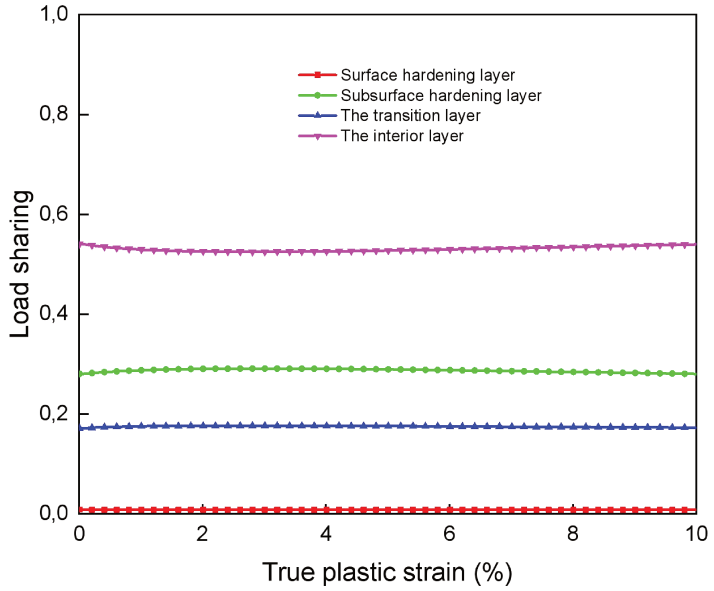

Fig. VI-9. Load sharing of different layers.

Fig.VI-9 shows the effect of the load sharing of different layers. The result shows that for the four layers, the fraction of the load sharing remains approximately stable with the development of the plastic strain. It can be seen that the surface hardening layer shares 29% of the load applied to the whole material twice of the volume fraction, which is about 14.6%. The three SMAT affected layers share about 46% of the load, while their volume fraction is only about 31%. As the strength of the three SMAT affected layers have higher flow strength, so they share more strength

compared to their volume fraction. It means that SMAT can effectively enhance the strength of the material by the influence of the additional three layers.

The microstructure and local mechanical behavior of gradient structure materials change with increasing depth from the top surface. Therefore, it can be concluded that the potential dislocation mechanism during plastic deformation is different at different depths. After SMAT treatment, the structure is definitively different from the top to the interior. In this study, we assume that the treated material is composed of four layers. However, the evolution of the dislocation and twinning, also, and synergistic effects between layers should be studied in the future.

6.6 Conclusions

In this chapter, 316L TWIP steel is subjected to SMAT, and the properties of the nanostructured surface material are attributed to the gradient microstructure formed from the treated surface to the inner region. A dislocation density-based model was successfully developed considering the effects of the grain size, twinning and dislocation density and strain rate based on the experimental results of EBSD, which is successfully compared to global tensile stress-strain curves available in the literature. It is worth noting that the results obtained from the proposed model are very consistent with the experimental measurements of the strength and work hardening of 316L steel.

The model was also implemented in a subroutine of ABAQUS Explicit to perform a 3D simulation of the nanoindentation test at different depths with different strain rates to study the properties of the gradient material after SMAT. The results show that the peak force of the force-displacement curve of the nanoindentation will be higher if it is close to the treated surface. Twinning effect is also studied, and the results indicate that twinning has an effect on the nanoindentation, and the effect is more pronounced when the indenter tip is indented, while when the indenter is away from the material, the effect of twinning on the nanoindentation is weaker. Moreover, the study of the evolution of plasticity shows that the initial plasticity is significantly limited until the plastic zone has grown to reach the surface of the sample. This means that plasticity is relatively easy to occur, and at the same time marks the beginning of the third state of the full plastic response. At last, by using the mixing rule, the elastoplastic response of the SMATed material is calculated, and the calculated results

show a good agreement with the experimental results. The calculated results show that the fraction of load sharing of the SMAT affected layers is relatively high despite its low volume fraction, which is due to the high flow stress of the SMAT affected layers.

CHAPTER 7 CONCLUSIONS AND PROSPECTS

7.1 Major contributions

This thesis focused on the study of SMAT effects on TWIP/TRIP steel with experimental, numerical, and analytical methods. The influence of SMAT on the microstructure of 304L TWIP/TRIP steel was first experimentally studied using SEM, XRD, and Nanoindentation. Based on the experimental results, a dislocation density model of TWIP/TRIP steel has been developed to investigate the characteristics of impacts during SMAT. With the FE model, the distribution of the grain size, the volume fraction of twin and martensite, and the dislocation density of austenite and martensite as the function of SMAT processing parameters were numerically simulated. To study the evolution of the damage during the SMAT process, damage was introduced in the dislocation density model. Finally, a dislocation density based visco-elastoplastic model considering the effect of grain size, dislocation density, twin, and strain rate was proposed to further understand the effects of SMAT on the mechanical behavior of 316L TWIP steel with gradient microstructure. Generally speaking, the results of this study led to several interesting findings that can help to better understand the effect of SMAT on materials.

This study made four major contributions that could be used to optimize SMAT process, namely:

1) Experimental study of the mechanical properties of SMATed samples.

2) Dislocation density based model for prediction of twinning and phase transformation during SMAT.

3) Dislocation density based visco-elastoplastic model coupled with GTN damage model for prediction of damage evolution during SMAT.

4) Dislocation density based visco-elastoplastic model for studying mechanical behavior of the material with gradient microstructure generated by SMAT.

The specific details of these four contributions are as follows:

Contribution 1: The SMAT conditions for the 304L steel and the sample preparation procedure were chosen to study the material properties obtained from SMAT. The residual volume fraction of austenite and the residual stress distribution at the top surface were studied by XRD. The obtained results (load-displacement, peak force, and average peak force) were interpreted subsequently in terms of SMAT induced changes along the cross-section of the SMATed sample. The results show that the grain size, phase transformation, and strain rate have a significant influence on the mechanical properties derived from nanoindentation.

Contribution 2: A dislocation density-based model considering the dislocation density and the volume fraction of twin and martensite related to the equivalent plastic strain was firstly proposed to study the strain hardening behavior of TWIP/TRIP steel. Then numerical simulation of a single impact was performed using the dislocation density-based model to study the basic SMAT process. Finally, the residual equivalent stress, the equivalent plastic strain, the dislocation density in the austenite and martensite, and the volume fraction of the twin and martensite after a single impact were analyzed. The study of the impact of the ball velocity shows that the maximum vertical displacement increases as the ball speed increases, and the residual vertical displacement is the result of permanent plastic deformation due to impact loadings, during which a certain amount of kinetic energy of the ball is converted into potential energy stored in the material in the form of plastic deformation, twinning and phase transformation.

Contribution 3: A dislocation density based viscoplastic constitutive model coupled with GTN damage, was first proposed to investigate the damaging process during SMAT for TWIP steels. Then numerical simulation of a single impact was performed using this coupled damage model to study the SMAT process. Finally, the capacity of this model was demonstrated by an application in the case of a 316L TWIP steel. The obtained results allow for predicting the induced residual stress, plastic strain, and damage fields. The results show that as the impact velocity increases, the damage value and the impact area increase because the damage development is considered to be entirely based on the effective plastic strain. The increase in impact velocity increases the equivalent plastic strain rate in the SMAT

process and the final equivalent plastic strain obtained after SMAT. Also, the results show that the depth affected by a single impact can reach 0.15 mm, while the maximum value of the void volume fraction is located at a distance of 0.1 mm from the impact surface. We can thus propose to remove such a depth to optimize the benefits of SMAT process.

Contribution 4: A dislocation density-based visco-elastoplastic model considering the influence of dislocation density, twinning, grain size, and strain rate was first successfully developed considering the effects of grain size, twinning and dislocation density, and strain rate based on the experimental results. Then the model was implemented in a subroutine of ABAQUS Explicit to perform a 3D simulation of the nanoindentation test at different depths with different strain rates. Lastly, the elastoplastic response of the SMAT treated material is calculated by using the mixing rule, and the calculated results show a good agreement with the experimental results. The results show also that the fraction of load sharing of the SMAT affected layers is relatively higher in comparison to the volume fraction of the SMAT affected layers as the flow stress of the SMAT affected layers is much higher.

7.2 Prospects

The models used in this work are, of course, incomplete and can be further improved. Extensive material characterization processes can be performed, including fatigue testing, up to higher strain rates, to assess cyclic behavior and strain rate sensitivity. High-temperature testing will also be useful considering the possible influence of the temperature increase during repeated impacts, whether it is in terms of thermal expansion or mechanical properties. The experimental data can then be used to select and construct appropriate material constitutive models and determine the material parameters of different materials. The microstructure is another important aspect. The development of crystal plasticity models (including cycling, high strain rate, and thermal behavior) will lead to a more physical understanding. The effect of grain size and crystal texture of the final material state can also be studied. In addition, single impact tests with different angles can be performed on single crystals with different crystallographic orientations to study the deformation mechanisms with SEM, EBSD, and TEM.

It could be very interesting to obtain uniform SMAT depth for complex geometries and optimize thermal parameters during SMAT, e.g., the temperature can affect the residual stresses through two different physical processes including heat production due to plastic strain and the thermal diffusion [10]. Existing research on SMAT hardening optimization only studies plain specimens, and few articles study complex geometries, such as those with curvature and edges. Since a ball can interact with another ball and the chamber during the SMAT process, it will impact the surface of the material multiple times. This will have an impact on intensity, coverage, and overall quality of the surface obtained after SMAT. Factors such as the number of balls and energy transfer of these indirect impacts also need to be evaluated in future studies.

In this study, only one impact has been considered. However, the balls used in SMAT perform a multi-directional impact rather than a single one. It is thus hard to predict the evolution of the properties of the material during SMAT with multi-impacts by modeling single impact process. Further study would be carried out considering the influence of the multi-impacts on the predicted results.

We mainly studied the evolution of material properties during the SMAT process in this work. However, it is also important to study the mechanical properties of SMATed materials. To understand the mechanical properties of SMATed materials, the mechanical properties of different mechanical deformation regions should be characterized at different depths (such as nanostructured layers). Since the thickness of the nanostructure layer is very small (depending on the SMAT strength, from a few microns to tens of microns), it is difficult to characterize its local mechanical properties. Nanoindentation technology is widely used for characterization of the small-scale mechanical behavior of materials such as thin films and multiphase materials. However, nanoindentation does not provide the details of the stress-strain of the materials under investigation. This technique can not highlight other important mechanical properties in the material such as the local stress distribution, the stress concentration, yield stress, stress-strain behavior, von-Mises stresses, etc. In order to overcome such inherent limitation, the FEM technique is used to simulate the experimental load-displacement curve (P-h curve) and the stress distributions beneath the nanoindentator. As the accuracy of results depend on the quality and adequacy of the model used, an example is to improve the accuracy of the hardness and elastic modulus, which can be obtained by calculating the contact stiffness through the

power-law approximation of the unloading curve instead of a linear approximation [204]. The accuracy of determining mechanical properties through nanoindentation may be affected for a variety of reasons, for example, insufficient data processing in the model or some specific characteristics or factors are not considered (such as pile-up, surface forces or temperature changes). So in the future work, these factors can be considered in the model to increase the accuracy.

Micro-pillar compression could also be used to study the mechanical properties and understand the deformation mechanism at the local scale. By using this technique, the stress-strain curve can be calculated from the load-displacement curve obtained after the compression test. It also allows access to other information, such as yield stress, which is more direct than nanoindentation technology. In addition, micro-pillar compression technology has not been widely used to study materials processed by SMAT with gradient microstructures [22], [205], [206].

As mentioned in Chapter 3, for mechanical surface treatment techniques such as SMAT, a gradient microstructure in the surface region of a structure can be generated by repeated impacts loadings. During the last decade, increasing research works are focused on experimental characterization and modeling of materials with gradient microstructure generated by various means [207]–[212]. For instance, the strain hardening of a gradient interstitial-free steel was quantitatively investigated using a developed dislocation density-based continuum-plasticity model by Li et al. [207]. In this model, the interaction of the component layers in the gradient structure is described by incorporating geometrically necessary dislocations (GNDs) and back stress. A dislocation density-based model considering the dual role in metal matrix composites (MMCs) was also developed by Dong et al. [208] to describe the factors affecting the strengthening mechanisms in Carbon nanotube (CNT)-reinforced MMCs with different matrix grain sizes. Furthermore, in order to describe the structure-property relation of austenite stainless steel with gradient nanostructure, a theoretical model was proposed by Zhu et al. [212]. However, modeling the gradient microstructure produced by SMAT of the TWIP/TRIP surface is still a difficult task. So in the future, we hope to consider the depth-dependent grain size distribution and nano twin-nano composite structure in our model. EBSD and micro-pillar milled using Focused Ion Beam (FIB) can be used to study the gradient microstructure of materials generated by SMAT. Then, the results (such as the stress-strain curve, the dislocation density of austenite and martensite, and the volume fraction of twin and

martensite) can be used to fit the parameters of the constitutive model at different depths of the gradient microstructure. The constitutive model developed in this work, based on the evolution of dislocation density, should be able to describe the main deformation mechanisms of TWIP/TRIP steel. In addition, the model can be implemented in ABAQUS Explicit subroutines, and numerical simulations can be performed to study the mechanical properties of SMAT processed cylindrical structures with gradient microstructures near the surface area.

RESUME ETENDU EN FRANCAIS

1 In troduction

Le SMAT peut transformer un matériau à gros grains au niveau de sa surface supérieure en un matériau nanostructuré. La fig. 1 montre une microstructure en coupe transversale typique d'un échantillon de titane pur après traitement SMAT pendant 30 min. Globalement, un gradient de microstructure avec une distribution de grains de quelques nanomètres à plusieurs micromètres peut être observée dans la région affectée par le SMAT. On distingue grossièrement trois régions différentes. Ce sont respectivement la couche nanostructurée, la région intérieure non affectée par SMAT et la région de transition entre elles.

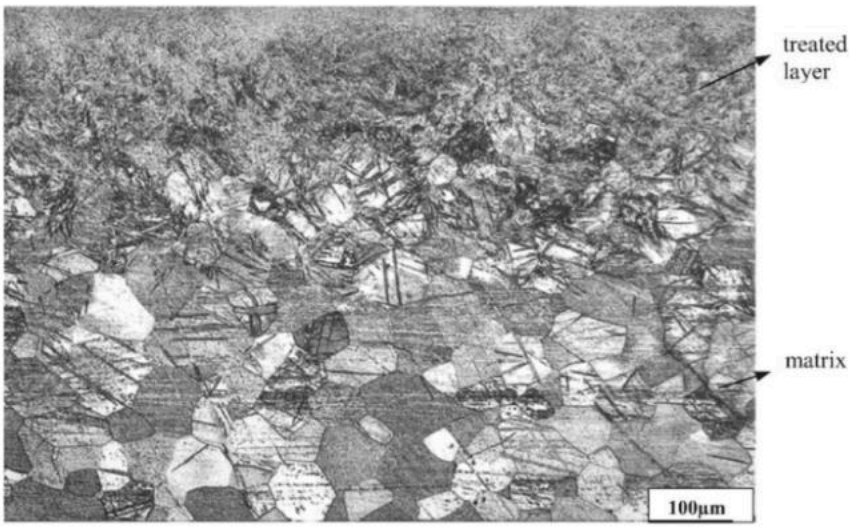

Fig. 1. Micrographie optique d'un échantillon de titane pur SMATé.

En raison de certaines excellentes propriétés mécaniques constatées des matériaux SMATés, il est intéressant d'étudier le processus SMAT à la fois expérimentalement et numériquement pour obtenir une meilleure compréhension et un meilleur contrôle du processus.

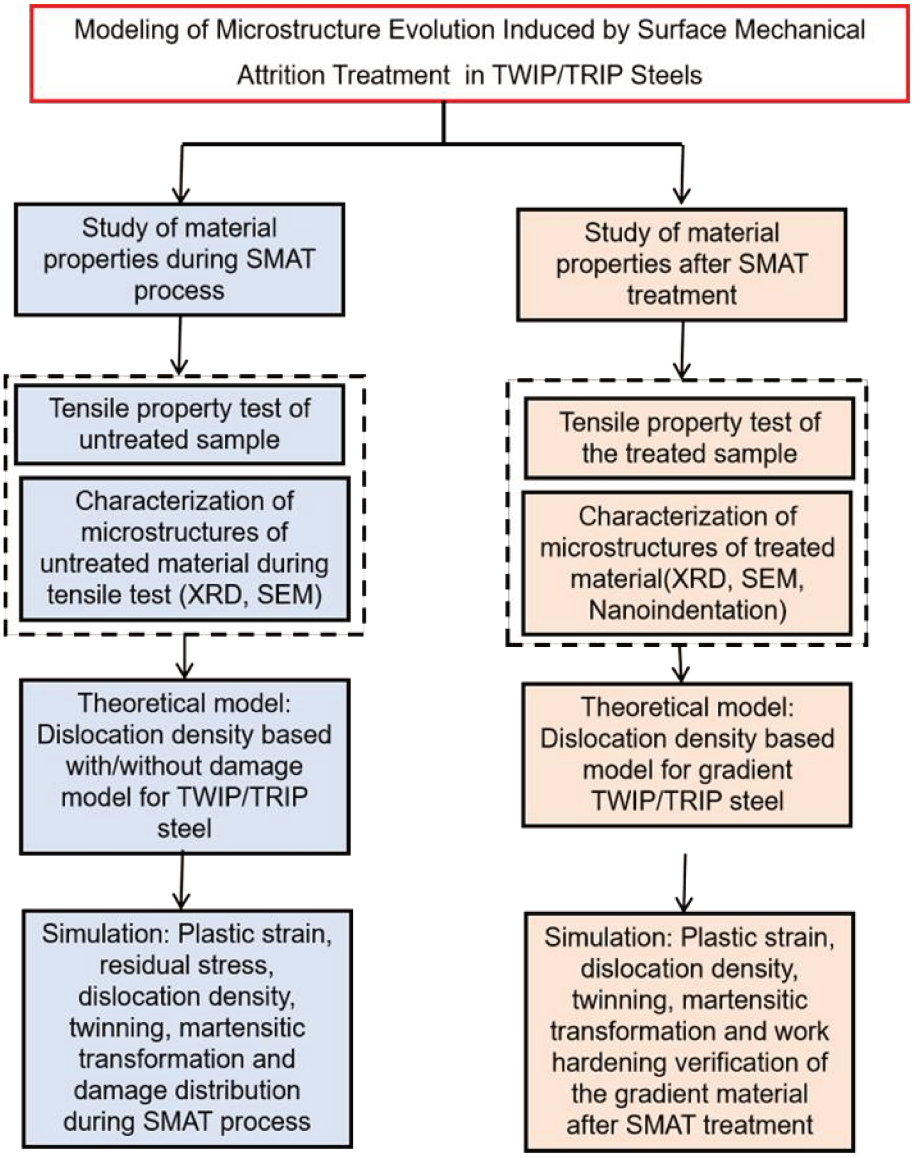

Fig. 2. Organigramme de ce travail.

Les aciers TWIP/TRIP attirent de plus en plus d'attention, en particulier dans les applications structurelles automobiles, en raison de leur capacité d'absorption d'énergie élevée et de leur résistance à la fatigue. Leurs comportements mécaniques en relation avec l'évolution de la microstructure au cours de la déformation ont été largement étudiés, et les mécanismes de déformation de ce type d'aciers, même complexes, ont été bien mis en évidence. Du point de vue métallurgique, les aciers TWIP/TRIP ont une intervalle étroite de l'énergie de fautes d'empilement (de 15 à 22 mJ/m^{-2}), ce qui est essentiel pour assurer la présence de maclage et de transformation martensitique pendant la déformation. Pour ce type de matériaux, au cours du

processus de déformation, le maclage et la transformation martensitique peuvent être induits par la déformation plastique. La présence de macles réduit le libre parcours moyen associé au glissement d'une dislocation. La martensite générée rend l'alliage plus dur et plus solide en raison de sa résistance mécanique supérieure à celle de l'austénite d'origine avant transformation. Par conséquent, il est intéressant d'étudier l'influence simultanée du maclage et de la transformation martensitique sur la résistance mécanique et notamment le phénomène de plasticité de ces matériaux pendant et après le traitement SMAT.

Cette thèse se concentre principalement sur l'étude du processus SMAT à travers la modélisation. La fig.2 montre l'organigramme de ce travail. Le manuscrit est organisé comme suit. Une étude bibliographique est présentée au chapitre 2, qui donne un aperçu du SMAT et du matériau étudié. La configuration du SMAT, les caractéristiques microstructurales et les propriétés des matériaux après SMAT sont introduites. Le mécanisme de raffinement de grains pendant SMAT est notamment étudié.

Le chapitre 3 présente la méthodologie et l'équipement utilisés dans ce travail, qui comprennent la microscopie électronique à balayage (SEM), la diffraction des rayons X (XRD) et la nanoindentation.

Dans le chapitre 4, un modèle de densité de dislocation pour l'acier TWIP/TRIP est développé et mis en œuvre pour étudier l'influence des paramètres de SMAT. Ensuite, un modèle éléments finis (EF) pour une simulation d'un seul impact est établi. La distribution et l'évolution du macle et de la martensite pendant SMAT sont évaluées numériquement.

Le chapitre 5 présente le modèle constitutif développé pour prendre en compte l'endommagement dans la modélisation. La subroutine VUMAT fournie par le code ABAQUS est utilisée. Une fonction d'évolution de l'endommagement pendant la déformation plastique basée sur le modèle de Gurson – Tvergaard – Needleman (GTN) est introduite dans le modèle constitutif de la densité de dislocation et programmée sous forme de subroutine. Dans la subroutine, l'algorithme d'Euler explicite est utilisé pour intégrer l'équation constitutive sur les points d'intégration de chaque élément. Ensuite, un modèle EF complet pour une simulation d'impact est établi. La distribution et l'évolution de macles, de la martensite et de l'endommagement pendant SMAT sont évaluées numériquement.

Au chapitre 6, le comportement micromécanique d'un acier TWIP 316L à microstructure à gradient est étudié par des tests de nanoindentation sur des coupes transversales à différentes distances de la surface traitée. Ensuite, un modèle basé sur la densité de dislocations est adapté en tenant compte des effets de la taille des grains, de la densité de dislocations, du maclage et du taux de déformation à partir des résultats expérimentaux. Le modèle est également implémenté dans une subroutine ABAQUS Explicit pour effectuer une simulation numérique 3D de nanoindentation à différentes profondeurs avec différentes vitesses de déformation pour étudier les propriétés du matériau après SMAT.

Au chapitre 7, un résumé de l'ensemble du travail est proposé et des perspectives sur les recherches futures sont abordées.

2 Étude expérimentale

Le matériau étudié dans ce chapitre est un acier inoxydable 304L fourni par la société Goodfellow. La Tab. 1 montre la composition chimique de cet alliage. La fig. 3 donne les dimensions de l'échantillon pour les essais de traction. L'échantillon a été usiné sous forme d'haltère avec une longueur de 20 mm et un diamètre de 3 mm dans la zone centrale.

Tab. 1. Composition chimique (% en poids) de l'acier 304L étudié.

Fe	C	Cr	Ni	Mn	Mo	Si	S	P	Cu	Co	V
Équilibre	0,003	18,22	6.0	1,6	0,45	0,5	0,005	0,01	0,8	0,1	0,1

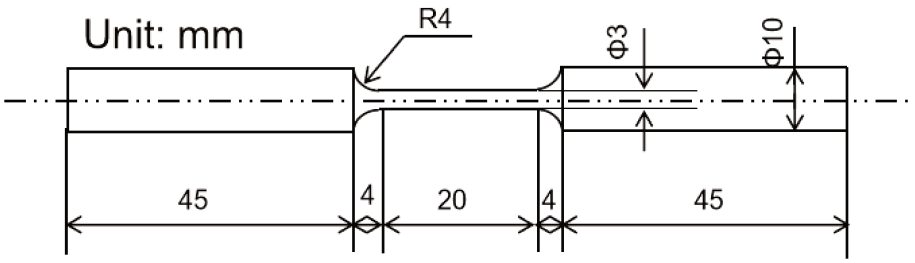

Fig. 3. Les dimensions de l'échantillon d'acier 304L.

2.1 Processus expérimentaux

L'échantillon a été traité par SMAT pour générer un gradient de microstructure dans la région proche de la surface. Le SMAT est basé sur l'impact multidirectionnel de billes sphériques avec la surface de l'échantillon. Comme la résistance mécanique de l'acier 304L n'est pas très élevée, des billes de petit diamètre sont choisies dans ce travail, et le diamètre de billes est de 2 mm. Le SMAT est réalisé grâce à une sonotrode à ultrasons de haute fréquence (20 kHz). Le SMAT est effectué pour couvrir toute la surface utile de l'échantillon. Concernant les conditions du SMAT, les échantillons sont traités par SMAT pendant 15 min à 30% de puissance du générateur, suivi d'un traitement de 5 min à 50% de puissance du générateur, ce qui correspond à une intensité de traitement relativement élevée.

2.2 Techniques de caractérisation des matériaux

Certaines caractéristiques de base, notamment la microstructure et les propriétés mécaniques de base de l'acier 304L, ont été étudiées par la DRX et la nanoindentation.

2.2.1 Diffraction des rayons X

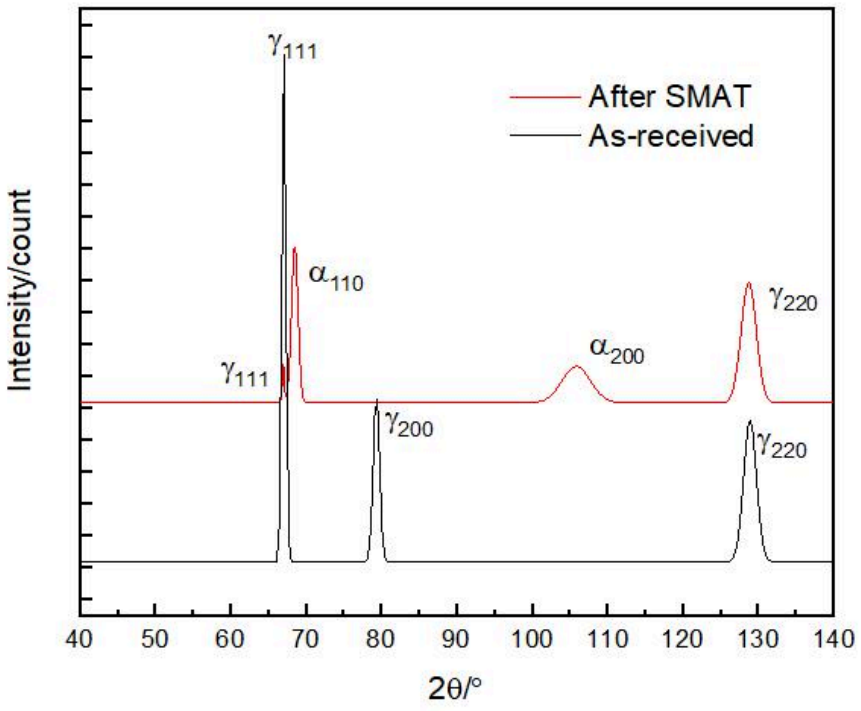

Fig. 4. Diffractogrammes de DRX de l'acier 304L avant et après SMAT.

La fig. 4 montre les diffractogrammes de l'échantillon 304L déformé avant et après SMAT. Le diffractogramme supérieur (rouge) correspond à l'échantillon après SMAT, et celui au-dessous (noir) correspond à l'échantillon avant SMAT, c'est-à-dire à l'état de réception. D'après les résultats montrés sur la fig. 4, il peut être observé qu'il n'y a que de l'austénite dans l'échantillon avant SMAT; tandis que pour l'échantillon après SMAT, il y a une transformation de phase de l'austénite en martensite et la fraction volumique de martensite augmente jusqu'à 78%.

L'analyse par DRX peut distinguer les constituants de la microstructure en fonction de leur structure cristallographique. Les pics de diffraction de l'austénite apparaissent aux positions 2θ différentes de celles de la martensite, ce qui permet de déterminer sélectivement la contrainte dans chacune des phases. La détermination de la contrainte par DRX a été réalisée pour la phase austénitique sur le pic {220} en utilisant un rayonnement X au Cr. La contrainte dans la phase martensitique a été déterminée sur le pic {200} en utilisant le même rayonnement X au Cr. Trois angles $\phi = 0^\circ, 45^\circ$ et 90° et treize angles $\psi = 0^\circ, \pm 23^\circ, \pm 33^\circ, \pm 42^\circ, \pm 50^\circ, \pm 59^\circ$ et $\pm 70^\circ$ ont été utilisés conformément à la norme de mesure des contraintes par rayons X.

La contrainte résiduelle et les incertitudes correspondantes dans différentes directions pour l'austénite et la martensite sont obtenues comme suit:

$$\sigma_{ij}^{\gamma} = \begin{pmatrix} \sigma_{11} & \sigma_{12} & \sigma_{13} \\ \sigma_{21} & \sigma_{22} & \sigma_{23} \\ \sigma_{31} & \sigma_{32} & \sigma_{33} \end{pmatrix} = \begin{pmatrix} -154.2 \pm 9.7 & 93.5 \pm 8.2 & -49.2 \pm 6.6 \\ 93.5 \pm 8.2 & -206.7 \pm 13.4 & 36.1 \pm 3.6 \\ -49.2 \pm 6.6 & 36.1 \pm 3.6 & 0 \end{pmatrix} \quad (1)$$

$$\sigma_{ij}^{\alpha} = \begin{pmatrix} \sigma_{11} & \sigma_{12} & \sigma_{13} \\ \sigma_{21} & \sigma_{22} & \sigma_{23} \\ \sigma_{31} & \sigma_{32} & \sigma_{33} \end{pmatrix} = \begin{pmatrix} 239.1 \pm 10.8 & -88.1 \pm 4.4 & 88.1 \pm 5 \\ -88.1 \pm 4.4 & -70.8 \pm 3.9 & 34.6 \pm 2.7 \\ 88.1 \pm 5 & 34.6 \pm 2.7 & 0 \end{pmatrix} \quad (2)$$

2.2.2 Nanoindentation

Dans cette partie, plusieurs indentations ont été réalisées sous la surface traitée à 8, 16, 30, 60, 120, 250 et 500 μm de profondeur, respectivement. Chaque test de nanoindentation a été exécuté à un rapport constant $\dot{h}/h$, égal à 0,005, 0,05 et 0,5/s, où h est le déplacement maximal dans l'échantillon, qui est de 800 nm. Cinq indentations ont été réalisées pour chaque profondeur avec une distance minimale L = 20 μm entre elles. Pour distinguer facilement chaque indentation, nous attribuons à chaque indentation un numéro, et le nombre se compose de deux parties. La première partie

est la profondeur de l'indentation, et la deuxième partie est la position de l'indentation de haut en bas pour chaque profondeur. Par exemple, la position 8-1 sur la fig. 5a représente l'indentation supérieure opérée à la profondeur de h = 8 µm de la surface traitée. La fig. 5b montre le résultat de l'observation par MEB de la zone d'indentation résiduelle. Comme le montre la fig. 5b, la taille de l'indentation est d'environ 5,5 µm. Les empreintes résiduelles observées montrent que le « pilling up » peut être observable lorsque les profondeurs de contact dépassent 50 nm.

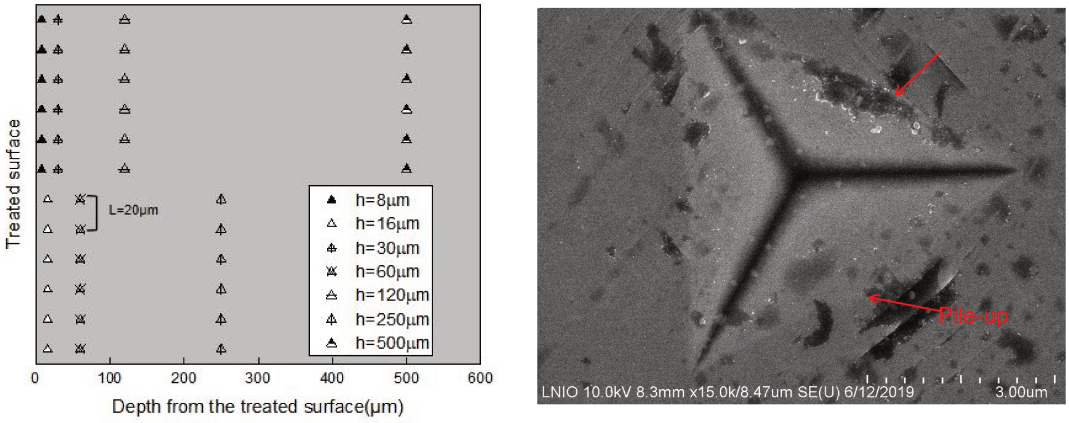

Fig. 5. (a) Illustration de la nanoindentation effectuée sur l'échantillon SMATed avec une vitesse de déformation 0,05/s, (b) Empreinte à 8 µm sous la surface traitée avec une vitesse de déformation 0,05/s. La flèche rouge indique un « pilling up », qui s'est produit pendant la nanoindentation.

Pour étudier l'influence de la taille des grains et de la vitesse de déformation sur la force durant la nanoindentation, la distribution de la force maximale moyenne des courbes charge-déplacement de la nanoindentation à différentes profondeurs avec des taux de déformation différents est montrée sur la fig. 6. Il peut être observé que la charge maximale a augmenté d'environ 20% de la région centrale à la zone nanocristalline avec un taux de déformation de 0,5/s. La charge d'indentation maximale est stabilisée à une profondeur d'environ 300 µm de la surface supérieure, ce qui indique que la profondeur de la région affectée par SMAT est d'au moins 300 µm. Par ailleurs, avec le même taux de déformation, la force maximale augmente avec la profondeur; puis, lorsque la profondeur est d'environ 20 µm, la force maximale atteint sa valeur maximale; puis la force maximale diminue avec l'augmentation de la profondeur dans la région affectée. De la fig.6, on peut voir que la vitesse de déformation a une influence significative sur la force maximale de la nanoindentation.

Lorsque la vitesse de déformation est plus élevée, la force maximale moyenne est également plus grande, c'est-à-dire que lorsque la vitesse de déformation augmente de 0,005/s à 0,5/s, la force maximale moyenne augmente de 10%.

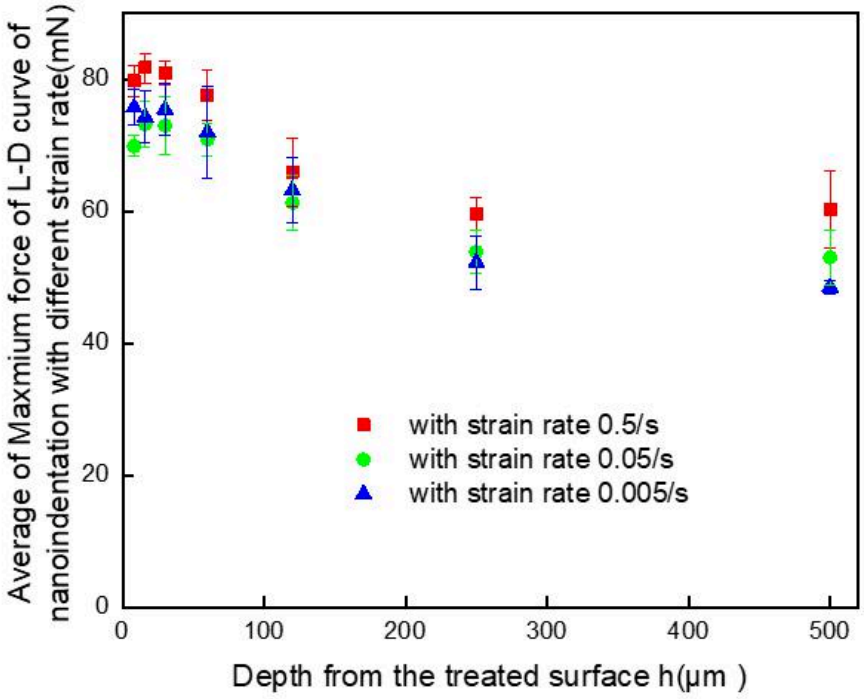

Fig. 6. Force maximale des courbes de charge-déplacement de la nanoindentation à différentes profondeurs avec différentes vitesses de déformation.

Les courbures des courbes de charge par nanoindentation de l'acier 304L sont présentées sur la fig. 7. On peut voir que la courbure est plus élevée dans la région nanocristalline avec une valeur maximale d'environ 124,8 GPa et elle se stabilise à une profondeur d'environ 250 μm en dessous de la surface traitée. Une variation d'environ 40% de la valeur de courbure peut être détectée entre la région nanocristalline et l'intérieur de la région non affectée. Cela est dû au fait que dans notre cas, non seulement l'exposant de durcissement par déformation varie, mais aussi l'effet du raffinement du grain réduit la taille du grain, tandis que la transformation martensitique se produit en raison de l'effet TRIP. Une plus petite taille de grain peut augmenter la limite d'élasticité selon la loi de Hall-Petch, et la transformation martensitique entraîne également une limite d'élasticité plus élevée. En effet, la limite

d'élasticité de la martensite est plus élevée que celle de l'austénite, ce qui peut expliquer la courbe de chargement plus élevée dans notre étude.

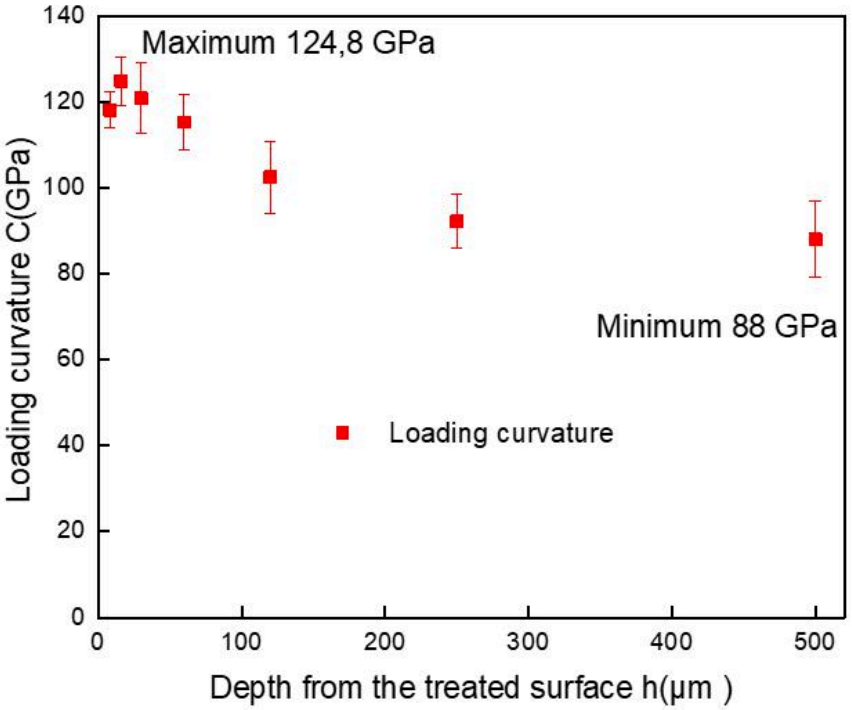

Fig. 7. Variation des courbures pour les courbes de charge par nanoindentation le long de la section transversale de l'acier 304L SMATed avec $\dot{h}/h = 0,05/s$.

3 Modèle basé sur la densité de dislocations sans l'endommagement

L'un des objectifs de ce travail est de modéliser le comportement mécanique des aciers TWIP/TRIP pendant les traitements des matériaux tel que SMAT, qui pourraient simultanément créer un maclage et une transformation martensitique par déformation. Il est important de noter que le processus de déformation pendant le SMAT engendre inévitablement une augmentation de la température du matériau déformé selon la littérature. Cependant, la température à la surface des matériaux est d'environ 50 à 100 ° C. L'augmentation de la température n'étant pas très élevée pour les aciers par rapport à leur température de fusion, l'effet de la température n'est donc pas pris en compte dans ce travail. La vitesse de déformation peut influencer le comportement mécanique, par exemple, en changeant la cinétique de la transformation martensitique. Pendant SMAT, le taux de déformation maximum peut atteindre $10^5/s$ évalué à la fois par des simulations numériques et des expériences. Il

serait donc intéressant de prendre en compte la vitesse de déformation dans le modèle pour décrire plus précisément le processus d'impact. Cependant, selon les résultats présentés dans la littérature, l'effet du taux de déformation n'est significatif que lorsque la déformation plastique accumulée est très élevée.

Par conséquent, pour tenir compte du maclage et de la transformation martensitique, la variation de la déformation totale de cisaillement plastique peut être décrite à l'aide d'une loi de mélange exprimée comme suit:

$$d\gamma = (1 - f_m)[(1 - f_t)d\gamma_a + \gamma_t df_t] + f_m d\gamma_m \tag{3}$$

La déformation de cisaillement plastique totale γ est la combinaison de l'austénite, la martensite et le maclage: γ_a est la contrainte de cisaillement liée au glissement de dislocation dans l'austénite, γ_t est la contrainte de cisaillement pour les macles, γ_m est la contrainte de cisaillement pour la martensite, et f_t , f_m sont respectivement la fraction volumique du maclage et celle de la transformation martensitique. Les indices *a* et *m* font respectivement référence à l'austénite et à la martensite.

La contrainte d'écoulement σ , qui est un scalaire, représente la valeur instantanée de la contrainte nécessaire pour continuer la déformation plastique du matériau. Il peut être calculé à l'aide d'une loi de mélange, en tenant compte de la somme pondérée des apports en austénite et martensite:

$$\sigma = (1 - f_m)\sigma_a + f_m \sigma_m \tag{4}$$

Pour la relation entre la contrainte d'écoulement σ et la densité de dislocation ρ pour l'austénite et la martensite, on suppose qu'elle obéit à la forme classique:

$$\sigma_i = \sigma_{0i} + \alpha_i M G_i b_i \sqrt{\rho_i} \quad i = a, m \tag{5}$$

où σ_0 est la contrainte d'écoulement initiale, α est un paramètre de matériau, M est le facteur Taylor. *G* et *b* sont respectivement le module de cisaillement et le vecteur de Burgers.

L'évolution de la densité de dislocations ρ par rapport à la déformation plastique effective ε peut être exprimée comme suit respectivement pour l'austénite et la martensite :

$$\frac{d\rho_a}{d\varepsilon} = \left(\frac{M - \beta\gamma_t (1 - f_m)(f_{t.\max} - f_t)}{(1 - f_m)(1 - f_t) + k f_m} \right) \left[\frac{1}{b_a} \left(\frac{1}{d_a} + \frac{f_t}{2c_t (1 - f_t)} + K_{p.a} \sqrt{\rho_a} \right) - K_{\alpha.a} \rho_a \right] \tag{6}$$

$$\frac{d\rho_m}{d\varepsilon} = \left(K.\frac{M - \beta\gamma_t(1-f_m)(f_{t.\max} - f_t)}{(1-f_m)(1-f_t) + kf_m} \right) \left[\frac{1}{b_m} \left(\frac{1}{d_m} + K_{p.m}\sqrt{\rho_m} \right) - K_{\alpha.m}\rho_m \right] \quad (7)$$

3.1 Simulation numérique par éléments finis

Pour simuler numériquement un tel processus d'impact, le modèle donné ci-dessus est implémenté dans une subroutine VUMAT du code ABAQUS. Un modèle EF tridimensionnel a été construit avec une forme cylindrique (Fig. 8). Le modèle a un diamètre de 8 mm et est suffisamment grand par rapport à la taille de la bille (2 mm). La hauteur du cylindre est de 1 mm, ce qui est beaucoup plus grande que la profondeur de pénétration atteinte par une charge d'impact (environ 200 μm). Ces dimensions choisies permettent d'éviter les effets de bord liés aux conditions aux limites sur les résultats de la simulation numérique. Le modèle cylindrique est maillé avec des éléments de brique en mode incompatible à huit nœuds (C3D8I).

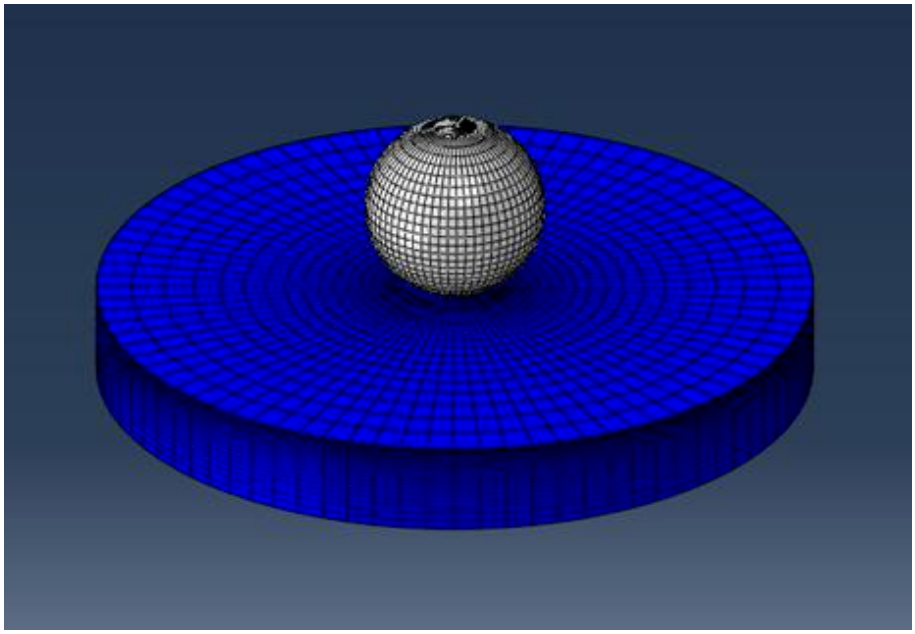

Fig. 8. Vue globale du modèle EF, y compris la bille et le matériau cible (cylindre).

3.2 Résultats et discussion

Les figs. 9a et 9b montrent les fractions volumiques de macles et de la martensite, respectivement, tracées sur un chemin passant par le centre de la région d'impact, pour

différentes vitesses de bille. À l'échelle globale, plus la vitesse d'impact appliquée est élevée, plus la fraction volumique de macles et de la martensite est élevée. On peut voir que lorsque la vitesse est de 3 m/s, la fraction volumique de macles et de la martensite est respectivement de 2,0% et 1,2%, et lorsque la vitesse est augmentée à 5 m/s, la fraction volumique est augmentée à 3,0 % et 4,0%, respectivement. Ces résultats signifient que la vitesse d'impact a un effet significatif sur la génération de macles induits par la déformation et sur la transformation de l'austénite en martensite.

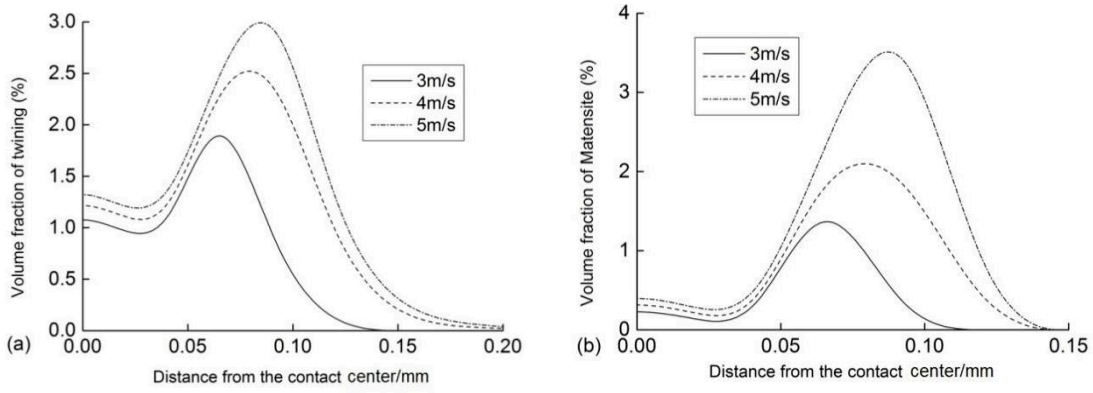

Fig. 9. Evolution de la fraction volumique des macles (a), et évolution de la transformation martensitique (b) obtenue avec différentes vitesses d'impact, tracées le long du chemin passant par le centre de la région d'impact sur la surface cible.

L'impact de la vitesse de la bille est également étudié dans ce travail sur la pénétration. Pour observer cet effet, on fait varier la vitesse d'impact de 3 m/s à 5 m/s. La fig. 10 montre la variation du déplacement vertical résiduel en fonction de la distance du centre de la zone de contact pour différentes vitesses de bille de 3 m/s, 4 m/s et 5 m/s, respectivement. Pour ces trois simulations d'impact, des billes de même diamètre (2 mm) et de même angle d'incidence ($\theta = 90$ °) ont été utilisées. Comme on peut le voir sur la fig. 10, le déplacement vertical maximal augmente avec l'augmentation de la vitesse de bille. Lorsque la vitesse d'impact passe de 3 m/s à 5 m/s, le déplacement passe de 4,2 mm à 7 mm. Le déplacement vertical résiduel est le résultat d'une déformation plastique permanente due aux chargements d'impact. Pendant les impacts, une certaine quantité d'énergie cinétique de la bille est convertie en énergie potentielle stockée dans le matériau sous forme de déformation plastique, de maclage et de transformation de phase. À une vitesse d'impact de 5 m/s, l'énergie cinétique de la bille est beaucoup plus élevée que celle pour une vitesse de 3 m/s,

donc plus d'énergie cinétique est convertie en énergie potentielle stockée dans le matériau.

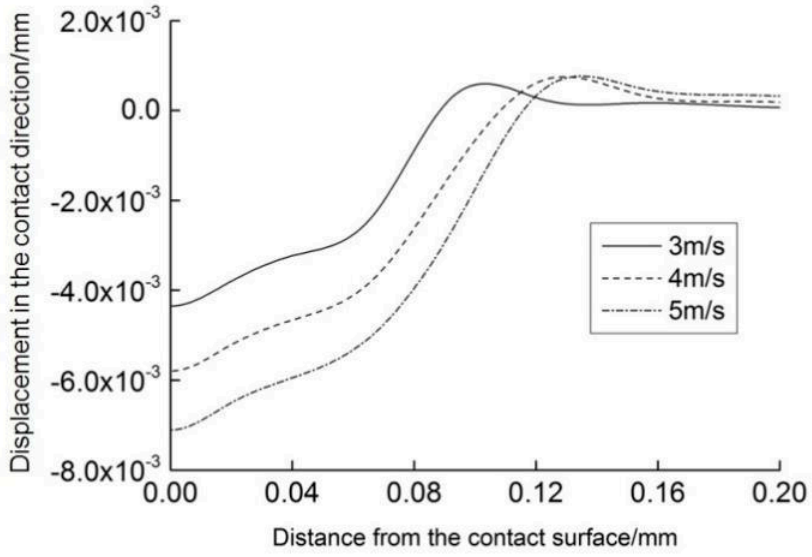

Fig. 10. Le déplacement des points sur la surface de contact obtenus pour différentes vitesses d'impact tracé en fonction de la distance du centre.

4 Modèle basé sur la densité de dislocations avec l'endommagement

Chen et al. (Chen et al., 2019) ont proposé un modèle basé sur la densité de dislocation pour décrire les propriétés de l'acier TWIP/TRIP. Le modèle peut prédire l'évolution des fractions volumiques de maclage et de transformation martensitique, ainsi que le comportement mécanique macroscopique. Dans ce chapitre, un modèle viscoplastique basé sur la densité de dislocation est proposé en considérant l'influence de la vitesse de déformation et l'endommagement.

Dans ce modèle, la contrainte d'écoulement σ_y est lié au paramètre directeur dans une équation cinétique définie par une loi de puissance:

$$\frac{\sigma_y}{\sigma_{ref}} = \left(\frac{\dot{\bar{\varepsilon}}^{vp}}{\dot{\varepsilon}_0} \right)^{1/m} \tag{8}$$

Pour prendre en compte la contribution du maclage, la variation de la déformation totale de cisaillement plastique peut être calculée à l'aide d'une loi de mélange exprimée comme suit:

$$d\gamma^{vp} = (1 - f_t) d\gamma_g^{vp} + \gamma_t df_t \tag{9}$$

La résistance mécanique à l'écoulement, σ_{ref} , des aciers TWIP est déterminée par les informations sur la microstructure, qui se compose de deux parties:

$$\sigma_{ref} = \sigma_0 + \sigma_f \tag{10}$$

La relation entre la densité de dislocation ρ et la déformation de cisaillement par dislocation γ peut s'écrire:

$$\frac{d\rho}{d\varepsilon^{\mathrm{vp}}} = \left(\frac{M - \beta\gamma_t \left(f_{t.\max} - f_t \right)}{1 - f_t} \right) \left(\frac{1}{b} \left(\frac{1}{d} + \frac{f_t}{2e(1 - f_t)} \right) + k_1 \sqrt{\rho} - k_2 \rho \right) \tag{11}$$

Une théorie de la plasticité développée par Gurson (Gurson, 1976) peut prendre en compte la dégradation de la capacité de supporter une charge par la présence de porosité dans les matériaux isotropes. La principale différence entre le modèle de Gurson et la plasticité classique est que la surface élastique dans le premier présente une dépendance aux contraintes hydrostatiques. Le modèle de dommages GTN peut être décrit par la relation suivante:

$$\Phi = \left(\frac{\sigma_e}{\sigma_y} \right)^2 + 2q_1 f^* Cosh\left(-\frac{3}{2} \frac{q_2 \sigma_m}{\sigma_y} \right) - (1 + q_3 f^{*2}) = 0 \tag{12}$$

Les paramètres impliqués dans cette équation sont définis comme suit: f^* est la fraction volumique de porosité dans le matériau, σ_y fait référence à la limite d'élasticité du matériau. σ_e est la contrainte équivalente macroscopique de von Mises, σ_m est la contrainte moyenne macroscopique, et q_1 , q_2 , q_3 sont des paramètres constitutifs introduits par Tvergaard pour amplifier l'effet de contrainte hydrostatique pour tous les niveaux de déformation afin de prédire plus précisément la déformation jusqu'à la rupture. Tvergaard a constaté que l'ensemble $q_1 = 1.5$, $q_2 = 1$, et $q_3 = 2.25$ est valable pour prédire les ruptures, en particulier pour l'acier 316L. Le modèle de Gurson décrit les matériaux jusqu'à la rupture comme une augmentation de la fraction de volume de vide jusqu'à un seuil critique. Tvergaard et Needleman (Needleman and Tvergaard, 1984) ont modifié la fraction de volume de vide effectif f , comme le montre l'équation suivante:

$$f^* = \begin{cases} f & \text{if} \quad f \le f_c \\ f_c + \dfrac{f_F - f_c}{f_f - f_c}(f - f_c) & \text{if} \quad f_c \le f \le f_f \\ f_F & \text{if} \quad f_f \le f \end{cases} \tag{13}$$

Dans les équations ci-dessus, f_c est une valeur critique de la fraction volumique de vide et f_f est la valeur de la fraction volumique de vide à laquelle il y a une perte complète de la capacité de supporter une charge dans le matériau, c'est-à-dire que le matériau est rompu. Noter que la valeur ultime, $f^* = f_F$, à laquelle la contrainte macroscopique de la capacité de supporter une charge disparaît, est donnée par $f_F = \dfrac{1}{q_1}$.

4.1 Simulation numérique par éléments finis

Un modèle EF tridimensionnel a été construit en utilisant le code ABAQUS Explicit pour étudier le processus d'impact et l'évolution de l'endommagement sous l'effet d'un seul impact. Le modèle présenté ci-dessus est implémenté dans une subroutine VUMAT via l'algorithme d'Euler. Certains détails de ce modèle EF sont illustrés à la fig. 11. Une bille d'acier d'un diamètre de 1,0 mm a été considérée pour impacter la surface avec un angle d'impact de 90°, c'est-à-dire que la direction de chargement est perpendiculaire à la surface impactée. Comme le montre la fig. 11, la cible est un cylindre d'un diamètre de d = 2 mm et d'une hauteur de 0,5 mm. Cette valeur de hauteur est suffisamment grande pour éviter les effets des conditions aux limites sur les résultats des simulations.

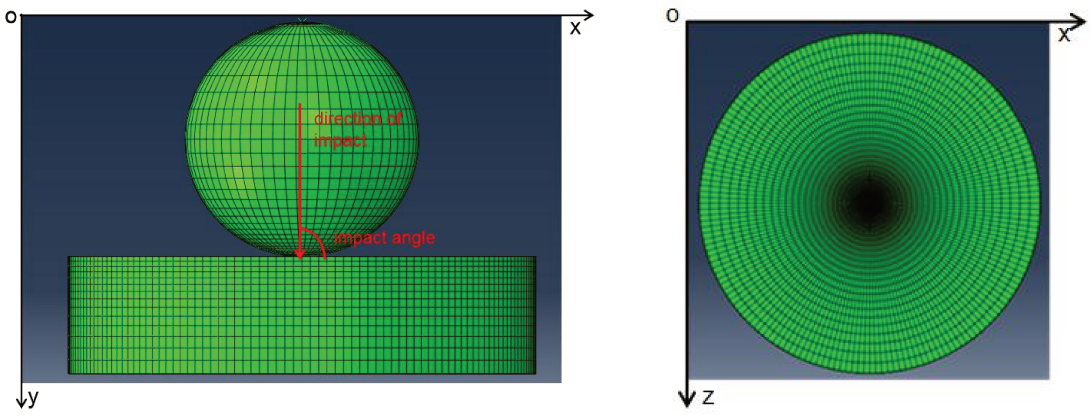

(a) (b)

Fig. 11. Modèle par éléments finis: (a) vue latérale du modèle montrant la cible cylindrique et la bille rigide (b) vue de dessus montrant des éléments plus raffinés dans la zone d'impact de la cible.

4.2 Résultats et discussion

La fig. 12 montre la distribution de différents paramètres après un seul impact avec une vitesse de 4 m/s. La contrainte résiduelle, la déformation plastique équivalente, la densité de dislocations, la fraction volumique de macles et l'endommagement induit par un seul impact sont présentés sur la surface cible impactée. En raison de l'apparition de l'endommagement, la résistance du matériau endommagé sera inférieure à la résistance du matériau sans dommage, en particulier lorsque la déformation plastique du matériau pendant la déformation est relativement importante. En raison de la réduction de la résistance, il est plus facile pour le matériau de développer de la déformation plastique avec endommagement pendant le processus SMAT. Comme les paramètres tels que la densité de dislocations, la fraction volumique de macle, etc. sont des fonctions de la déformation plastique, par rapport au matériau sans endommagement, leurs valeurs changeront également en conséquence avec des règles de distribution fondamentalement similaires. On peut voir que tous ces paramètres ont une distribution globale très similaire sur la surface supérieure, comme la distribution des paramètres sans endommagement observé dans le chapitre 4. Pour la distribution de la densité de dislocations, la fraction volumique de macles et de la martensite du modèle développé au chapitre 4 sans endommagement comparé à celui avec endommagement dans le chapitre 5, on obtient des grandeurs similaires presque au même endroit, notamment là où la déformation plastique équivalente est la plus grande. Dans les deux modèles, la distribution de la contrainte résiduelle équivalente maximale de von Mises dépend fortement de la déformation plastique équivalente stockée dans le matériau après un impact. La déformation plastique équivalente est directement liée à l'évolution de la microstructure. On peut voir que globalement tous ces paramètres ont une distribution très similaire sur la surface impactée. Selon la fig. 12a, la contrainte résiduelle équivalente maximale atteint 635 MPa après un seul impact. La déformation plastique équivalente stockée est également observée après un seul impact, comme le montre la fig. 12b. Comme le développement des dislocations et l'augmentation de la fraction volumique des macles sont tous deux liés à la déformation plastique et au taux de déformation, la fraction volumique maximale de macles est située presque au même

endroit où la déformation plastique est maximale. Comme observé sur la fig. 12c, la densité de dislocations de la phase austénitique est augmentée d'environ trois ordres de grandeur après un seul impact de $1*10^{11}$ à $1.26*10^{14}\ m^{-2}$. La fig. 12d révèle que la fraction volumique de macles est augmentée jusqu'à 2,6% sous l'effet d'un seul impact, par rapport à l'état initial avant cet impact. La fig. 12e montre la contrainte résiduelle obtenue, qui se répartit symétriquement par rapport à la ligne médiane du modèle. La contrainte résiduelle de compression maximale est de 635 MPa et située à une profondeur d'environ 0,15 mm de la surface impactée.

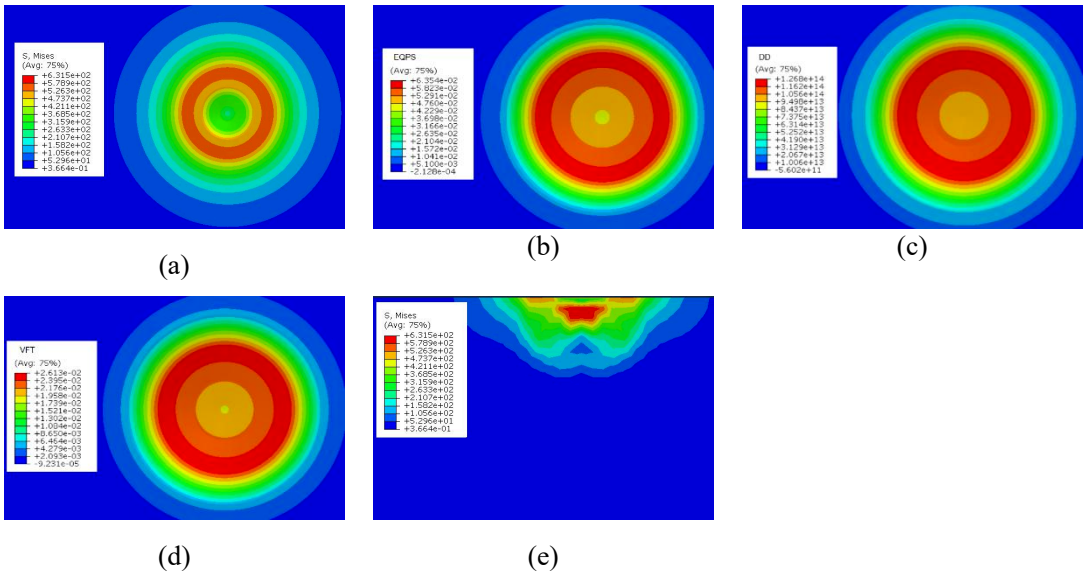

Fig. 12. Distribution de (a) contrainte résiduelle équivalente (EQRS) (MPa), (b) déformation plastique équivalente (EQPS), (c) densité de dislocations (DD) (m^{-2}), et (d) fraction volumique de macle (VFT) sur la surface cible traitée et (e) contrainte résiduelle équivalente (EQRS) (MPa) en profondeur obtenue après un seul impact avec une vitesse d'impact de 4 m/s.

La fig. 13 montre la variation du déplacement vertical résiduel en fonction de la distance du centre de la zone de contact, après un impact de bille avec différentes vitesses de bille de 2 m/s, 3 m/s et 4 m/s, respectivement. Pour ces trois simulations, un même diamètre de bille (2 mm) et un même angle d'incidence ($\theta = 90°$) ont été utilisés. Sur la fig. 13, on peut voir que le déplacement vertical maximal est augmenté avec l'augmentation de la vitesse de la bille. Le déplacement passe de 16 µm à 32 µm pour une vitesse d'impact augmentée de 2 m/s à 4 m/s. En effet, le déplacement vertical résiduel est la conséquence d'une déformation plastique permanente générée par le chargement d'impact. Lors d'un tel impact, une certaine quantité d'énergie

cinétique de la bille a été transformée en énergie potentielle stockée dans le matériau sous forme de déformation plastique, de maclage, etc. Dans le cas d'une vitesse d'impact de 4 m/s, l'énergie cinétique de la bille est beaucoup plus élevée que celle de 2 m/s, et par conséquent plus d'énergie cinétique a été transformée en énergie potentielle stockée dans le matériau. Considérant les concepts de base des différentes méthodes de grenaillage, la rugosité de surface obtenue est due à la nature aléatoire de l'impact des billes métalliques. Comme le grenaillage, la rugosité obtenue après SMAT, liée au déplacement vertical, est importante. En effet, l'impact des billes métalliques peut conduire à un retrait plus profond et plus large pour le SMAT. Comme on peut le voir sur la fig. 13, après la récupération de la déformation élastique d'un matériau après SMAT, les empreintes restantes obtenues avec des vitesses différentes ont presque la même largeur, tandis que leurs profondeurs sont différentes. Par conséquent, on peut conclure que l'augmentation de la vitesse d'impact peut augmenter la concentration de déformation et par conséquent le niveau de contrainte résiduelle pour les matériaux SMATé.

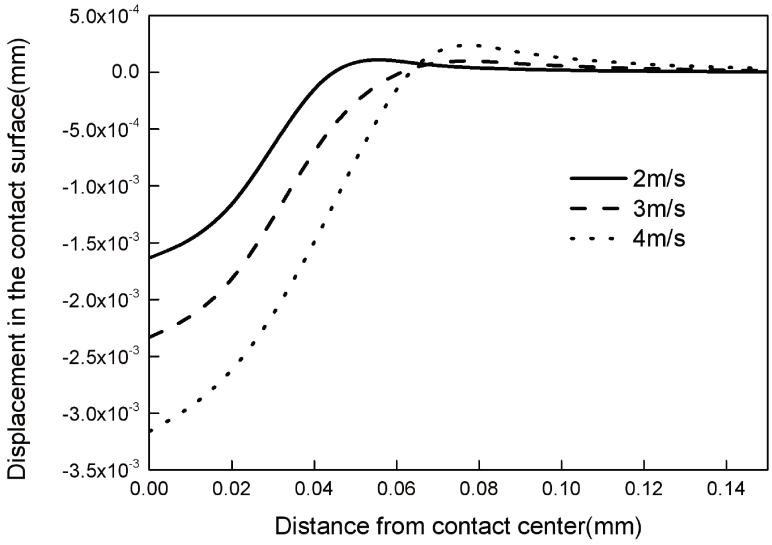

Fig. 13. Variation du déplacement résiduel après un seul impact pour les points de la surface de contact en fonction de la distance au centre, obtenue avec différentes vitesses d'impact dans le plan $\left(o,\vec{x},\vec{y}\right)$.

Cependant, une attention particulière doit être portée à la présence de l'endommagement induit par le sur-traitement lorsque l'intensité du traitement est trop

élevée. Comme pour l'énergie de la rupture des verres métalliques, la déformation élastique sera arrêtée lorsque l'énergie développée est égale à l'énergie de rupture par cisaillement ou à l'énergie de dilatation critique. Pour les matériaux ductiles, l'énergie d'entrée peut également être liée au travail de cisaillement et de dilatation. Le travail de cisaillement peut induire un glissement des dislocations provoquant la déformation plastique, tandis que le travail de dilatation est induit par la contrainte hydrostatique, qui ne peut pas provoquer de déformation plastique. Une fois que le travail de dilatation atteint la valeur critique, une fracture se produit, ce qui constitue une motivation de ce travail pour étudier le processus d'endommagement dû à un seul impact.

5 Modélisation du gradient induit par SMAT dans le matériau

Selon les travaux d'Estrin (Estrin and Mecking, 1984) et nos précédents travaux , la contrainte d'écoulement σ_y est lié au paramètre directeur dans une équation cinétique définie par une loi de puissance:

$$\frac{\sigma_y}{\sigma_{ref}} = \left(\frac{\dot{\bar{\varepsilon}}^{vp}}{\dot{\varepsilon}_0} \right)^{1/m} \tag{14}$$

où σ_{ref} est la contrainte d'écoulement de référence, $\dot{\varepsilon}_0$ est la vitesse de déformation de référence, et m est la sensibilité à la vitesse de déformation.

Pour prendre en compte la contribution du jumelage, la variation de la déformation totale de cisaillement plastique γ^p peut être décrit en utilisant une règle de mélange exprimée comme suit:

$$d\gamma^p = (1 - f_t) d\gamma_g^p + \gamma_t df_t \tag{15}$$

où γ_g^p est une contrainte de cisaillement plastique par glissement de dislocation, γ_t est la contrainte de cisaillement plastique de jumelage, f_t est la fraction volumique du jumelage.

La mesure de la résistance mécanique à l'écoulement, σ_{ref} , de l'acier TWIP est supposé contenir les informations sur la microstructure, qui se compose de trois parties:

$$\sigma_{ref} = \sigma_0 + \sigma_f + \sigma_{GB} \tag{16}$$

où σ_0 est la contrainte de frottement due à une solution solide, σ_f est liée au durcissement isotrope induit par les dislocations forestières, et σ_{GB} est la contrainte arrière liée à l'écrouissage cinématique. σ_f peut être exprimée par la relation de Taylor comme:

$$\sigma_f = \alpha M G b \sqrt{\rho} \tag{17}$$

où α est une constante matérielle, M est le facteur Taylor. G, b et ρ sont respectivement le module de cisaillement, le vecteur de Burgers et la densité de dislocation. σ_{GB} est défini comme:

$$\sigma_{GB} = \frac{K_{HP}}{\sqrt{d}} \tag{18}$$

où K_{HP} est la constante de Hall-Petch et d indique la taille des grains.

La relation entre la densité de dislocation ρ et la contrainte de cisaillement plastique par dislocation γ_g^p peut être exprimée comme suit:

$$\frac{d\rho}{d\gamma_g^p} = \left(\frac{M - \beta\gamma_t \left(f_{t.\max} - f_t \right)}{1 - f_t} \right) \left(\frac{1}{b} \left(\frac{1}{d} + \frac{f_t}{2e(1 - f_t)} \right) + k_1 \sqrt{\rho} - k_{20} \left(\frac{\dot{\bar{\varepsilon}}^{vp}}{\dot{\varepsilon}_0} \right)^{1/n} \rho \right) \tag{19}$$

5.1 Simulation numérique par éléments finis

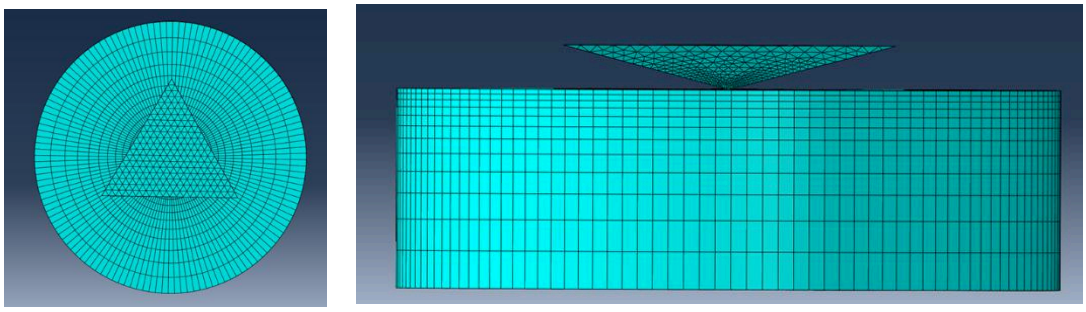

(a) (b)

Fig. 14. Modèle par éléments finis: (a) vue de dessus du modèle montrant la cible et l'indenteur rigide, (b) vue latérale montrant le maillage dans la zone d'indentation de la cible.

Dans ce travail, quatre indentations à une distance spécifique sous la surface SMATé: 3, 70, 300 et 600 µm, ont été réalisées en utilisant la mesure de rigidité

continue avec le module élastique calculé en utilisant la méthode d'Oliver et Pharr. Un modèle tridimensionnel pour la nanoindentation a été construit, comme le montre la fig. 14. L'indenteur de Berkovich a été défini comme un solide rigide. En revanche, le corps a été établi comme une pièce déformable constituée d'éléments briques en mode incompatible à huit nœuds (C3D8I), où le maillage est plus fin autour de la zone de contact et progressivement plus grand loin de la nanoindentation. Le diamètre de l'échantillon est de 10 mm, avec une profondeur de 5 mm. Le coefficient de frottement entre le pénétrateur et l'acier 316L TWIP est fixé à 0,2, ce qui est typique pour l'analyse de nanoindentation. Pour la nanoindentation avec une valeur constante de $\dot{h}/h$, comme le montre la fig. 14a, le modèle par éléments finis est réalisé en utilisant le mode de commande en déplacement. Le paramètre indépendant dans la modélisation par éléments finis est le taux de chargement, réglé sur la même valeur que la mesure d'indentation. Pour les paramètres d'entrée, un module d'Young de 200 GPa et un coefficient de Poisson de 0,3 sont utilisés. Quant aux conditions aux limites, seul le bas de la pièce est encastré pour bloquer tous les mouvements.

5.2 Résultats des simulations

Comme le montre la Fig. 15, les courbes expérimentales charge-déplacement sont comparées aux résultats de la modélisation, à différentes profondeurs de 3, 70, 300 et 600 μm, avec une vitesse de déformation $\dot{h}/h = 0,05/s$ où h est le déplacement de l'indenteur. Comme le SMAT génère une nanostructure, la force maximale de la courbe force-déplacement de la nanoindentation sera plus élevée si elle est plus proche de la surface traitée (en effet plus la profondeur de la surface traitée est petite, plus la taille des grains est petite). La force maximale à la surface supérieure est deux fois plus grande que celle dans la zone non affectée par SMAT. Il peut être observé que les résultats expérimentaux et les résultats de prédiction par EF ont une bonne cohérence dans les étapes de chargement initial et final à différentes profondeurs au cours du processus de chargement. Cependant, les valeurs prévues au stade intermédiaire de chargement sont inférieures aux valeurs expérimentales, mais la différence n'est pas très significative. On peut donc conclure que le modèle peut relativement bien prédire le processus de chargement.

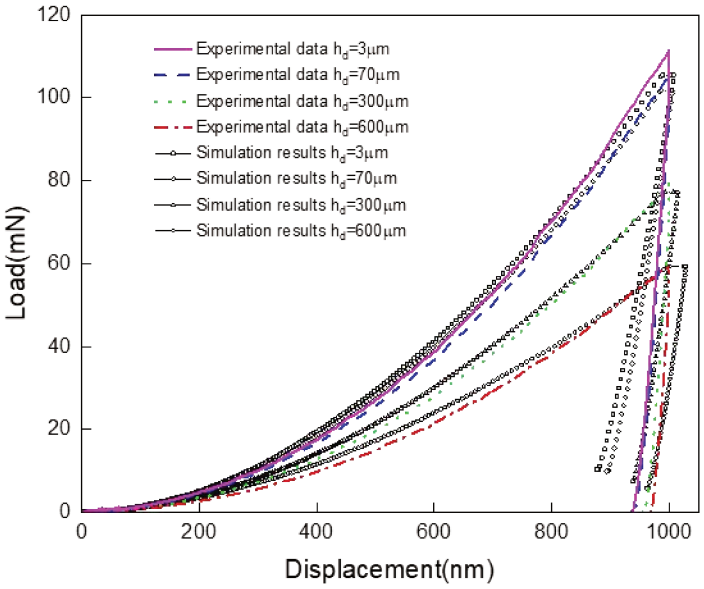

(a)

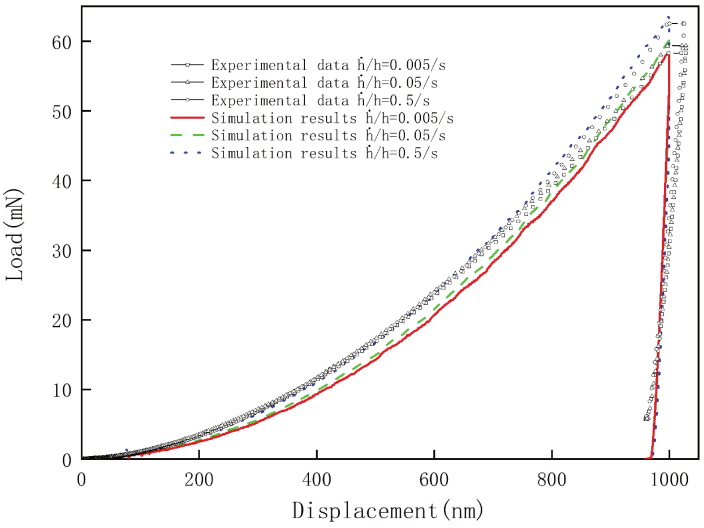

(b)

Fig. 15. Comparaisons des courbes de charge expérimentales avec les résultats de la modélisation par EF à différentes profondeurs 3, 70, 300 et 600 μm avec une vitesse de déformation ḣ/h = 0,05/s (a). et avec différents taux de déformation ḣ/h = 0,005, 0,05 et 0,5/s à la profondeur 600 μm (b).

5.3 Comportement mécanique du matériau traité par SMAT

L'acier 316L SMATé peut être considéré comme une structure à gradient composée de différentes couches avec des microstructures et des propriétés

mécaniques différentes. On distingue approximativement quatre régions différentes. Ce sont respectivement la couche de durcissement superficiel, la couche de durcissement inférieure, la région intérieure non affectée par SMAT et la région de transition entre les deux dernières.

En suivant la règle de mélange, le comportement global de déformation visco-élastoplastique des matériaux nanostructurés à gradient peut être exprimé:

$$\sigma_y^t = \sum_{i=1}^{N} f_i \sigma_y^i \tag{20}$$

où σ_y^t est la contrainte d'écoulement moyenne du matériau à gradient, N est le nombre de couches, σ_y^i est la contrainte d'écoulement de la ième couche. fi est la fraction volumique de la ième couche qui peut être calculée en divisant l'aire de la ième couche par la totalité de la section transversale du matériau dégradé, comme indiqué dans la Tab. 2.

Tab. 2. La fraction volumique de la ième couche.

La couche	La couche de durcissement de surface	Couche de durcissement souterraine	La région de transition	La région intérieure non touchée par le SMAT
F_{je} (%)	0,33	15,64	14,58	69,44

Quatre courbes contrainte-déformation calculées par le modèle de densité de dislocations sont représentées sur la fig. 16, qui correspondent aux quatre couches distinctes. Comme le montre la fig. 17, en utilisant les quatre relations contrainte-déformation calculées, la relation contrainte-déformation de l'acier 316L SMATé a été calculée en moyennant les 4 contributions. La fig. 17 montre également la relation contrainte-déformation expérimentale du matériau traité. On peut voir que la résistance du matériau SMATé est améliorée, bien que l'épaisseur de la couche de renforcement soit beaucoup plus petite que le substrat non traité à cœur.

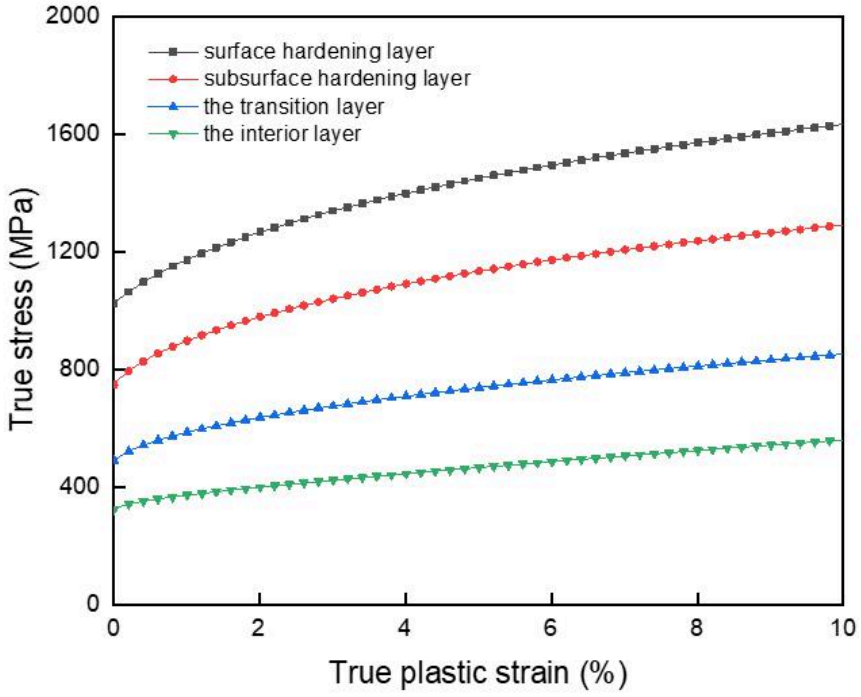

Fig. 16. Courbes contrainte-déformation pour différentes couches.

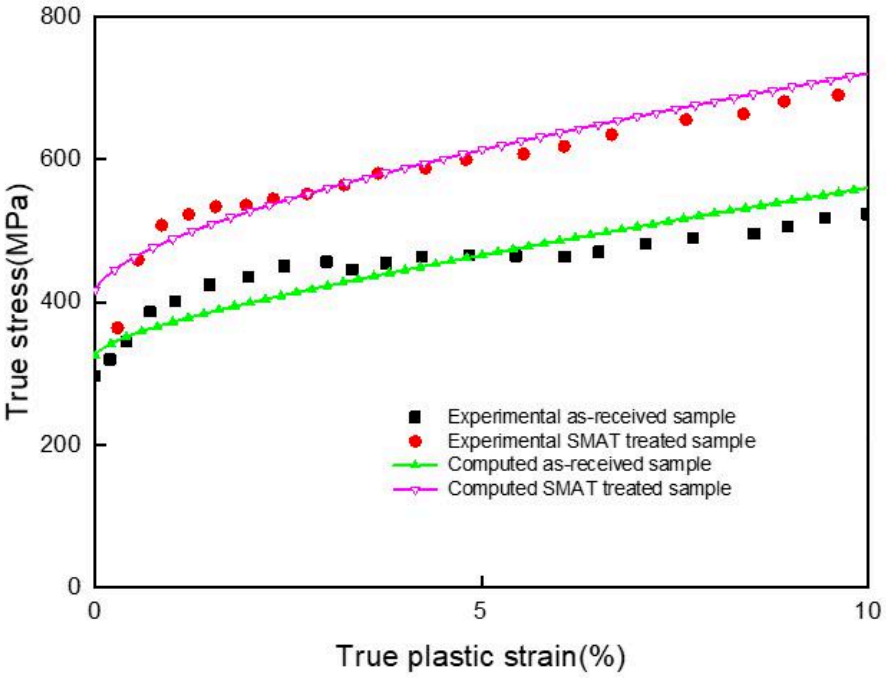

Fig. 17. Courbes contrainte-déformation calculées et expérimentales.

6 Contributions et perspectives

6.1 Contributions majeures

Cette thèse s'est centrée sur l'étude des effets de SMAT sur l'acier TWIP/TRIP avec des méthodes expérimentales, numériques et analytiques. L'influence de SMAT sur la microstructure de l'acier 304L TWIP/TRIP a d'abord été étudiée expérimentalement en utilisant les techniques SEM, XRD et de nanoindentation. Basé sur les résultats expérimentaux, un modèle de densité de dislocations de l'acier TWIP/TRIP a été développé pour étudier les caractéristiques des impacts pendant le SMAT. Avec le modèle EF, la distribution de la taille des grains, la fraction volumique de macle et de martensite, et la densité de dislocations de l'austénite et de la martensite en fonction des paramètres d'impact ont été simulées numériquement. Pour étudier l'évolution de l'endommagement au cours du processus SMAT, l'endommagement a été introduit dans le modèle de densité de dislocations. Enfin, un modèle élastoviscoplastique basé sur la densité de dislocations prenant en compte l'effet de la taille des grains, de la densité de dislocations, du maclage et du taux de déformation a été proposé pour mieux comprendre les impacts du SMAT sur le comportement mécanique de l'acier 316L TWIP avec un gradient de microstructure. De manière générale, les résultats de cette étude ont conduit aux nombreuses découvertes intéressantes qui peuvent aider à mieux comprendre l'effet du SMAT sur les matériaux.

Contribution 1: Les conditions SMAT pour l'acier 304L et la procédure de préparation des échantillons ont été choisies pour étudier les propriétés du matériau pendant le SMAT. La fraction volumique résiduelle d'austénite et la distribution des contraintes résiduelles à la surface supérieure ont été étudiées par DRX. Les résultats obtenus ont été interprétés ultérieurement en termes de changements induits par SMAT le long de la section transversale de l'échantillon SMATé. Les résultats montrent que la taille des grains, la transformation de phase et la vitesse de déformation ont une influence significative sur les propriétés mécaniques observées par nanoindentation.

Contribution 2: Un modèle basé sur la densité de dislocations prenant en compte la fraction volumique de macles et de martensite liée à la déformation plastique équivalente a d'abord été proposé pour étudier le comportement mécanique de l'acier

TWIP/TRIP. Ensuite, une simulation numérique d'un seul impact a été réalisée en utilisant le modèle basé sur la densité de dislocations pour étudier le processus SMAT de base. Enfin, la contrainte résiduelle équivalente, la déformation plastique équivalente, la densité de dislocations dans les phases d'austénite et de martensite, et la fraction volumique de macles et de martensite après un seul impact ont été analysées.

Contribution 3: Un modèle constitutif viscoplastique basé sur la densité de dislocation couplé à un modèle d'endommagement GTN, a été proposé pour la première fois pour étudier le processus d'endommagement pendant le SMAT pour les aciers TWIP. Ensuite, une simulation numérique d'un seul impact a été réalisée à l'aide de ce modèle d'endommagement couplé pour étudier le processus SMAT. Enfin, la capacité de ce modèle a été démontrée par une application dans le cas d'un acier TWIP 316L. Les résultats obtenus permettent de prédire la contrainte résiduelle induite, la déformation plastique et le champ d'endommagement. Les résultats montrent qu'avec l'augmentation de la vitesse d'impact, l'endommagement et la zone d'impact augmentent car le développement des dommages est considéré comme entièrement basé sur la déformation plastique effective. L'augmentation de la vitesse d'impact augmente le taux de déformation plastique équivalente dans le processus SMAT et la déformation plastique équivalente finale obtenue après SMAT. De plus, les résultats montrent que la profondeur affectée par un seul impact peut atteindre 0,15 mm, tandis que la valeur maximale de la fraction volumique de vide est située à une distance de 0,1 mm de la surface d'impact. Nous pouvons donc proposer d'enlever, par exemple par polissage, une telle profondeur pour optimiser les bénéfices du procédé SMAT.

Contribution 4: Un modèle visco-élastoplastique tenant compte de l'influence de la densité de dislocations, du maclage, de la taille des grains et de la vitesse de déformation a d'abord été développé à partir des résultats expérimentaux. Ensuite, le modèle a été implémenté dans une subroutine d'ABAQUS Explicit pour effectuer une simulation 3D du test de nanoindentation à différentes profondeurs avec différents taux de déformation. Enfin, la réponse élastoplastique du matériau traité par SMAT est calculée en utilisant la loi de mélange, et les résultats calculés montrent un bon accord avec les résultats expérimentaux.

6.2 Perspectives

Les modèles utilisés dans ce travail sont, bien entendu, incomplets et peuvent encore être améliorés. D'autres caractérisations des matériaux peuvent être effectuées, y compris des essais de fatigue, jusqu'à des taux de déformation plus élevés, pour évaluer le comportement cyclique et la sensibilité du taux de déformation. Des essais à haute température seraient également utiles compte tenu de l'influence possible de l'augmentation de température lors d'impacts répétés, que ce soit en termes de dilatation thermique ou de propriétés mécaniques.

Les données expérimentales peuvent ensuite être utilisées pour sélectionner et construire des théories constitutives des matériaux appropriés et identifier les paramètres de différents matériaux. Par exemple, les matériaux étudiés dans ce travail sont supposés obéir au critère d'écoulement de Von Mises, qui est principalement utilisé pour les matériaux ductiles, comme les métaux. Ce critère d'écoulement s'applique uniquement aux matériaux isotropes. Cependant, tous les métaux et alliages sont fondamentalement anisotropes en raison de la distribution des grains et de leur structure cristalline. Si les grains sont orientés de manière aléatoire et sont en grand nombre, le comportement macroscopique est approximativement isotrope. Cependant, si les grains sont principalement orientés dans une direction spécifique, le comportement du matériau ne sera plus macroscopiquement isotrope. Dans la déformation plastique globale des métaux, l'effet de l'anisotropie est généralement ignoré. Étant donné que de nombreuses approximations sont également impliquées dans la solution, on peut considérer que la prise en compte de l'anisotropie n'affecte pas le résultat. Cependant, dans le cas d'une tôle, sa formabilité et son étirage sont significativement affectés par l'anisotropie engendrée lors du laminage. Hill a proposé un critère d'écoulement pour les matériaux anisotropes. Ce critère est une extension de celui de von Mises. Lorsque l'anisotropie est négligeable, ce critère redonne celui de von Mises.

La microstructure est un autre aspect important. Le développement de modèles de plasticité cristalline (tenant compte de différents paramètres tels que le cyclage, la vitesse de déformation élevée et le comportement thermique) conduira à une compréhension plus physique. De plus, des essais d'impact avec différents angles pourraient être effectués sur des monocristaux avec différentes orientations

cristallographiques pour étudier les mécanismes de déformation avec MEB, EBSD et MET.

Il pourrait également être très intéressant d'obtenir une profondeur de SMAT uniforme pour des géométries complexes et d'optimiser les effets thermiques pendant le SMAT, par exemple, la température qui peut affecter les contraintes résiduelles et peut évoluer par le biais de deux processus physiques différents : la production de chaleur due à la déformation plastique et la diffusion thermique. Les recherches existantes sur l'optimisation du SMAT étudient uniquement des éprouvettes simples, et peu d'articles étudient les géométries complexes, telles que celles avec courbure et arêtes.

Puisqu'une bille interagit avec une autre bille et/ou la chambre pendant le processus SMAT, elle impactera la surface du matériau plusieurs fois. Cela aura un impact sur l'intensité, la recouvrement et la qualité globale du SMAT. Dans cette étude, un seul impact a été considéré. Cependant, les billes utilisées dans SMAT effectuent plusieurs impacts plutôt qu'un seul. Il est donc difficile de prédire l'évolution des propriétés du matériau lors du SMAT avec multi-impacts en modélisant le processus d’un seul impact Une étude plus approfondie serait à mener compte tenu de l'influence des multi-impacts sur les résultats obtenus.

Nous avons principalement étudié l'évolution de certaines propriétés des matériaux et à certaines échelles au cours du processus SMAT dans ce travail. Cependant, il est également important d'étudier d’autres propriétés mécaniques des matériaux SMATés. Pour ce faire, les propriétés mécaniques des différentes régions de déformation mécanique peuvent être caractérisées à différentes profondeurs (telles que les couches nanostructurées). L'épaisseur de la couche de nanostructure étant très faible (en fonction des paramètres du procédé SMAT, de quelques microns à quelques dizaines de microns), il est difficile de caractériser ses propriétés mécaniques locales. La technique de nanoindentation est largement utilisée pour la caractérisation aux petites échelles, notamment pour avoir le comportement mécanique des matériaux tels que les films minces et plus particulièrement la dureté. Cependant, la nanoindentation ne fournit pas nécessairement les détails de la contrainte-déformation des matériaux étudiés.

Cette technique ne peut pas mettre en évidence d'autres propriétés mécaniques importantes dans le matériau telles que la distribution locale des contraintes, la

concentration des contraintes, la limite d'élasticité, le comportement contrainte-déformation, les contraintes de von-Mises, etc.

Afin de surmonter cette limitation inhérente, la méthode EF est utilisée pour simuler la courbe charge-déplacement (courbe P-h) et les distributions de contraintes sous le nanoindentateur. La précision des résultats dépend de la qualité et de l'adéquation du modèle utilisé. La précision de la détermination des propriétés mécaniques par nanoindentation peut être affectée pour diverses raisons, par exemple, un traitement des données insuffisant dans le modèle ou certaines caractéristiques ou facteurs spécifiques ne sont pas pris en compte. Ainsi, dans les travaux futurs, ces facteurs peuvent être pris en compte dans le modèle pour augmenter la précision.

La compression de micro-piliers pourrait également être utilisée pour étudier les propriétés mécaniques et comprendre le mécanisme de déformation à l'échelle locale. En utilisant cette technique, la courbe contrainte-déformation peut être calculée à partir de la courbe charge-déplacement obtenue après l’essai de compression. Il permet également d'accéder à d'autres informations, telles que la limite d'élasticité, qui est plus directement obtenue par rapport à la technique de nanoindentation. De plus, la technique de compression de micro-piliers n'a pas encore été largement utilisée pour étudier les matériaux traités par SMAT avec des microstructures à gradient.

Comme mentionné au chapitre 3, pour les techniques de traitement mécanique de surface telles que le SMAT, un gradient de microstructure dans la région de surface d'une pièce peut être générée par des impacts répétés. Au cours de la dernière décennie, de plus en plus de travaux de recherche se concentrent sur la caractérisation expérimentale et la modélisation de matériaux à microstructure à gradient générée par divers moyens. Par exemple, l'écrouissage d'un acier a été étudié quantitativement en utilisant un modèle de plasticité continue basé sur la densité de dislocations développé par Li et al (Li et al., 2017). Dans ce modèle, l'interaction des couches de composants dans la structure du gradient est décrite en incorporant les dislocations géométriquement nécessaires (GND) et les contraintes internes. Un modèle basé sur la densité des dislocations tenant compte du double rôle dans les composites à matrice métallique (MMC) a également été développé par Dong et al (Dong et al., 2015). pour décrire les facteurs affectant les mécanismes de renforcement dans les MMC renforcées de nanotubes de carbone avec différentes tailles de grains de matrice. De plus, afin de décrire la relation structure-propriété de l'acier inoxydable austénite avec

la nanostructure à gradient, un modèle théorique a été proposé par Zhu et al (Zhu et al., 2017). Cependant, la modélisation de gradients de microstructure produite par SMAT à la surface reste une tâche difficile. Ainsi, nous espérons prendre en compte la variation de la taille de grains dépendante de la profondeur et la structure composite du matériau dans notre modèle. L'EBSD associé à des micro-piliers obtenus à l'aide d'un faisceau d'ions focalisés (FIB) peuvent être utilisés pour étudier le gradient de microstructure des matériaux générés par SMAT. Ensuite, les résultats (tels que la courbe contrainte-déformation, la densité de dislocations de l'austénite et de la martensite, et la fraction volumique des macles et de la martensite) peuvent être utilisés pour ajuster les paramètres du modèle constitutif à différentes profondeurs du gradient de microstructure. Le modèle constitutif, basé sur l'évolution de la densité de dislocations, devrait pouvoir décrire les principaux mécanismes de déformation de l'acier TWIP/TRIP. De plus, le modèle peut être implémenté dans les subroutines d'ABAQUS, et des simulations numériques peuvent être effectuées pour étudier les propriétés mécaniques.

REFERENCES

[1] S. Wang, W. Cai, J. Li, W. Wei, and J. Hu, “A novel rapid D.C. plasma nitriding at low gas pressure for 304 austenitic stainless steel,” *Mater. Lett.*, vol. 105, pp. 47–49, 2013, doi: 10.1016/j.matlet.2013.04.031.

[2] H. M. Cobb, *The history of stainless steel*, vol. 48, no. 07. ASM International, 2011.

[3] Q. Wang, M. K. Khan, and C. Bathias, “Current understanding of ultra-high cycle fatigue,” *Theor. Appl. Mech. Lett.*, vol. 2, no. 3, p. 031002, 2012, doi: 10.1063/2.1203102.

[4] G. Feng, L. Shi, J. Lü, and K. Lu, “Investigation of surface nanocrystallization of a low carbon steel induced by ultrasonic shot peening,” *Jinshu Xuebao/Acta Metall. Sin.*, vol. 36, no. 3, pp. 300–303, 2000.

[5] S. Curtis, E. R. De Los Rios, C. A. Rodopoulos, and A. Levers, “Analysis of the effects of controlled shot peening on fatigue damage of high strength aluminium alloys,” *Int. J. Fatigue*, vol. 25, no. 1, pp. 59–66, 2002, doi: 10.1016/S0142-1123(02)00049-X.

[6] J. Wang, J. Han, W. Li, Z. Yang, Z. Li, and Y. Zhao, “Analytical modelling of shot-peening residual stress on welding carbon steel surface layer,” *J. Wuhan Univ. Technol. Mater. Sci. Ed.*, vol. 31, no. 6, pp. 1352–1362, 2016, doi: 10.1007/s11595-016-1538-x.

[7] O. Unal and R. Varol, “Surface severe plastic deformation of AISI 304 via conventional shot peening, severe shot peening and repeening,” *Appl. Surf. Sci.*, vol. 351, pp. 289–295, 2015, doi: 10.1016/j.apsusc.2015.05.093.

[8] Y. Mutoh, G. H. Fair, B. Noble, and R. B. Waterhouse, “the Effect of Residual Stresses Induced By Shot-Peening on Fatigue Crack Propagation in Two High Strength Aluminium Alloys,” *Fatigue Fract. Eng. Mater. Struct.*, vol. 10, no. 4, pp. 261–272, 1987, doi: 10.1111/j.1460-2695.1987.tb00205.x.

[9] T. Hong, J. Y. Ooi, and B. A. Shaw, “A numerical study of the residual stress pattern from single shot impacting on a metallic component,” *Adv. Eng. Softw.*, vol. 39, no. 9, pp. 743–756, 2008, doi: 10.1016/j.advengsoft.2007.10.002.

[10] S. Rouquette, E. Rouhaud, M. François, A. Roos, and J. L. Chaboche, “Coupled thermo-mechanical simulations of shot impacts: Effects of the temperature on the residual stress field due to shot-peening,” *J. Mater. Process. Technol.*, vol. 209, no. 8, pp. 3879–3886, 2009, doi: 10.1016/j.jmatprotec.2008.09.006.

[11] M. R. Menezes, C. Godoy, V. T. L. Buono, M. M. M. Schvartzman, and J. C. Avelar-Batista Wilson, “Effect of shot peening and treatment temperature on wear and corrosion resistance of sequentially plasma treated AISI 316L steel,” *Surf. Coatings Technol.*, vol. 309, pp. 651–662, 2017, doi:

10.1016/j.surfcoat.2016.12.037.

[12] N. R. Tao, M. L. Sui, J. Lu, and K. Lua, “Surface nanocrystallization of iron induced by ultrasonic shot peening,” *Nanostructured Mater.*, vol. 11, no. 4, pp. 433–440, 1999, doi: 10.1016/S0965-9773(99)00324-4.

[13] A. Levers and A. Prior, “Finite element analysis of shot peening,” *J. Mater. Process. Technol.*, vol. 80–81, pp. 304–308, 1998, doi: 10.1016/S0924-0136(98)00188-5.

[14] A. Heydari Astaraee, R. Miresmaeili, S. Bagherifard, M. Guagliano, and M. Aliofkhazraei, “Incorporating the principles of shot peening for a better understanding of surface mechanical attrition treatment (SMAT) by simulations and experiments,” *Mater. Des.*, vol. 116, pp. 365–373, 2017, doi: 10.1016/j.matdes.2016.12.045.

[15] F. A. Guo, K. Y. Zhu, N. Trannoy, and J. Lu, “Examination of thermal properties by scanning thermal microscopy in ultrafine-grained pure titanium surface layer produced by surface mechanical attrition treatment,” *Thermochim. Acta*, vol. 419, no. 1–2, pp. 239–246, 2004, doi: 10.1016/j.tca.2004.02.018.

[16] J. Z. Lu *et al.*, “Grain refinement mechanism of multiple laser shock processing impacts on ANSI 304 stainless steel,” *Acta Mater.*, vol. 58, no. 16, pp. 5354–5362, 2010, doi: 10.1016/j.actamat.2010.06.010.

[17] D. H. Shin, I. Kim, J. Kim, and K. T. Park, “Grain refinement mechanism during equal-channel angular pressing of a low-carbon steel,” *Acta Mater.*, vol. 49, no. 7, pp. 1285–1292, 2001, doi: 10.1016/S1359-6454(01)00010-6.

[18] X. Feaugas and H. Haddou, “Grain-size effects on tensile behavior of nickel and AlSl 316L stainless steel,” *Metall. Mater. Trans. A Phys. Metall. Mater. Sci.*, vol. 34 A, no. 10, pp. 2329–2340, 2003, doi: 10.1007/s11661-003-0296-5.

[19] P. Mann, H. Y. Miao, A. Gariépy, M. Lévesque, and R. R. Chromik, “Residual stress near single shot peening impingements determined by nanoindentation and numerical simulations,” *J. Mater. Sci.*, vol. 50, no. 5, pp. 2284–2297, 2015, doi: 10.1007/s10853-014-8792-0.

[20] P. S. Prevéy, “X-Ray Diffraction Characterization of Residual Stresses Produced By Shot Peening,” in *Shot Peening Theory and Application*, 1990, vol. c, no. 513, pp. 81–93.

[21] M. Calcagnotto, D. Ponge, E. Demir, and D. Raabe, “Orientation gradients and geometrically necessary dislocations in ultrafine grained dual-phase steels studied by 2D and 3D EBSD,” *Mater. Sci. Eng. A*, vol. 527, no. 10–11, pp. 2738–2746, 2010, doi: 10.1016/j.msea.2010.01.004.

[22] Z. Sun, D. Retraint, B. Guelorget, and L. Waltz, “Micro-pillar compression tests to characterize the mechanical behavior of a nanocrystalline layer induced by SMAT in a 316L stainless steel,” *Mater. Tech.*, vol. 103, no. 3, p. 304, 2015, doi: 10.1051/mattech/2015028.

[23] B. C. De Cooman, “Structure-properties relationship in TRIP steels containing carbide-free bainite,” *Curr. Opin. Solid State Mater. Sci.*, vol. 8, no. 3–4, pp. 285–303, 2004, doi: 10.1016/j.cossms.2004.10.002.

[24] S. Lee, W. Woo, and B. C. de Cooman, “Analysis of the Tensile Behavior of 12 pct Mn Multi-phase ($\alpha + \gamma$) TWIP + TRIP Steel by Neutron Diffraction,” *Metall. Mater. Trans. A Phys. Metall. Mater. Sci.*, vol. 47, no. 5, pp. 2125–2140, 2016, doi: 10.1007/s11661-016-3407-9.

[25] J. Mahieu, J. Maki, B. C. De Cooman, and S. Claessens, “Phase transformation and mechanical properties of Si-free CMnAl transformation-induced plasticity-aided steel,” *Metall. Mater. Trans. A Phys. Metall. Mater. Sci.*, vol.

33, no. 8, pp. 2573–2580, 2002, doi: 10.1007/s11661-002-0378-9.

[26] B. C. De Cooman, O. Kwon, and K. G. Chin, "State-of-the-knowledge on TWIP steel," *Mater. Sci. Technol.*, vol. 28, no. 5, pp. 513–527, 2012, doi: 10.1179/1743284711Y.0000000095.

[27] E. I. Galindo-Nava and P. E. J. Rivera-Díaz-del-Castillo, "Understanding martensite and twin formation in austenitic steels: A model describing TRIP and TWIP effects," *Acta Mater.*, vol. 128, pp. 120–134, 2017, doi: 10.1016/j.actamat.2017.02.004.

[28] D. T. Pierce, J. A. Jiménez, J. Bentley, D. Raabe, and J. E. Wittig, "The influence of stacking fault energy on the microstructural and strain-hardening evolution of Fe-Mn-Al-Si steels during tensile deformation," *Acta Mater.*, vol. 100, pp. 178–190, 2015, doi: 10.1016/j.actamat.2015.08.030.

[29] O. Bouaziz, S. Allain, and C. Scott, "Effect of grain and twin boundaries on the hardening mechanisms of twinning-induced plasticity steels," *Scr. Mater.*, vol. 58, no. 6, pp. 484–487, 2008, doi: 10.1016/j.scriptamat.2007.10.050.

[30] W. S. Choi, B. C. De Cooman, S. Sandlöbes, and D. Raabe, "Size and orientation effects in partial dislocation-mediated deformation of twinning-induced plasticity steel micro-pillars," *Acta Mater.*, vol. 98, pp. 391–404, 2015, doi: 10.1016/j.actamat.2015.06.065.

[31] E. J. Seo, J. K. Kim, L. Cho, J. Mola, C. Y. Oh, and B. C. De Cooman, "Micro-plasticity of medium Mn austenitic steel: Perfect dislocation plasticity and deformation twinning," *Acta Mater.*, vol. 135, pp. 112–123, 2017, doi: 10.1016/j.actamat.2017.06.014.

[32] A. Y. Chen *et al.*, "The influence of strain rate on the microstructure transition of 304 stainless steel," *Acta Mater.*, vol. 59, no. 9, pp. 3697–3709, 2011, doi: 10.1016/j.actamat.2011.03.005.

[33] J. Talonen and H. Hänninen, "Formation of shear bands and strain-induced martensite during plastic deformation of metastable austenitic stainless steels," *Acta Mater.*, vol. 55, no. 18, pp. 6108–6118, 2007, doi: 10.1016/j.actamat.2007.07.015.

[34] N. R. Tao, Z. B. Wang, W. P. Tong, M. L. Sui, J. Lu, and K. Lu, "An investigation of surface nanocrystallization mechanism in Fe induced by surface mechanical attrition treatment," *Acta Mater.*, vol. 50, no. 18, pp. 4603–4616, Oct. 2002, doi: 10.1016/S1359-6454(02)00310-5.

[35] K. Lu and J. Lu, "Surface nanocrystallization (SNC) of metallic materials-presentation of the concept behind a new approach," *J. Mater. Sci. Technol.*, vol. 15, no. 3, pp. 193–197, 1999.

[36] J. Azadmanjiri, C. C. Berndt, A. Kapoor, and C. Wen, "Development of Surface Nano-Crystallization in Alloys by Surface Mechanical Attrition Treatment (SMAT)," *Crit. Rev. Solid State Mater. Sci.*, vol. 40, no. 3, pp. 164–181, 2015, doi: 10.1080/10408436.2014.978446.

[37] B. Arifvianto, Suyitno, and M. Mahardika, "Effect of sandblasting and surface mechanical attrition treatment on surface roughness, wettability, and microhardness distribution of AISI 316L," *Key Eng. Mater.*, vol. 462–463, no. 3, pp. 738–743, 2011, doi: 10.4028/www.scientific.net/KEM.462-463.738.

[38] K. Dai and L. Shaw, "Comparison between shot peening and surface nanocrystallization and hardening processes," *Mater. Sci. Eng. A*, vol. 463, no. 1–2, pp. 46–53, 2007, doi: 10.1016/j.msea.2006.07.159.

[39] K. Lu and J. Lu, "Nanostructured surface layer on metallic materials induced by surface mechanical attrition treatment," *Mater. Sci. Eng. A*, vol. 375–377,

no. 1-2 SPEC. ISS., pp. 38–45, 2004, doi: 10.1016/j.msea.2003.10.261.

[40] M. Schilling-Praetzel, F. Hegemann, and G. Gottsstein, “Influence of temperature of shot peening on fatigue life,” in *Proc. ICSP*, 1993, vol. 5, pp. 227–238.

[41] X. An, Q. Lin, S. Qu, G. Yang, S. Wu, and Z.-F. Zhang, “Influence of stacking-fault energy on the accommodation of severe shear strain in Cu-Al alloys during equal-channel angular pressing,” *J. Mater. Res.*, vol. 24, no. 12, pp. 3636–3646, 2009.

[42] T. Roland, D. Retraint, K. Lu, and J. Lu, “Fatigue life improvement through surface nanostructuring of stainless steel by means of surface mechanical attrition treatment,” *Scr. Mater.*, vol. 54, no. 11, pp. 1949–1954, 2006, doi: 10.1016/j.scriptamat.2006.01.049.

[43] A. Q. Lu, G. Liu, and C. M. Liu, “Microstructural evolution of the surface layer of 316L stainless steel induced by mechanical attrition,” *Acta Metall. Sin. -Chinese Ed.*, vol. 40, pp. 943–947, Sep. 2004.

[44] J. Rawers, F. Croydon, R. Krabbe, and N. Duttlinger, “Tensile characteristics of nitrogen enhanced powder injection moulded 316L stainless steel,” *Powder Metall.*, vol. 39, no. 2, pp. 125–129, 1996, doi: 10.1179/pom.1996.39.2.125.

[45] I. Üçok, T. Ando, and N. J. Grant, “Property enhancement in Type 316L stainless steel by spray forming,” *Mater. Sci. Eng. A*, vol. 133, no. C, pp. 284–287, 1991, doi: 10.1016/0921-5093(91)90070-4.

[46] X. H. Chen, J. Lu, L. Lu, and K. Lu, “Tensile properties of a nanocrystalline 316L austenitic stainless steel,” *Scr. Mater.*, vol. 52, no. 10, pp. 1039–1044, 2005.

[47] H. W. Zhang, Z. K. Hei, G. Liu, J. Lu, and K. Lu, “Formation of nanostructured surface layer on AISI 304 stainless steel by means of surface mechanical attrition treatment,” *Acta Mater.*, vol. 51, no. 7, pp. 1871–1881, 2003, doi: 10.1016/S1359-6454(02)00594-3.

[48] N. Tao, H. Zhang, J. Lu, and K. Lu, “Development of Nanostructures in Metallic Materials with Low Stacking Fault Energies during Surface Mechanical Attrition Treatment (SMAT),” *Mater. Trans.*, vol. 44, no. 10, pp. 1919–1925, 2003, doi: 10.2320/matertrans.44.1919.

[49] K. A. Johnson, L. E. Murr, and K. P. Staudhammer, “Comparison of residual microstructures for 304 stainless steel shock loaded in plane and cylindrical geometries: Implications for dynamic compaction and forming,” *Acta Metall.*, vol. 33, no. 4, pp. 677–684, 1985, doi: 10.1016/0001-6160(85)90031-8.

[50] S. S. Hecker, M. G. Stout, K. P. Staudhammer, and J. L. Smith, “Effects of Strain State and Strain Rate on Deformation-Induced Transformation in 304 Stainless Steel: Part I. Magnetic Measurements and Mechanical Behavior,” *Metall. Trans. A*, vol. 13, no. 4, pp. 619–626, 1982, doi: 10.1007/BF02644427.

[51] H. L. Chan, H. H. Ruan, A. Y. Chen, and J. Lu, “Optimization of the strain rate to achieve exceptional mechanical properties of 304 stainless steel using high speed ultrasonic surface mechanical attrition treatment,” *Acta Mater.*, vol. 58, no. 15, pp. 5086–5096, 2010, doi: 10.1016/j.actamat.2010.05.044.

[52] Y. Sun, “Sliding wear behaviour of surface mechanical attrition treated AISI 304 stainless steel,” *Tribol. Int.*, vol. 57, pp. 67–75, 2013, doi: 10.1016/j.triboint.2012.07.015.

[53] J. Zhou, Z. Sun, P. Kanouté, and D. Retraint, “Effect of surface mechanical attrition treatment on low cycle fatigue properties of an austenitic stainless steel,” *Int. J. Fatigue*, vol. 103, pp. 309–317, 2017, doi:

10.1016/j.ijfatigue.2017.06.011.
[54] K. K. Singh, S. Sangal, and G. S. Murty, “Hall-Petch behaviour of 316L austenitic stainless steel at elevated temperatures,” *Mater. Sci. Technol.*, vol. 18, no. 10, pp. 1168–1178, 2002, doi: 10.1179/026708302225005927.
[55] Z. B. Wang *et al.*, “Effect of surface nanocrystallization on friction and wear properties in low carbon steel,” *Mater. Sci. Eng. A*, vol. 352, no. 1–2, pp. 144–149, 2003.
[56] J. Z. Xiao, K. K. Leung, and H. W. Kui, “Mechanism of grain refinement in undercooled Cu30Ni70,” *Appl. Phys. Lett.*, vol. 67, no. 5, p. 3111, 1995, doi: 10.1063/1.114850.
[57] H. C. Shin, T. K. Ha, and Y. W. Chang, “Kinetics of deformation induced martensitic transformation in a 304 stainless steel,” *Scr. Mater.*, vol. 45, no. 7, pp. 823–829, 2001, doi: 10.1016/S1359-6462(01)01101-0.
[58] P. Behjati, A. Kermanpur, and A. Najafizadeh, “Application of martensitic transformation fundamentals to select appropriate alloys for grain refining through martensite thermomechanical treatment,” *Metall. Mater. Trans. A*, vol. 44, no. 8, pp. 3524–3531, 2013.
[59] F. Gauzzi, R. Montanari, G. Principi, and M. E. Tata, “AISI 304 steel: anomalous evolution of martensitic phase following heat treatments at 400 °C,” *Mater. Sci. Eng. A*, vol. 438–440, no. SPEC. ISS., pp. 202–206, 2006, doi: 10.1016/j.msea.2006.02.116.
[60] B. Han and Z. Xu, “Martensite microstructure transformed from ultra-fine-grained Fe-32%Ni alloy austenite,” *Mater. Sci. Eng. A*, vol. 487, no. 1–2, pp. 64–67, 2008, doi: 10.1016/j.msea.2007.09.056.
[61] M. Bigdeli Karimi, H. Arabi, A. Khosravani, and J. Samei, “Effect of rolling strain on transformation induced plasticity of austenite to martensite in a high-alloy austenitic steel,” *J. Mater. Process. Technol.*, vol. 203, no. 1–3, pp. 349–354, 2008, doi: 10.1016/j.jmatprotec.2007.10.029.
[62] A. H. Cottrell and D. Hull, “Extrusion and intrusion by cyclic slip in copper,” *Proc. R. Soc. London. Ser. A. Math. Phys. Sci.*, vol. 242, no. 1229, pp. 211–213, 1957, doi: 10.1098/rspa.1957.0170.
[63] P. J. E. Forsyth, “Slip-band damage and extrusion,” *Proc. R. Soc. London. Ser. A. Math. Phys. Sci.*, vol. 242, no. 1229, pp. 198–202, 1957, doi: 10.1098/rspa.1957.0168.
[64] K. H. and T. S., “Application of fracture mechanics to very small cracks,” *Int Conf Mech Behav. Mater.*, pp. 627–631, 1976.
[65] S. Suresh, “Crack deflection: implications for the growth of long and short fatigue cracks,” *Metall. Trans. A*, vol. 14, no. 11, pp. 2375–2385, 1983.
[66] A. Needleman and V. Tvergaard, “An analysis of ductile rupture in notched bars,” *J. Mech. Phys. Solids*, vol. 32, no. 6, pp. 461–490, 1984, doi: 10.1016/0022-5096(84)90031-0.
[67] E. R. De Los Rio, A. Navarro, and A. Navarro, “Considerations of grain orientation and work hardening on short-fatigue-crack modelling,” *Philos. Mag. A Phys. Condens. Matter, Struct. Defects Mech. Prop.*, vol. 61, no. 3, pp. 435–449, 1990, doi: 10.1080/01418619008231926.
[68] R. K. Bolingbroke and J. E. King, “A comparison of long and short fatigue crack growth in a high strength aluminum alloy,” in *The Behavior of Short Fatigue Cracks*, 1986, p. 101.
[69] A. F. Blom, A. Hedlund, W. Zhao, and A. Fathulla, “Short fatigue crack growth behaviour in Al2024 and Al7475,” in *The Behaviour of Short Fatigue*

Cracks, 1986, pp. 37–66, [Online]. Available: http://www.gruppofrattura.it/ocs/index.php/esis/EGF1/paper/download/9682/6393.

[70] A. Navarro and E. R. De Los Rios, "Fatigue crack growth modelling by successive blocking of dislocations," *Proc. R. Soc. A Math. Phys. Eng. Sci.*, vol. 437, no. 1900, pp. 375–390, 1992, doi: 10.1098/rspa.1992.0067.

[71] K. Tanaka, "Engineering formulae for fatigue strength reduction due to crack-like notches," *Int. J. Fract.*, vol. 22, no. 2, pp. R39–R46, 1983, doi: 10.1007/BF00942722.

[72] R. A. Smith and K. J. Miller, "Prediction of fatigue regimes in notched components," *Int. J. Mech. Sci.*, vol. 20, no. 4, pp. 201–206, 1978, doi: 10.1016/0020-7403(78)90082-6.

[73] C. Vallellano, A. Navarro, and J. Domínguez, "Fatigue crack growth threshold conditions at notches. Part II: generalization and application to experimental results," *Fatigue Fract. Eng. Mater. Struct.*, vol. 23, no. 2, pp. 123–128, 2000.

[74] S. Curtis, E. R. De los Rios, C. A. Rodopoulos, and A. Levers, "Analysis of the effects of controlled shot peening on fatigue damage of high strength aluminium alloys," *Int. J. Fatigue*, vol. 25, no. 1, pp. 59–66, 2003.

[75] Y. Bergström and H. Hallén, "An improved dislocation model for the stress-strain behaviour of polycrystalline α-Fe," *Mater. Sci. Eng.*, vol. 55, no. 1, pp. 49–61, 1982, doi: 10.1016/0025-5416(82)90083-0.

[76] U. F. Kocks, "Laws for work-hardening and low-temperature creep," *J. Eng. Mater. Technol.*, vol. 98, no. 1, pp. 76–85, 1976.

[77] Y. Estrin and H. Mecking, "A unified phenomenological description of work hardening and creep based on one-parameter models," *Acta Metall.*, vol. 32, no. 1, pp. 57–70, 1984, doi: 10.1016/0001-6160(84)90202-5.

[78] D. J. Bammann, "An internal variable model of viscoplasticity," *Int. J. Eng. Sci.*, vol. 22, no. 8–10, pp. 1041–1053, 1984, doi: 10.1016/0020-7225(84)90105-8.

[79] E. P. Busso, "A continuum theory for dynamic recrystallization with microstructure-related length scales," *Int. J. Plast.*, vol. 14, no. 4–5, pp. 319–353, 1998, doi: 10.1016/S0749-6419(98)00008-4.

[80] O. G. Lademo, O. S. Hopperstad, and M. Langseth, "Evaluation of yield criteria and flow rules for aluminum alloys," *Int. J. Plast.*, vol. 15, no. 2, pp. 191–208, 1999, doi: 10.1016/S0749-6419(98)00064-3.

[81] N. A. Fleck and J. R. Willis, "A mathematical basis for strain-gradient plasticity theory. Part II: Tensorial plastic multiplier," *J. Mech. Phys. Solids*, vol. 57, no. 7, pp. 1045–1057, 2009, doi: 10.1016/j.jmps.2009.03.007.

[82] A. L. Gurson, "Continuum Theory of Ductile Rupture By Void Nucleation and Growth - 1. Yield Criteria and Flow Rules for Porous Ductile Media.," *Am. Soc. Mech. Eng.*, vol. 99, no. 76-Mat-CC, pp. 2–15, 1976.

[83] D. A. Wang, W. Y. Chien, K. C. Liao, J. Pan, and S. C. Tang, "A gurson yield function for anisotropic porous sheet metals and its applications to failure prediction of aluminum sheets," *J. Mech.*, vol. 19, no. 1, pp. 161–168, 2003, doi: 10.1017/S1727719100004160.

[84] V. Tvergaard, "Influence of voids on shear band instabilities under plane strain conditions," *Int. J. Fract.*, vol. 17, no. 4, pp. 389–407, 1981, doi: 10.1007/BF00036191.

[85] D. Steglich, T. Siegmund, and W. Brocks, "Micromechanical modeling of damage due to particle cracking in reinforced metals," *Comput. Mater. Sci.*, vol.

16, no. 1–4, pp. 404–413, 1999, doi: 10.1016/s0927-0256(99)00083-x.

[86] M. Rachik, J. M. Roelandt, and A. Maillard, “Some phenomenological and computational aspects of sheet metal blanking simulation,” *J. Mater. Process. Technol.*, vol. 128, no. 1–3, pp. 256–265, 2002, doi: 10.1016/S0924-0136(02)00460-0.

[87] Z. Chen, Z. Sun, and B. Panicaud, “Constitutive modeling of TWIP/TRIP steels and numerical simulation of single impact during Surface Mechanical Attrition Treatment,” *Mech. Mater.*, vol. 122, pp. 69–75, 2018, doi: 10.1016/j.mechmat.2018.04.005.

[88] P. Solin, D. Andrs, J. Cerveny, and M. Simko, “PDE-independent adaptive h p-FEM based on hierarchic extension of finite element spaces,” *J. Comput. Appl. Math.*, vol. 233, no. 12, pp. 3086–3094, 2010, doi: 10.1016/j.cam.2009.05.030.

[89] H. Nguyen-Xuan, C. T. Wu, and G. R. Liu, “An adaptive selective ES-FEM for plastic collapse analysis,” *Eur. J. Mech. A/Solids*, vol. 58, pp. 278–290, 2016, doi: 10.1016/j.euromechsol.2016.02.005.

[90] N. SUDHEER, K. V. KUMAR, and B. H. V PRASAD, “Design and Analysis of Car Bumper by using Cosmos Software In Frontal Crashes,” 2017.

[91] J. B. Leblond, “Mathematical modelling of transformation plasticity in steels II: Coupling with strain hardening phenomena,” *Int. J. Plast.*, vol. 5, no. 6, pp. 573–591, 1989, doi: 10.1016/0749-6419(89)90002-8.

[92] A. J. Nathan and A. Scobell, “How China sees America,” in *Foreign Affairs*, 2012, vol. 91, no. 5, pp. 1689–1699, doi: 10.1017/CBO9781107415324.004.

[93] G. Feng, L. Shi, J. Lü, and K. Lu, “Investigation of surface nanocrystallization of a low carbon steel induced by ultrasonic shot peening,” *Jinshu Xuebao/Acta Metall. Sin.*, vol. 36, no. 3, pp. 300–303, Mar. 2000.

[94] I. Maizlish, “The scattering of X-rays,” *J. Franklin Inst.*, vol. 197, no. 5, pp. 667–690, 1924, doi: 10.1016/S0016-0032(24)90651-X.

[95] Z. P. Bazant and P. D. Bhat, “Endochronic Theory of Inelasticity and Failure of Concrete,” *ASCE J Eng Mech Div*, vol. 102, no. 4, pp. 701–722, 1976.

[96] A. L. Patterson, “The scherrer formula for X-ray particle size determination,” *Phys. Rev.*, vol. 56, no. 10, pp. 978–982, 1939, doi: 10.1103/PhysRev.56.978.

[97] H. Wern, T. Maas, and N. Koch, “OF THE X-RAY STRESS ANALYSIS TECHNIQUE IN This document was presented at the Denver X-ray Conference (DXC) on Applications of X-ray Analysis . Sponsored by the International Centre for Diffraction Data (ICDD). This document is provided by ICDD in coop,” *Adv. X-ray Anal.*, vol. 44, no. c, pp. 128–133, 2001.

[98] B. D. Cullity, *Elements of X-ray Diffraction*. Addison-Wesley Publishing, 1956.

[99] V. R. Preedy, *Selenium: Chemistry, analysis, function and effects*, vol. 2015-Janua, no. 9. Royal Society of Chemistry, 2015.

[100] P. Haušild, V. Davydov, J. Drahokoupil, M. Landa, and P. Pilvin, “Characterization of strain-induced martensitic transformation in a metastable austenitic stainless steel,” *Mater. Des.*, vol. 31, no. 4, pp. 1821–1827, 2010, doi: 10.1016/j.matdes.2009.11.008.

[101] Y. F. Shen, X. X. Li, X. Sun, Y. D. Wang, and L. Zuo, “Twinning and martensite in a 304 austenitic stainless steel,” *Mater. Sci. Eng. A*, vol. 552, pp. 514–522, 2012, doi: 10.1016/j.msea.2012.05.080.

[102] M. Dollé, S. Patoux, and T. J. Richardson, “Lithium insertion chemistry of phosphate phases with the lipscombite structure,” *J. Power Sources*, vol. 144,

no. 1, pp. 208–213, 2005, doi: 10.1016/j.jpowsour.2004.12.028.
[103] P. S. Prevey, “X-Ray Diffraction Residual Stress Techniques,” *Mater. Charact.*, vol. 10, pp. 380–392, 2018, doi: 10.31399/asm.hb.v10.a0001761.
[104] S. A. Kim and W. L. Johnson, “Elastic constants and internal friction of martensitic steel, ferritic-pearlitic steel, and α-iron,” *Mater. Sci. Eng. A*, vol. 452–453, pp. 633–639, 2007, doi: 10.1016/j.msea.2006.11.147.
[105] K. Tanaka, H. Kimachi, Y. Akiniwa, K. Suzuki, and Y. Sakaid, “Single Crystal Elastic Constants of ^{2}-Silicon Nitride Determined by X-Ray Powder Diffraction,” *Zair. Soc. Mater. Sci. Japan*, vol. 49, no. 12Appendix, pp. 249–254, 2000, doi: 10.2472/jsms.49.12Appendix_249.
[106] F. Chu, M. Lei, S. A. Maloy, T. E. Mrrchell, A. Migliori, and J. Garrett, “Single crystal elastic constants of nbsi2,” *Philos. Mag. B Phys. Condens. Matter; Stat. Mech. Electron. Opt. Magn. Prop.*, vol. 71, no. 3, pp. 373–382, 1995, doi: 10.1080/13642819508239040.
[107] M. Ortiz, A. A. Pochettino, J. L. Lebrun, and G. Maeder, “X-Ray elastic constants in textured Zr-base materials,” *Metall. Trans. A*, vol. 24, no. 2, pp. 389–396, 1993, doi: 10.1007/BF02657326.
[108] Z. Liu, Y. Peng, C. Chen, J. Gong, and Y. Jiang, “Effect of surface nanocrystallization on low-temperature gas carburization for AISI 316L austenitic stainless steel,” *Int. J. Press. Vessel. Pip.*, vol. 182, p. 104053, 2020, doi: 10.1016/j.ijpvp.2020.104053.
[109] J. Lu, *Handbook of measurement of residual stresses*, vol. 34, no. 04. Fairmont Press, 1996.
[110] O. S. Zaroog, C. Yap, W. Ken, A. Noorlina, and A. Manap, “Current and Challenge of Residual Stress Measurement Techniques,” *Int. J. Sci. Res.*, vol. 3, no. 9, pp. 210–216, 2014.
[111] J. Ma and R. Sisson, “Residual Stress Measurement of AISI 304 Stainless Steel Nuclear Canister Plates by X-ray Diffraction,” 2015.
[112] International Standard Organization, “ISO/IEC 17025 General requirements for the competence of testing and calibration laboratories,” *International Standard*, vol. 2005. AS ISO/IEC, pp. 1–36, 2005, doi: 10.1109/IEEESTD.2015.7106438.
[113] British Standards Institution, “Non-destructive Testing - Test Method for Residual Stress analysis by X-ray Diffraction,” *Bs En 153052008*, no. January, 2009.
[114] I. Nikitin and I. Altenberger, “Comparison of the fatigue behavior and residual stress stability of laser-shock peened and deep rolled austenitic stainless steel AISI 304 in the temperature range 25-600 °C,” *Mater. Sci. Eng. A*, vol. 465, no. 1–2, pp. 176–182, 2007, doi: 10.1016/j.msea.2007.02.004.
[115] P. K. Sharp, J. Q. Clayton, and G. Clark, “THE FATIGUE RESISTANCE OF PEENED 7050-T7451 ALUMINIUM ALLOY—REPAIR AND RE-TREATMENT OF A COMPONENT SURFACE,” *Fatigue Fract. Eng. Mater. Struct.*, vol. 17, no. 3, pp. 243–252, 1994.
[116] M. R. James, “The relaxation of residual stresses during fatigue,” in *Residual stress and stress relaxation*, Springer, 1982, pp. 297–314.
[117] J. Liu and M. Pang, “Fatigue life prediction of shot-peened steel,” *Int. J. Fatigue*, vol. 43, pp. 134–141, 2012.
[118] D. V. Girish, M. M. Mayuram, and S. Krishnamurthy, “Influence of shot peening on the surface durability of thermomechanically treated en 24 steel spur gears,” *Tribol. Int.*, vol. 30, no. 12, pp. 865–870, 1997, doi:

10.1016/S0301-679X(97)00073-X.
[119] K. Herrmann, N. M. Jennett, W. Wegener, J. Meneve, K. Hasche, and R. Seemann, “Progress in determination of the area function of indenters used for nanoindentation,” *Thin Solid Films*, vol. 377–378, pp. 394–400, 2000, doi: 10.1016/S0040-6090(00)01367-5.
[120] C. A. Schuh, “Nanoindentation studies of materials,” *Mater. Today*, vol. 9, no. 5, pp. 32–40, 2006, doi: 10.1016/S1369-7021(06)71495-X.
[121] A. Fischer-Cripps, and D. Nicholson, “Nanoindentation. Mechanical Engineering Series,” *Appl. Mech. Rev.*, vol. 57, no. 2, pp. B12–B12, 2004, doi: 10.1115/1.1704625.
[122] L. Li, L. Shen, G. Proust, C. K. S. Moy, and G. Ranzi, “Three-dimensional crystal plasticity finite element simulation of nanoindentation on aluminium alloy 2024,” *Mater. Sci. Eng. A*, vol. 579, pp. 41–49, 2013, doi: 10.1016/j.msea.2013.05.009.
[123] A. Montagne, C. Tromas, V. Audurier, and J. Woirgard, “A new insight on reversible deformation and incipient plasticity during nanoindentation test in MgO,” *J. Mater. Res.*, vol. 24, no. 3, pp. 883–889, 2009, doi: 10.1557/jmr.2009.0127.
[124] Y. Wang, D. Raabe, C. Klüber, and F. Roters, “Orientation dependence of nanoindentation pile-up patterns and of nanoindentation microtextures in copper single crystals,” *Acta Mater.*, vol. 52, no. 8, pp. 2229–2238, 2004, doi: 10.1016/j.actamat.2004.01.016.
[125] A. G. Quarrell, *The Hardness of Metals*, vol. 170, no. 4333. Oxford university press, 1952.
[126] X. Li and B. Bhushan, “A review of nanoindentation continuous stiffness measurement technique and its applications,” *Mater. Charact.*, vol. 48, no. 1, pp. 11–36, 2002, doi: 10.1016/S1044-5803(02)00192-4.
[127] W. T. Y. Tze, S. Wang, T. G. Rials, G. M. Pharr, and S. S. Kelley, “Nanoindentation of wood cell walls: Continuous stiffness and hardness measurements,” *Compos. Part A Appl. Sci. Manuf.*, vol. 38, no. 3, pp. 945–953, 2007, doi: 10.1016/j.compositesa.2006.06.018.
[128] M. R. Maschmann, Q. Zhang, F. Du, L. Dai, and J. Baur, “Length dependent foam-like mechanical response of axially indented vertically oriented carbon nanotube arrays,” *Carbon N. Y.*, vol. 49, no. 2, pp. 386–397, 2011, doi: 10.1016/j.carbon.2010.09.034.
[129] N. Moharrami and S. J. Bull, “A comparison of nanoindentation pile-up in bulk materials and thin films,” *Thin Solid Films*, vol. 572, pp. 189–199, 2014.
[130] S. A. S. Asif, K. J. Wahl, and R. J. Colton, “Nanoindentation and contact stiffness measurement using force modulation with a capacitive load-displacement transducer,” *Rev. Sci. Instrum.*, vol. 70, no. 5, pp. 2408–2413, 1999, doi: 10.1063/1.1149769.
[131] K. Tosha, “Influence of Residual Stresses on the Hardness Number in the Affected Layer Produced by Shot Peening,” in *Second Asia–Pacific Forum on Precision Surface Finishing and Deburring Technology*, 2002, pp. 48–54.
[132] Z. Chen, Z. Sun, and B. Panicaud, “Investigation of ductile damage during surface mechanical attrition treatment for TWIP steels using a dislocation density based viscoplasticity and damage models,” *Mech. Mater.*, vol. 129, pp. 279–289, 2019, doi: 10.1016/j.mechmat.2018.12.009.
[133] L. N. Zhu, B. S. Xu, H. D. Wang, and C. B. Wang, “Effect of residual stress on the nanoindentation response of (100) copper single crystal,” *Mater. Chem.*

Phys., vol. 136, no. 2–3, pp. 561–565, 2012, doi: 10.1016/j.matchemphys.2012.07.026.

[134] T. Y. Tsui, W. C. Oliver, and G. M. Pharr, "Influences of stress on the measurement of mechanical properties using nanoindentation: Part I. Experimental studies in an aluminum alloy," *J. Mater. Res.*, vol. 11, no. 3, pp. 752–759, 1996, doi: 10.1557/JMR.1996.0091.

[135] C. E. K. Mady, S. A. Rodriguez, A. G. Gómez, and R. M. Souza, "Effects of mechanical properties, residual stress and indenter tip geometry on instrumented indentation data in thin films," *Surf. Coatings Technol.*, vol. 205, no. 5, pp. 1393–1397, 2010, doi: 10.1016/j.surfcoat.2010.07.097.

[136] M. K. Khan, M. E. Fitzpatrick, S. V. Hainsworth, and L. Edwards, "Effect of residual stress on the nanoindentation response of aerospace aluminium alloys," *Comput. Mater. Sci.*, vol. 50, no. 10, pp. 2967–2976, 2011, doi: 10.1016/j.commatsci.2011.05.015.

[137] J. Lee, C. Lee, and B. Kim, "Reverse analysis of nano-indentation using different representative strains and residual indentation profiles," *Mater. Des.*, vol. 30, no. 9, pp. 3395–3404, 2009, doi: 10.1016/j.matdes.2009.03.030.

[138] C. Ye *et al.*, "Gradient nanostructure and residual stresses induced by Ultrasonic Nano-crystal Surface Modification in 304 austenitic stainless steel for high strength and high ductility," *Mater. Sci. Eng. A*, vol. 613, pp. 274–288, 2014, doi: 10.1016/j.msea.2014.06.114.

[139] M. Frija, T. Hassine, R. Fathallah, C. Bouraoui, and A. Dogui, "Finite element modelling of shot peening process: Prediction of the compressive residual stresses, the plastic deformations and the surface integrity," *Mater. Sci. Eng. A*, vol. 426, no. 1–2, pp. 173–180, 2006, doi: 10.1016/j.msea.2006.03.097.

[140] V. Lemiale, Y. Estrin, H. S. Kim, and R. O'Donnell, "Forming nanocrystalline structures in metal particle impact," *Metall. Mater. Trans. A Phys. Metall. Mater. Sci.*, vol. 42, no. 10, pp. 3006–3012, 2011, doi: 10.1007/s11661-010-0588-5.

[141] X. C. Zhang, J. Lu, and S. Q. Shi, "A computational study of plastic deformation in AISI 304 induced by surface mechanical attrition treatment," *Mech. Adv. Mater. Struct.*, vol. 18, no. 8, pp. 572–577, 2011, doi: 10.1080/15376494.2011.621828.

[142] L. Remy, "Kinetics of f.c.c. deformation twinning and its relationship to stress-strain behaviour," *Acta Metall.*, vol. 26, no. 3, pp. 443–451, 1978, doi: 10.1016/0001-6160(78)90170-0.

[143] O. Bouaziz and N. Guelton, "Modelling of TWIP effect on work-hardening," *Mater. Sci. Eng. A*, vol. 319–321, pp. 246–249, 2001, doi: 10.1016/S0921-5093(00)02019-0.

[144] E. S. Perdahcioglu and H. J. M. Geijselaers, "A macroscopic model to simulate the mechanically induced martensitic transformation in metastable austenitic stainless steels," *Acta Mater.*, vol. 60, no. 11, pp. 4409–4419, 2012, doi: 10.1016/j.actamat.2012.04.042.

[145] L. Li, S. Liu, B. Ye, S. Hu, and Z. Zhou, "Quantitative analysis of strength and plasticity of a 304 stainless steel based on the stress-strain curve," *Met. Mater. Int.*, vol. 22, no. 3, pp. 391–396, 2016, doi: 10.1007/s12540-016-5466-2.

[146] S. Allain, J. P. Chateau, and O. Bouaziz, "Constitutive model of the TWIP effect in a polycrystalline high manganese content austenitic steel," *Steel Res.*, vol. 73, no. 6–7, pp. 299–302, 2002, doi: 10.1002/srin.200200212.

[147] H. Mecking and U. F. Kocks, "Kinetics of flow and strain-hardening," *Acta*

Metall., vol. 29, no. 11, pp. 1865–1875, 1981, doi: 10.1016/0001-6160(81)90112-7.

[148] D. R. Steinmetz *et al.*, "Revealing the strain-hardening behavior of twinning-induced plasticity steels: Theory, simulations, experiments," *Acta Mater.*, vol. 61, no. 2, pp. 494–510, 2013, doi: 10.1016/j.actamat.2012.09.064.

[149] M. I. Latypov, S. Shin, B. C. De Cooman, and H. S. Kim, "Micromechanical finite element analysis of strain partitioning in multiphase medium manganese TWIP+TRIP steel," *Acta Mater.*, vol. 108, pp. 219–228, 2016, doi: 10.1016/j.actamat.2016.02.001.

[150] F. Liu, W. J. Dan, and W. G. Zhang, "Strain hardening model of twinning induced plasticity steel at different temperatures," *Mater. Des.*, vol. 65, pp. 737–742, 2015, doi: 10.1016/j.matdes.2014.10.008.

[151] L. Huang, J. Lu, and M. Troyon, "Nanomechanical properties of nanostructured titanium prepared by SMAT," *Surf. Coatings Technol.*, vol. 201, no. 1–2, pp. 208–213, 2006, doi: 10.1016/j.surfcoat.2005.11.090.

[152] N. Lecain, "Tutorial of Hertzian Contact Stress Analysis," *Coll. Opt. Sci. Univ. Arizona, Tucson, AZ USA 85721*, vol. 6, no. 3, pp. 1–8, 2011, [Online]. Available: https://www.windpowerengineering.com/how-to-maintain-wind-turbine-gearbox-oil-health/.

[153] B. K. C. Ganesh, W. Sha, N. Ramanaiah, and A. Krishnaiah, "Effect of shotpeening on sliding wear and tensile behavior of titanium implant alloys," *Mater. Des.*, vol. 56, pp. 480–486, 2014, doi: 10.1016/j.matdes.2013.11.052.

[154] X. Yang, J. Zhou, and X. Ling, "Study on plastic damage of AISI 304 stainless steel induced by ultrasonic impact treatment," *Mater. Des.*, vol. 36, pp. 477–481, 2012, doi: 10.1016/j.matdes.2011.11.023.

[155] I. Doghri, "Numerical implementation and analysis of a class of metal plasticity models coupled with ductile damage," *Int. J. Numer. Methods Eng.*, vol. 38, no. 20, pp. 3403–3431, 1995, doi: 10.1002/nme.1620382004.

[156] P. K. Zysset and A. Curnier, "An implicit projection algorithm for simultaneous flow of plasticity and damage in standard generalized materials," *Int. J. Numer. Methods Eng.*, vol. 39, no. 18, pp. 3065–3082, 1996, doi: 10.1002/(SICI)1097-0207(19960930)39:18<3065::AID-NME997>3.0.CO;2-8.

[157] J. F. Charles, Y. Y. Zhu, A. M. Habraken, S. Cescotto, and M. Traversin, "A fully coupled elasto-plastic damage theory for anisotropic materials," *Stud. Appl. Mech.*, vol. 45, no. C, pp. 33–42, 1997, doi: 10.1016/S0922-5382(97)80005-0.

[158] J. Mahieu, J. Maki, B. C. De Cooman, and S. Claessens, "Phase transformation and mechanical properties of Si-free CMnAI transformatio ...," *Metall. Mater. Trans. A Phys. Metall. Mater. Sci.* , vol. 33, no. August, pp. 2573–2580, 2002, [Online]. Available: https://www.scopus.com/inward/record.uri?eid=2-s2.0-0036695762&partnerID=40&md5=aefbacabd399c5900b97c1f9704b47fe.

[159] A. G. Franklin, "Comparison between a quantitative microscope and chemical methods," *J. Iron Steel Inst.*, vol. 207, no. 2, pp. 181–186, 1969.

[160] N. K. Nichols, "On the numerical integration of a class of singular perturbation problems," *J. Optim. Theory Appl.*, vol. 60, no. 3, pp. 439–452, 1989, doi: 10.1007/BF00940347.

[161] B. C. Simonsen and S. Li, "Mesh-free simulation of ductile fracture," *Int. J. Numer. Methods Eng.*, vol. 60, no. 8, pp. 1425–1450, 2004, doi:

10.1002/nme.1009.
[162] M. J. Worswick and P. Pelletier, “Numerical simulation of ductile fracture during high strain rate deformation,” *EPJ Appl. Phys.*, vol. 4, no. 3, pp. 257–267, 1998, doi: 10.1051/epjap:1998269.
[163] L. Xue, “Constitutive modeling of void shearing effect in ductile fracture of porous materials,” *Eng. Fract. Mech.*, vol. 75, no. 11, pp. 3343–3366, 2008, doi: 10.1016/j.engfracmech.2007.07.022.
[164] W. Qi, H. Kelei, and L. Qishao, “Implicit numerical algorithm for multibody dynamics with constraint equations [J],” *Chinese J. Comput. Mech.*, vol. 4, 1999.
[165] D. Jin and S. Lin, *Advances in Mechanical and Electronic Engineering*, vol. 177 LNEE, no. VOL. 2. Springer, 2012.
[166] M. Palengat, G. Chagnon, D. Favier, H. Louche, C. Linardon, and C. Plaideau, “Cold drawing of 316L stainless steel thin-walled tubes: Experiments and finite element analysis,” *Int. J. Mech. Sci.*, vol. 70, pp. 69–78, 2013, doi: 10.1016/j.ijmecsci.2013.02.003.
[167] S. Sinha, J. A. Szpunar, N. A. P. Kiran Kumar, and N. P. Gurao, “Tensile deformation of 316L austenitic stainless steel using in-situ electron backscatter diffraction and crystal plasticity simulations,” *Mater. Sci. Eng. A*, vol. 637, pp. 48–55, 2015, doi: 10.1016/j.msea.2015.04.005.
[168] T. N. Nguyen, T. Siegmund, V. Tomar, and J. J. Kruzic, “Interaction of rate- and size-effect using a dislocation density based strain gradient viscoplasticity model,” *J. Mech. Phys. Solids*, vol. 109, pp. 1–21, 2017, doi: 10.1016/j.jmps.2017.07.022.
[169] A. Kami, B. M. Dariani, A. Sadough Vanini, D. S. Comsa, and D. Banabic, “Numerical determination of the forming limit curves of anisotropic sheet metals using GTN damage model,” *J. Mater. Process. Technol.*, vol. 216, pp. 472–483, 2015, doi: 10.1016/j.jmatprotec.2014.10.017.
[170] M. K. Samal, K. Balani, M. Seidenfuss, and E. Roos, “An experimental and numerical investigation of fracture resistance behaviour of a dissimilar metal welded joint,” *Proc. Inst. Mech. Eng. Part C J. Mech. Eng. Sci.*, vol. 223, no. 7, pp. 1507–1523, 2009, doi: 10.1243/09544062JMES1416.
[171] L. Zhang, R. Hebert, J. T. Wright, A. Shukla, and J. H. Kim, “Dynamic response of corrugated sandwich steel plates with graded cores,” *Int. J. Impact Eng.*, vol. 65, pp. 185–194, 2014, doi: 10.1016/j.ijimpeng.2013.11.011.
[172] M. Ahmed, D. Wexler, G. Casillas, D. G. Savvakin, and E. V. Pereloma, “Strain rate dependence of deformation-induced transformation and twinning in a metastable titanium alloy,” *Acta Mater.*, vol. 104, pp. 190–200, 2016, doi: 10.1016/j.actamat.2015.11.026.
[173] S. S. S. Kumar, T. Raghu, P. P. Bhattacharjee, G. A. Rao, and U. Borah, “Strain rate dependent microstructural evolution during hot deformation of a hot isostatically processed nickel base superalloy,” *J. Alloys Compd.*, vol. 681, pp. 28–42, 2016, doi: 10.1016/j.jallcom.2016.04.185.
[174] Y. Wan, B. Sun, and B. Gu, “Multi-scale structure modeling of damage behaviors of 3D orthogonal woven composite materials subject to quasi-static and high strain rate compressions,” *Mech. Mater.*, vol. 94, pp. 1–25, 2016, doi: 10.1016/j.mechmat.2015.11.012.
[175] Z. Q. Liu, R. T. Qu, and Z. F. Zhang, “Elasticity dominates strength and failure in metallic glasses,” *J. Appl. Phys.*, vol. 117, no. 1, p. 14901, 2015, doi: 10.1063/1.4905349.

[176] Q. Q. Duan, B. Wang, P. Zhang, K. Yang, and Z. F. Zhang, “Improvement of notch fatigue properties of ultra-high CM400 maraging steel through shot peening,” *J. Mater. Res.*, vol. 32, no. 23, pp. 4424–4432, 2017, doi: 10.1557/jmr.2017.358.

[177] K. Dai and L. Shaw, “Analysis of fatigue resistance improvements via surface severe plastic deformation,” *Int. J. Fatigue*, vol. 30, no. 8, pp. 1398–1408, 2008, doi: 10.1016/j.ijfatigue.2007.10.010.

[178] Y. Wang and Y. T. Cheng, “A nanoindentation study of the viscoplastic behavior of pure lithium,” *Scr. Mater.*, vol. 130, pp. 191–195, 2017, doi: 10.1016/j.scriptamat.2016.12.006.

[179] X. Chen, I. A. Ashcroft, R. D. Wildman, and C. J. Tuck, “A combined inverse finite element – elastoplastic modelling method to simulate the size-effect in nanoindentation and characterise materials from the nano to micro-scale,” *Int. J. Solids Struct.*, vol. 104–105, pp. 25–34, 2017, doi: 10.1016/j.ijsolstr.2016.11.004.

[180] X. Xiao, L. Chen, L. Yu, and H. Duan, “Modelling nano-indentation of ion-irradiated FCC single crystals by strain-gradient crystal plasticity theory,” *Int. J. Plast.*, vol. 116, pp. 216–231, 2019, doi: 10.1016/j.ijplas.2019.01.005.

[181] D. T. Pierce, K. Nowag, A. Montagne, J. A. Jimenez, J. E. Wittig, and R. Ghisleni, “Single Crystal Elastic Constants of TWIP Steel Determined From Nanoindentation,” *Microsc. Microanal.*, vol. 19, no. S2, pp. 1052–1053, 2013, doi: 10.1017/s1431927613007253.

[182] K. Li *et al.*, “Strain rate dependence on the evolution of microstructure and deformation mechanism during nanoscale deformation in low carbon-high Mn TWIP steel,” *Mater. Sci. Eng. A*, vol. 742, pp. 116–123, 2019, doi: 10.1016/j.msea.2018.11.006.

[183] J. L. Zhang, S. Zaefferer, and D. Raabe, “A study on the geometry of dislocation patterns in the surrounding of nanoindents in a TWIP steel using electron channeling contrast imaging and discrete dislocation dynamics simulations,” *Mater. Sci. Eng. A*, vol. 636, pp. 231–242, 2015, doi: 10.1016/j.msea.2015.03.078.

[184] A. F. Gerday, M. Ben Bettaieb, L. Duchêne, N. Clément, H. Diarra, and A. M. Habraken, “Interests and limitations of nanoindentation for bulk multiphase material identification: Application to the β phase of Ti-5553,” *Acta Mater.*, vol. 57, no. 17, pp. 5186–5195, 2009, doi: 10.1016/j.actamat.2009.07.020.

[185] N. Zaafarani, D. Raabe, R. N. Singh, F. Roters, and S. Zaefferer, “Three-dimensional investigation of the texture and microstructure below a nanoindent in a Cu single crystal using 3D EBSD and crystal plasticity finite element simulations,” *Acta Mater.*, vol. 54, no. 7, pp. 1863–1876, 2006, doi: 10.1016/j.actamat.2005.12.014.

[186] G. B. Viswanathan, E. Lee, D. M. Maher, S. Banerjee, and H. L. Fraser, “Direct observations and analyses of dislocation substructures in the α phase of an α/β Ti-alloy formed by nanoindentation,” *Acta Mater.*, vol. 53, no. 19, pp. 5101–5115, 2005, doi: 10.1016/j.actamat.2005.07.030.

[187] Z. Chen, Z. Sun, D. Retraint, and B. Panicaud, “Numerical simulations of impacts during Surface Mechanical Attrition Treatment using crystal plasticity model in finite element method,” in *Congrès français de mécanique*, 2017.

[188] G. Olson and M. Cohen, “Dislocation theory of martensitic transformations,” in *Dislocations in solids*, North-Holland, 1986, p. 117.

[189] M. R. Stoudt, L. E. Levine, A. Creuziger, and J. B. Hubbard, “The fundamental

relationships between grain orientation, deformation-induced surface roughness and strain localization in an aluminum alloy," *Mater. Sci. Eng. A*, vol. 530, no. 1, pp. 107–116, 2011, doi: 10.1016/j.msea.2011.09.050.

[190] J. Kim, Y. Estrin, and B. C. De Cooman, "Application of a dislocation density-based constitutive model to Al-alloyed TWIP steel," *Metall. Mater. Trans. A Phys. Metall. Mater. Sci.*, vol. 44, no. 9, pp. 4168–4182, 2013, doi: 10.1007/s11661-013-1771-2.

[191] C. Braccesi, F. Cianetti, G. Lori, and D. Pioli, "An equivalent uniaxial stress process for fatigue life estimation of mechanical components under multiaxial stress conditions," *Int. J. Fatigue*, vol. 30, no. 8, pp. 1479–1497, 2008, doi: 10.1016/j.ijfatigue.2007.09.011.

[192] Y. Estrin, "Dislocation-density-related constitutive modeling," *Unified Const. laws Plast. Deform.*, vol. 1, pp. 69–106, 1996.

[193] B. Devincre, T. Hoc, and L. Kubin, "Dislocation mean free paths and strain hardening of crystals," *Science (80-.).*, vol. 320, no. 5884, pp. 1745–1748, 2008, doi: 10.1126/science.1156101.

[194] Z. S. You, L. Lu, and K. Lu, "Tensile behavior of columnar grained Cu with preferentially oriented nanoscale twins," *Acta Mater.*, vol. 59, no. 18, pp. 6927–6937, 2011, doi: 10.1016/j.actamat.2011.07.044.

[195] S. Shu, J. Lu, and D. Li, "A systematic study of the validation of Oliver and Pharr's method," *J. Mater. Res.*, vol. 22, no. 12, pp. 3385–3396, 2007, doi: 10.1557/jmr.2007.0428.

[196] D. Bernoulli, S. C. Cao, J. Lu, and M. Dao, "Enhanced repeated frictional sliding properties in 304 stainless steel with a gradient nanostructured surface," *Surf. Coatings Technol.*, vol. 339, pp. 14–19, 2018, doi: 10.1016/j.surfcoat.2018.01.081.

[197] Y. Wu, B. Guelorget, Z. Sun, R. Déturche, and D. Retraint, "Characterization of gradient properties generated by SMAT for a biomedical grade 316L stainless steel," *Mater. Charact.*, vol. 155, p. 109788, 2019.

[198] H. Q. Sun, Y. N. Shi, M. X. Zhang, and K. Lu, "Plastic strain-induced grain refinement in the nanometer scale in a Mg alloy," *Acta Mater.*, vol. 55, no. 3, pp. 975–982, 2007, doi: 10.1016/j.actamat.2006.09.018.

[199] D. K. Patel and S. R. Kalidindi, "Correlation of spherical nanoindentation stress-strain curves to simple compression stress-strain curves for elastic-plastic isotropic materials using finite element models," *Acta Mater.*, vol. 112, pp. 295–302, 2016, doi: 10.1016/j.actamat.2016.04.034.

[200] Q. Feng, C. Jiang, Z. Xu, L. Xie, and V. Ji, "Effect of shot peening on the residual stress and microstructure of duplex stainless steel," *Surf. Coatings Technol.*, vol. 226, pp. 140–144, 2013, doi: 10.1016/j.surfcoat.2013.03.047.

[201] M. Chemkhi, "Nanocristallisation superficielle couplée à la nitruration plasma pour augmenter les propriétés de fatigue et d'usure d'alliages métalliques." Troyes, 2014.

[202] A. N. Eraslan, "Von Mises' yield criterion and nonlinearly hardening rotating shafts," *Acta Mech.*, vol. 168, no. 3–4, pp. 129–144, 2004, doi: 10.1007/s00707-004-0088-z.

[203] D. Banabic, "Limit strains in the sheet metals by using the new Hill's yield criterion (1993)," *J. Mater. Process. Technol.*, vol. 92–93, pp. 429–432, 1999, doi: 10.1016/S0924-0136(99)00179-X.

[204] G. M. Pharr, "An improved technique for determining hardness and elastic modulus using load and displacement sensing indentation experiments," *J.*

Mater. Res., vol. 7, no. 6, pp. 1564–1583, 1992, doi: 10.1557/JMR.1992.1564.

[205] D. Tumbajoy-Spinel, S. Descartes, J. M. Bergheau, H. Al-Baida, C. Langlade, and G. Kermouche, "Investigation of graded strengthened hyper-deformed surfaces by impact treatment: Micro-percussion testing," in *IOP Conference Series: Materials Science and Engineering*, 2017, vol. 194, no. 1, p. 12024, doi: 10.1088/1757-899X/194/1/012024.

[206] D. Tumbajoy-Spinel *et al.*, "Microstructural and micromechanical investigations of surface strengthening mechanisms induced by repeated impacts on pure iron," *Mater. Des.*, vol. 147, pp. 56–64, 2018, doi: 10.1016/j.matdes.2018.03.014.

[207] J. Li, G. J. Weng, S. Chen, and X. Wu, "On strain hardening mechanism in gradient nanostructures," *Int. J. Plast.*, vol. 88, pp. 89–107, 2017, doi: 10.1016/j.ijplas.2016.10.003.

[208] S. Dong, J. Zhou, D. Hui, Y. Wang, and S. Zhang, "Size dependent strengthening mechanisms in carbon nanotube reinforced metal matrix composites," *Compos. Part A Appl. Sci. Manuf.*, vol. 68, pp. 356–364, 2015, doi: 10.1016/j.compositesa.2014.10.018.

[209] J. S. Lewis, W. J. Lackey, and S. Vaidyaraman, "Model for prediction of matrix microstructure for carbon/carbon composites prepared by forced flow-thermal gradient CVI," *Carbon N. Y.*, vol. 35, no. 1, pp. 103–112, 1997, doi: 10.1016/S0008-6223(96)00121-2.

[210] B. Akgöz and Ö. Civalek, "A microstructure-dependent sinusoidal plate model based on the strain gradient elasticity theory," *Acta Mech.*, vol. 226, no. 7, pp. 2277–2294, 2015, doi: 10.1007/s00707-015-1308-4.

[211] A. Le Pécheur, F. Curtit, M. Clavel, J. M. Stephan, C. Rey, and P. Bompard, "Thermo-mechanical FE model with memory effect for 304L austenitic stainless steel presenting microstructure gradient," *Int. J. Fatigue*, vol. 45, pp. 106–115, 2012, doi: 10.1016/j.ijfatigue.2012.05.016.

[212] L. Zhu, H. Ruan, A. Chen, X. Guo, and J. Lu, "Microstructures-based constitutive analysis for mechanical properties of gradient-nanostructured 304 stainless steels," *Acta Mater.*, vol. 128, pp. 375–390, 2017, doi: 10.1016/j.actamat.2017.02.035.

Zhenglin CHEN

Doctorat : Matériaux, Mécanique, Optique, Nanotechnologie

Année 2020

Modélisation de l'évolution de microstructures induite par SMAT pour des aciers TWIP/TRIP

Ce travail est centré sur la modélisation de l'évolution de microstructures induite par le procédé SMAT pour des aciers TWIP/TRIP. Les caractéristiques de base d'un acier TWIP/TRIP sont mises en évidence par MEB, DRX et nanoindentation. La nanoindentation est appliquée sur différentes couches pour l'étude des propriétés mécaniques du matériau à gradient de microstructure. Un modèle basé sur la densité de dislocations tenant compte de l'influence du maclage et de la transformation de phase martensitique dans un acier TWIP/TRIP est proposé pour étudier l'influence des paramètres induits par SMAT. Ensuite, la densité de dislocations dans l'austénite et celle dans la martensite ainsi que les fractions volumiques de macles et de martensite au cours d'un impact sont évaluées numériquement avec un modèle d'éléments finis. Par ailleurs, afin d'étudier l'évolution de l'endommagement pendant le processus d'impact, l'endommagement a été introduit dans le modèle de la densité de dislocations. Enfin, un modèle visco-élastoplastique basé sur la densité de dislocations considérant l'effet de la taille de grain, le maclage et le taux de déformation a été proposé afin de mieux comprendre les effets du SMAT sur les propriétés mécaniques d'un acier TWIP/TRIP avec gradient de microstructure. Ainsi, pour étudier la réponse globale du matériau SMATé, la loi de mélange est utilisée en considérant le gradient du matériau comme une structure composée de différentes couches avec des microstructures et des propriétés mécaniques différentes.

Mots clés : SMAT – dislocations dans les cristaux – maclage (cristallographie) – acier inoxydable – transformations martensitiques.

Modeling of Microstructure Evolution Induced by Surface Mechanical Attrition Treatment in TWIP/TRIP Steels

This work focuses on modeling the microstructure evolution induced by SMAT in TWIP and/or TRIP steels. The features of the generated gradient microstructure of a 304L TWIP/TRIP steel are characterized by SEM, XRD, and nanoindentation. Nanoindentation is applied on different layers for the investigation of the mechanical properties of the gradient microstructure. Based on the experimental results, a dislocation density model considering the influence of twinning and martensitic transformation of TWIP/TRIP steel is proposed to investigate the effect of SMAT controlling parameters. Then the dislocation density of the austenite and that of the martensite as well as the volume fraction of twinning and martensitic transformation during impact loading is numerically evaluated using a full finite element model. Afterwards, to study the evolution of the damage during the SMAT process, the damage was introduced in the dislocation density model. Finally, a dislocation density based visco-elastoplastic model considering the effect of grain size, dislocation density, twin, and strain rate was proposed to further understand the effect of impact loadings on the mechanical properties of TWIP/TRIP steel with gradient microstructure based on the results of nanoindentation tests. Then to study the overall elastoplastic response of the SMATed material, the rule of mixtures is used by considering the gradient material as a gradient structure consisting of different layers with distinct microstructures and mechanical properties.

Keywords: SMAT – dislocations in crystals – twinning (crystallography) – steel, stainless – martensitic transformations.

Thèse réalisée en partenariat entre :

Ecole Doctorale "Sciences pour l'Ingénieur"